Intramolecular Charge Transfer and Proton Transfer in Heterogeneous Environments

A dissertation

As partial fulfilment for the degree of

Doctor of philosophy in Chemistry

By

Ashim Malakar
10612203

Department of Chemistry

Indian Institute of Technology Guwahati

Guwahati 781039

Assam, India

Statement

The work contained in this thesis entitled "**Intramolecular Charge Transfer and Proton Transfer in Heterogeneous Environments**" is the outcome of the research work carried out by me under the supervision of Dr. G Krishnamoorthy, Department of Chemistry, Indian Institute of Technology Guwahati, India.

In the present thesis the general practice of the scientific observations are reported and whenever needed, the work on the findings of other investigations are described and thus due acknowledgements have been made.

27th December, 2017

Ashim Malakar

Department of Chemistry

IIT Guwahati

Guwahati Assam, India-781039

Dr. G. Krishnamoorthy
Associate Dean, Research & Development
& Professor of Chemistry

INDIAN INSTITUTE OF TECHNOLOGY GUWAHATI
Guwahati 781 039, Assam, India
Tel: +91 – 0361 – 258 2315 (W), 258 4315 (H)
Fax: +91 – 0361 – 2582349
E-mail: gkrishna@iitg.ernet.in, gkrishna_2000@yahoo.com

Certificate

It is certified that the work contained in thesis entitled "**Intramolecular Charge Transfer and Proton Transfer in Heterogeneous Environments**" by Ashim Malakar is an authentic record of the results obtained from the research work carried out under my supervision in the Department of Chemistry, Indian Institute of Technology Guwahati, India.

Guwahati
28 December 2017

G. Krishnamoorthy

Dedicated to my

Family

ACKNOWLEDGEMENT

Working for the accomplishment of this thesis has been the most incredible journey of my life, which would not have been possible without these people.

First and foremost, I would like to thank my thesis supervisor Dr. G Krishnamoorthy for giving me an opportunity to work in a very interesting area of research. I am very grateful to him for his continuous guidance, important advices and stimulating discussions. In spite of his busy schedule, he always happily spent time to analyze the problems and gave needed suggestions for the betterment of my work. Some of his remarkable qualities such as, patience and devotion towards his work, his continuous zeal to achieve perfection, and a very attractive communication skill, will always inspire me. The experience of working with him will definitely have far-reaching influence in my life. I consider it an honor to work under him.

I would like to express my deepest gratitude to Dr. Biman B Mandal and K. Anki Reddy for his valuable help during the course of my research work.

I wish to thank my doctoral committee members, Prof. V. Manivannan and Prof. Mohammad Qureshi, Department of Chemistry and Prof. R swaminathan, Department of Bioscience and bioengineering, for their valuable suggestions and efforts during my thesis work.

My sincere thanks to Dr. Nihar dash, Dr. Francis A S Chipem and Dr. Anasuya Mishra, alumni from our research group for their co-operative assistance in learning the basic concepts and providing me with continuous encouragement throughout my PhD tenure. Also, I am particularly grateful to Saugata Santosh for their supports in experiments and computations. I am also thankful to all of our research group members Minati, Himadree, Ila for their constant help in the Lab. I cannot forget to thank my friends Seim da, Kiran, Manash Sanjay, Subrat, Saty, Romen, Abu da for their lovely support in making my stay at IIT Guwahati memorable.

I like to thank my colleague Deep for his constant encouragement to complete this tiresome journey. My special thanks goes to all the faculty and staff members of Department of Chemistry and Central Instruments Facility, IIT Guwahati, for their supports and co-operations during all this time.

Last but not the least, I am thankful from my heart to my wife Sangita and mother for constant support and encouragement to survive every hurdle of my life.

Ashim Malakar

SYNOPSIS

Intramolecular Charge Transfer and Proton Transfer In Heterogeneous Environments

Intramolecular charge transfer (ICT) and proton transfer (PT) are fundamental ultrafast processes those occurs upon photo excitation of molecules. They often lead to dual emission from the normal state and the ICT/tautomer state. Fluorophores comprising of electron donor and electron acceptor group connected by a single bond, upon excitation to local excited state undergoes ICT that may lead to an ICT state. Among various hypothesis put forward, the twisted ICT (TICT) model proposed by Grabowski et al. is the wide accepted one. In TICT mechanism the donor group undergoes rotation to form a perpendicular geometry with respect to the rest of the molecule giving a more polar and stable state called TICT state. Excited state intramolecular proton transfer (ESIPT) occurs in systems where an acidic group and a basic group are linked by a hydrogen bond. Upon excitation, the acidity of the acidic group and the basicity of the basic group increases which results in a tautomer in the excited state. The TICT and the tautomer emissions are highly stoke shifted and are very sensitive to environment. Controlling these emissions by different heterogeneous media will be interesting in the field of sensing and other applications. The enhanced emission can be achieved through molecular aggregation. The behaviour of a few ICT and ESIPT molecules in heterogeneous environments are investigated in this thesis. In addition, aggregation induced enhanced emission (AIEE) of the ESIPT molecules are studied. The thesis is divided into seven chapters and contents are briefed below:

Chapter 1: Introduction

Chapter 1 gives a short account of ICT and ESIPT processes. The brief literature review of fluorophore-nanoparticle interaction and AIEE are also included in this chapter. The chapter ends with scope of the present work.

Chapter 2: Materials, method and instrumentation

Chapter 2 provides the details of the materials used in the present work and the methods used for the analysis, calculations and preparation of the samples. In addition, short

descriptions of UV-Visible absorption spectrophotometer, steady-state and time resolved fluorimeters, field emission scanning electron microscope (FESEM) and transmission electron microscopy (TEM) are presented.

Chapter 3: Silvernanoparticles induced dual emission from 2-(4′-N, N dimethylaminophenyl)pyridoimidazole: Enhanced TICT emission in β-Cyclodextrin.

In this chapter the interactions of the silver nanoparticles with 2-(4′-N,N-dimethylaminophenyl) benzimidazole and its nitrogen substituted analogues, 2-(4′-N,N-dimethylaminophenyl) pyridoimidazoles are investigated by absorption, steady-state and time resolved fluorescence, FESEM and TEM techniques.

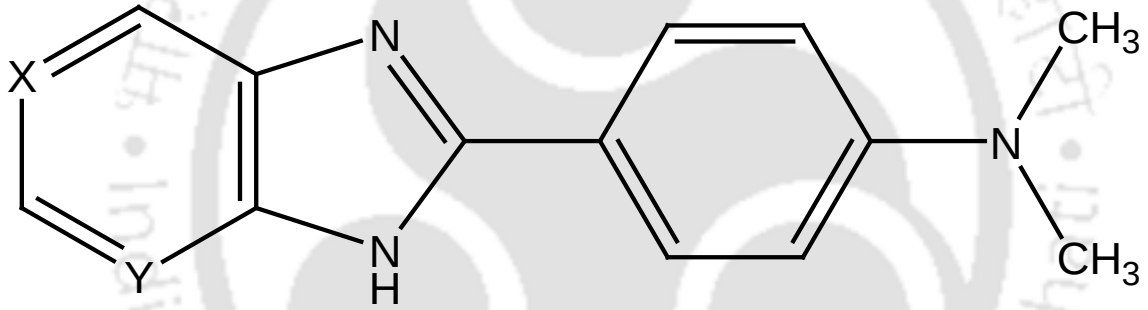

X = Y = CH DMAPBI

X = CH, Y = N DMAPIP-b

X = N, Y = CH DMAPIP-c

Chart 1. Structures of DMAPBI, DMAPIP-b and DMAPIP-c.

The surface plasmon resonance band, FESEM and TEM images of the particles suggest that the fluorophores can stabilize the nanoparticles even in the absence of any other stabilizing agent. On the other hand, in the absence of fluorophores the nanoparticles are unstable and coagulate. In contrary to the earlier literature reports that interactions of nanoparticles with ICT or TICT species quenches their fluorescence, to the best of our knowledge, the first ever formation of TICT state by interactions of nanoparticles with the fluorophores is observed. The formation of TICT state in 2-(4′-N, N-dimethylaminophenyl)pyridoimidazoles results in dual emission. The TICT emissions from

the nanoparticle-fluorophore complexes are weak. But the emissions become prominent upon complexation with β-cyclodextrin.

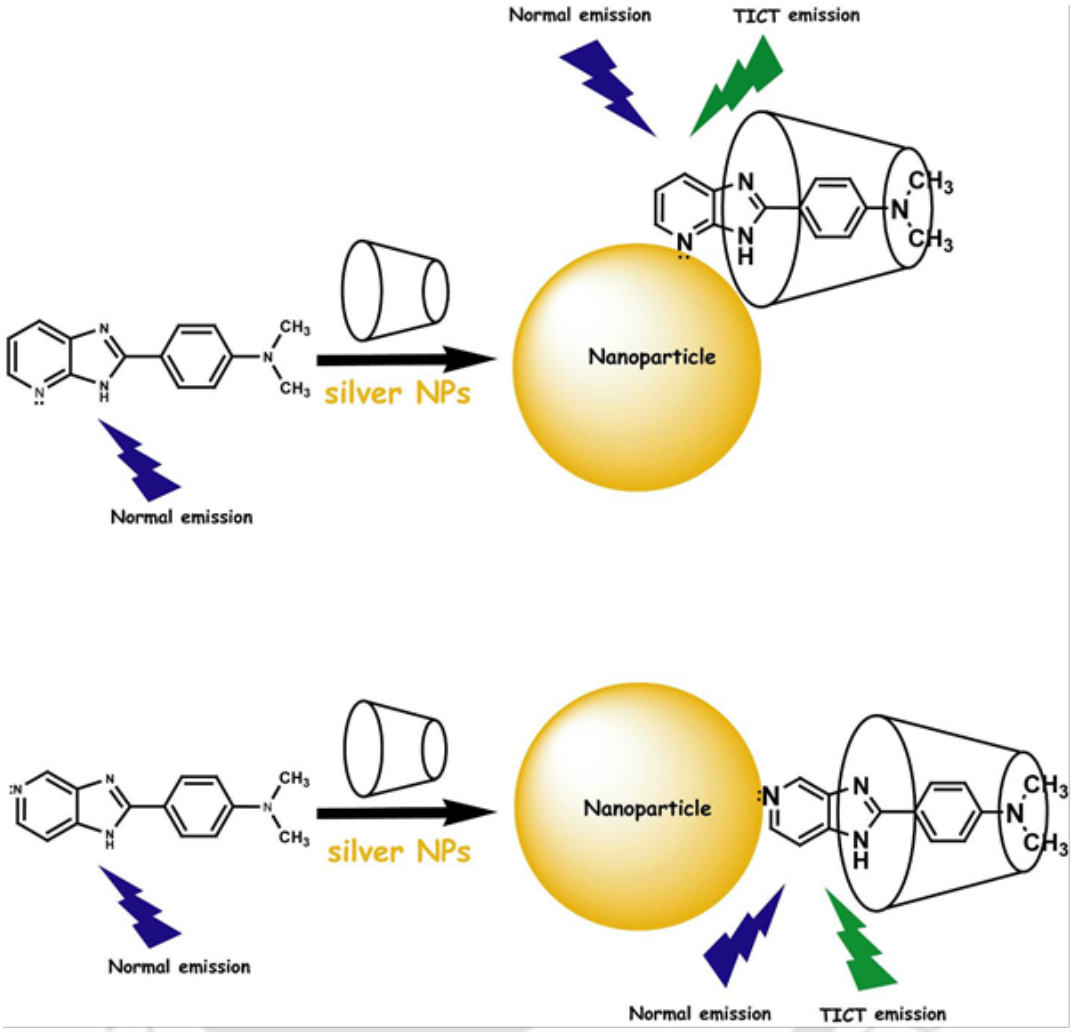

Figure 1: Schematic representation of complex formation and dual emission

Chapter 4: Extraction of fluorophores from nanoparticles composite by micelles

Silver nanoparticles in water were prepared by reducing silver nitrate salt using simple borohydride reduction method without any other common stabilizing agent. The hydroxyl ion present in solution acted as stabilizer at specific pH of 10. The ICT fluorophores used in the chapter 3 are used for the studies in present chapter.

All three fluorophores interact with silver nanoparticles prepared in water through the ring nitrogen. Static quenching was observed for all the fluorophores. The fluorescence of the fluorophores can be recovered by addition of surfactant. The micelle separates the

nanoparticles and extract the fluorophores from the nanocomposite. The micelles were found to be well efficient to extract the fluorophores from the nanoparticles surface into their hydrophobic cavities. It seems that the CTAB has stronger interaction with the nanoparticles than TX-100. Compared to TX-100, nearly one fifteen of the CTAB concentration is sufficient to equalize the original intensity. The enhancement in the TICT emission of DMAPIP-c is more than that of its normal emission

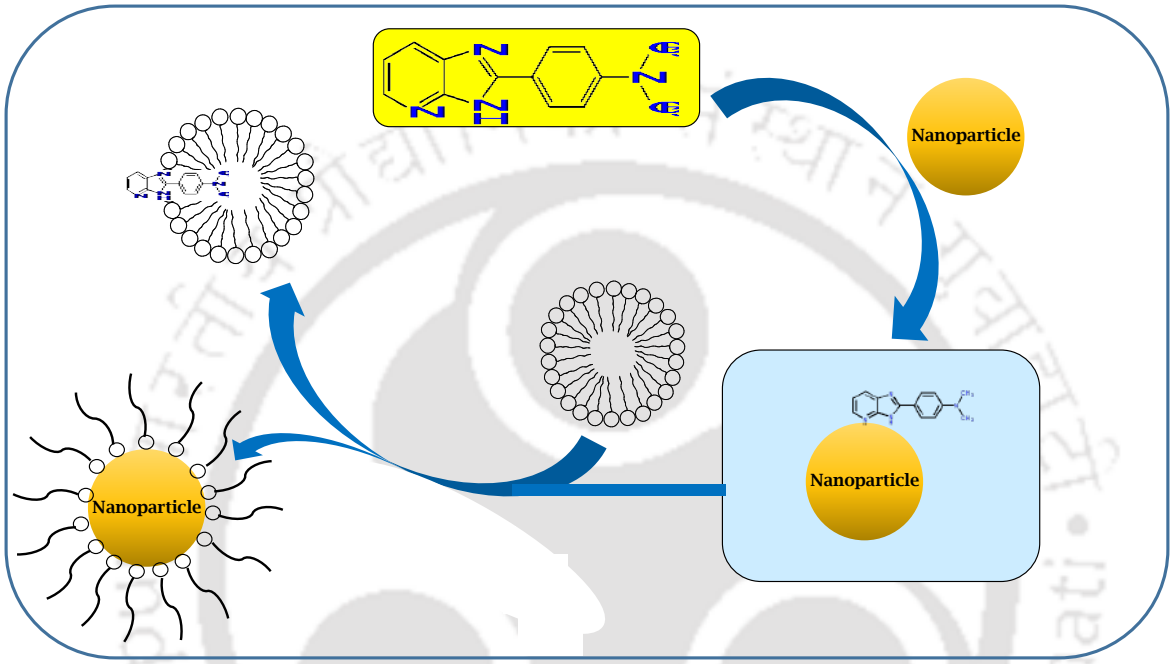

Figure 2: Schematic representation of extraction of fluorophores from the nanoparticles by micelle.

Chapter 5: Effect of silver nanoparticles on the ICT fluorophores inside BSA

Serum albumins are globular proteins with a high percentage in blood plasma. It is reported that DMAPBI and DMAPIP-b bind inside BSA. The chapter briefs the effect of nanoparticles on the fluorophore-BSA complex. In addition to DMAPBI and DMAPIP-b, DMAPIP-c was also investigated. DMAPBI and DMAPIP-b binds at site I binding site of BSA. Addition of silver nanoparticles to these systems lead to some conformational changes in the tertiary structure of the protein leading to exposure of the fluorophores. The blue shift of the BSA emission in presence of silver nanoparticles confirms the conformational change of the BSA (instead of total denaturation). These fluorophores-nanoparticles interaction resulted in the quenching of the fluorophore emission with bathochromic shift. The

magnitude of the quenching of the fluorescence of the fluorophores by nanoparticles in presence and absence of BSA confirmed that the fluorophores didn't detached from the BSA pocket.

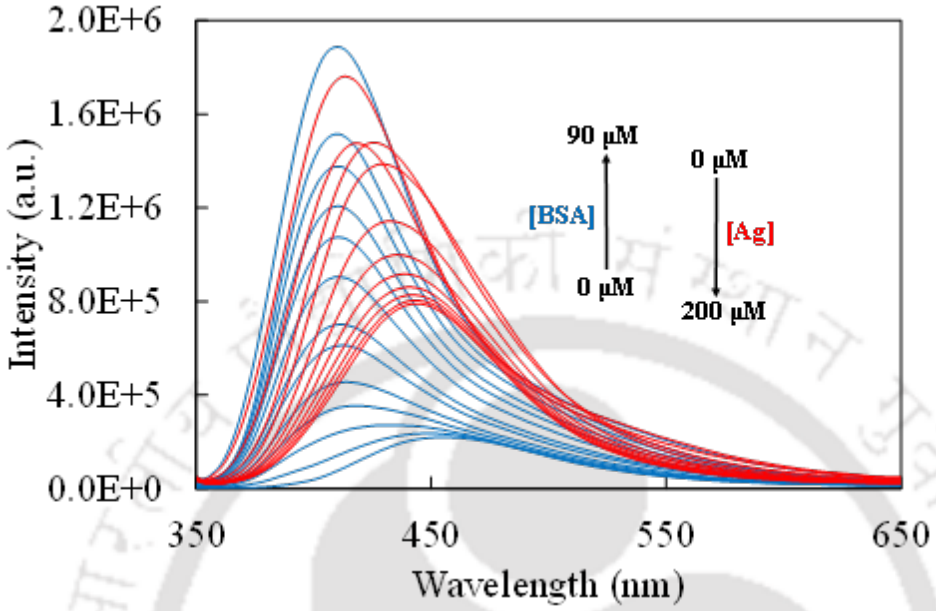

Figure 3: Effect of BSA on DMAPIP-b followed by addition of silver nanoparticles in water.

Chapter 6: Suppression of ESIPT of 2-(2'-hydroxyphenyl)benzimidazole (HPBI) and its nitrogenous analogues on the surface of nanoparticles

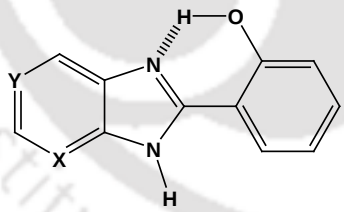

***cis*-Enol**

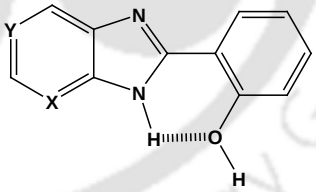

***trans*-Enol**

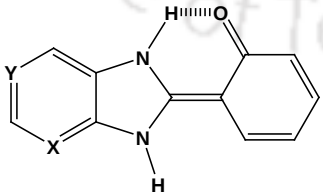

Keto

X = Y= CH HPBI

X = N, Y = CH HPIP-b

X = CH, Y = N HPIP-c

Chart 6.1. Structure of 2-(2′-hydroxyphenyl) benzimdazole (HPBI), 2-(2′-hydroxyphenyl)-3*H*-imidazo-[4, 5-*b*] pyridine (HPIP-b) and 2-(2'-hydroxyphenyl)-3*H*-imidazo-[4,5-*c*] pyridine (HPIP-c).

2-(2'-Hydroxyphenyl)benzimdazole (HPBI) and its nitrogen substituted analogous, 2-(2'-hydroxyphenyl)-3H-imidazo[4,5-b]pyridine (HPIP-b) and 2-(2'-hydroxyphenyl)-3H-imidazo[4,5-c]pyridine (HPIP-c) undergo ESIPT in different environments. The normal emission was obtained from the trans-enol form and the keto emission was observed due to ESIPT of cis-enol. In this chapter, the ESIPT processes of these molecules on surface of silver nanoparticles were elaborated. Silver nanoparticles reduced the fluorescence of both the emissions of HPBI without any significant shift in the spectrum. But the decrease in the fluorescence of HPIP-b and HPIP-c were accompanied by a huge bathochromic shift of the tautomer band. These red shifts indicate that the interactions occurs through the pyridyl nitrogen which increases the conjugation.

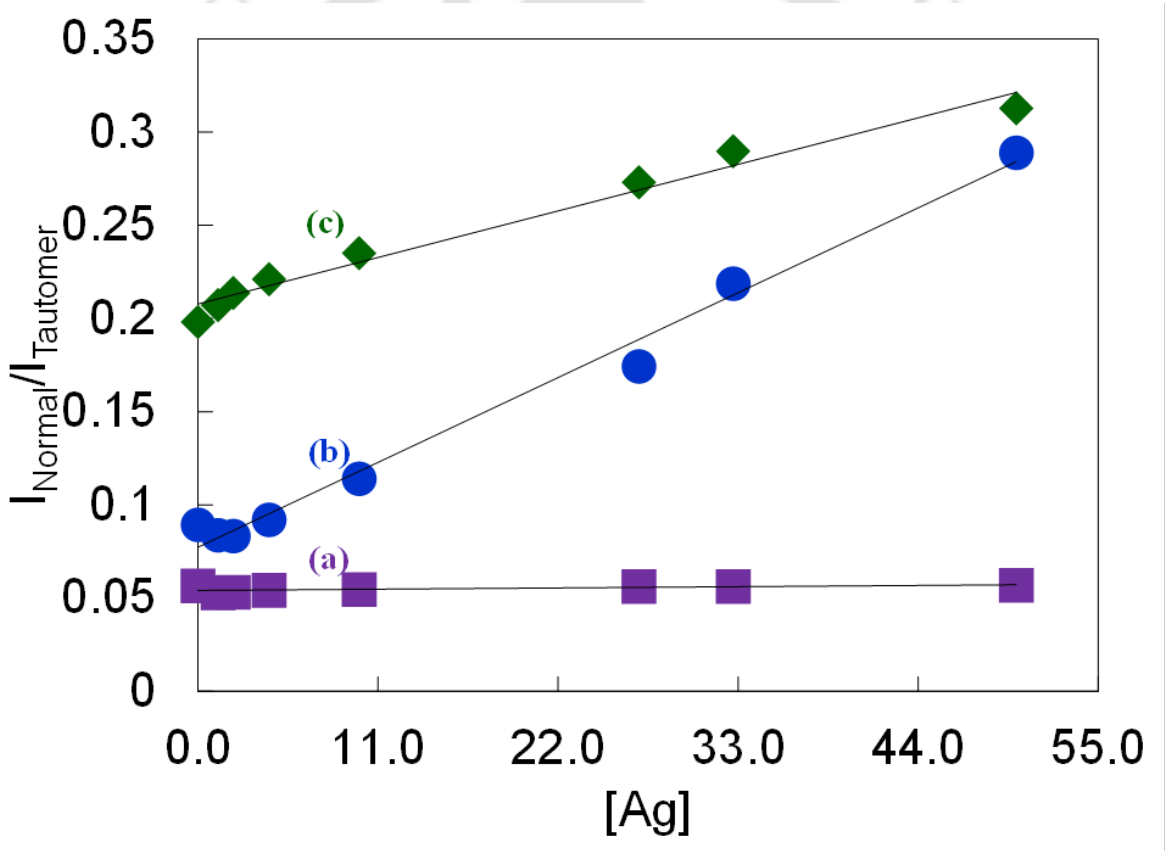

Figure 6.10: Intensity ratio plot of normal band to tautomer band of (a) HPBI, (b) HPIP-c and (c) HPIP-c at different concentrations of silver nanoparticles [0-50 μM]

The intensity ratios depicted that the normal band intensity increases at the cost of tautomer emission in pyridoimidazoles. As the interaction occurs through pyridyl nitrogen, due to conjugation the charge flow from the azole nitrogen to pyridyl nitrogen. This reduces the basicity of the azole nitrogen which weakens the intramolecular hydrogen bond. Therefore,

the ESIPT process was hindered on the surface of nanoparticles. Proton transfer is affected most in HPIP-c followed by HPIP-b and is less in case of HPBI.

Chapter 7: Facilesynthesis of spindles, rods and niddles from 2-(2′-hydroxyphenyl) benzimidazole analogues: Aggregation induced enhanced emission from excited state intramolecular proton transfer

In the previous chapter, it is found that the ESIPT of HPBI and its analogous was suppressed by silver nanoparticles. In this chapter the enhancement of the ESIPT emission from the same set of fluorophores was achieved through aggregation. Compared to their low emissive molecular level, the aggregated structures provide intense emission. This chapter is divided into two sections. First section describes the AIEE of HPBI and its mechanism. The next section elaborates the effect of nitrogen substitution on the aggregation process.

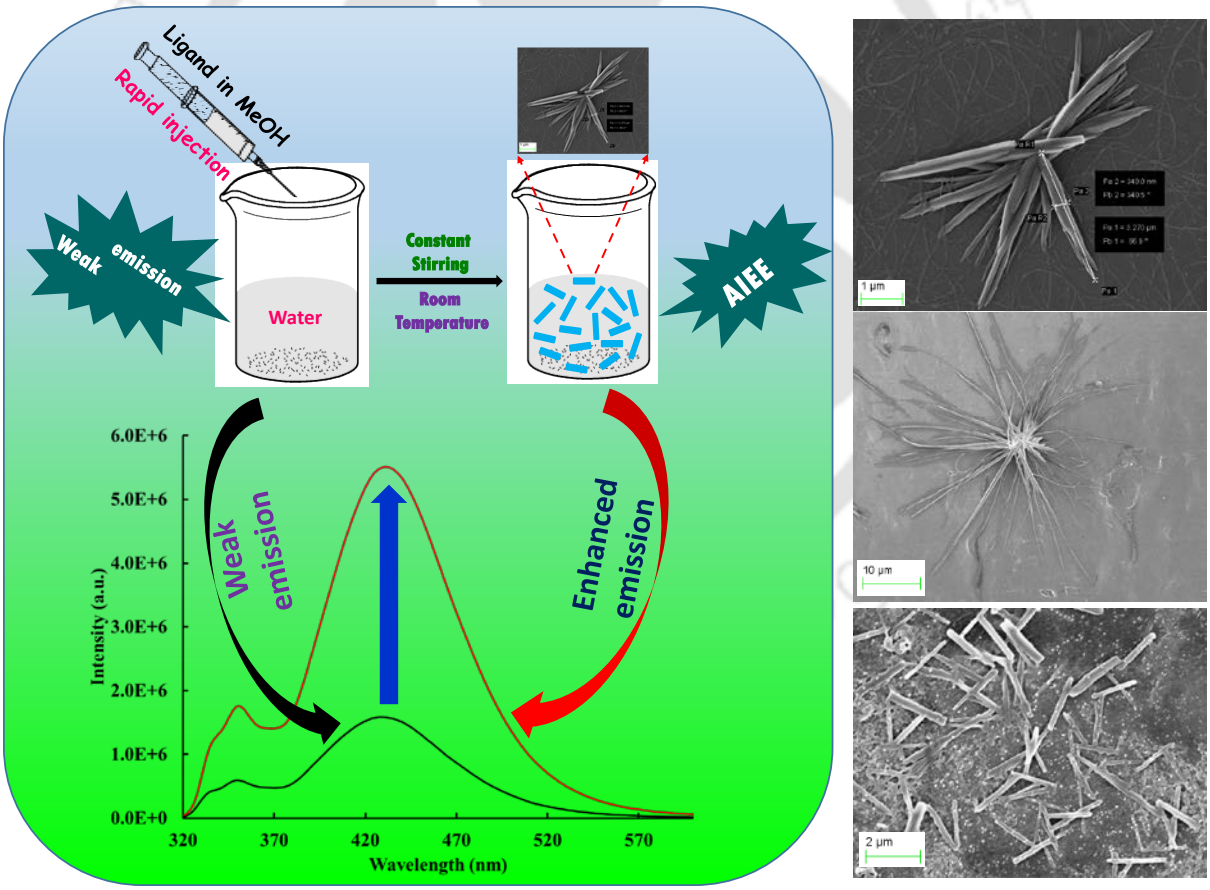

Figure 5: Schematic representation of re-precipitation process and the aggregated products.

The studies reveal that HPBI is capable of emitting AIEE. HPBI aggregates to form spindles shapes and structures were measured to be few hundred nm diameter and few µM long.

Comparative study with 2-phenylbenzimidazole suggests that the presence of hydroxyl group is crucial for AIEE from HPBI. The fluorescence lifetime of the HPBI also increases upon aggregation. The restriction in intramolecular rotations is responsible for the enhanced emission from aggregates. The permeability of the aggregated structures inside the HeLa cells was also studied. These aggregations make HPBI as effective system for cell straining whereas the monomeric compound failed to give any visible fluorescence inside the cells under identical condition. To obtain further insight, molecular simulation were carried out with explicit solvent system. Simulation study also indicates the formation of aggregates. It suggests that both hydrophobic interaction and hydrogen bonding play the roles in the aggregation process. It also reveals that HPBIs exhibit some sort of twisted conformation in the aggregated structure thereby they avert the π-π stacking.

Alike to HPBI, its pyridoimidazoles analogues also emit AIEE. However, nitrogen substitution in benzene ring affected the size and shape of the aggregated structures. HPIP-b aggregated to form long needles, whereas HPIP-c aggregated to form small rods during re-precipitation process. However, alike HPBI, the aggregated structures of its nitrogen substituted analogues exhibit emission within cell whereas their monomers failed to show any fluorescence under same condition.

Chapter 8: Summary and scope for future work

The thesis is summarized in the last chapter and it ends with scope for future work.

Contents

		Page
List of Abbreviation		xxiii
List of Charts		xxv
List of Figures		xxvii
List of Schemes		xxxiii
List of Tables		xxxv
References		xxxvii
Chapter 1: Introduction		
1.1.0.	Fluorescence	3
1.1.1.	Factors affecting fluorescence	3
1.1.2.	Intramolecular charge transfer	4
1.1.2.1.	Factors affecting ICT	5
1.1.3.	Intramolecular proton transfer	6
1.1.3.1.	Factors affecting ESIPT	7
1.2.	Reactions at heterogeneous medium	8
1.2.1.	Metal nanoparticles	8
1.2.2.	Importance of silver	8
1.2.3.	Fluorophore metal nanoparticle interaction	9
1.2.3.1	Fluorescence quenching by nanoparticles	10
1.2.3.2	Fluorescence enhancement by nanoparticles	11
1.2.3.3.	Application of fluorophore-nanoparticles interactions	12
1.3.	Motivation of the present work	14
Chapter 2: Materials, Methods and Instrumentations		
2.0.	Introduction	19
2.1.	Materials	19
2.1.1.	Solvents	19
2.1.2.	Metal Salts	19
2.1.3.	Other Chemicals	19
2.1.4.	Synthesis of silver nanoparticles in DMF	20
2.1.5.	Synthesis of silver nanoparticles in water	21
2.1.6.	Synthesis of organic nanoparticles by re-precipitation Method	23
2.2.	Preparation of Samples	24
2.2.1.	In Solvents	24
2.2.2.	Preparation of fluorophore-nanoparticles solutions	24
2.2.3.	Preparation of protein and micelle samples	24
2.4.	Instruments	25
2.4.1.	pH Meter	25
2.4.2.	Absorption Spectrometer	25
2.4.3.	Steady state spectrofluorimeter	25
2.4.4.	Time Resolved Spectrofluorimeter	27
2.4.5.	Field emission scanning electron microscopy	29

2.4.6.	Transmission Electron Microscopy	32
Chapter 3: Silver nanoparticles induced dual emission from 2-(4′-N,N-dimethylaminophenyl) pyridoimidazole: Enhanced TICT emission in β-Cyclodextrin		
3.0.	Introduction	37
3.1.	Growth and stabilization of the nano particles	38
3.2.	Fluorescence characteristics	40
3.3.	Effect of β cyclodextrin	44
3.4.	Conclusion	48
Chapter 4: Extraction of ICT fluorophores from nanoparticles composite by micelles		
4.0.	Introduction	51
4.1.	Effect of nanoparticles on the fluorophore	51
4.2.	Effect of micelle on fluorophore-nanoparticles composite	53
4.2.1.	Effect of CTAB on the fluorophore-nano composite	53
4.2.2.	Effect of TX-100 on the fluorophore-nano composite	57
4.3.	Conclusion	60
Chapter 5: Effect of silver nanoparticles on the ICT fluorophores inside BSA		
5.0.	Introduction	63
5.1.	Effect of BSA on the fluorophores	63
5.2.	Effect of silver nanoparticles on fluorophore-BSA complex	66
5.3.	Lifetime analysis	72
5.4.	Conclusion	74
Chapter 6: Suppression of ESIPT of 2-(2'-hydroxyphenyl) benzimidazole (HPBI) and its nitrogenous analogues on the surface of nanoparticles		
6.0.	Introduction	77
6.1.	Synthesis and stabilization of the silver nanoparticles	78
6.2.	Characterization from TEM, FESEM and DLS	79
6.3.	Fluorescence characteristics	81
6.4.	Fluorescence Lifetime	88
6.5.	Conclusion	90
Chapter 7: Facile synthesis of spindles, rods and niddles from 2-(2′-hydroxyphenyl) benzimidazole analogues: Aggregation induced enhanced emission from excited state intramolecular proton transfer		
7.0.	Introduction	93
7.1.	Aggregation of HPBI	94
7.1.1.	Absorption characteristics	94
7.1.2.	Fluorescence characteristics	96
7.1.3.	Time resolved fluorescence	98
7.1.4.	Morphology and Imaging	100
7.1.5.	Mechanism of AIEE	104
7.1.6.	Molecular dynamics simulation	105
7.1.7.	Conclusion	109

7.2.	Effect of nitrogen substitution of aggregation	109
7.2.1.	Absorption characteristics	110
7.2.2.	Fluorescence characteristics	112
7.2.3.	Lifetime Analysis	113
7.2.4.	Morphology	114
7.2.5.	Cell Culture and Imaging	116
7.2.6.	Molecular Dynamics Study	118
7.2.7.	Conclusion	123
Chapter 8: Summary and Scope for future work		
8.1.	Summary	127
8.2.	Scope for future work	129

List of Abbreviation

AIEE	Aggregation Induced Emission Enhancement
BSA	Bovine serum albumin
CD	Cyclodextrin
CT	Charge Transfer
CTAB	Cetyltrimethylammonium bromide
DLS	Dynamic Light Scattering
DMABN	Dimethylaminobenznitrile
DMAPBI	2-(4′-N, N-dimethylaminophenyl) benzimidazole
DMAPIP-b	2-(4′-N,N-dimethylaminophenyl) imidazo[4,5-b]pyridine
DMAPIP-c	2-(4′-N,N-dimethylaminophenyl) imidazo[4,5-c]pyridine
DMF	Dimethyl-form amide
EA	Electron Affinity
ESIPT	Excited State Intramolecular Proton Transfer
FESEM	Field Emission Electron Microscopy
HPBI	2-(2′-hydroxyphenyl) benzimdazole and
HPIP-b	2-(2′-hydroxyphenyl)-3H-imidazo-[4, 5-b] pyridine
HPIP-c	2-(2'-hydroxyphenyl)-3H-imidazo-[4,5-c] pyridine
HPLC	High-performance liquid chromatography
ICT	Intramolecular Charge Transfer
IP	Ionization potential
IR	Infra Red
kDa	Kilo Dalton
LASER	Light Amplification by Stimulated Emission of Radiation
LE	Local Excited
MICT	Mesomeric Intramolecular Charge Transfer
NPs	nanoparticles
PMT	photomultiplier tube
PICT	Planner Intramolecular Charge Transfer
RICT	Rehybridized Intramolecular Charge Transfer
SDS	Sodium dodecyl sulfate
SPR	Surface Plasmon Resonance
TCSPC	Time-correlated Single Photon Counting
TEM	Transmission Electron Microscopy
TICT	Twisted Intramolecular Charge Transfer
TX-100	Triton-X 100
UV-VIS	Ultra violet visible
WICT	Wagged Intramolecular Charge Transfer
˚C	˚Centigrade
λ_{ex}	Excitation wavelength
λ_{em}	Emission wavelength
ϕ	Quantum yield
τ	Exited Sate Lifetime

List of Charts

Chapter 3	
Chart 3.1.	Structures of 2-(4′-N, N-dimethylaminophenyl)benzimidazole (DMAPBI), 2-(4′-N,N-dimethylaminophenyl) imidazo[4,5-b]pyridine (DMAPIP-b) and 2-(4′-N,N-dimethylaminophenyl) imidazo[4,5-c]pyridine (DMAPIP-c)
Chapter 6	
Chart 6.1.	Structure of 2-(2′-hydroxyphenyl) benzimdazole (HPBI), 2-(2′-hydroxyphenyl)-3*H*-imidazo-[4, 5-*b*] pyridine (HPIP-b) and 2-(2′-hydroxyphenyl)-3*H*-imidazo-[4,5-*c*] pyridine (HPIP-c).
Chapter 7	
Chart 7.1.1.	Different forms of HPBI
Chart 7.2.1.	Structure of HPBI, HPIP-b and HPIP-c.

List of Figures

Chapter 2

Figure 2.1.	Pictures of silver solution in the pH range 2.5 to 12.5.
Figure 2.2	Surface plasmon resonance spectrum, TEM and FESEM images of silver nanoparticles prepared in water at pH 9.97. Inset shows the DLS spectrum of silver nanoparticles with an average diameter of 25±5 nm.
Figure 2.3	Block diagram of a TCSPC instrument
Figure 2.4	Schematic diagram of FESEM
Figure 2.5	Schematic diagram of TEM

Chapter 3

Figure 3.1	Growth of silver nanoparticles in (a) absence of fluorophore and in presence of (b) DMAPBI, (c) DMAPIP-b, (d) DMAPIP-c.
Figure 3.2	FESEM images of nanoparticles in presence and absence of three fluorophores within an hour of preparation (left side) and after 24 h (right side). The insets show the vials containing the silver nanoparticles after respective time scales.
Figure 3.3	TEM images of nanoparticles in presence of (a) DMAPBI, (b) DMAPIP-b, (c) DMAPIP-c and (d) Electron diffraction pattern of the nanoparticles.
Figure 3.4	Fluorescence spectra of (A) DMAPBI (λ_{exc} = 331 nm), (B) DMAPIP-b, (C) DMAPIP-b [normalised] (λ_{exc} = 347 nm) and DMAPIP-c (λ_{exc} = 323 nm) at different concentrations of nanoparticles and the inset show the plot fluorescence ratio against silver concentration. The fluorescence ratio plots are obtained by using the integrated area of the fluorescence spectrum.
Figure 3.5	(a) Normalized absorption spectrum of the nanoparticles and the fluorescence spectra of (b) DMAPBI, (c) DMAPIP-c and (d) DMAPIP-b
Figure 3.6	Fluorescence decay of all the fluorophores in the (a) absence of nanoparticles and β- CD (b) presence of nanoparticles (c) presence of nanoparticles and β-CD along with (d) the instrument response function and residue.
Figure 3.7	Fluorescence spectra of (a) DMAPBI, (b) DMAPIP-b and (c) DMAPIP-c in the presence of nanoparticles and β-CD. Figure (a) inset shows the fluorescence ratio against silver concentration. The fluorescence ratio plots are obtained by using the integrated area of the fluorescence spectrum. Figure (b) shows the normalized fluorescence spectrum in presence of highest concentration of nanoparticles as dotted line. [Inset show the plot of intensity ratio of longer wavelength (510 nm) to shorter wavelength (407 nm) against silver concentration. Figure (c) inset shows the plot of intensity

ratio of longer wavelength (480 nm) to shorter wavelength (395 nm) against silver concentration.

Figure 3.8 Reduction of silver (II) nitrate in DMF to silver zero within 10 minutes at room temperature.

Chapter 4

Figure 4.1 Fluorescence spectra of (a) DMAPBI (λ_{exc} = 336 nm), (b) DMAPIP-b (λ_{exc} = 350 nm) and (c) DMAPIP-c (λ_{exc} = 336 nm), (d) Intensity ratio plot of all three fluorophores in water at different concentration of silver (nanoparticles).

Figure 4.2 Fluorescence spectra of (a) DMAPBI (λ_{exc} = 336 nm) and (b) DMAPBI-nanoparticle composite (λ_{exc} = 336 nm) at different concentrations of CTAB. Plot of intensity at emission maxima of DMAPBI at different concentrations of CTAB (c) for fluorophore nano composite and (d) in absence of nanoparticle.

Figure 4.3 Fluorescence spectra of (a) DMAPIP-b-nanoparticles composite (λ_{exc} = 345 nm) and (b) DMAPIP-b (λ_{exc} = 345 nm) at different concentrations of CTAB. Plot of intensity at emission maxima of DMAPIP-b at different concentrations of CTAB (c) for fluorophore nano composite and (d) in absence of nanoparticle.

Figure 4.4 Fluorescence spectra of (a) DMAPIP-c-nanoparticles composite (λ_{exc} = 336 nm) and (b) DMAPIP-c (λ_{exc} = 336 nm) at different concentrations of CTAB. Plot of intensity at emission maxima of DMAPIP-c at different concentrations of CTAB (c) for fluorophore nano composite and in absence of nanoparticle (inset). (d) Plot of intensity ratio of DMAPIP-c and fluorophore nanocomposite at different concentrations of CTAB.

Figure 4.5 Fluorescence spectra of (a) DMAPBI-nanoparticles composite (λ_{exc} = 336 nm) and (b) DMAPIP-b-nanoparticles composite (λ_{exc} = 336 nm) at different concentrations of TX-100.

Figure 4.6. Plot of intensity at emission maxima of (a) DMAPBI-nanocomposite (b) DMAPBI and (c) DMAPIP-b–nanocomposite (d) DMAPIP-b at different concentrations of TX-100

Figure 4.7 Fluorescence spectra of (a) DMAPIP-c - nanoparticles composite (λ_{exc} = 336 nm) and (b) DMAPIP (λ_{exc} = 336 nm) at different concentrations of TX-100. Plot of intensity at emission maxima of DMAPIP-c at different concentrations of TX-100 (c) for fluorophore nano composite and in absence of nanoparticle (inset). (d) Plot of intensity ratio of DMAPIP-c and fluorophore nanocomposite at different concentrations of CTAB.

Chapter 5

Figure 5.1 The emission spectra of DMAPIP-c (λ_{ex} = 336 nm) in presence of increasing concentration of BSA [0-90 µM].

Figure 5.2 Emission spectra of DMAPBI at different concentrations of BSA (red lines) followed by the addition of increasing concentration of silver nanoparticles (violet lines)

Figure 5.3 Excitation spectra of DMAPBI at different concentrations of BSA (red lines) followed by the addition of increasing concentration of silver nanoparticles (violet lines)

Figure 5.4 Emission spectra of DMAPBI-BSA (λ_{ex} = 280 nm) at different concentrations of silver nanoparticles.

Figure 5.5 Stern Volmer plot of BSA at different concentration of silver nanoparticles.

Figure 5.6 Emission spectra of DMAPIP-b with varying concentration of BSA (blue lines) and the red lines are the emission spectra of DMAPIP-b in 90 μM of BSA at different concentration of nanoparticles.

Figure 5.7 Emission spectra of DMAPIP-c at different concentrations of BSA followed by different concentrations of silver nanoparticles.

Figure 5.8 Plot of intensity ratio of TICT vs normal band of DMAPIP-c at different concentrations of silver nanoparticles.

Figure 5.9 Plot of intensity ratio of TICT vs normal band of DMAPIP-b at different concentrations of silver nanoparticles.

Figure 5.10 Fluorescence decay of DMAPIP-b in the (b) absence of BSA and nanoparticles (c) presence of BSA and nanoparticles (d) presence of BSA along with (a) instrument response function and residue.

Chapter 6

Figure 6.1 Growth of nanoparticles in (a) absence of fluorophores, and in presence of (b) HPBI, (c) HPIP-b, and (d) HPIP-c in DMF

Figure 6.2 FESEM (upper panel) and TEM (lower panel) images of silver nanoparticles in presence of HPBI (a), HPIP-b (b) and HPIP-c (c) within an hour of preparation (inset: photograph of the vials containing nanoparticles)

Figure 6.3 DLS study of Ag nanoparticles in (a) absence of any fluorophore and in presence of (b) HPBI, (c) HPIP-b, and (d) HPIP-c.

Figure 6.4 Fluorescence characteristics of HPBI with the increasing concentrations of silver nanoparticles [0-32 μM]. Inset shows the intensity ratio plot of (a) normal and (b) tautomer band at different concentrations of silver nanoparticles

Figure 6.5 Fluorescence characteristics of HPIP-b with increasing concentrations of silver nanoparticles [0-50 μM]. Inset shows the intensity ratio plot of (a) normal and (b) tautomer band at different concentrations of silver nanoparticles [0-50 μM].

Figure 6.6 Fluorescence characteristics of HPIP-c with increasing concentrations of silver nanoparticles [0-50 μM]. Inset shows the intensity ratio plot of HPIP-b at various concentrations of silver nanoparticles.

Figure 6.7 Normalized (a) absorption spectrum of silver nanoparticles, and fluorescence spectra of (b) HPBI, (c) HPIP-b and (d) HPIP-c with respect to tautomer emission.

Figure 6.8 Excitation spectra of HPIP-c at various concentrations of silver nanoparticles [0-50 μM] monitored at λ_{em} = 346 nm.

Figure 6.9 Excitation spectra of HPIP-c at various concentrations of silver nanoparticles [0-50 μM] monitored at λ_{em} = 457 nm.

Figure 6.10 Intensity ratio plot of normal band to tautomer band of (a) HPBI, (b) HPIP-c and (c) HPIP-c at different concentrations of silver nanoparticles [0-50 μM]

Figure 6.11 Plot of τ_0/τ of (a) HPBI, (b) HPIP-b and (c) HPIP-c at different concentrations of silver nanoparticles.

Chapter 7

Figure 7.1.1 Absorption spectra of HPBI in water (.....), methanol (— -) and in re-precipitation mixture at — 0 min, — 10 min, — 30 min, — 60 min, — 120 min, — 180 min, —300 min, — 360 min, — 24 hrs. Inset shows the expanded spectra of HPBI in water and aggregated mixture in the 350 nm-450 nm region.

Figure 7.1.2 Fluorescence spectra of the re-precipitated mixture of HPBI with increasing time (λ_{exc} = 310 nm).

Figure 7.1.3 Fluorescence spectra of HPBI in (A) methanol, (B) water and (C) aggregate solution. Inset shows the intensity ratio of tautomer emission to normal emission (I_T/I_N).

Figure 7.1.4 Fluorescence decay of (b) HPBI in water and the (c) re-precipitate solution along with (a) instrument response function and the residue.

Figure 7.1.5 Absorption and fluorescence spectra of the re-precipitated mixture of PBI with increasing time.

Figure 7.1.6 FESEM images of the samples made from aqueous suspensions of HPBI after re-precipitation after 10 minutes at different magnifications.

Figure 7.1.7 Fluorescence microscopy images of HPBI after 10 min of re-precipitation observed under white light [left] and excited with UV light (λ_{ex}=350 nm) [right].

Figure 7.1.8 Time dependent evaluation of aggregate formation of HPBI. Left panel bright field and right panel fluorescence image of aggregates after (a) 30 min (b) 100 min (c) 300 min and (d) 24 hours. Scale bar represent 100 microns.

Figure 7.1.9 In vitro cytotoxicity test of HPBI on HeLa cells using MTT assay. Each point represents the mean SD (n = 3). ** show significant differences between control and respective group at $p < 0.01$.

Figure 7.1.10 Representative phase and fluorescent images showing HeLa cells treated with 5 μM aggregates of the HPBI [1st row] and with base molecule [2nd row] (4 hrs). Scale bar represents 50 microns.

Figure 7.1.11 Plot of emission intensity of HPBI at 465 nm in methanol with the increasing concentration of glycerol, (λ_{exc} = 310 nm).

Figure 7.1.12 Snapshot of the simulation box at the end of 4 ns NVT run. Water molecules (green colour), methanol molecules (red colour), and HPBI molecules (blue).

Figure 7.1.13 Orientation of HPBI molecules in aggregates from molecular dynamics simulation at various time steps in the "BONDS" representation of VMD.

Figure 7.2.1 Absorption spectra of HPIP-b in water (green line) and of reprecipitate mixture (dotted line) after 13 days. Inset shows the expanded spectra of HPBI in water and aggregated mixture in the 350 nm-450 nm region.

Figure 7.2.2 Absorption spectra of HPIP-c in water (Red line) and of reprecipitate mixture (dotted line) after 13 days. Inset shows the expanded spectra of HPBI in water and aggregated mixture in the 400 nm-450 nm region.

Figure 7.2.3 Fluorescence spectra of HPIP-b in (a) water and (b) 2% v/v water methanol re-precipitation mixture.

Figure 7.2.4 Fluorescence spectra of HPIP-c in (a) water and (b) 2% v/v water methanol re-precipitation mixture.

Figure 7.2.5 Fluorescence decay of normal emission of HPIP-b (b) in water, (c) in reprecipitate solution and HPIP-c (d) in water, (e) reprecipitate solution, (a) is the instruments response function with residuals.

Figure 7.2.6 Fluorescence microscopy images of HPIP-b and HPIP-c after 10 min of re-precipitation observed under white light [right] and excited with UV light (λex=350 nm) [left].

Figure 7.2.7 FESEM images of the samples made from aqueous suspensions of HPIP-b (left side) and HPIP-c (right side) after re-precipitation in water with 2% v/v methanol after 24 hours.

Figure 7.2.8 In vitro cytotoxicity test of compounds on HeLa cells using MTT assay. Each point represents the mean ± SD (n = 3). ** and * show significant differences between control and respective group at $p < 0.01$ and $p < 0.05$, respectively.

Figure 7.2.9 Representative phase and fluorescent images showing HeLa cells treated with 5 µM aggregates of the HPIP-b (4 hrs.). Scale bar represents 50 microns.

Figure 7.2.10 Representative phase and fluorescent images showing HeLa cells treated with 5 µM aggregates of the HPIP-c (4 hrs.). Scale bar represents 50 microns.

Figure 7.2.11 Chemical structures of HPIP-b (a) and HPIP-c (b) with atom labels. Simulation snapshot (c), Color code: Methanol (blue), HPIP-b (green) and water (red).

Figure 7.2.12 Distance between two HPIP molecules as a function of simulation time.

Figure 7.2.13 Number of water molecules around HPIP molecues and hydrogen bonds with water.

Figure 7.2.14 L-J potential energy and electrostatic potential energy between HPIP molecules.
Figure 7.2.15 Distance between Nitrogen atoms of one HPIP and oxygen atom of other HPIP molecule, which formed an aggregate.
Figure 7.2.16 Representative orientations of two HPIP molecules in the state of aggregation. (a-b) for HPIP-b and (c-d) for HPIP-c.

List of Schemes

Chapter 1	
Scheme 1.1.	Schematic representation of formation of TICT state
Scheme 1.2	Schematic representation of the four level cyclic process of ESIPT
Chapter 2	
Scheme 2.1	Schematic representation of the silver nanoparticles preparation and their stabilization in DMF.
Scheme 2.2	Formation of aggregated structures from re-precipitation of fluorophores in water with 2% v/v methanol.
Chapter 3	
Scheme 3.1	Schematic representation of complex formation and dual emission
Scheme 4.1	Effect of CTAB on nanocomposite of fluorophore and nanoparticle.

List of Tables

Chapter 3	
Table 3.1	The fluorescence characteristics of fluorophores in different environments.
Chapter 4	
Table 4.1	Emission λ_{max} (nm) of the fluorophores in water and nanoparticles.
Table 4.2	Emission λ_{max} (nm) values of all fluorophores in water, nanoparticles, CTAB and in composite system of CTAB and nanoparticles.
Table 4.3	Emission λ_{max} (nm) values of all fluorophores in water, nanoparticles, TX-100 and in composite system of TX-100 and nanoparticles.
Table 4.4	The critical micelle concentration (CMC, mM) and the concentration of the surfactant (mM) to equalize the initial intensity of the fluorophore before addition of nanoparticles.
Chapter 5	
Table 5.1	Fluorescence lifetime values of DMAPBI, DMAPIP-b and DMAPIP-c in presence of BSA and silver nanoparticles.
Chapter 6	
Table 6.1	Lifetime values of the fluorophores and their composites with nanoparticles are summarized in the table.
Chapter 7	
Table 7.1.1	Lifetime values of the monomer and the aggregates monitored at normal and tautomer band.
Table 7.1.2	List of possible intermolecular hydrogen bond Donor-Acceptor pairs from VMD analysis. For atoms refer Figure 10 (f).
Table 7.2.1	Fluorescence lifetime of the monomer and the aggregates of HPIP-b and HPIP-c.

Chapter 1

Introduction

1.1.0. Fluorescence:

Fluorescence has become an important asset of recent research. It is a powerful tool for structural investigation and determining the dynamics of matter or living systems at molecular or supramolecular level **[1-5]**. The processes such as photoisomerization, photoionization, photodissociation, proton transfer, charge transfer and acid-base reaction may compete with molecular emission. Even these competing processes also sometime makes the fluorimetric technique as a more interesting one.

1.1.1. Factors affecting fluorescence:

The factors capable of altering the fluorescence of a fluorophore can be divided into structural and environmental factors. From the structural point of view, fluorescence is best observed in aromatic molecules containing the $\pi\pi^*$ emitting state. With increase in conjugation high quantum yield can be achieved with a bathochromic shift in the spectrum. However, some heterocyclic aromatic systems such as furan, pyrrole etc. are non-fluorescent owing to the presence of low lying $n\pi^*$ state which prefer the triplet state and avert fluorescence. Substitution of halogen in aromatic rings decreases the fluorescence and the effect is dominant for substitution by heavier halogens. Substitution by heavier atoms increases the spin-orbit coupling. Similar effect is observed on substitution of a carbonyl or carboxylic acid due to $n\pi^*$ state. On the other hand, electron donating substituents such as OH, OR, NH_2, NHR and NR_2 increase the molar absorption coefficient and also red shift the absorption and fluorescence spectra. Moreover the spectra are broad and often blurred compared to the parent hydrocarbons.

The nature of the solvents plays crucial role in the fluorescence emissions. The solvent induced shift in the emission band is called solvatochromic shift. The more or less stabilization of the fluorophore in the excited state relative to ground state owing to the solute-solvent interaction is responsible for this shift. Generally fluorophores with high excited state dipole moment are susceptible for solvent induced change. The major factors related to solvatochromism comprise of polarity, viscosity, heavy atom effect and hydrogen bonding. The polar solvents decrease the energy of $\pi\pi^*$ state. The viscosity of the medium increases the fluorescence by decreasing the collisional deactivation. The heavy atom containing solvents enhance phosphorescence and the hydrogen bonding with hetero atom

of the aromatic ring increases the quantum yield. The non-radiative pathways such as collisional deactivation, intramolecular vibration and rotation are directly proportional to the increase in temperature. Hence, the temperature increase can lead to the quenching of the fluorescence intensity. The fluorescence decay and quantum yield of molecules containing proton donors or acceptors vary drastically with change in pH.

1.1.2. Intramolecular charge transfer:

Molecules composed of electron donor and electron acceptor, upon excitation go to local excited state where charge transfer from the donor to acceptor group can occur. This leads to structural and electronic rearrangement within the molecule and an increase in molecular dipole moment is also observed. The molecule often undergoes relaxation towards a highly polar state called intramolecular charge transfer (ICT) state and exhibits dual emission **[6-18]**. Different mechanisms **[5]** have been proposed about the formation of the ICT state, namely twisted ICT (TICT) **[6]**, wagged ICT (WICT) **[7]**, rehybridized ICT (RICT) **[8, 9]**, planar ICT (PICT) **[10, 11]** and mesomeric (MICT) **[12, 13]**.

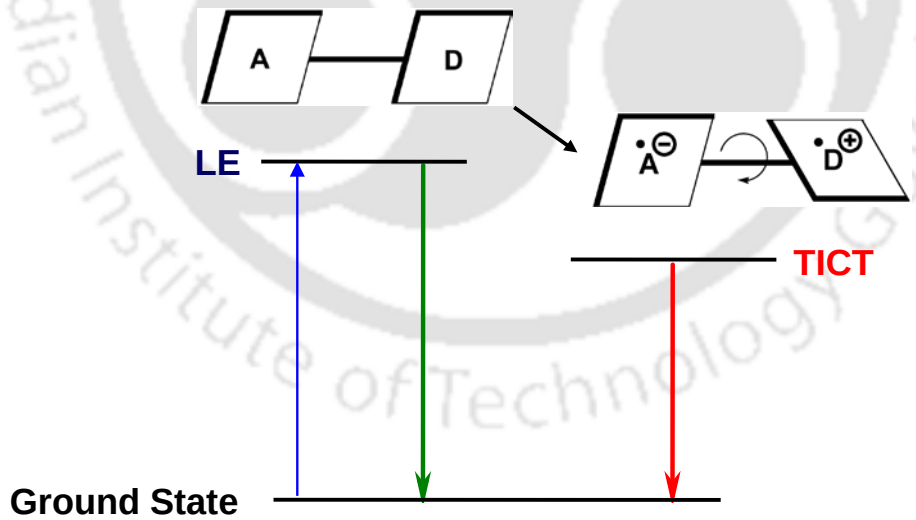

Scheme 1.1. Schematic representation of formation of TICT state

In those models, Grabowski's TICT and Zachariasse's PICT models are most accepted models. According to TICT model, the ICT process is accompanied by twisting of the electron donor to a position perpendicular to other part of the molecule **[Scheme 1.1.]**.

But, a planar structure was proposed for the emitting state in the PICT model. A solvent induced vibronic coupling was proposed to take place between the locally excited and CT states leading to formation of a final planar structure. Direct measurement of the structure of the emitting species is experimentally difficult. But large circumstantial evidences are available to support both the models **[19-21]**.

The strength of donor and acceptor groups controls the energy gap between the excited locally excited state and the ICT state which determines the intensity of the ICT state **[13]**.

$$E_{ICT} - ELE < 0 \quad \ldots\ldots 1.1$$

From the experiment energy of the locally excited state (E_{LE}) can be obtained and the energy of the ICT state (E_{ICT}) is approximated as below

$$E_{ICT} = IP(D) - EA(A) + C + \Delta E_{sol} \quad \ldots\ldots 1.2$$

Ionization potential IP(D) gives the donor capability to release an electron and the electron affinity EA(A) reflects the acceptor ability to bind it. The positive and negative charges produced by electron transfer attract each other that stabilizes the system by the coulomb energy, C. The ion pair was further stabilized by the solvation energy, ΔE_{sol}.

1.1.2.1. Factors affecting ICT:

Polarity, viscosity and the hydrogen bonding are the main factors which affect the ICT process. According to TICT model, the ICT state accompanies charge separation and twisting motion of the electron donor **[11-13]**. The polarity of the medium enhances the rate constant for the formation of TICT state. Hence, TICT is favored in polar environment than in nonpolar media. As the twisting motion is retarded by the viscosity of the medium, it is expected to hinder the TICT process. However, for small rotating group containing molecules, viscosity has no effect on the TICT process even up to moderate viscosity **[35-37]**. It affects only at very high viscosity **[38-40]**. But, the viscosity effect is larger for bulky rotating groups **[41]**. The viscosity dependence of TICT emission renders the TICT exhibiting molecules as useful probes for micro-viscosity **[42-47]**. With increase in polarity, the quantum yield and lifetime of the normal emission reduces with a small bathochromic shift. Though the TICT emission also undergoes a red shift, the quantum yield initially

increases and after reaching a maximum reduces with further enhancement in polarity **[12, 13, 48-51]**. An enhancement in polarity facilitates the formation of the TICT state and it also rises the nonradiative decay rate from TICT singlet state to low lying triplet and/or ground state.

The hydrogen bonding of the solvent with the molecule also affects the TICT process. Cazeau-Dubroca et al. hypothesized that in DMABN and its analogues, the TICT emission is due to the hydrogen bonding of the solvents with the donor group. They suggested that such a hydrogen bonding results in the formation of a ground state pre-twisted conformer and the excitation of the pre-twisted conformers yield the TICT emission **[52-56]**. In esters of (*N*,*N*-dimethylaminonaphthyl)acrylic acid also it was speculated that the hydrogen bonding effect was due to pretwisted conformers **[57]**. Dreuw *et al.* predicted that in gas phase it is the dimethylamino nitrogen hydrogen bonded complex but not the carboxylate hydrogen bonded molecule that is responsible for the ICT emission from 4-(dimethylamino)methylbenzoate **[58]**. On the other hand, few others predicted that the hydrogen bonding of the solvent with donor inhibits the formation **[59, 60]**. Fansi et al. suggested that it is the hydrogen bonding of the solvent with acceptor that twist the acceptor in 2-(4'-aminophenyl)pyridoimidazoles that results in the of TICT state **[61]**. But, Yoon et al. suggested that the hydrogen bonding with acceptor makes the acceptor more coplanar with the benzene ring which enhances the charge flow from the benzene ring to the acceptor **[62, 63]**. Later Krishnamoorthy et al. proposed that the charge flow is enhanced by the hydrogen bonding of the solvent with acceptor of 2-(4'-N,N-dimethylaminophenyl)imidazo[4,5]pyridines which helps the formation TICT state **[64, 65, 66, 67]**. In 4-(*N*,*N*-dimethylamino)pyrimidine also the hydrogen bonding with the acceptor was reported to favor TICT emission by increasing the electron withdrawing ability **[68]**.

1.1.3. Intramolecular proton transfer:

Since the acidity of the acid and the basicity of the base increases upon excitation in molecules. When there is a contact between the acidic and basic group by intramolecular hydrogen bond, the photo excitation may cause excited state intramolecular proton transfer (ESIPT). The tautomer formed by ESIPT is unstable in the ground state, therefore undergoes reverse proton transfer in the ground state to produce the original structure. **[Scheme 1.2]**.

The normal emission is less Stokes shifted but the tautomer emission is highly Stokes shifted. The emissions are sensitive to environmental factors such polarity, hydrogen bonding etc.

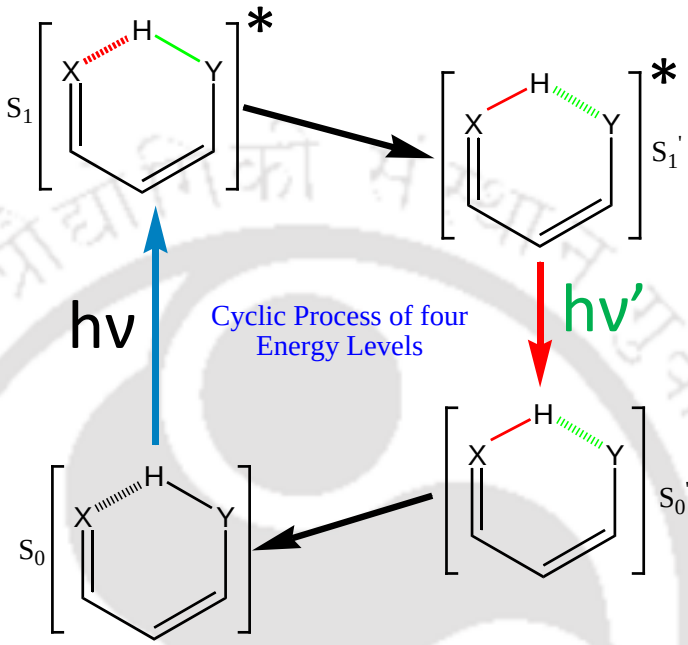

Scheme 1.2. Schematic representation of the four level cyclic process of ESIPT

1.1.3.1. Factors affecting ESIPT

The environmental factors as well as the molecular structures influence the position and the intensities of normal and the tautomer emissions. The polarity and hydrogen bonding capacity of the media are crucial factors in ESIPT **[69]**. The nonpolar environment favors the ESIPT than the polar and protic environment **[70, 71]**. Solvents such as dimethylsulfoxide, methanol, water etc. break the prerequisite intramolecular hydrogen bond in ESIPT molecules by strong intermolecular hydrogen bonding. This depletes the tautomer emission and enhances the normal emission. Due to weak nature of five-membered cyclic intramolecular hydrogen bonded ring structures such as in 3-hydroxyflavone the effect is more in these molecules **[72]**. However, non-polar solvents favor the cyclic intramolecular hydrogen bond structures which lead to proton transfer in the excited state. The ESIPT does not depend on the viscosity of the environment. However, in polar environments, there are few evidences of viscosity effect on the rate of ESIPT **[73]**.

Substitution affects the ESIPT process, the spectral position and the quantum yield **[74-82]**. Therefore, an ESIPT molecule with desired properties can be obtained by making specific substitution in a suitable position of the molecular framework. ESIPT molecules are used as photo stabilizers, probes, sensors, laser dyes and molecular devices **[83-97]**.

1.2. Reactions at heterogeneous medium

In recent time reactions occurring at the heterogeneous systems have gained significant attention **[98-110]**. Many heterogeneous systems such as metal and organic nanoparticles **[111-115]**, cyclodextrin **[116-120]**, micelles **[121-123]**, proteins like serum albumin **[123-126]** etc. play a vital role in controlling different photophysical processes. The formation of guest-host complexes is common phenomenon in these types of systems and studied by various groups **[116-126]**. The dye-macrocycle complexes can be used for model system for energy transfer study.

1.2.1. Metal nanoparticles

The physical and chemical properties of materials gradually change from solid state to molecular level as a function of particle size. The transition region between bulk solid and single molecule is represented by the nanoparticles. Nanotechnology has become a part and parcel of today's life. The typical behavior of the nanoparticles depends on their small dimensions. This increase in the surface to volume ratio leads to more number of surface atoms in comparison to those in lattice core. In the absence of any adsorbed molecules on the nanosurface, the surface atoms are highly active and their contribution to overall behavior of the particle is different from those present at the core. The size and shape dependent unique tunable optical properties [**127-132]**, catalytic **[133-137]**, antibacterial and antimicrobial **[138-144]** activities of the nanoparticles make them as foundation pillar in modern research.

1.2.2. Importance of silver

Since coinage silver has been playing an important role throughout history of mankind [**92]**. Its ability to reflect light was the major admirable fact in the ancient times. With more understanding and the control of the atomic world, its applications have become far more

sophisticated. Silver is used in electronics, catalysis and structural materials nowadays. But silver can offer a completely different set of applications involving light when they are fashioned into structures with nanometer-sized dimensions. Silver is probably the most important and advantageous material in plasmonics in comparison to Au, Al, Li, Cu etc. owing to its ability to support surface plasmons in visible and near infrared regions **[146, 147]**. The black colored aggregates of Ag nanoparticles has been known for its widespread use in photography and staining of biological tissues **[148]**. Silver also has the highest electrical and thermal conductivity among all metals, making it an ideal candidate for electrical applications. Silver nanostructures are largely used in plasmonic applications outside a human body (e.g., plasmonic antennas and circuits for concentrating and guiding light), where they have consistently reported much better performance than gold based nanostructures **[149-152]**. For large scale plasmonic applications the cost of the metal plays a vital role. Among the concerned metals for plasmons, silver is relatively cheaper one **[153]**. Although both aluminum and copper are cheaper, they have limitation in terms of the plasmons they can support. Another important factor is the easy fabrication of nanostructures of different size and shape. Over the past decade, Au, Ag, and Pd have all been prepared in a large variety of nanostructures using different chemical methods **[154]**. Taking into account the unsuitability of Pd for plasmonic applications, Au and Ag are the most promising, and indeed the most widely used materials in plasmonics. The disappointing fact of gold is the price which is almost 50 times more expensive than is silver. The material cost, easy fabrication of various structures, large scale plasmonic application vote for silver to be one of the best metal over others.

1.2.3. Fluorophore metal nanoparticle interaction:

The fabrication of nanometarials through the interaction of nanoparticles with fluorophores has been studied extensively owing to their real world applications **[155-164]**. These interactions mainly involve two major outcomes. The energy transfer from the fluorophores to nanoparticles resulted in the quenching of the fluorescence of fluorophores **[165-179]**. Following the advantages of the surface characteristics and high stability of the nanoparticles, silver nanoparticles have been studied extensively as fluorescence quenchers, the reason being manifold. The spherically shaped metal nanoparticles have no defined dipole moment like the dyes, so energy transfer to the nanometarials takes place for any

orientation of the donor relative to the surface and the large absorption cross section near the plasmon resonance enhances their performance as energy acceptors. But metal enhanced fluorescence **[180-192]** also have equal consequences as quenching. Many studies have been done to establish the criteria for the quenching or enhancement. Studies revealed that the size and shape of the nanoparticles, fluorophore-nanoparticle distance, anchoring group of the nanoparticles, nature and localized surface plasmon resonance of the nanoparticles may play major roles in determining the dominating process. The observation of enhancement and quenching depends on the magnitude of the electric field at the particle surface and the dielectric dispersion of the materials **[193,194].** Studies reveal that quenching process dominates at small sizes of the nanoparticles and radiative enhancement at larger sizes **[195,196].** Additionally when fluorophores are very close to the metal surface, the fluorescence quenching effect competes with other favorable effects **[197]** and it dominates within 5 nm from the surface of metallic particles. At larger distances the enhancement starts to overrule the quenching and reaches its maximum at about 10 nm from the metal surface **[198,199]**. At larger metal-fluorophore separation, the enhancement effect gradually decreases. The unique properties of metal nanoparticles were attributed to the absorption and scattering characteristics of the nanoparticles, typically referred to as the extinction cross section **[200]**.

The utility of the nanoparticles-fluorophores interaction has been evolved with time. These system can provide a range of applications in different fields such as catalysis, bio-sensing and chemical sensor for toxic anions such as cyanide, quantitative detection of protein, drug delivery, antibacterial study, cellular imaging, p^H sensing etc. **[201-214]**. These applications depend upon the size, the shape and the morphology of the nanoparticles.

1.2.3.1. Quenching of fluorescence by nanoparticles:

The fluorescence intensity of 1, 4-dihydroxy-2, 3-dimethyl-9, 10-anthraquinone was quenched dynamically by tin oxide nanoparticles **[165]**. Kang et al. developed a near infrared contrast agent conjugated gold nanoparticle *via* a short peptide spacer. It was used for characterization of different types of cancer **[166]**. The energy transfer from Rhodamine G to gold nanoparticles were found to be shape dependent. Maximum energy transfer rate was obtained for the spherical particles compared to other shaped particles **[167]**. Kong et

al. developed a new, simple and rapid sensing platform for for dye-labelled single stranded DNA probes **[168]**. Whiteley et al. showed resonance energy transfer from arginine kinase to small sized gold and silver nanoparticles with probable implications against trypanosomiasis in clinical trials **[169]**. Caires et al. demonstrated that depending on its concentration silver nanoparticles quenches the fluorescence of the chlorophyll by static or dynamic way **[170]**. The importance of distance between donor and acceptor in the efficiency of energy transfer systems was shown by Han Zuilhof et.al. Blue-emitting amine terminated Si nanoparticles (size, 1.57 nm) functionalized with a Ru bipyridine complex separated by three different chain length showed distance dependent energy transfer. Studies revealed that the energy transfer rate was highest in the nanoparticles-complex separated by the shortest alkyl chain **[171]**. Fluorescence quenching of cumarin 120 by CdS nanoparticles was investigated by Onganer et al. The nanoparticles formed non-fluorescent complex with coumarin 120 **[172]**. Khanjari et al. studied the fluorescence quenching of rhodamine 6G and 4-hydroxycoumarin by silver nanoparticles **[173]**. Ramanibai et al. found that the fluorescence of textile dyes waste was quenched by silver nanoparticles through FRET **[174]**. Ramakrishnan et al. found that smaller silver nanoparticles were more efficient quencher of fluorescence compared to the larger ones **[175]**. Viscosity dependent fluorescence quenching of a perylene derivative was demonstrated by Asiri et al. **[176]**. In this static quenching increasing the viscosity of the medium leads to a cage effect which enhances fluorophore uptake on silver nanoparticles surfaces thereby enhances fluorescence quenching. Acuna et al. found that 10.4 nm is the approximate distance between a fluorophore and a 10 nm nanoparticle for 50% energy transfer **[177]**. Patra et al. studied the energy transfer from coumarin 480 dye to gold nanoparticles, both confined to Y-zeolite. It reveals that the quenching efficiency is much higher in the case of confined dye molecules in zeolite and surface-immobilized gold nanoparticles compared to free nanoparticles. This is due to the unidirectional energy transfer from aligned dye molecules in the cavity of zeolite to the immobilized gold nanoparticles on the surface of the zeolite [**179**].

1.2.3.2. Fluorescence enhancement by nanoparticles:

Haghgoo et al. synthesized a selective fluorescence "turn-on" nano sensor for methamphetamine based on 1, 8-naphthalimide-thiophene derivative immobilized on silica nanoparticles **[180]**. The derivative displayed significant fluorescence enhancement in the

presence of methamphetamine which is much more intensified after being attached to silica nanoparticles. Dorsinville et al. showed that the fluorescence of Rhodamine B can be enhanced in the vicinity of silver nanoparticles **[181]**. The enhanced fluorescence of quercetin-silver nanoparticles composite was used as a fluorescence probe for nucleic acids detection and analysis of protoplasts **[182]**. Paul et al. developed an assay for organophosphates sensing using silica coated silver nanoparticles. 10 times enhancement in fluorescence of organophosphate hydrolase by nanoparticles enabled a 2 ppb detection limit for the system **[183]**. Hai et al. observed that the enhancement in the fluorescence of rhodamine B, dispersed in the polymer matrix of poly(methylmethacrylate), spin coated on silver nanoparticles immobilized glass surface depends on the thickness of the film **[184]**. The self-assembly of silver nanoparticles with cationic polyacrylamide into microcomposite enhances the fluorescence emission of fluorescein isothiocyanate more compared to silver nanoparticles. [**185**]. Rai et al. showed the fluorescence enhancement of Tb^{3+} ions doped in aluminosilicate glass by spherical silver nanoparticles **[186]**. The fluorescence intensity of $Ru(bpy)_2^{3+}$ was enhanced by silver nanoparticle as a core with silica shell. The presence of silver core was very essential for the fluorescence enhancement **[187]**. The fluorescence of Cyanine 3 and Cyanine 5-labeled ribosomal initiation complexes showed an enhancement near 50 nm silver particles by 4 and 5.5 fold, respectively. This enhancement was used for studies in protein translation **[188]**. Teolato et al. showed the amplification of fluorescence intensity of fluorophore attached onto silica nanoparticle. **[190]**. Li et al. studied the effect of core nanoparticles on the fluorescence enhancement of cationic conjugated polymer attached to it. They showed that the silica nanoparticles that contain the silver core were more efficient in enhancing the fluorescence of polymer than those without silver core. The system was proven to be effective for cellular imaging due to its low toxicity **[192]**.

1.2.3.3. Application of fluorophore-nanoparticles interactions:

Gold nanoparticle based optical biosensors for the qualitative detection of organophosphate present in chemical warfare agents and pesticides was developed by Wild et al. **[201]**. Based on the high quench of fluorescence of fluorescein a novel label-free fluorescent sensor for ultrasensitive detection of protamine and heparin was established by Yao et al **[202]**. Adsorption of protamine to the nanoparticle breaks the fluorescein-nanoparticles complex resulting in the recovery of the fluorescein molecules fluorescence. Again addition of

heparin to protamine-nanoparticles complex releases the free nanoparticles to attach with fluorescein again. Rezwan et al. synthesized three different photostable dual-labeled fluorescent core/shell silica nanoparticles with high fluorescence intensity, well-defined shape, size and surface for cellular localization studies in multiple stained cells **[203]**. Sun et al. have developed a rapid, simple, cost effective and highly sensitive sensor for clenbuterol residues present in swine feed samples. This sensor is based on gold nanoparticles-rhodamine B composite where the quenched fluorescence intensity of rhodamine B was recovered during the congregation of nanoparticles by clenbuterol **[204]**. Chen et al. designed a new near infrared fluorogenic nanoprobe containing FG- boron-dipyrromethene and Poly(lactic-co-glycolic acid) nanoparticles for in vitro and in vivo imaging of human cancer cells **[205]**. A bio-sensing platform using silver nanoparticle as a core with silica shell-DNA-Cynine3 nanostructure was designed by Yu et al. for the detection of Hg^{2+}, Ag^{+} and coralyne. The enhanced fluorescence of Cyanine 3 by silver core for a definite silica thickness was the foundation for the selective detection **[206]**. Quantitative detection of cyanide ion and hydrogen peroxide was developed by Dong et.al using fluorophore nanoparticle interaction **[207]**. Colorimetric determination of dopamine using gold nanoparticles and hydrolysate of thioglycolic acid was presented by He et al. The aggregation of nanoparticles in the presence of dopamine and thioglycolic acid resulted in a color change from red to purple which produced a quantitative detection limit of dopamine in urine and blood serum **[208]**. Corma et al. synthesized surface-modified silica nanoparticles for the delivery of camptothecin to tumor cell. In vivo bio-distribution, therapeutic efficacy and biocompatibility of the nanoparticle-camptothecin composite was evaluated in human colorectal cancer xenografts using the fluorescence emission of Cyanine 5.5 **[209]**. A novel luminescent sensor for malathion using chitosan capped silver nanoparticles as fluorophore was developed by John et al. The addition of malathion resulted in the red shift in the absorbance and decrease in the emission intensity of the chitosan-nanoparticles composite through aggregation **[210]**. Zheng et al. established a new system for direct detection of tetracycline hydrochloride and chlortetracycline hydrochloride in aqueous solution **[211]**. Calcium phosphate nanoparticles with embedded with near-infrared emitting indocyanine green were used by Erhan et al. for in vivo imaging of human breast cancer cell **[212]**. A disposable electrochemiluminescence immunosensor for protein detection was designed based on the quenching effect of carbon nanoparticles on the

emission of $Ru(bpy)_3^{2+}$ **[213]**. The application of gold nanoparticles in enhancing the efficiency of an electrochemical sensor for the detection of mercury ion was studied by Chunhai Fan et al. The highly sensitive electrochemical sensor containing thymine-rich, mercury-specific oligonucleotide probe for the detection of Hg^{2+} ions in aqueous solution gave a read out signal for quantitative detection of Hg^{2+}. But gold nanoparticle-based sensing strategy brought about an amplification factor of more than 3 orders of magnitude, leading to a lower limit of detection. This gold nanoparticles based Hg^{2+} sensor was found to exhibit high selectivity **[214]**.

1.3. Motivation for the present work:

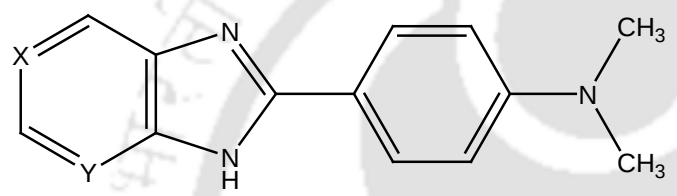

X = Y = CH DMAPBI

X = CH, Y = N DMAPIP-b

X = N, Y = CH DMAPIP-c

Chart 1.1. Structures of 2-(4′-N, N-dimethylaminophenyl) benzimidazole (DMAPBI), 2-(4′-N, N-dimethylaminophenyl) imidazo[4,5-b]pyridine (DMAPIP-b) and 2-(4′-N,N-dimethylaminophenyl) imidazo[4,5-c]pyridine (DMAPIP-c)

The primary motivation of the present work was to study the effect of nanoparticles on the ICT active molecules in different environments. The silver nanoparticles was used for these studies. The choice of silver nanoparticles for this study over other nanoparticles is due to the easy preparation, lesser health issue and cost effectiveness. Intramolecular charge transfer (ICT) is an environment sensitive fundamental process occurring in several natural processes. Therefore ICT active molecules open up practical applications in various fields. One of such emerging application involves the interaction with different nanoparticles which mainly resulted in either quenching or enhancement of intensity of the fluorophore. Biologically important fluorophores 2-(4'-*N*,*N*-dimethylaminophenyl)imidazo[4,5-b]pyridine (DMAPIP-b) and 2-(4'-*N*,*N*-dimethylaminophenyl)imidazo[4,5-c]pyridine (DMAPIP-c) lack TICT emission in aprotic solvent **[64, 66]**. It will be interesting to find whether these TICT emission can be achieved

through the interaction with silver nanoparticles in aprotic solvent. After successful achievement of TICT emission in aprotic solvent, the quest is extended to aqueous medium where the reversible attachment of the fluorophore to the nanoparticles surface was investigated using micelle. The serum albumin is a protein present in plasma and help to transport various biological molecules. Since nanoparticles are part of everyday life the effect on nanoparticle on the protein-molecules complex will be an interesting topic of research. Therefore, the effect of silver nanoparticle on the complexes of DMAPBI, DMAPIP-b and DMAPIP-c with bovine serum albumin (BSA) is investigated.

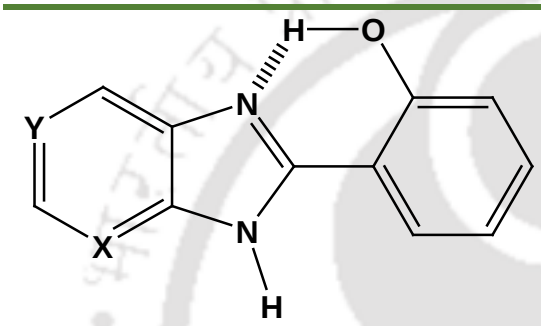

X = Y= CH	**HPBI**
X = N, Y = CH	**HPIP-b**
X = CH, Y = N	**HPIP-c**
X = Y = N	**HPP**

Chart 1.2. Structure of 2-(2'-hydroxyphenyl)benzimidazole (HPBI), 2-(2'-hydroxyphenyl)-3*H*-imidazo[4,5-*b*]pyridine (HPIP-b) and 2-(2'-hydroxyphenyl)-3*H*-imidazo[4,5-*c*]pyridine (HPIP-c)

Like to ICT emission, proton transfer also plays vital roles in nature. As ICT emissions were influenced by silver nanoparticles, it is more likely that ESIPT emissions will also be susceptible to nanoparticle environment. Therefore a set of ESIPT fluorophores namely 2-(2'-hydroxyphenyl)benzimidazole (HPBI), 2-(2'-hydroxyphenyl)-3*H*-imidazo[4,5-*b*]pyridine (HPIP-b) and 2-(2'-hydroxyphenyl)-3*H*-imidazo[4,5-*c*]pyridine (HPIP-c) were studied in presence of silver nanoparticles. Numerous research have been done regarding aggregation of ESIPT fluorophores. But no clear mechanism had been put forward for the aggregate formation. Hence, aggregation of these fluorophores were studied to understand the effect of aggregation on ESIPT. Along with this, imaging part of the aggregates were taken into account for showing their importance in real field also.

Chapter 2

Materials, Methods and Instrumentations

2.0. Introduction:

This chapter summary the details of the solvents, metal salts and other chemicals used in the present works. The synthetic procedures of silver nanoparticles in DMF and aqueous system without any common stabilizing agent are demonstrated in the chapter. The sample preparations and analysis techniques are also discussed. A brief descriptions on the major instrumentations used in the experiments such as UV-Visible absorption spectrophotometer, steady-state and time-resolved fluorimeters, field emission scanning electron microscopy and transmission electron microscopy are provided.

2.1. Materials:

Details of the materials utilized in the present work are given below.

2.1.1. Solvents:

- Acetonitrile, CH_3CN (HPLC grade, Spectrochem Pvt. Ltd., India)
- Dichloromethane, CH_2Cl_2 (AR grade, Merk India)
- Dimethylsulfoxide, $(CH_3)_2SO$ (HPLC grade, Rankem India)
- Ethyl Alcohol, CH_3CH_2OH (ACS grade, Merck India)
- Methyl Alcohol, CH_3OH (HPLC grade, Rankem India)
- *N*,*N*-Dimethylformamide, $N(CH_3)_2CHO$ (HPLC grade, Rankem India)
- Water, H_2O (Millipore water)

All the solvents were tested and found free of spurious fluorescence in the region of spectral measurement before use.

2.1.2. Metal Salts:

- Silver nitrate, $AgNO_3$ (99.0%, Sigma Aldrich)

2.1.3. Other Chemicals:

- The fluorophores (DMAPBI, DMAPIP-b, DMAPIP-c, HPBI, HPIP-b and HPIP-c) were present in the laboratory in pure form. The details of the synthesis were reported elsewhere **[66, 215-219]**.
- Bovine serum albumin (BSA, 98%, Merck India)
- β -Cyclodextrin (β-CD, Sigma Aldrich)
- Cetyltrimethylammonium bromide (CTAB, 98%, Sigma Aldrich)

- ❖ Sodium dodecyl sulfate (SDS, 98%, Sigma Aldrich)
- ❖ Sodium hydroxide (Merck India)
- ❖ Sulphuric Acid (AR grade, Rankem India)
- ❖ Triton X-100 [$C_{14}H_{22}O(C_2H_4O)_n$] (97%, Merck India)

2.1.4. Synthesis of silver nanoparticles in DMF:

The silver nano particles were prepared by the reduction of silver ions by DMF, in the absence of common stabilizing agents **[220]**.

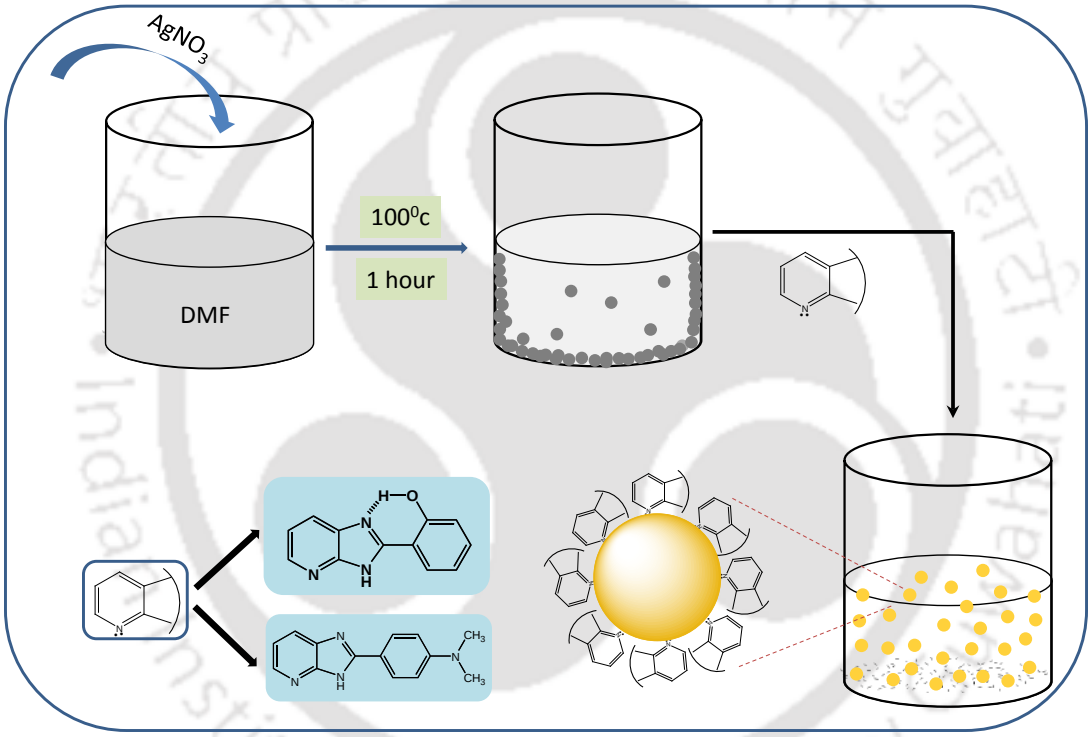

Scheme 2.1: Schematic representation of the silver nanoparticles preparation and their stabilization in DMF.

Silver nitrate (0.1 mM) was used as a source for silver. The reaction was continued at 100^0 C for one hour. Within 1 hour, the silver nitrate salt was reduced to silver zero through the following reaction.

$$HCONMe_2 + 2Ag+ + H_2O \longrightarrow 2Ag^0 + Me_2NCOOH + 2H^+$$

The carbamic acid formed in the reaction was decomposed at the high temperature used in this procedure. The high temperature also favours the evaporation the resulted amine produced by the decomposition.

$$Me_2NCOOH \longrightarrow CO_2 + Me_2NH$$

The zero valent silver thus produced resulted in the formation of silver nanoparticles. The colour of the solution proceed through different phases at different time scale in the absence of any stabilizing agent. Initially, the solution colour become yellow flowed by brown and eventually shiny metal particles deposit on the wall of the glass like silver mirror. These unstable nanoparticles are stabilized by a set of ICT and ESIPT fluorophores which is going to be discussed in the respective chapters. **[See chapter 3 and 6]**

2.1.5. Synthesis of silver nanoparticles in water:

Silver nanoparticles in aqueous medium were synthesized by simple sodium borohydride reduction procedure. 400 µL of 10 mM silver nitrate was added to 100 mL of Millipore water in a culture tube. Sodium hydroxide or dilute sulphuric acid solution was added to the solution to maintain different p^H of the solutions. 22 solutions are prepared having p^H ranging from 2.7 to 12.4 to find out the exact range of p^H suitable for the nanoparticles synthesis. After preparing these solutions, small amount of sodium borohydride solution was added till the appearance of the golden yellow colour. The appearance of the golden yellow colour indicates the formation of silver nanoparticles. The colours obtained for different solutions having different p^H values are found to be different. This indicates the nanoparticles formed at different p^H have different stability. The nanoparticles are well stabilized in two p^H ranges, 5 to 6 and around 10. This is also clear from the **Figures 2.1**.

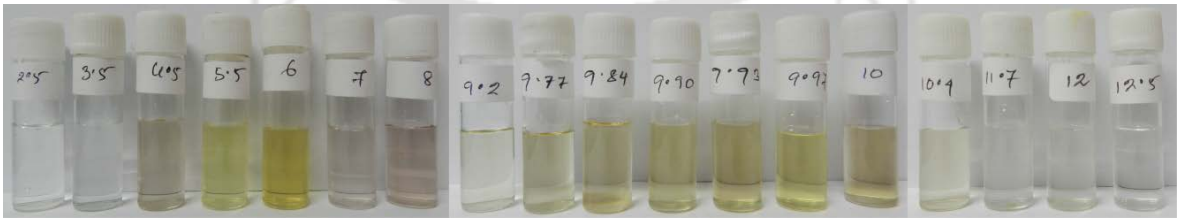

Figure 2.1: Pictures of silver solution in the p^H range 2.5 to 12.5.

The formation of silver nanoparticles was confirmed by the visual change in colour, which is from colour less to golden yellow. This is further proved by the sharp SPR band at 410 nm which is characteristics of silver nanoparticles.

The UV-VIS study showed that except p^H 2.69, all solutions appeared golden yellow colour immediately after the addition of borohydride solution indicating the formation of silver nanoparticles. But after 5 hours, the high absorbance of the characteristics SPR band sustains for the solutions having p^H 9.97. **Figure 2.2** shows the maximum SPR absorbance of the solution prepared at p^H 9.97.

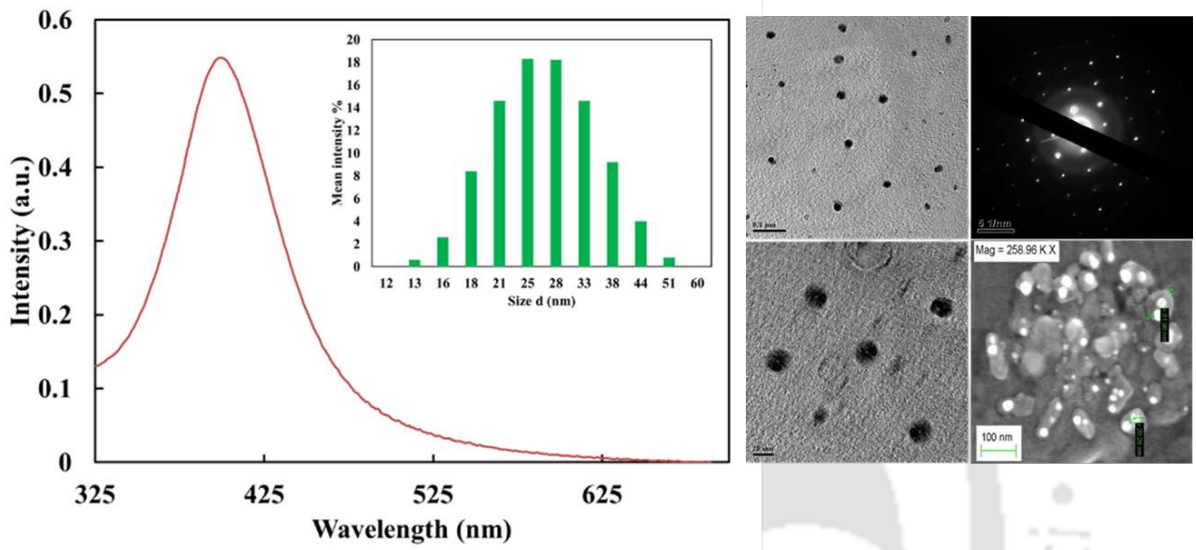

Figure 2.2: Surface plasmon resonance spectrum, TEM and FESEM images of silver nanoparticles prepared in water at p^H 9.97. Inset shows the DLS spectrum of silver nanoparticles with an average diameter of 25±5 nm.

All the other solutions, the absorbance of the characteristic peak decreases with a broadened spectrum. In case of solutions having p^H 4.25, 8 and 10 there is clear dual band at around 530 nm. This is a clear indication of the formation of bigger sized particles by agglomeration due to the lack of enough stabilizes in solutions. The specie which is responsible for the different stability of the nanoparticles is directly related to the p^H of the solution. From the equations we can clearly observed the evolution of hydroxyl ion during the reaction procedure. The presence of these anions in the nanoparticles solution is well established by the high basicity of the solution. However the final nanoparticles solutions, prepared in acidic condition are also equally basic in nature as that prepared in basic medium. This confirms the formation of the OH ion during nanoparticles formation as explained below-

$$NaBH_4 + 4H_2O \longrightarrow 4H_2 + NaB(OH)_4$$

$$AgNO_3 + NaOH \longrightarrow AgOH + NaNO_3 \xrightarrow{NaB(OH)_4} Ag^0 + OH^- + NaNO_3^- + B(OH)_3$$

2.1.6. Synthesis of organic nanoparticles by re-precipitation Method:

Aqueous suspensions of small organic particles had been prepared by re-precipitation method by various research groups **[221-224]**. This simple and mild method, based on a solvent exchange, has been widely developed during the past few years and has proved to be very useful in preparing nano and microcrystals of various organic dyes. It consists of dissolving the organic compound in a hydrophilic solvent, and then pouring a small volume of this concentrated solution into a large volume of water. The organic compound then precipitates, thus leading to the formation of particles in aqueous suspension.

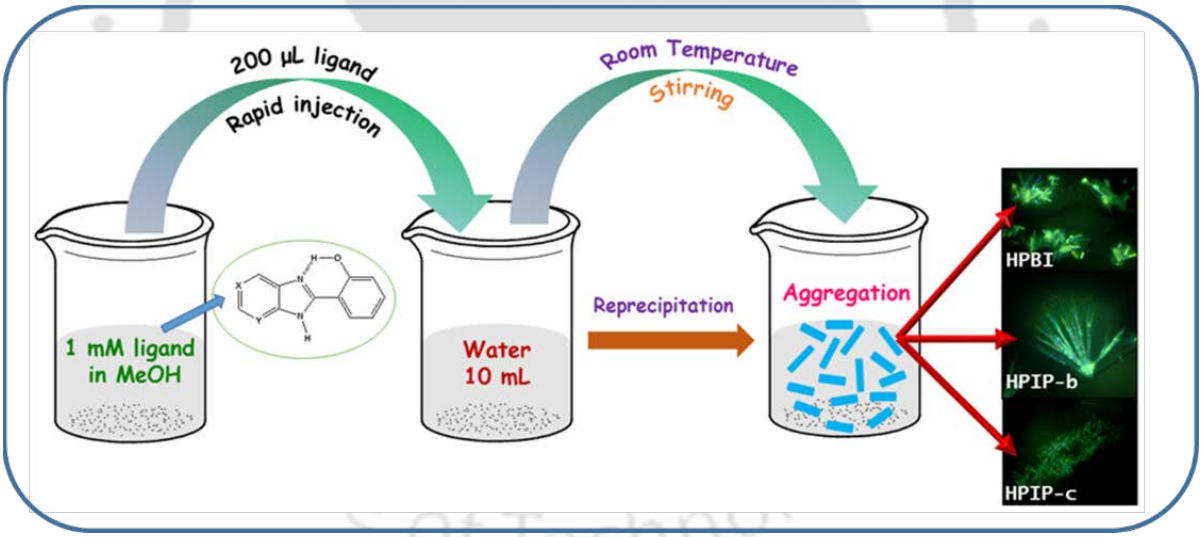

Scheme 2.2: Formation of aggregated structures from re-precipitation of fluorophores in water with 2% v/v methanol.

In the chapter 7, the aggregated organic particles were prepared by this re-precipitation method. Stock solutions of 2-(2'-hydroxyphenyl)benzimdazole and its pyridyl analogues (1 mM) in methanol were prepared. 200 µL of these solutions were very rapidly injected into culture tubes containing 10 mL of water, and the mixtures were stirred at room temperature **[Scheme 2.2]**. The process was monitored by absorption and fluorescence spectrometers to ascertain the aggregation induced enhanced emission.

2.2. Preparation of Samples:

2.2.1. In Solvents:

1 mM stock solution of the fluorophore was prepared in methanol. From the 1 mM solution 100 µL solution was pipette out to a volumetric. The complete evaporation of the methanol was done by keeping the solution overnight at in the oven at ~ 50 ºC. After complete removal of methanol, 10 ml of desired solvent was added. The flask was shaken well to dissolve the compound completely. Dilute solution of sodium hydroxide and sulphuric acid was used for maintaining different p^H of the aqueous solutions. The final concentration of all the fluorophores for any absorption or fluorescent measurement was 10 µM unless otherwise mentioned.

2.2.2. Preparation of fluorophore-nanoparticles solutions:

In this procedure 100 µL of fluorophore solution (1 mM) in methanol was dried at 50 ˚C in a volumetric flask. 500 µL was taken from the nanoparticles solution prepared as discussed in section 2.1.4 and added to the dried fluorophore. Finally the volume was made up to 10 ml and used in various spectroscopic studies. In case of fluorophore-nanoparticles-β-CD composite, 170.2 gm of β-CD was added to the dried fluorophore prior to nanoparticles solution. The solution was diluted to 10 mL and kept for further study. The concentration of β-CD was 15 mM. The 10 µM fluorophore solution in 15 mM β-CD was prepared by adding the required amount of CD to the dried fluorophore in 10 mL volumetric flask. For the preparation of fluorophore-nanoparticles solution in water, 10 mL of NPs solution prepared by the method described in section 2.1.7 was added to the pre dried fluorophore in a 10 mL volumetric flask.

2.2.3. Preparation of protein and micelle samples:

Aqueous phosphate buffer solution of pH 7.0 ± 0.1 was used to prepare the protein samples. Appropriate amount of protein solution was added to the dried fluorophore. Micelles-fluorophore solutions were prepared by adding required amount of respective micelle solution in volumetric flask containing the dried fluorophore. The p^H of the solutions was maintained by adding very small quantity or acid or base.

2.4. Instruments:

2.4.1. pH Meter:

The pH of different solutions was measured using Jenway pH Meter (Model No 3510). The pH meter was calibrated by using three different standard buffer solutions (pH 4.0, pH 7.0 and pH 10.0) within a range of ± 0.01-0.02 pH units before a measurement was performed.

2.4.2. Absorption Spectrometer:

Absorption spectrum is the most widely used spectroscopic technique which provides the wavelength of a transition and the corresponding molar extinction coefficient (ε_λ) of a chromophore under investigation. The modern ultraviolet-visible spectrometer consists of light source, monochromator, detector, amplifier and recording devices. Quartz cells to hold the sample are used for the measurement of the absorption spectra. In the present work, the absorption spectra were recorded on a Varian Cary 100 or a Perkin Elmer Lambda 25 double beam ultraviolet-visible spectrometer. Deuterium and tungsten lamps are used as UV and visible sources, respectively. In Cary 100, a photomultiplier tube (PMT) is used as detector.

2.4.3. Steady state spectrofluorimeter:

Steady state fluorescence spectra were recorded on JobinYvonSpex Fluoromax 4 spectrofluorimeter. Optical system of spectrofluorimeter consists of a light source, monochromators, sample holder, a detector, shutters, polarizers if necessary, and a beam splitter. The beam splitter consists of a quartz plate which reflect a few percent of the exciting light towards a quantum counter or a photodiode. Xenon arc lamp is the most common light source used in fluorimeters which can provide uniform intensity over a broad spectral range from UV to near infrared. The excitation wavelength is selected by the excitation monochromator. Fluorescence is collected at right angles with respect to the incident beam and the emitted light is detected through a monochromator by a PMT. Automatic scanning of wavelengths is done by motorized monochromator which is controlled by electronic devices and the computer. The emission spectrum reveals the variation of fluorescence intensity as a function of λ_{em} (the wavelength at which the fluorescence is observed) at fixed excitation wavelength (λ_{exc}). The excitation spectrum

shows the variation of fluorescence intensity as a function of λ_{exc} with fixed λ_{em}. The monochromators of spectrofluorimeter are equipped with gratings, so that for a given width of the input and output slits, the monochromators operate at a constant band pass expressed in wavelength. Hence the spectra are recorded as a function of wavelength and not wavenumber. The fluorescence spectra are needed to be corrected for the distortion by the wavelength dependence of several components of the instrument.

The emission spectrum is distorted by the wavelength dependence of the emission monochromator efficiency and the photomultiplier response. In general, the correction factors are measured using a calibrated tungsten lamp or by a standard fluorescent dye whose corrected emission spectrum has been reported. Emission correction factors are provided by the manufacture in all the three instruments used.

The excitation spectrum is distorted by the different intensity of exciting light. This difference in intensity rooted from the wavelength dependent lamp intensity and the transmission efficiency of the excitation monochromator. Because the quantum counter evades the wavelength dependence of the sensitivity of the sample and the reference photomultiplier. The ratio of the fluorescence signal from the sample to that from the quantum counter or photodiode, as a function of the excitation wavelength, provides in principle corrected excitation spectra. However, such correction procedures may be insufficient regarding very accurate measurements. In fact, the optical geometry of the reference channel is not identical to that of the main channel, and the wavelength dependence of optical parts (e.g. focal length of lenses) may introduce some distortion into the excitation spectrum. It is then recommended to use correction factors obtained by using a fluorophore absorbing in the same wavelength range as that of the sample to be studied, and whose absorption spectrum is identical to its excitation spectrum. The ratio of the measured excitation spectrum of this reference compound – as described above using the quantum counter – to the absorption spectrum provides the correction factors that can be stored in the computer. It should be noted that most commercially available instruments are delivered with a file containing the correction factors. Fluoromax 4 is equipped with single excitation monochromator with 150 W xenon arc lamp as light source and Hamamatsu red sensitive PMT R928 as detector.

2.4.4. Time Resolved Spectrofluorimeter:

The time required for a population of N electronically excited fluorophores to decrease exponentially by a factor of a to N/a via the loss of energy through fluorescence and other nonradiative processes is known as fluorescence lifetime which range from 10 femtosecond to nanosecond. It is independent of way of measurement owing to its intrinsic property. It is considered as a state function, as it is independent of the initial perturbation conditions like excitation wavelength, one or multiphoton excitation, duration of light exposure, fluorescence intensity and fluorophore concentration. Since fluorescence occurs from an energetically unstable state, fluorescence lifetime is sensitive to internal and external factors. The internal factor comprises of the fluorophore structure and the external factors include temperature, polarity, viscosity and the presence of fluorescence quenchers.

There are two ways to determine the fluorescence lifetime of the fluorophores, frequency-domain and time-domain **[225-231].** They have different instrumentation setups and follow different data acquisition methods, however, both approaches are mathematically equivalent and their data can be interconverted by Fourier transform. In frequency domain method, the incident light is sinusoidally modulated at high frequencies such that the emission occurs at the same frequency as the incident light. The difference between the incident and emitted light is that the emitted light experiences a phase delay and change in the amplitude relative to the excitation light (demodulation). Data are acquired with photomultipliers or charge-coupled devices equipped with a gain modulator. In time-domain method, the sample to be analyzed is excited with a short light pulse from a light source with sufficient delay between pulses. The light source can be flash lamp, pulsed laser, laser diode, or LED. Various methods are available for data collection. The most common technique is the time correlated single photon counting (TCSPC) which is applied in this work **[230,231]**. Figure 2.3 explains schematically the working principle of a TCSPC instrument. In TCSPC method, the light source beam is split into start and stop signal pulses. The start signal pulse travels to a PMT or micro-channel plate (MCP) photomultiplier which activates the time-to-amplitude converter (TAC). The stop signal pulse travels through the sample. The growth of ramp signal in TAC is stopped by this pulse. The TAC output can be amplified by an amplifier, and this analogue pulse of height corresponding to a measured time of the signal goes through further processing to convert to digital pulse through the

analogue to digital converter. Since the fluorophores emit photons at different relaxation times following their excitation by radiation, the decay time of single molecules must have a certain rate rather than occurring at a specific time with excitation. The principle of TCSPC is the detection of single photons and the measurement of their arrival times in respect to a reference signal from the light source. The TCSPC method needs a high repetitive light source to accumulate a sufficient number of photons since this is a statistical method and requires many numbers of statistical data precision. The time measurement of the start and stop sequence is represented by an increase of a memory value in a histogram. Thus, this experiment must be repeated many times to gather sufficient photons in the full range of delays between excitation and emission. The resulting histogram counts versus the time channels on the x-axis represents the curve of fluorescence decay profiles. In most cases, the TCSPC technique has limits for the temporal resolution and lifetime range measurable for the fluorescence lifetimes. Therefore, for the curve fittings the method involving linearization of the fitting function and least-squares fitting is the most widely used deconvolution technique. The fluorescence temporal profiles were derived by deconvolution procedures with the instrument response using nonlinear least-squares fittings.

In the present work, fluorescence lifetimes were measured with the use of LifeSpec II from Edinburgh Instruments. LifeSpec II employs Hamamatsu MCP detector that has response time of 50 ps. The light sources used to excite the sample were 308 nm LED from PicoQuant and 375 nm laser diode from Edinburgh with full pulse widths of 635 ps and 2 ps, respectively at half-maximum. Time-resolved data were analyzed with reconvolution method based on discrete components analysis model using the FAST software **[232]** developed by the Edinburgh Instruments Ltd. The goodness of fit was determined by the reduced χ^2 values and weighted residuals (X) which were between the range of ± 6. The reduced χ^2 and weighted residuals (X) are given by the following equations.

$$\chi^2 = \sum_i w_i^2 \frac{[S_i - F_i]^2}{n} \quad \text{..... 2.1}$$

$$X_i = W_i (S_i - F_i) \quad \text{..... 2.2}$$

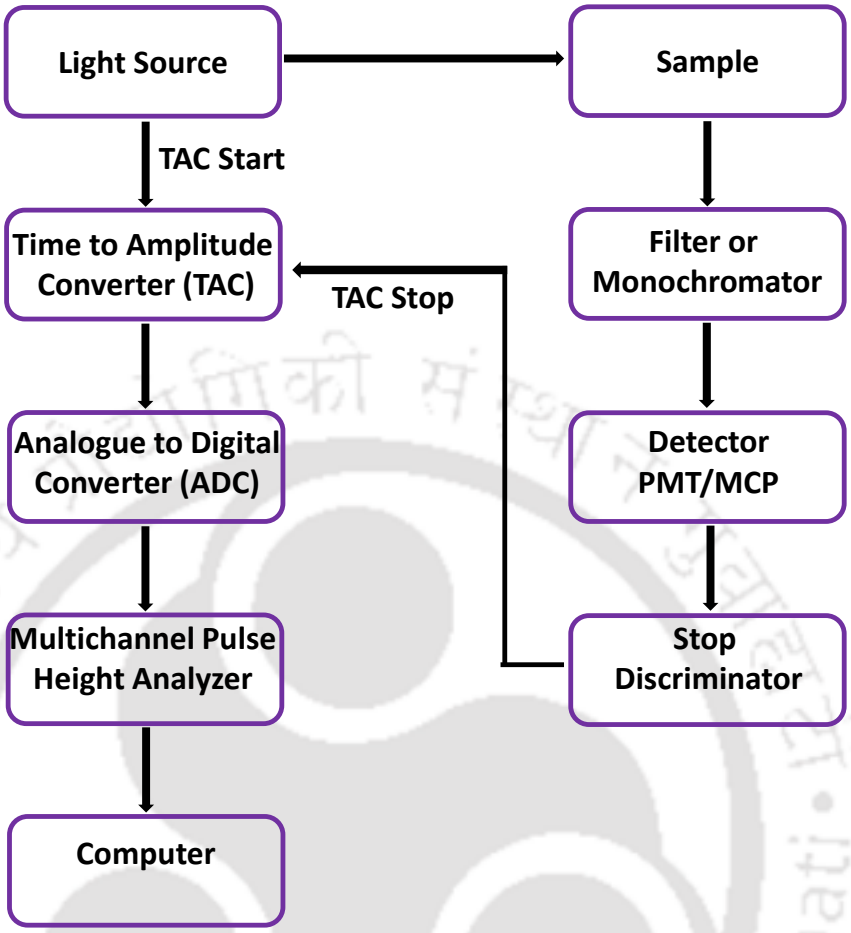

Figure 2.3: Block diagram of a TCSPC instrument

Where W_i, F_i, and S_i are the weighting factor, measured value, and fitted value, respectively and n is the number of fitted data points subtracted by the number of lifetime parameters used in the fit.

2.4.5. Field emission scanning electron microscopy:

Field emission scanning electron microscopy (FESEM) provides topographical and elemental information at different magnifications ranging up to 5,00,000x depending on the conductivity of the sample. FESEM primarily consists of an electron gun as a source of electrons, a column with lenses, apertures and an object chamber where the samples with conductive layer can be mounted on a special holder. The sigma model of FESEM instrument was used for recording images manufactured by Zeiss.

Electron gun: The field emission electron gun is a cold cathode field emitter. An extremely thin and sharp tungsten needle with tip diameter <100 nm functions as a cathode in front of a primary and secondary anode. The emission of electrons are collected by placing the filament in a huge electrical potential gradient of magnitude of 0.5 to 30 KV. The electron beam produced by the field emission source is about 1000 times smaller than in a standard microscope which implies markedly better image quality. Field emission sources provide enhanced performance, reliability and lifetime.

The column chamber contains the electro-magnetic lenses such as condenser lens, scan coils, stigmator coils and objective lens to focus the electron beam. These electromagnetic lenses consist of a coil of wire which generates a magnetic field across the lens gap between the pole pieces.

Condenser lens: It controls the amount of demagnification. The current in the condenser determines the diameter of the beam. A low current results in a small diameter and higher current results in a higher diameter. A narrow beam has the advantage of better resolution. But the worse signal to noise ratio is a major disadvantage.

Stigmator coils: The stigmator coils are utilized to correct irregularities in the x and y deflection of the beam and thus to obtain a perfectly round-shaped beam. When the beam is not circular, but ellipsoidal, the image looks blurred and stretched.

Objective lens: It focuses the electron beam onto the specimen. It is the lowest lens in the column. At a short working distance the objective lens needs to apply a greater force to deflect the electron beam. The shortest working distance produces the smallest beam diameter, the best resolution, but also the poorest depth of field.

Scan coils: It consist of upper and lower coils which deflect the electron beam over the object according to a zig-zag pattern. The formation of the image on the monitor occurs in synchrony with this scan movement. The scan velocity determines the refreshing rate on the screen and the amount of noise in the image. Rapid scan resulted in rapid refreshing which always yield low signal with more noise.

Object chamber: After the object has been covered by a conductive layer, it is mounted on a special holder. The object is inserted through an exchange chamber into the high vacuum part of the microscope and anchored on a moveable stage. The object can be repositioned in the chamber by means of a joy stick that steers in left-right axis, or forward and backward.

In addition, the object can be tilted, rotated and moved in Z direction. The "secondary electron emission" detector is located at the rear of the object holder in the chamber.

A focused beam of electrons is used to generate an image or to analyze the specimen. For operation, the gun head, the column and specimen chamber have to be evacuated. The pre vacuum pump and turbo pump evacuate the specimen chamber. Vacuum in the specimen chamber is measured by penning gauge. Colum chamber valve remained closed until the detected pressure is not ready for operation. After vent command, column chamber valve closes and N2 gas flows into the specimen chamber through vent valve.

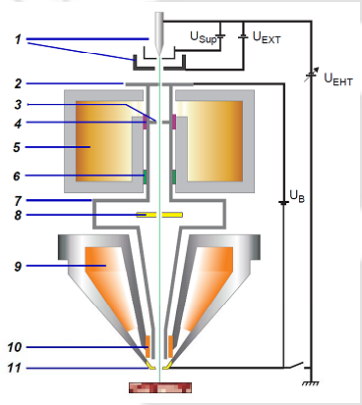

1. Schottky field emitter
2. Anode
3. Multi-hole aperture
4. Gun/aperture alignment system
5. Condenser lens
6. Sigmator
7. Linear tube
8. In-lens detector
9. Scan coils and sigmator
10. Objective cap

Figure 2.4: Schematic diagram of FESEM

Electron Gun emits electrons. The beam of electrons passes through anode aperture. Electron beam passes through a 30 µm multi-hole aperture. Other aperture sizes can be selected by using the gun/aperture alignment system. Condenser lens controls the amount of demagnification. Stigmator makes sure the beam is rotationally symmetrical. Anode and linear tube are connected to form the beam booster. Beam booster provides better protection against external stray fields. Objective lens focuses the electron beam onto the specimen. Objective lens consists of electromagnetic and electrostatic lens. Deflection system consists of a set of scan coils to move the electron beam in a point-to-point scan process. Two imaging modes are used for analysing the samples. In-lens image mode is located on the beam path. Secondary electrons having low energy are used in this mode. The energy is usually less than 50 eV. This is located on the wall of the specimen chamber. In backscattered electron image mode higher energy electrons (>50 eV) are used. This is located below final lens.

2.4.6. Transmission Electron Microscopy:

The transmission electron microscope is a very powerful tool for material science. A high energy beam of electrons is passed through a very thin sample and the interactions between the electrons and the atoms can be used to observe features such as the crystal structure, dislocations and grain boundaries. Chemical analysis can also be performed. TEM can be used to study the growth of layers, their composition and defects in semiconductors. High resolution can be used to analyse the quality, shape, size and density of quantum wells, wires and dots. The TEM operates on the same basic principles as the light microscope but uses electrons instead of light. Because the wavelength of electrons is much smaller than that of light, the optimal resolution attainable for TEM images is many orders of magnitude better than that from a light microscope. Thus, TEM can reveals the finest details of internal structure.

TEM consists of electron gun, condenser lenses, image-producing system which consist of the objective lens, movable specimen stage, intermediate and projector lenses and an image recording system. TEM images were collected by using JEM 2100 model, manufactured by JEOL.

Electron gun: An electron gun produces the electron beam and the condenser system focuses the beam onto the object. The source of electrons, the cathode, is a heated V-shaped tungsten filament or a sharply pointed rod of LaB_6. The filament is surrounded by a control grid known as Wehnelt cylinder, with a central aperture arranged on the axis of the column. The cathode and control grid are at a negative potential equal to the desired accelerating voltage and are insulated from the rest of the instrument. The final electrode of the electron gun is the anode, which takes the form of a disk with an axial hole. Electrons are emitted from the cathode, left the shield and accelerate toward the anode. With adequate stabilization of the high voltage, electrons pass through the central aperture at a constant energy. The control and alignment of the electron gun are critical in ensuring satisfactory operation.

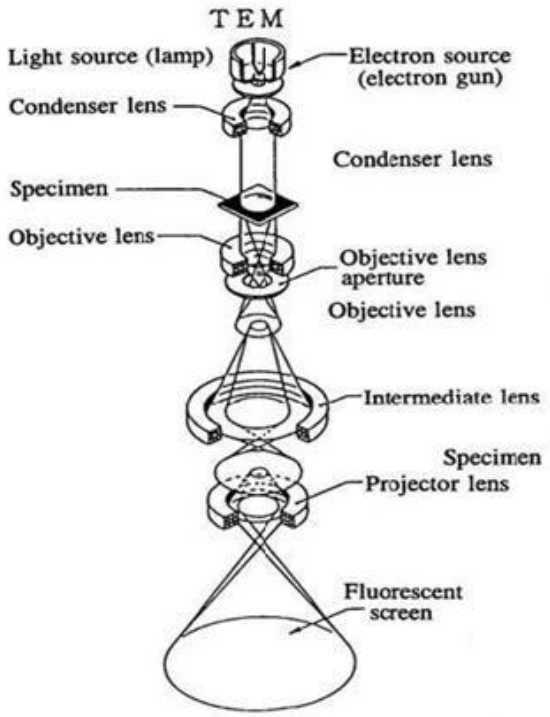

Figure 2.5: Schematic diagram of TEM

Condenser system: The intensity and angular aperture of the beam are controlled by the condenser lens system between the gun and the specimen. A single lens may be used to convert the beam onto the object, but, more commonly, a double condenser is employed. In this the first lens is strong and produces a reduced image of the source, which is then imaged by the second lens onto the object. Such an arrangement is economical of space between the electron gun and the object stage and is more flexible, because the reduction in size of the image of the source (and hence the final size of illuminated area on the specimen) may be varied widely by controlling the first lens. The use of a small spot size minimizes disturbances in the specimen due to heating and irradiation.

The image-producing system: The image-producing system consist of the objective lens, movable specimen stage, intermediate and projector lenses which focus the electrons passing through the specimen to form a real, highly magnified image. The specimen grid is placed in a small holder in a movable specimen stage. The objective lens with short focal length (1–5 mm) produces a real intermediate image that is further magnified by the projector lens or lenses. A single projector lens may provide a range of magnification of 5:1. Modern instruments employ two projector lenses (one called the intermediate lens) to permit

a greater range of magnification and to provide a greater overall magnification. For practical reasons of image stability and brightness, the microscope is often operated to give a final magnification of 1,000–250,000X on the screen. If a higher final magnification is required, it may be obtained by photographic or digital enlargement. The quality of the final image in the electron microscope depends largely upon the accuracy of the various mechanical and electrical adjustments with which the various lenses are aligned to one another and to the illuminating system.

Image recording: The image-recording system converts the electron image into some form perceptible to the human eye. It consists of a fluorescent screen for viewing and focusing the image and a digital camera for permanent records. In addition, a vacuum system consisting of pumps and their associated gauges and valves and power supplies are required. The electron image is monochromatic and must be made visible to the eye either by allowing the electrons to fall on a fluorescent screen fitted at the base of the microscope column or by capturing the image digitally for display on a computer monitor. Computerized images are stored in a format such as TIFF or JPEG and can be analysed or image-processed prior to publication. The identification of specific areas of an image, or pixels with specified characteristics, allows spurious colours to be added to a monochrome image. This can be an aid to visual interpretation and teaching and can create a visually attractive picture from the raw image.

Chapter 3

Silver nanoparticles induced dual emission from 2-(4′-N,N-dimethylaminophenyl) pyridoimidazoles : Enhanced TICT emission in β-Cyclodextrin

3.0. Introduction:

The construction of fluorescent nanometarials has been a matter of interest throughout the last decade. In this context the behavior of the fluorophore in presence of nanoparticles is vital. Fluorescence quenching as well as intensity enhancement in the vicinity of nanoparticles were reported by different research groups **[see introduction, section 1.2.3.1 and 1.2.3.2]**. Among them the quenching of the ICT or TICT state by nanoparticles is of prime importance as these states are very sensitive to microenvironments. However energy transfer and charge transfer from the fluorophore to nanoparticles also play important role.

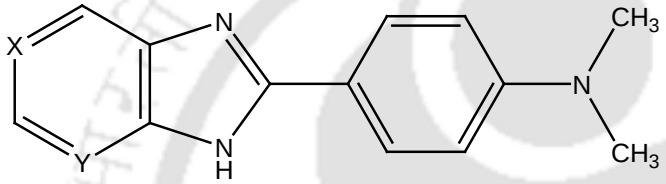

X = Y = CH DMAPBI

X = CH, Y = N DMAPIP-b

X = N, Y = CH DMAPIP-c

Chart 3.1. Structures of 2-(4′-N, N-dimethylaminophenyl) benzimidazole (DMAPBI), 2-(4′-N, N-dimethylaminophenyl) imidazo[4,5-b]pyridine (DMAPIP-b) and 2-(4′-N,N-dimethylaminophenyl) imidazo[4,5-c]pyridine (DMAPIP-c)

2-(4′-N,N-dimethylaminophenyl) imidazo[4,5-b]pyridine (DMAPIP-b) and 2-(4′-N,N-dimethylaminophenyl) imidazo[4,5-c]pyridine (DMAPIP-c) are biologically active molecules **[64, 66, 233, 67]**. DMAPIP-b has been shown to act as an inhibitor for of Aurora-A, Aurora-B and Aurora-C kinases which play a key role in the regulation of mitosis, and are implicated in cancer initiation and progression **[234, 235]**. It was already proved that these molecules are capable of acting as probes in different environments **[65, 236-238]**. DMAPIP-b as well as DMAPIP-c exhibit dual emissions which are solvent specific. These dual emitting behavior is prominent only in protic solvent and the presence of the hetero atom as well as its involvement in hydrogen bonding with solvent plays an important role **[64, 66, 233, 67]**. It was already proved that DMAPIP-b can be used as a qualitative water sensor in micro heterogeneous systems. It mentioned above that the charge transfer from the fluorophore to the nanoparticles can quench the ICT state. In this chapter, work has been done to find out whether silver nanoparticles can induce the formation of TICT state in these

fluorophores which eventually will emit dual emission in aprotic solvent. For better understanding, the interactions of nanoparticles with 2-(4′-N, N-dimethylaminophenyl) benzimidazole (DMAPBI) was also carried out, which has no pyridyl nitrogen.

3.1. Growth and stabilization of the nano particles:

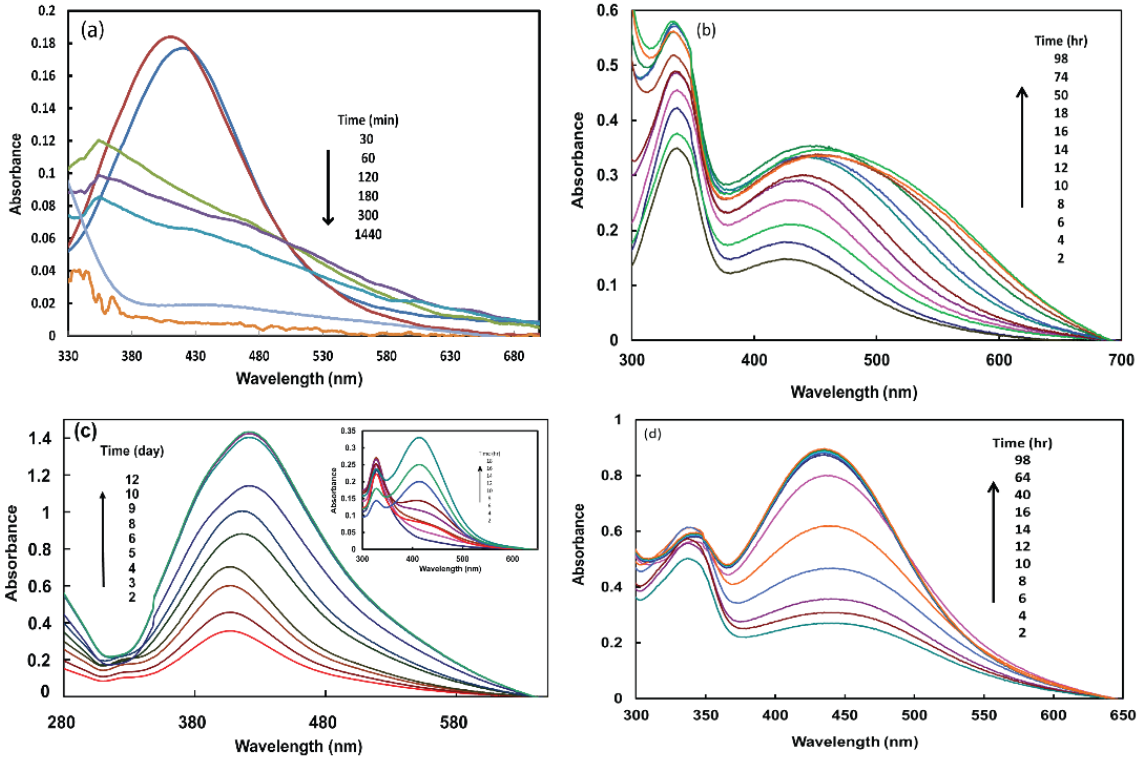

Figure 3.1: Growth of silver nanoparticles in (a) absence of fluorophore and in presence of (b) DMAPBI, (c) DMAPIP-b, (d) DMAPIP-c.

The nanoparticles were allowed to grow in the absence and the presence of fluorophores. The growth was followed by SPR band (420 nm) of silver nanoparticles **[Figure 3.1]**. In absence of fluorophores the absorbance of the SPR band decreases with time. On the other hand in the presence of fluorophores, the absorbance of the SPR band increases and it follows the order DMAPIP-b > DMAPIP-c > DMAPBI. While DMAPBI and DMAPIP-c assist the growth of the nanoparticles for several hours, DMAPIP-b facilitates the nanoparticles to grow even up to 10 days.

The absorption spectrum of the nanoparticles in presence of DMAPBI is broader compared to those in the presence of DMAPIP-b and DMAPIP-c. The full width at half maximum in the presence of DMAPBI, DMAPIP-b and DMAPIP-c are 10,500 cm^{-1}, 7000

cm^{-1} and 7700 cm^{-1}, respectively. Depending upon the stabilizing capacity of fluorophores different numbers of nanoparticles are formed. This is also suggested by the difference in absorbance value of the SPR band of the particles.

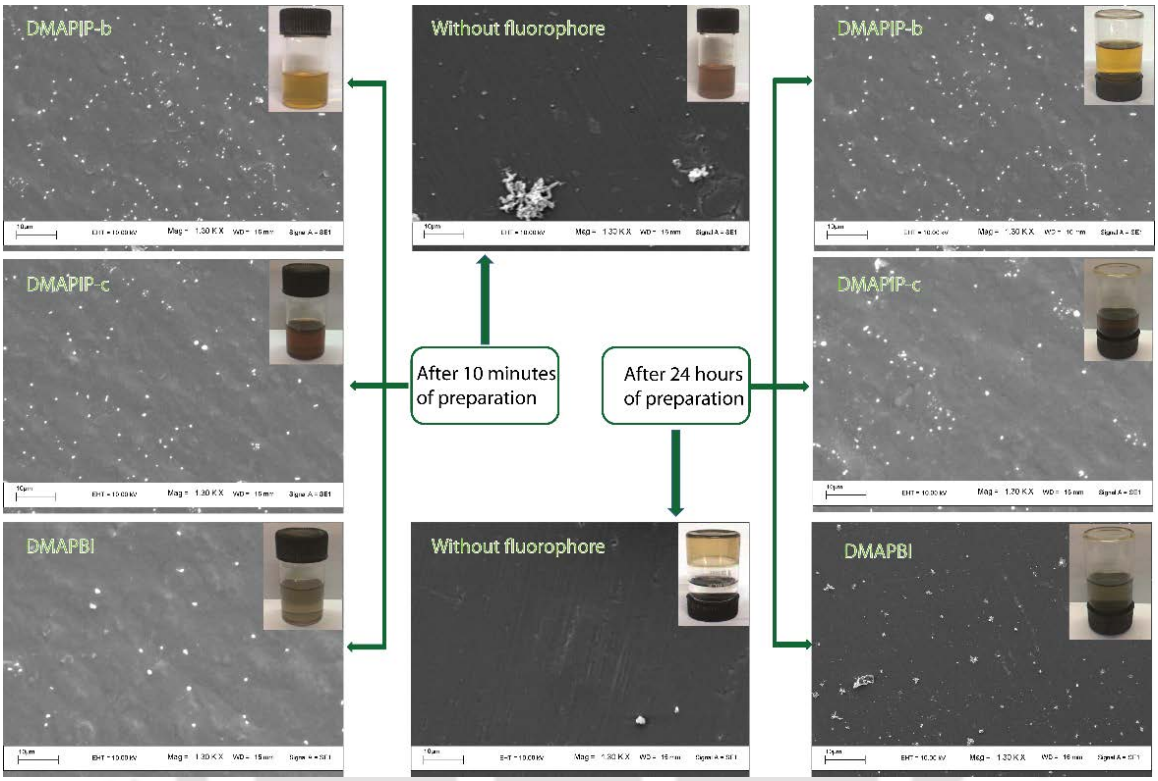

Figure 3.2: FESEM images of nanoparticles in presence and absence of three fluorophores within an hour of preparation (left side) and after 24 h (right side). The insets show the vials containing the silver nanoparticles after respective time scales.

The FESEM images and the photographs of the vials containing nanoparticles are presented in **[Figure 3.2]**. In the absence of fluorophores, after 24 h all the silver particles stick on the glass surface and the solution becomes transparent. The FESEM image also confirms the absence of nanoparticles in the solution. This result is consistent with the study reported by Pastoriza-Santos and Liz- Marzán where silver nanoparticles in the absence of stabilizer electro statically attach onto the glass surfaces and only very small amount of particles disperse in the solution **[see materials and method section 2.1.4]**. However, in presence of the fluorophores, silver particles do not stick on the side of the wall even after 24 h and it is substantiated by FESEM **[Figure 3.2]** and TEM images **[Figure 3.3]**.

TEM images also indicate that the average size of the particles grown in presence of DMAPIP-b is relatively smaller than those grown in the presence of DMAPIP-c. These

results clearly establish that the fluorophores interact with the nanoparticles and the interactions lead to stabilization of the nanoparticles.

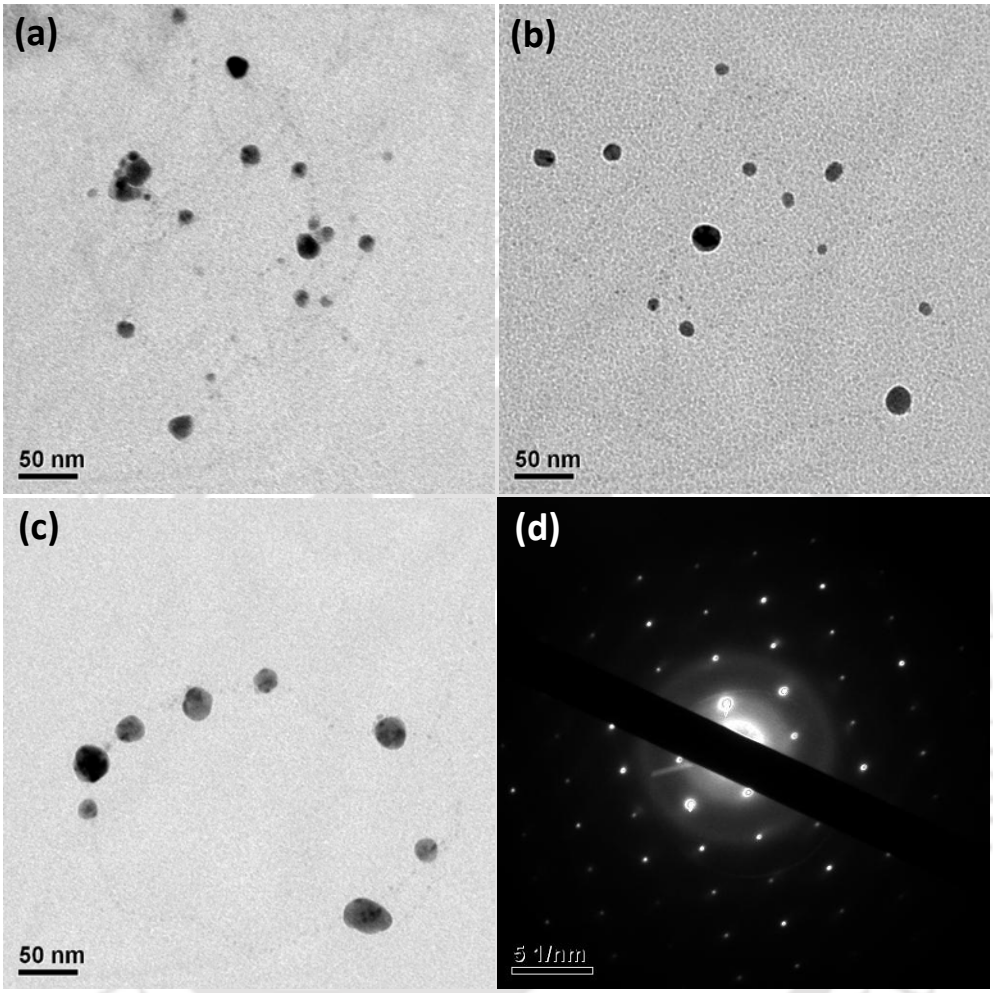

Figure 3.3: TEM images of nanoparticles in presence of (a) DMAPBI, (b) DMAPIP-b, (c) DMAPIP-c and (d) Electron diffraction pattern of the nanoparticles.

The stabilization depends on the presence and the position of the pyridyl nitrogen. Pyridoimidazoles stabilize the nanoparticles more than DMAPBI and it follows the order DMAPIP-b > DMAPIP-c > DMAPBI. In other words the pyridyl nitrogen plays an important role in these interactions and the stabilization of the nanoparticles.

3.2. Fluorescence characteristics:

The fluorescence emission intensity of all the fluorophores **[Figure 3.4]** got bathochromically decreased with progressive addition of silver nanoparticles. The shift in DMAPBI was very little whereas the pyridine nitrogen derivatives suffers shift of 10-12 nm

[Table 3.1] towards red side. These observed bathochromic shifts pointed towards the involvement of pyridine nitrogen in the interaction with nanoparticles. These interactions increases the charge flow form the donor dimethylamino moiety to the heterocyclic ring which indeed resulted in red shifted emission spectra. If these interaction happens through the dimethylamino group, there would have been a hypsochromic shift in the spectrum due to the decreased charge flow from the donor.

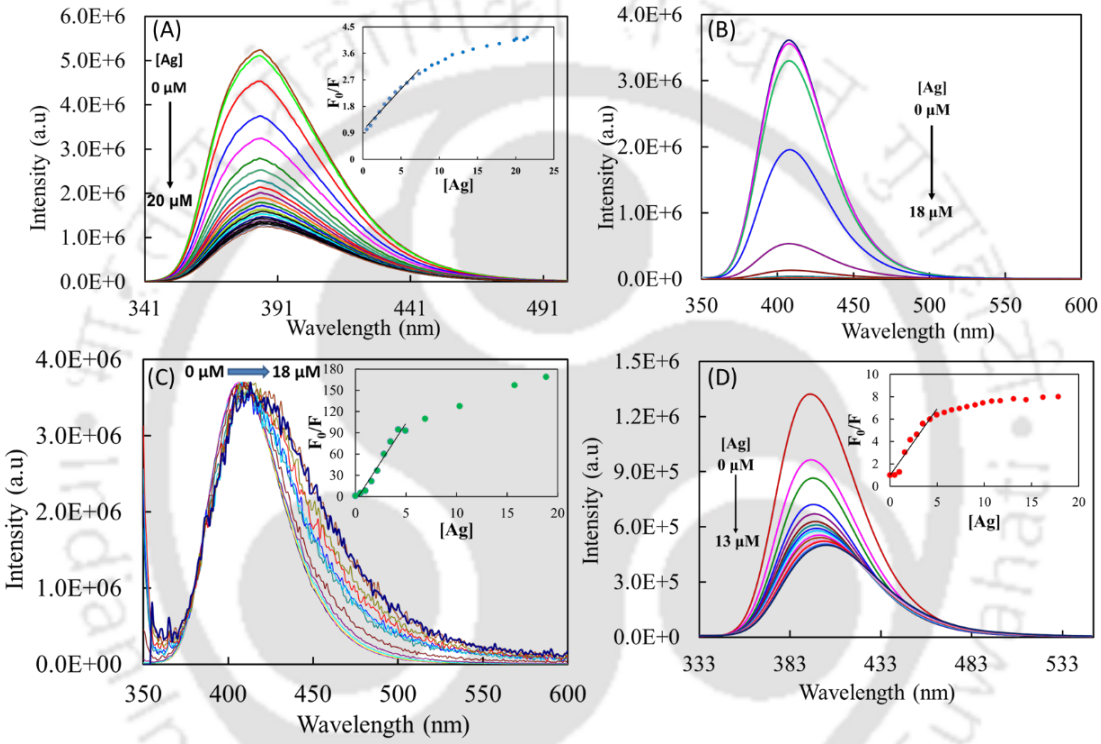

Figure 3.4: Fluorescence spectra of (A) DMAPBI (λ_{exc} = 331 nm), (B) DMAPIP-b, (C) DMAPIP-b [normalised] (λ_{exc} = 347 nm) and DMAPIP-c (λ_{exc} = 323 nm) at different concentrations of nanoparticles and the inset show the plot fluorescence ratio against silver concentration. The fluorescence ratio plots are obtained by using the integrated area of the fluorescence spectrum.

The energy transfer from the fluorophore to nanoparticles causes fluorescence quenching. The large overlap between the SPR band of the nanoparticles and the emission spectra of the fluorophores **[Figure 3.5]** established the possibility of energy transfer among these moieties which can lead to fluorescence quenching. This overlap was found to be higher for DMAPIP-b compared to other derivatives **[Figure 3.5]**. Even though similar red shifts were obtained for the pyridoimidaoles, more efficient quenching was observed in case

of DMAPIP-b **[Figure 3.4]**. This strengthened the energy transfer hypothesis also. Hence the quenching of these fluorophores could be a cumulative effect of both charge and energy transfer process.

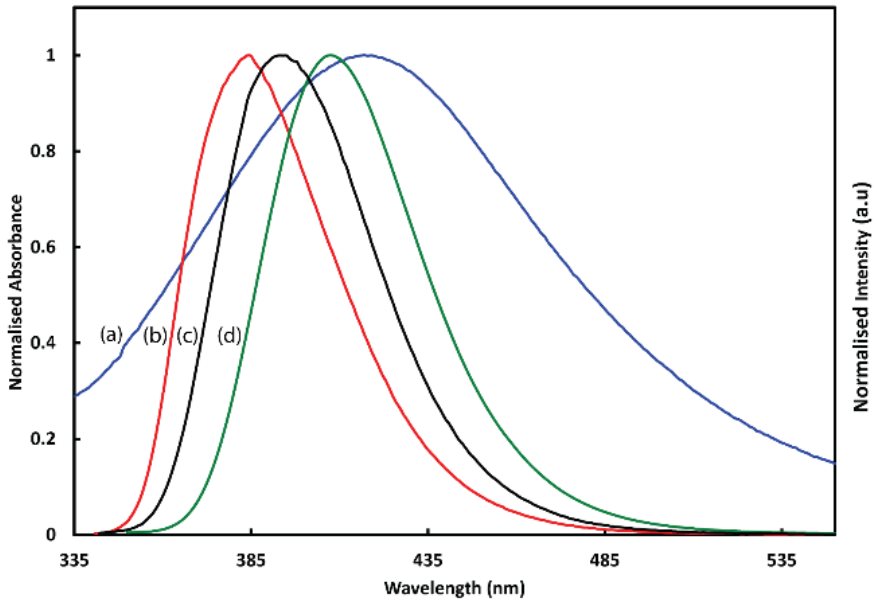

Figure 3.5. (a) Normalized absorption spectrum of the nanoparticles and the fluorescence spectra of (b) DMAPBI, (c) DMAPIP-c and (d) DMAPIP-b.

The photophysics of these pyridoimidazoles has been well studied in different environments **[64-67, 233, 236-238]**. In aprotic solvent, DMAPIP-b and DMAPIP-c were characterized by single emission emit single emission. But these fluorophores were equipped with dual emissions in protic solvents. The emission in the shorter wavelength is like normal emission and the longer emission occurs from the TICT state. The hydrogen bonding of the solvent with the pyridyl nitrogen plays a vital role in dual emission and it induced the TICT emission in these molecules. The increase in the hydrogen bond donating ability of the solvents increases the formation of TICT state.

The intensity ratio of the longer wavelength to the shorter wavelength increases with the increasing concentrations of nanoparticles. But no clear dual emission was monitored except long tailing in longer wavelength. The time resolved fluorescence of these fluorophores in presence of nanoparticles was expected to bring more light into this discussion **[Table 3.1]**. Single exponential decay with same life time were measured for DMAPBI [**Figure 3.6]** in presence and absence of nanoparticles. The pyridoimidazole

derivatives also exhibit monoexponential decay in aprotic solvent **[Table 3.1].** But higher chi square values were obtained for monoexponential fit in presence of nanoparticles. However the bi-exponential fits **[Table 3.1]** yielded good chi square values. These fittings pointed towards the fact that the decays of pyridoimidazoles in presence of nanoparticles are bi-exponential and emissions were occurring from two excited states. **Figure 3** demonstrated that the fluorescence decays of all the fluorophores. These behaviors further predict that DMAPIP-b and DMAPIP-c are interacting with nanoparticle through pyridyl nitrogen.

Table 3.1: The fluorescence characteristics of fluorophores in different environments.

	λ_{max}^{f} (nm)	$\Delta\lambda$ (nm)	τ (ns)	χ^2	τ_1 (ns)	τ_2 (ns)	χ^2
DMAPBI							
In absence of β-CD and nanoparticle	385		1.21	0.94			
In presence nanoparticle	387	2	1.10	0.98			
In presence of β-CD	385	0	1.21	1.10			
In presence of β-CD and nanoparticle	390	5	1.12	0.96			
DMAPIP-b							
In absence of β-CD and nanoparticle	408		1.51	1.07			
In presence nanoparticle	406	4	1.71	1.48	1.49 (89.18)	1.89 (10.82)	1.07
In presence of β-CD	410	2	1.52	1.06			
In presence of β-CD and nanoparticle	450, 525	42	3.35	2.23	1.47 (56.24)	5.20(43.76)	1.04
DMAPIP-c							
In absence of β-CD and nanoparticle	395		1.40	1.00			
In presence nanoparticle	404	9	1.37	1.38	1.48 (79.53)	1.83 (20.47)	1.05
In presence of β-CD	398	3	1.39	1.00			
In presence of β-CD and nanoparticle	396	1	1.40	2.38	1.40 (65.04)	2.38(34.96)	1.05

Δλ – shift in the fluorescence maximum relative to that in the absence of β-CD and nanoparticle.

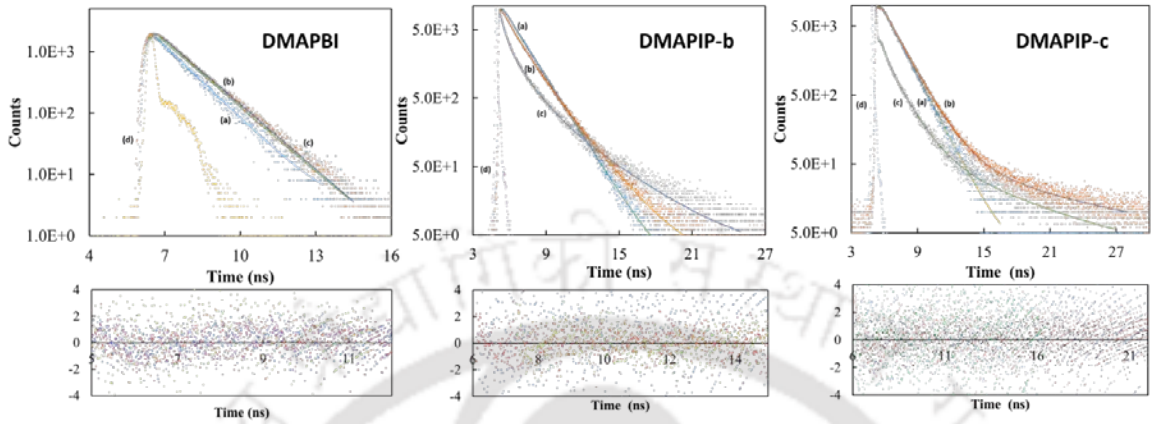

Figure 3.6: Fluorescence decay of all the fluorophores in the (a) absence of nanoparticles and β- CD (b) presence of nanoparticles (c) presence of nanoparticles and β-CD along with (d) the instrument response function and residue.

3.3. Effect of β cyclodextrin:

β-CD has been a useful candidate for guest-host chemistry throughout the decades **[11-15]**. It effects the photophysical properties of the fluorophores through selective encapsulation of the dyes. More importantly the non-radiative decays of the ICT molecules were found to be decreased inside the nanosized cavity of the β-CD **[65, 237, 244, 245]**. Experimentation of the fluorophore-nano composite in presence of β-CD were carried to strengthen the dual emission from the pyridoimidazoles derivatives.

In aprotic solvent like DMF, β-CD didn't show any effect on the fluorescence characteristics of the all the three fluorophores **[Table 3.1]**. But the fluorescence intensity was found to be quenched in presence of nanoparticles **[Figure 3.7]**. These quenching was accompanied by red shift. DMAPIP-b suffered maximum amount of shift compared to the other analogues. In addition to that, the spectra were broadened with the increasing concentration of nanoparticles. For higher concentration of nanoparticles, clear dual emission was observed for DMAPIP-b **[Figure 3.7b]**. The intensity ratio of the higher wavelength to the lower wavelength was found to be increased and got saturated at 7 μM nanoparticles concentration **[Figure 3.7b]**. From the lifetime analysis, clear bi-exponential decay was obtained **[Table 1]**. In addition to that, the percentage of the second component

increases significantly for the CD-DMAPIP-b-nanoparticles composite. But compared to DMAPIP-b, TICT emission was not so pronounced for DMAPIP-c **[Figure 3.7c]**. Only for higher concentration of nanoparticles, the intensity ratio got enhanced. The percentage of the new component in lifetime also got enhanced only by a small amount **[Table 3.1]**. These spectroscopic analysis clearly revealed that the CD-fluorophore-nanoparticles composite of the pyridoimidazoles emit dual emission. However the same composite of DMAPBI showed single emission as in absence of CD **[Figure 3.7a]**.

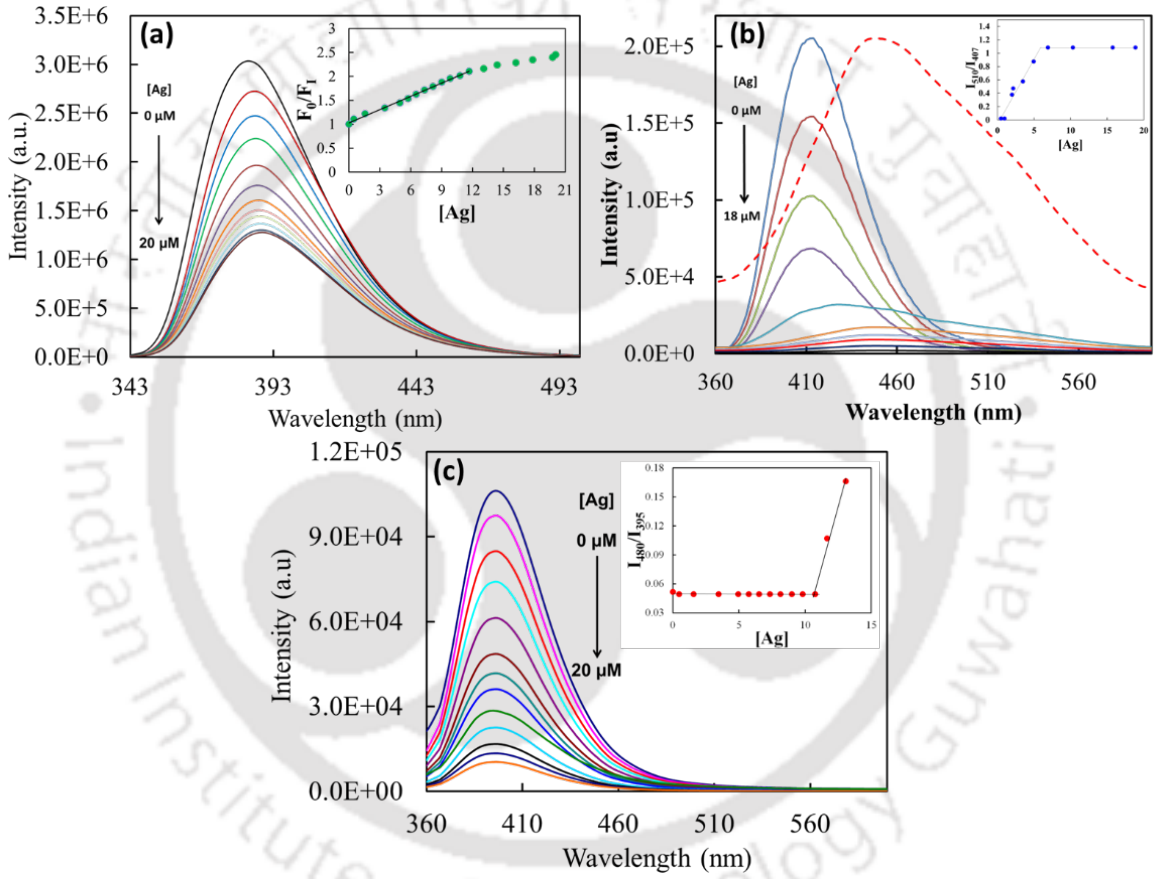

Figure 3.7: Fluorescence spectra of (a) DMAPBI, (b) DMAPIP-b and (c) DMAPIP-c in the presence of nanoparticles and β-CD. Figure (a) inset shows the fluorescence ratio against silver concentration. The fluorescence ratio plots are obtained by using the integrated area of the fluorescence spectrum. Figure (b) shows the normalized fluorescence spectrum in presence of highest concentration of nanoparticles as dotted line. [Inset show the plot of intensity ratio of longer wavelength (510 nm) to shorter wavelength (407 nm) against silver concentration. Figure (c) inset shows the plot of intensity ratio of longer wavelength (480 nm) to shorter wavelength (395 nm) against silver concentration.

The TICT emission from the CD-fluorophore-nanoparticles composite for pyridoimidazoles suggests that the nanoparticles interact with the fluorophores through the pyridyl nitrogen and the dimethylaminophenyl group is present inside the CD cavity **[Scheme 3.1]**. In such orientation, the inclusion complex formed with β-CD removed the solvation shell around the dimethyl amino moiety **[Scheme 3.1]**.

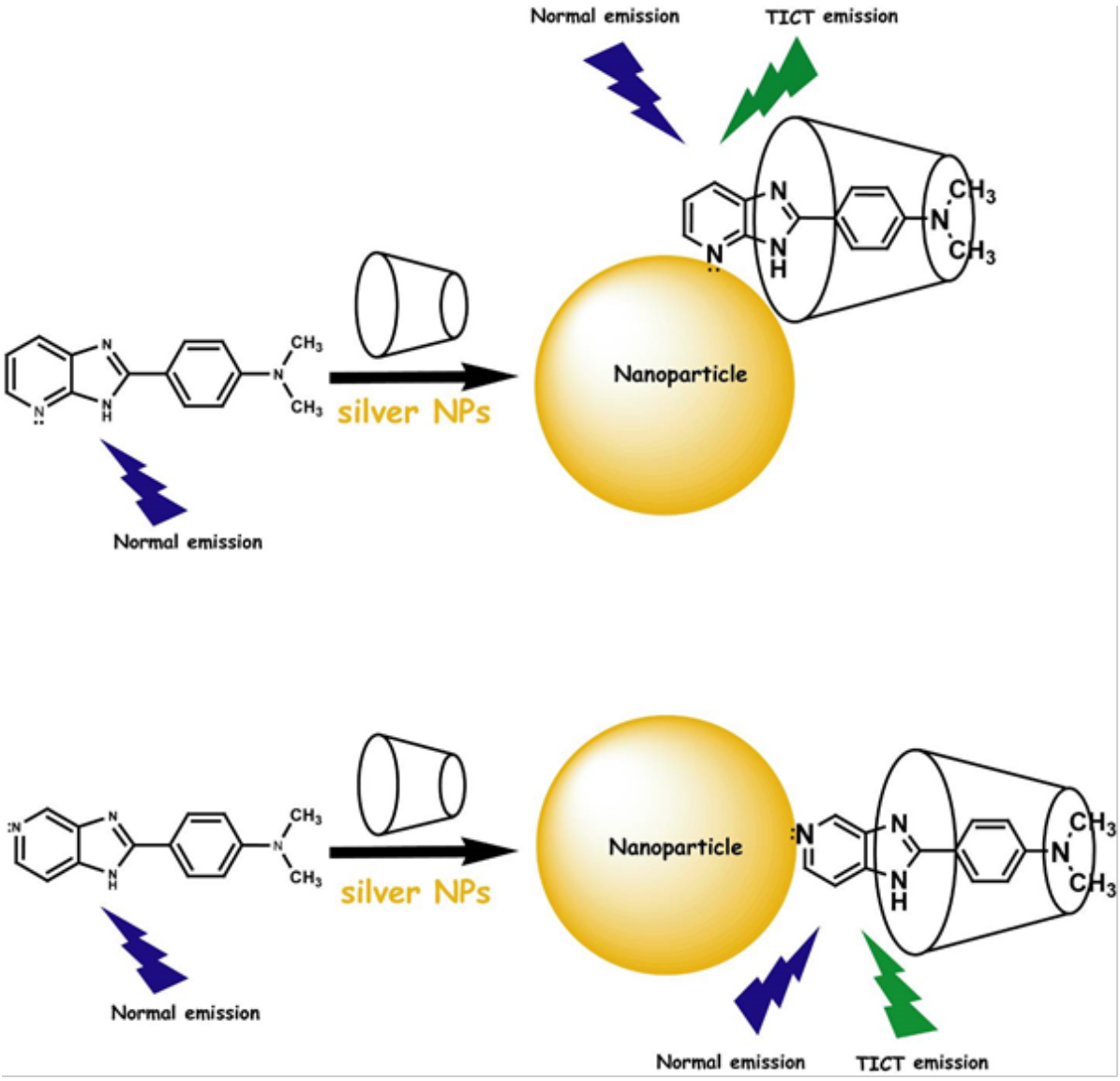

Scheme 3.1: Schematic representation of complex formation and dual emission

The TICT state is expected to be stabilized more by solvation than other electronic states. Consequently, the removal of the solvation by complexation with β-CD leads to more destabilization of the TICT state than other states. This increases the energy gap between the TICT state and the low lying states thereby it reduces the non-radiative decay and enhances the TICT emission. Therefore, clear dual emissions are observed from

nanoparticle– fluorophore–CD ternary composites. Higher TICT fluorescence observed from DMAPIP-b than that from DMAPIP-c further suggests that the location of the pyridyl nitrogen plays a major role, not only in the interactions of these fluorophores with nanoparticles but also in the charge transfer process. Dual emission from these fluorophores can be achieved from protonation or interaction with metal with the pyridine nitrogen atom **[246-247]**. These type of interaction create a huge bathochromic shift of 40 nm - 42 nm in the absorbance of the fluorophores. For example protonation shift the absorbance of DMAPIP-b and DMAPIP-c by 41 nm and 33 nm respectively **[66, 247].** But during the interaction with nanoparticles, small bathochromic shifts were obtained for the pyridoimdazoles. The shift in DMAPIP-b and DMAPIP-c were found to be 8 nm and 2 nm respectively **[Table 3.1]**. Hence these are the metal nanoparticles, not the metal ions which induced dual emission in these derivatives. Giving more support to this conclusion, these fluorophores were brought into the contact of the silver metal ion in DMF. But the reduction of silver (II) ion to zero valent metal by DMF resulted in the formation of black precipitate with 5 minutes **[Figure 3.8]**. This clearly depict that the silver (II) ion can't be present in DMF to interact with the fluorophores owing to its fast reduction. Hence silver nanoparticles are responsible for all the spectroscopic changes happened in this experiment.

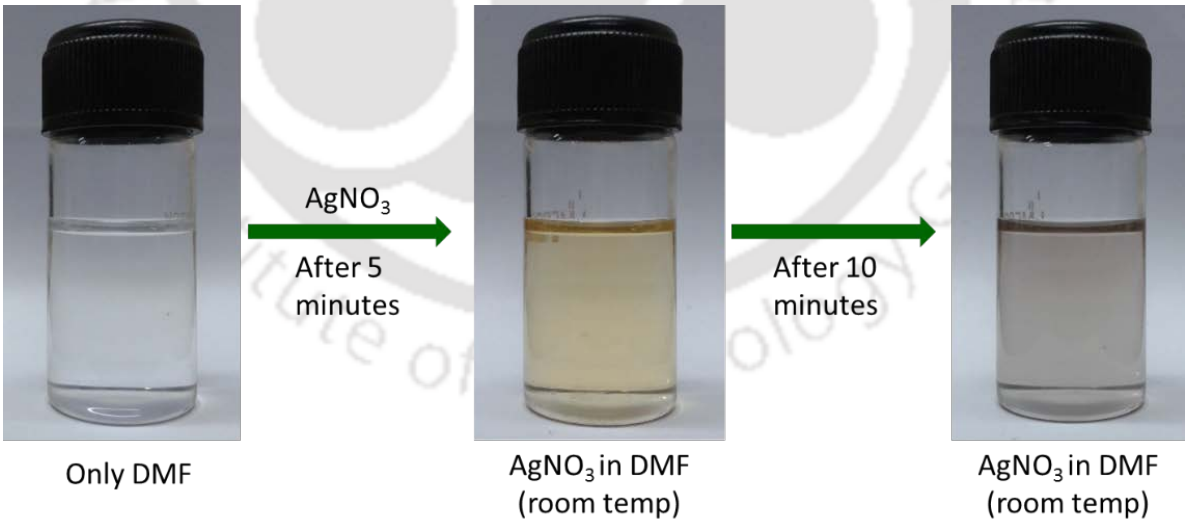

Figure 3.8: Reduction of silver (II) nitrate in DMF to silver zero within 10 minutes at room temperature.

TICT emission induced by nanoparticles is not reported till now for any fluorophore. However Ghosh et al has studied the charge transfer from coumarin derivatives to TiO_2 nanoparticles **[248, 249]**. They have reported the quenching of the ICT emission due to this

charge transfer which depend on the nature of the ICT state and the distance between the charge localization and nanoparticles surface. But the fluorophores in this present study differs from those coumarin derivatives in such a way that charge transfer from the coumarin causes quenching of the ICT state whereas the charge transfer from the pyridoimidazole derivatives to silver nanoparticles induces TICT fluorescence. In other words silver nanoparticles induced dual emission from 2-(4′-N, N-dimethylaminophenyl)imidazopyridines in aprotic solvent and enhanced by the confined environment of β-CD.

3.4. Conclusion:

All the fluorophores interact with the silver nanoparticles. The interaction happens through the hetero atoms. The pyridine nitrogen atom is responsible in the pyridoimidazoles whereas in DMAPBI interaction occur through imidazole nitrogen atom. While the energy transfer from the fluorophores to nanoparticles quenches the fluorescence of all the fluorophores, the charge transfer from 2-(4′-N, N-dimethylaminophenyl)imidazopyridines to nanoparticles induce dual emission. The confined environment from the nanosized cavity of β-CD enhances the TICT emission. The complexation with b-CD decreases the non-radiative rate and enhances the fluorescence. The ternary composite is formed by the encapsulation of the dimethylaminophenyl group inside the β-CD nanocavity with the pyridyl nitrogen on the surface of the nanoparticles. The interaction through pyridine nitrogen induces dual emission in the pyridoimidazoles. In the absence of pyridyl nitrogen, DMAPBI interacts with the nanoparticle through the imidazole nitrogen.

Chapter 4

Extraction of ICT fluorophores from nanoparticles composite by micelles

4.0. Introduction:

In the previous chapter, it is shown that ICT fluorophores, DMAPBI and its nitrogen substituted derivatives DMAPIP-b and DMAPIP-c have stronger interaction with nanoparticles in non-aqueous solvent. It leads to stabilization of nanoparticles **[250]**. The longer wavelength emission of DMAPIP's enhanced upon complexation with CD. In the present chapter possible extraction of these fluorophores from the surface of the nanoparticles in aqueous micelle are presented. The outcome of the presence of a specific micelle in the vicinity of these fluorophore-nano composite is a very interesting topic in targeted drug delivery. Very few literature reports are available regarding this context. Energy transfer in a hybrid nano-composite combining fluorescent dyes and ultra-small (< 3 nm) silver nanocrystals in a block copolymer micelle was studied by Raino et al. **[251]**.The utilization of nanoparticles embedded self-assemblies of pluronic P-123 micelle for controlled nano surface energy transfer by tuning the precise location of donor dyes was investigated by Sarkar et al. **[252]**. Purkayastha et al. suggested that the orientation of a probe on the surface of silver nanoparticles in micelle is controlled by the nature of the micelle **[253]**.

4.1. Effect of nanoparticles on the fluorophore:

Table 4.1. Emission λ_{max} (nm) of the fluorophores in water and nanoparticles.

Fluorophores	In Water	In presence of nanoparticles
DMAPBI	400	400
DMAPIP-b	453	455
DMAPIP-c	420, 518	420, 518

All the fluorescence spectra are recorded at the p^H in which the respective fluorophores remain as neutral molecules in water. For DMAPBI, the p^H of the solutions are maintained at 8 whereas for pyridoimidazoles the spectra are recorded at p^H 9. In water DMAPBI exhibits strong emission at 400 nm in water. Addition of nanoparticle leads to quenching of this fluorescence **[Figure 4.1]**. Though the fluorescence intensity decreases,

the position of the band is unaffected by nanoparticle. This indicates the formation of non-fluorescent complex between fluorophore and nanoparticle. Alike DMAPBI, the emission intensity of pyridoimidazoles is also quenched in presence of nanoparticles, but a little red shift was observed in the emission spectra of DMAPIP-b **[Figure 4.1]**. As discussed in the previous chapter, the interaction of the nanoparticles occurs through the pyridyl nitrogen. This increases the conjugation and causes the bathochromic shift. But in DMAPBI, imidazole nitrogen is the most possible site of interaction in the absence of pyridyl ring. The intensity ratio plot indicates that the emission of pyridoimidazoles quenches more rapidly compared to that of DMAPBI. Hence, it is confirmed that interaction through pyridyl nitrogen is more favorable compared to that through imidazole nitrogen. However, among the pyridoimidazoles, the fluorescence of DMAPIP-b is quenched more compared to that of DMAPIP-c **[Figure 4.1]**.

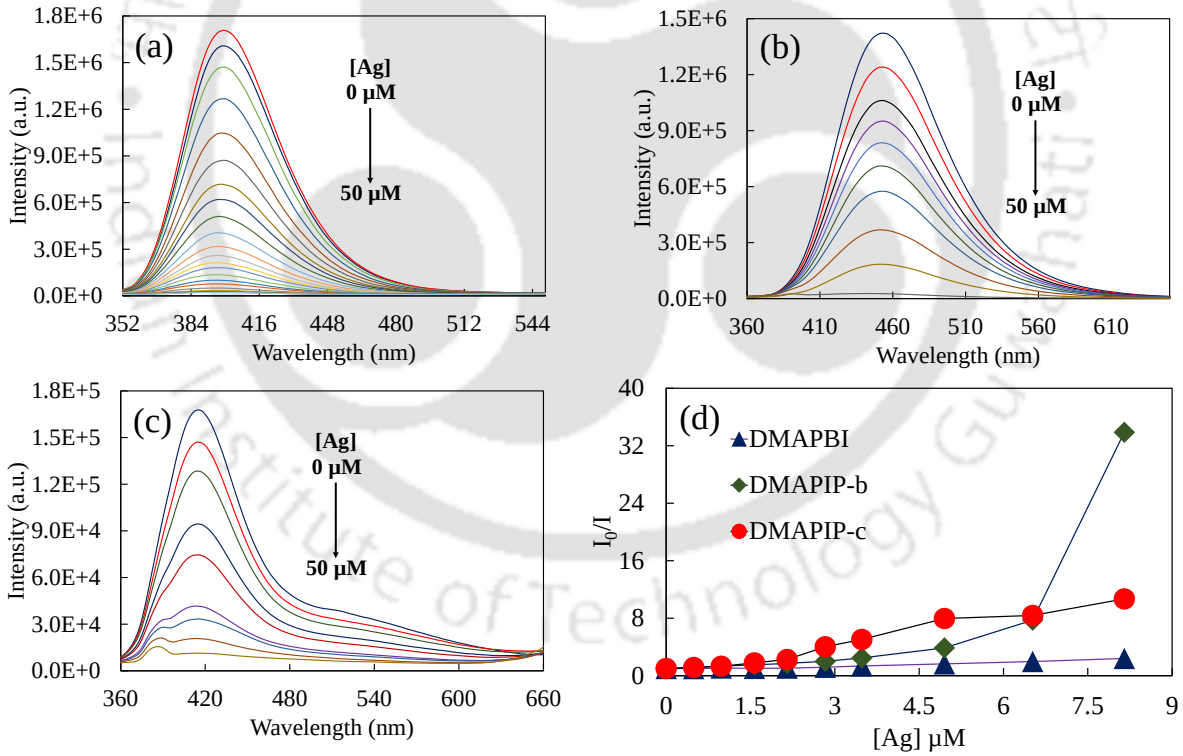

Figure 4.1: Fluorescence spectra of (a) DMAPBI (λ_{exc} = 336 nm), (b) DMAPIP-b (λ_{exc} = 350 nm) and (c) DMAPIP-c (λ_{exc} = 336 nm), (d) Intensity ratio plot of all three fluorophores in water at different concentration of silver (nanoparticles).

In water, the TICT emission is clearly perceived only in the emission spectra of DMAPIP-c. Upon addition of nanoparticles the TICT emission is also quenched along with normal emission.

4.2. Effect of micelle on fluorophore-nanoparticles composite:

In the absence of any other stabilizer, binding with the fluorophores stabilizes the nanoparticles **[Section 3.2.]**. Surfactants are known stabilizer of nanoparticles **[254-270]** and therefore, micelles have been used to synthesize nanoparticles composed of alloys, metal oxides, inorganic molecules, and noble metals like silver **[256]**. Thus, the effects of ionic and non-ionic surfactants on nanocomposite are studied.

4.2.1. Effect of CTAB on the fluorophore-nano composite:

Upon addition of CTAB to the nanocomposite of DMAPBI, the fluorescence is recovered **[Figure 4.2.a]**. This enhancement is higher than the original fluorescence intensity of the fluorophore in the absence of nanoparticle and surfactant. The enhancement is also accompanied by 5 nm blue shift in the spectrum. The higher enhancement and shift of fluorescence suggest the fluorophore does not simply detach off from the nanoparticle, it also might have bind with micelles. To confirm that the shift is due to binding of the fluorophore with micelle, the effect of CTAB on the fluorophore was studied **[Figure 4.2.b]**.

Table 4.2. Emission λ_{max} (nm) values of all fluorophores in water, nanoparticles, CTAB and in composite system of CTAB and nanoparticles.

Fluorophores	In Water	In presence of nanoparticles	In presence of nanoparticles and CTAB	In CTAB
DMAPBI	400	400	395	395
DMAPIP-b	453	455	424	424
DMAPIP-c	420, 518	420, 518	399, 493	398, 495

The emission maximum matches with that of the fluorophore in micelle suggesting the fact that the detached fluorophore is not present in the aqueous medium, but inside the micelle **[Table 4.2]**. However, the fluorescence intensity in the presence of nanoparticles is different from that in the absence of nanoparticle. This suggests that the presence of nanoparticle affects the micelle.

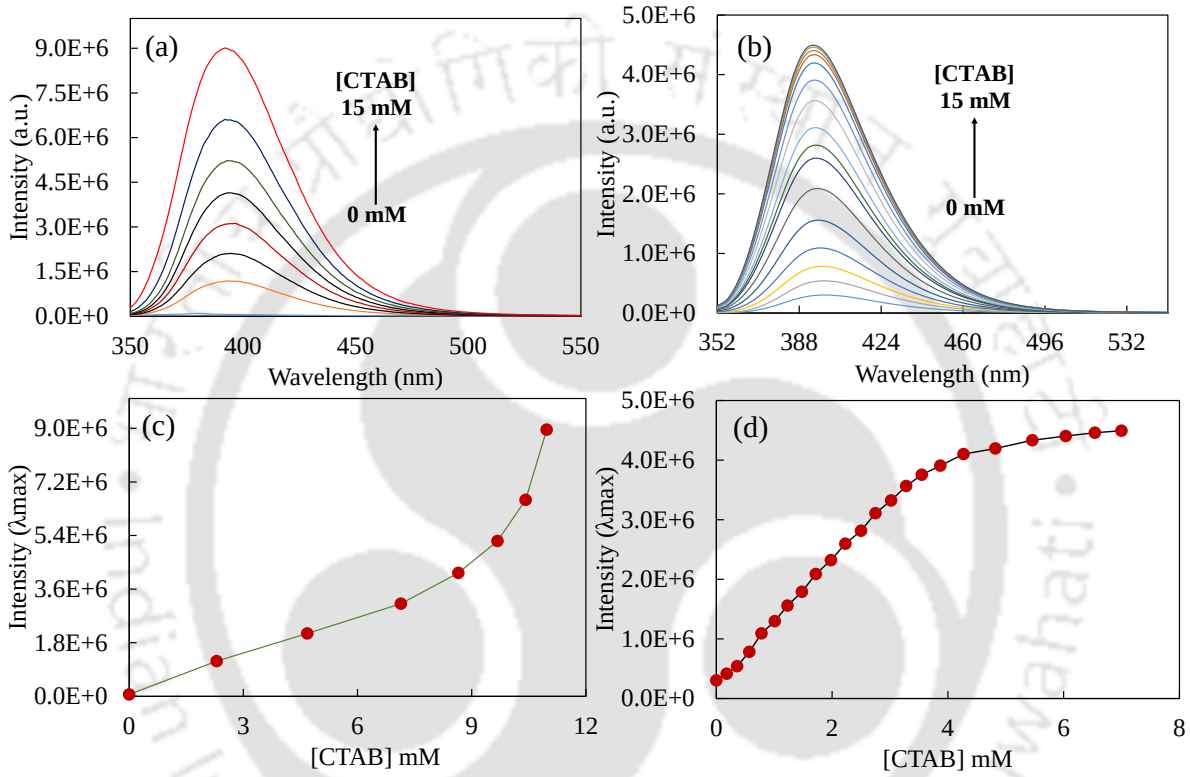

Figure 4.2: Fluorescence spectra of (a) DMAPBI (λ_{exc} = 336 nm) and (b) DMAPBI-nanoparticle composite (λ_{exc} = 336 nm) at different concentrations of CTAB. Plot of intensity at emission maxima of DMAPBI at different concentrations of CTAB (c) for fluorophore nano composite and (d) in absence of nanoparticle.

Alike to DMAPBI, the fluorescence of DMAPIP-b also undergoes blue shift with enhancement in intensity upon addition of CTAB micelle **[Figure 4.3]**. The amount of hypsochromic shift observed for the nanocomposite and free fluorophore in presence of CTAB matches with each other **[Table 4.2]**. Henceforth, it can be concluded that CTAB extracted the fluorophore from the nanoparticles surface into its hydrophobic cavity.

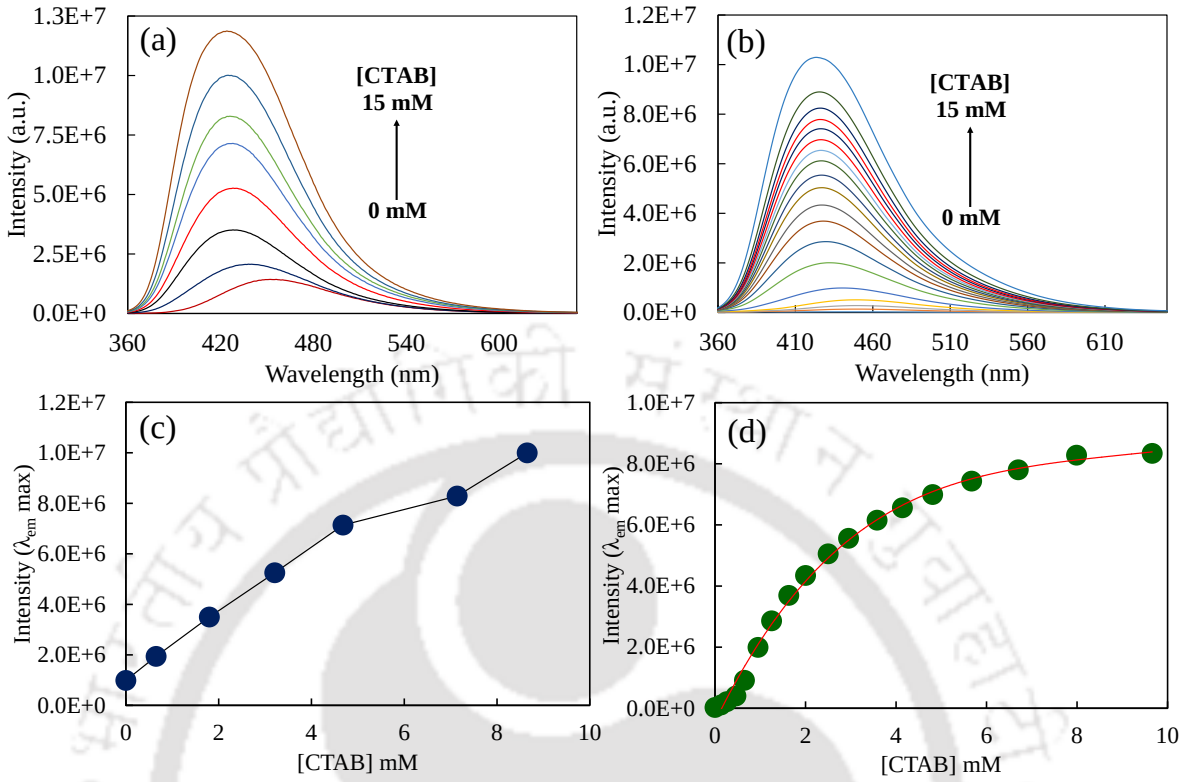

Figure 4.3: Fluorescence spectra of (a) DMAPIP-b-nanoparticles composite (λ_{exc} = 345 nm) and (b) DMAPIP-b (λ_{exc} = 345 nm) at different concentrations of CTAB. Plot of intensity at emission maxima of DMAPIP-b at different concentrations of CTAB (c) for fluorophore nano composite and (d) in absence of nanoparticle.

Both normal and TICT emission of DMAPIP-c are enhanced upon addition of CTAB to DMAPIP-c nanoparticle composite. The enhancement of TICT band is much higher compared to that of normal band for all the concentrations of micelle. The intensity ratio plot strengthened this fact. The emission maxima of fluorophore nano composite matches with that of fluorophore in presence of 15 mM CTAB **[Table 4.2]**. However, the enhancement in the TICT emission is more in presence of nanoparticle than in its absence. This further supports the hypothesis that the presence of nanoparticle affects the micelle.

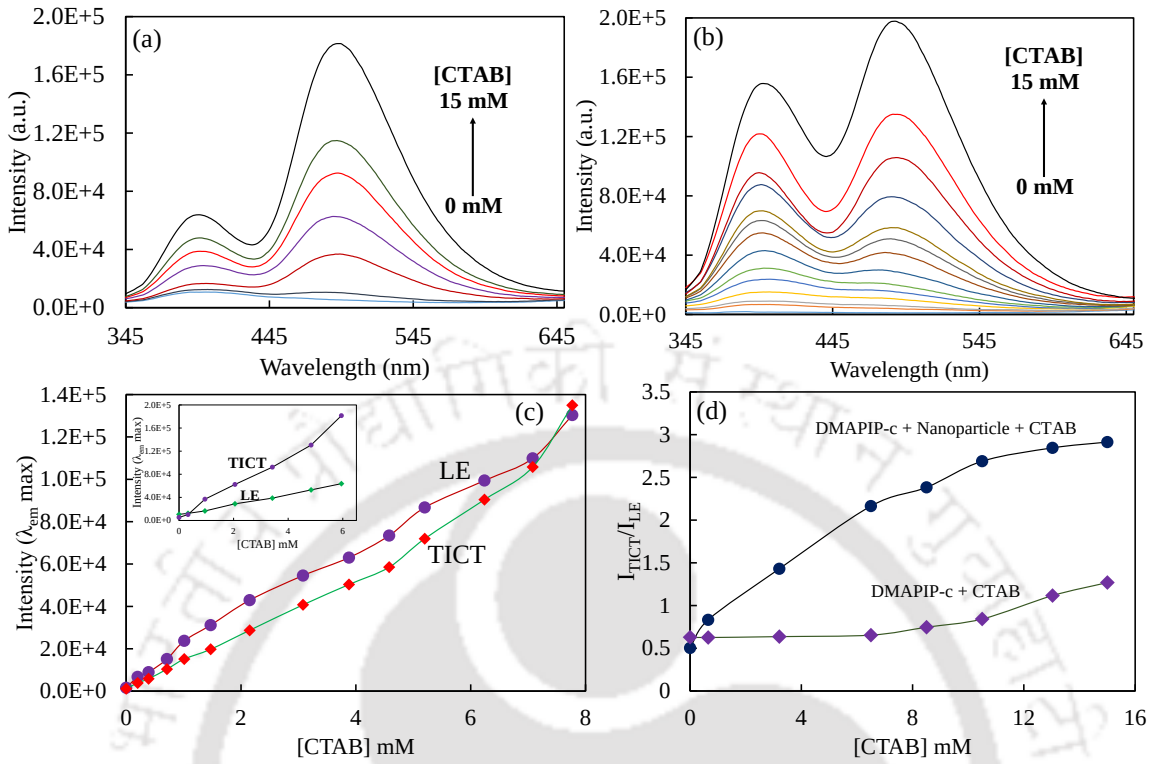

Figure 4.4: Fluorescence spectra of (a) DMAPIP-c-nanoparticles composite (λ_{exc} = 336 nm) and (b) DMAPIP-c (λ_{exc} = 336 nm) at different concentrations of CTAB. Plot of intensity at emission maxima of DMAPIP-c at different concentrations of CTAB (c) for fluorophore nano composite and in absence of nanoparticle (inset). (d) Plot of intensity ratio of DMAPIP-c and fluorophore nanocomposite at different concentrations of CTAB.

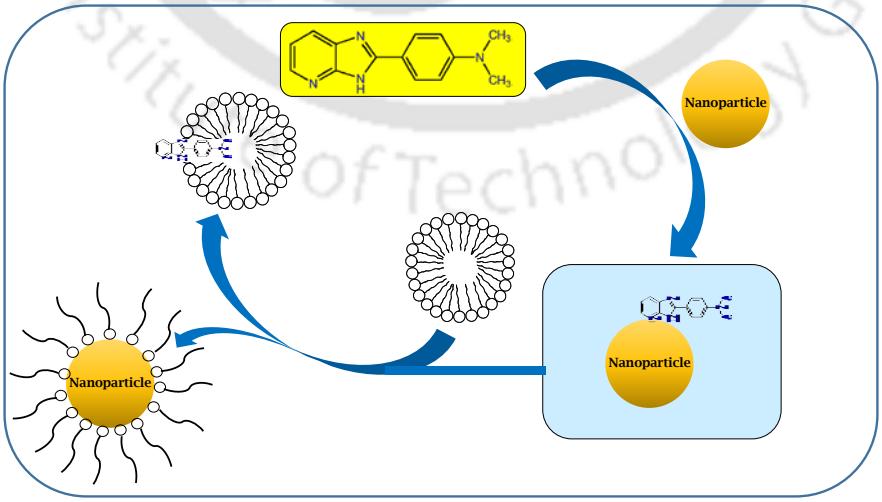

Scheme 4.1. Effect of CTAB on nanocomposite of fluorophore and nanoparticle.

The effect of CTAB on nanocomposite is shown in **Scheme 4.1.** In the absence of other stabilizer, DMAPIP-b interact with nanoparticles to stabilize them which leads to fluorescence quenching. Upon addition of CTAB the fluorophores are replaced by the surfactant and therefore DMAPIP-b got detached from the nanoparticles. The fluorophore binds in the micelle formed by excess surfactant.

4.2.2. Effect of TX-100 on the fluorophore-nano composite:

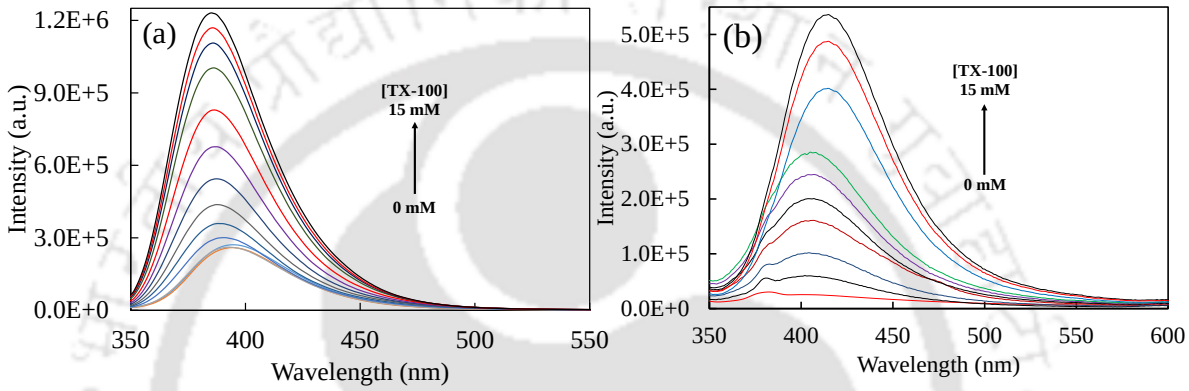

Figure 4.5: Fluorescence spectra of (a) DMAPBI-nanoparticles composite (λ_{exc} = 336 nm) and (b) DMAPIP-b-nanoparticles composite (λ_{exc} = 336 nm) at different concentrations of TX-100.

To understand the effect of surfactant charge on the recovery process, CTAB is replaced by non-ionic TX-100. The effect of TX-100 on the fluorescence of DMAPBI-nanocomposite and DMAPIP-b-nanocomposite are displayed in **Figure 4.5**. The fluorescence of both were enhanced upon addition of TX-100. The fluorescence of the fluorophore at higher concentration of TX-100 is higher than those of the fluorophore in aqueous medium. The emission maxima of the fluorophores in TX-100 in the absence and the presence of the nanoparticles are matching with each other **[Table 4.3]**. All these suggest that like CTAB, TX-100 not only detached the fluorophores from the nanoparticle, but also encapsulated the molecules. However, similar to the addition of CTAB, the change in fluorescence intensity of the fluorophores with TX-100 concentration in the presence and the absence of the nanoparticles are different **[Figure 4.6]**.

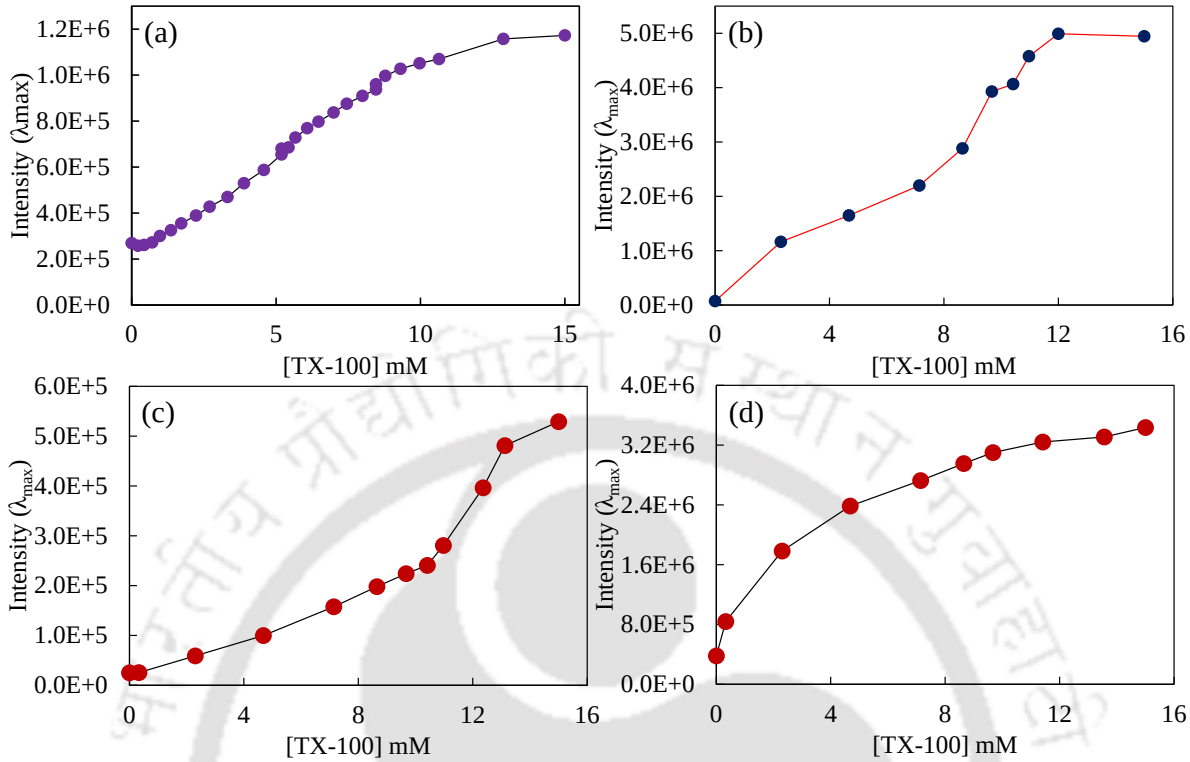

Figure 4.6. Plot of intensity at emission maxima of (a) DMAPBI-nanocomposite (b) DMAPBI and (c) DMAPIP-b–nanocomposite (d) DMAPIP-b at different concentrations of TX-100

Table 4.3. Emission λ_{max} (nm) values of all fluorophores in water, nanoparticles, TX-100 and in composite system of TX-100 and nanoparticles.

Fluorophores	In Water	In presence of nanoparticles	In presence of nanoparticles and TX-100	In TX-100
DMAPBI	400	400	382	382
DMAPIP-b	453	455	416	416
DMAPIP-c	420, 518	420, 518	396, 482	398, 495

The other pyridine substituted analogous DMAPIP-c behaves in a similar fashion as that of DMAPIP-b depicted by the **Figure 4.7**. However, in DMAPIP-c clear dual emission is observed. Like the addition of CTAB, with addition of TX-100, the relative enhancement in the TICT emission of DMAPIP-c is more in the presence of nanoparticle than that in the absence of nanoparticle. The hypsochromic shifts in the emission maxima of both normal and TICT emission in TX-100 are more in the presence of the nanoparticle **[Table 4.3]**. The blue shift is more significant in case of TICT emission than the normal emission. Since, the TICT emission is more sensitive to environment, it is better indicator of environment that the normal emission. It shows that the micelle in the presence and the absence of nanoparticles are different.

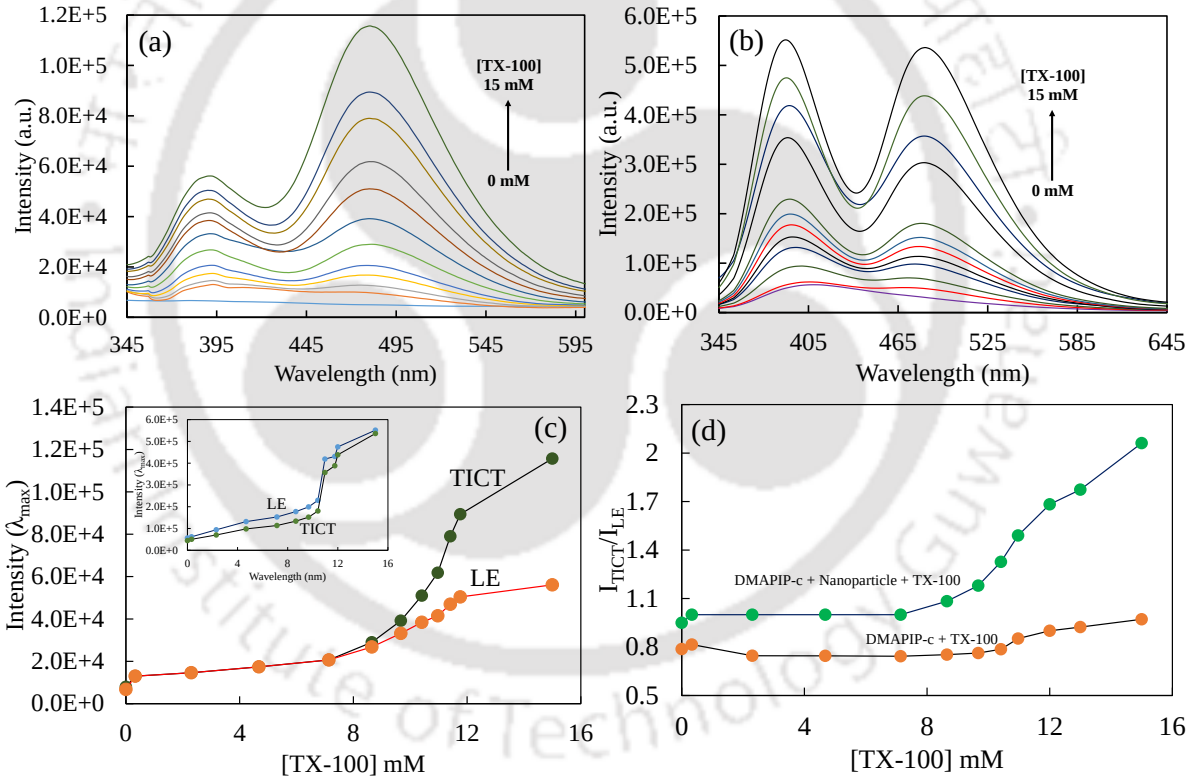

Figure 4.7: Fluorescence spectra of (a) DMAPIP-c - nanoparticles composite (λ_{exc} = 336 nm) and (b) DMAPIP (λ_{exc} = 336 nm) at different concentrations of TX-100. Plot of intensity at emission maxima of DMAPIP-c at different concentrations of TX-100 (c) for fluorophore nano composite and in absence of nanoparticle (inset). (d) Plot of intensity ratio of DMAPIP-c and fluorophore nanocomposite at different concentrations of CTAB.

Table 4.4. The critical micelle concentration (CMC, mM) and the concentration of the surfactant (mM) to equalize the initial intensity of the fluorophore before addition of nanoparticles.

	CMC	DMAPBI	DMAPIP-b
CTAB	1.0	1.1	0.9
TX-100	0.1	15	15

The addition of nanoparticles quenches the fluorescence of the fluorophores. To understand the effect of surfactant charge on the recovery process, the concentration of the surfactant which is required to equalize the intensity of the fluorophores before the addition of nanoparticle are tabulated in **Table 4.4**. This may give an indication about the effect of individual surfactant on the recovery process. Since in case of DMAPIP-c, the enhancement of TICT emission in the presence of nanoparticles is higher than in the absence of nanoparticles, it is difficult to compare. Therefore, it is not included in **Table 4.4**. The concentration of the surfactant required to equalize the intensity of the fluorophores before the addition of nanoparticle is nearly same for both DMAPBI and DMAPIP-b. Interestingly, even though the critical micelle concentration (CMC) of CTAB is higher than that of TX-100, the required concentration is lower with CTAB than TX-100. It appears that the CTAB has more interaction with nanoparticles than TX-100.

4.3. Conclusion:

All three fluorophores interact with silver nanoparticles prepared in water through the ring nitrogen. Static quenching was observed for all the fluorophores. The fluorescence of the fluorophores can be recovered by addition of surfactant. The micelle separates the nanoparticles and extract the fluorophores from the nanocomposite. The micelles were found to be well efficient to extract the fluorophores from the nanoparticles surface into their hydrophobic cavities. It seems that the CTAB has stronger interaction with the nanoparticles than TX-100. Compared to TX-100, nearly one fifteen of the CTAB concentration is sufficient to equalize the original intensity. The enhancement in the TICT emission of DMAPIP-c is more than that of its normal emission.

Chapter 5

Effect of silver nanoparticles on the ICT fluorophores inside BSA

5.0. Introduction:

Serum albumins are globular protein and are the major constituents of blood plasma. Through hydrophobic, hydrophilic and hydrogen bonding interactions various bioactive molecules bind these transport proteins **[238, 271-275]**. Therefore, these proteins are still used as model systems to understand the protein-ligand and protein-solvent interactions. BSA is the most studied and characterized serum albumin. The precursor of BSA protein has 607 amino acids. During secretion an N-terminal 18-residue signal peptide is cut off from the precursor protein, henceforth the initial protein product contains 589 amino acid residues. An additional 4 amino acids are cleaved to yield the mature BSA protein that contains 583 amino acids. Thus, BSA is a single-chain transporting protein of 583 amino acids having a molecular weight of 66 kDa, out of which a large number of charged residues are located toward the surface. It has two tryptophan residues, Trp-134 and Trp-213. The nine loops held together by 17 disulphide bonds resulting in three domains I, II, and III each consisting of two subdomains A and B forms the primary structure of BSA. BSA has two binding sites referred to as site I and site II located in the cavities of subdomains IIA and IIIA, respectively.

Nowadays metal nanoparticles are used for various medicinal applications thereby human and animals are directly exposed to them. Therefore, biocompatibility and the change in structure of the targeted proteins in presence of the nanoparticles are the matter of apprehension which mainly involve the unfolding of protein structure in presence of nanoparticles.

Heterocycles are biologically active molecules and they bind with proteins. In the present study, the fate of DMAPBI and DMAPIPs present within BSA pocket upon addition of silver nanoparticles by spectroscopic analysis was investigated. The morphological changes of BSA when exposes the fluorophores to the nanoparticles environments is emphasized in this work.

5.1. Effect of BSA on the fluorophores:

The knowledge on the binding of the molecules will be required to understand the effect of nanoparticle on the BSA possessing guest molecules. The interactions of DMAPBI

and DMAPIP-b with BSA were investigated earlier in our group. However, no studies were carried about the binding of the other nitrogenous derivative DMAPIP-c with BSA. Therefore, in the present work the effect of BSA on DMAPIP-c was investigated first. Upon addition of BSA the fluorescence spectrum of DMAPIP-c undergoes a blue shift with enhancement in emission **[Figure 5.1]**. The changes indicate that the guest molecule enters the BSA.

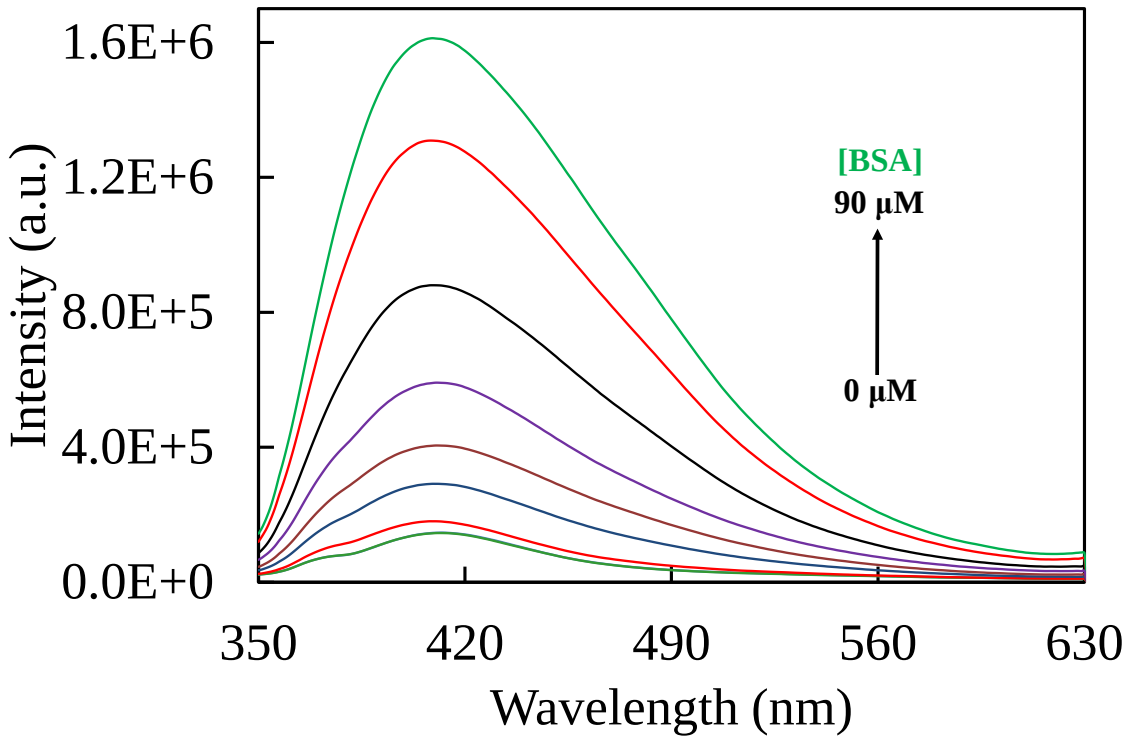

Figure 5.1: The emission spectra of DMAPIP-c (λ_{ex} = 336 nm) in presence of increasing concentration of BSA [0-90 µM].

The enhancement of emission intensity points towards the fact that the hydrophobicity of the environment is dominating over the hydrogen bonding with hetero atom. The result also depicts that the fluorophore remain deeper inside the BSA pocket.

The earlier studies by our group suggest that both DMAPBI and DMAPIP-b underwent blue shift in the fluorescence spectra in presence of BSA **[238, 271]**. However, the emission intensity of DMAPBI decreases with the gradual addition of BSA whereas like for DMAPIP-c, enhanced emission intensity was observed for DMAPIP-b. Within BSA the nature of emission characteristics are controlled by two factors: (i) the increase in the

hydrophobicity of the environment and (ii) hydrogen bonding with heteroatom. It has been already proved that upon increasing the polarity of the environment, bathochromic shifts were observed in the fluorescence spectra of these ligands **[276-279]**. These bathochromic shifts are the results of stabilization of the ICT state by dipolar and hydrogen bonding interactions. The observed hypsochromic shifts in the emission spectra of the DMAPIP-c in the presence of BSA indicate that the ligands are moving into a hydrophobic environment from a hydrophilic environment. The stronger stabilization of the ICT state by dipolar interaction decreases the energy gap between emitting state and ground state which increases the nonradiative decay. Therefore, the weak emission of DMAPIP-c in water became stronger with movement of the ligand from the hydrophilic environment (water) to hydrophobic BSA. In BSA, the dipolar interactions decrease, which destabilizes the ICT state and increases the energy gap between ICT and low-lying state. In other words, it is expected to increase the radiative emission by decreasing nonradiative decay which enhances the fluorescence intensity of DMAPIP-c. Unlike hydrophobicity hydrogen bonding with heteroatoms quenches the fluorescence **[276-279]**. The enhancement of fluorescence intensity due to hydrophobicity predominates over the fluorescence quenching by hydrogen bonding. On the other hand, the environment of DMAPBI is less hydrophobic as suggested by the spectral shift. Therefore, quenching owing to hydrogen bonding dominates over the enhancement in fluorescence caused by the hydrophobicity of the environment. Further, the change in the fluorescence intensity of DMAPBI is much smaller compared with DMAPIP-b and DMAPIP-c. The binding location predicted by docking studies of DMAPBI and DMAPIP-b also supports the hypothesis. The different orientation of DMAPBI in BSA compared with DMAPIP-b might also have a role in this difference in behavior. It is reported in the literatures, both DMAPBI and DMAPIP-b form inclusion complexes with β-CD **[277-279,237]**. In both inclusion complexes, the dimethylaminophenyl group was present inside the hydrophobic basket and the heterocyclic ring was present outside the β-CD nanocavity. The azole nitrogen was located near the rim and forms hydrogen bond with rim hydroxyl group of the host and/or water present near the rim. Thus, it is clear that the dimethylaminophenyl prefers the hydrophobic environment and heterocyclic ring prefers the hydrogen bonding environment. Therefore, it is no surprise that the dimethylaminophenyl ring of DMAPBI is present inside the protein cavity and the heterocyclic ring is projected outside. DMAPBI has only one basic center (azole nitrogen)

in its heterocyclic ring to accept the hydrogen bond. On the other hand, DMAPIP-b has one extra heteroatom, pyridyl nitrogen, which also forms hydrogen bond with amino acid residue. This stabilizes the presence of heterocyclic ring inside the cavity, in other word, facilitates the reverse orientation of the DMAPIP-b inside BSA **[238]**. DMAPIP-c also has pyridyl nitrogen therefore, similarities in the spectral changes of DMAPIP-c with DMAPIP-b no surprise and it shows that the binding orientation of DMAPIP-c in BSA is same as that of DMAPIP-b.

5.2. Effect of silver nanoparticles on fluorophore-BSA complex

The fluorescence emission of DMAPBI is quenched with a blue shift upon addition of BSA **[Figure 5.2]**.

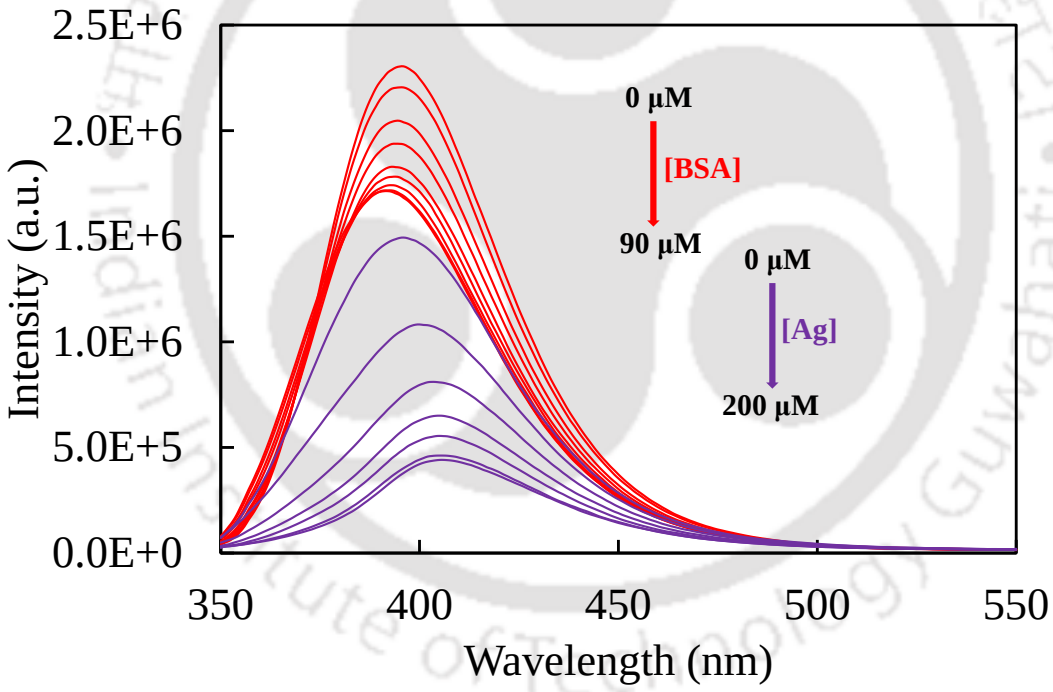

Figure 5.2: Emission spectra of DMAPBI at different concentrations of BSA (red lines) followed by the addition of increasing concentration of silver nanoparticles (violet lines)

This decrease in emission intensity saturated at 70 µM of BSA. These changes indicate the binding of the molecule with BSA and is consistent with the earlier report **[271]**. Addition of silver nanoparticles to the DMAPBI-BSA complex further quenches the fluorescence of DMAPBI. But unlike the addition of BSA, it leads to a 15 nm red shift in the spectrum. The

excitation spectra also red shifted by 32 nm after the addition of silver nanoparticles to BSA-fluorophore complex **[Figure 5.3]**. The change in the nature of the shift in emission maxima before and after the addition nanoparticles indicated the change in environment of the fluorophore. The hydrophobic environment created by BSA changes towards more hydrophilic in nature as soon as the nanoparticles are added.

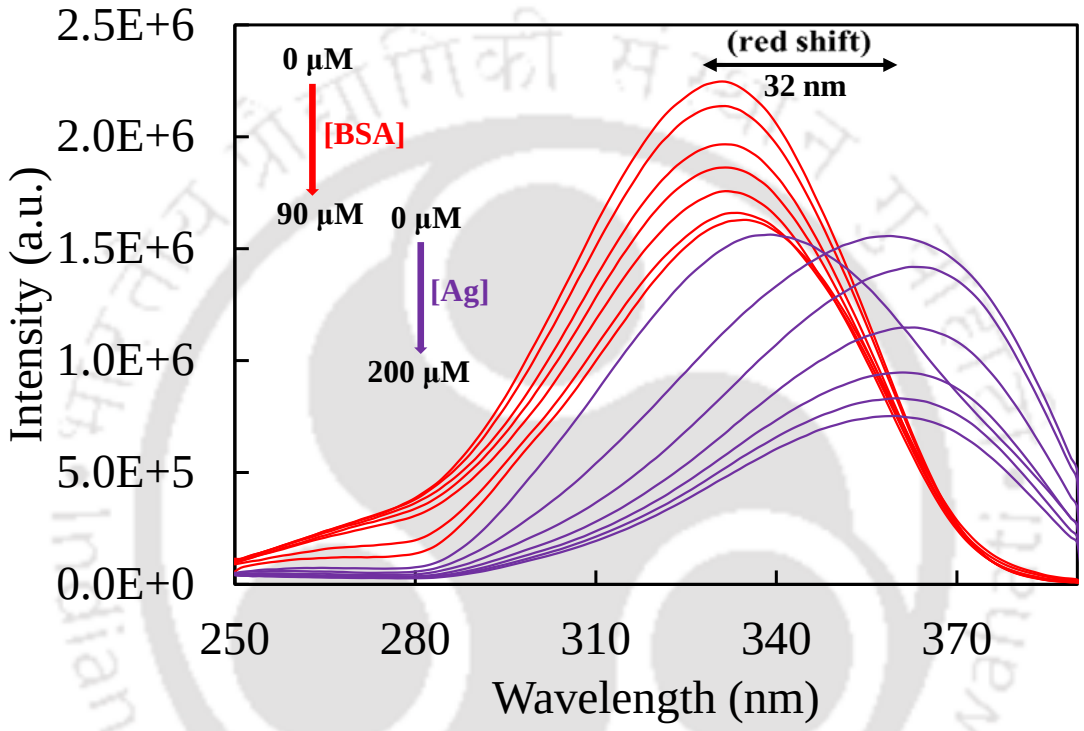

Figure 5.3: Excitation spectra of DMAPBI at different concentrations of BSA (red lines) followed by the addition of increasing concentration of silver nanoparticles (violet lines)

To understand the change in the protein structure in presence of nanoparticles, the DMAPBI-BSA was excited at 280 nm, the absorption maximum of BSA **[Figure 5.4]**. When excited at 280 nm, in addition to the emission spectrum of the fluorophore, the band corresponding to the tryptophan of BSA was also observed at 350 nm. With progressive addition of nanoparticles, the fluorescence of BSA decreases with blue shift. These results show that not only the environment of fluorophore, but the environment of tryptophan also changes upon addition of nanoparticles.

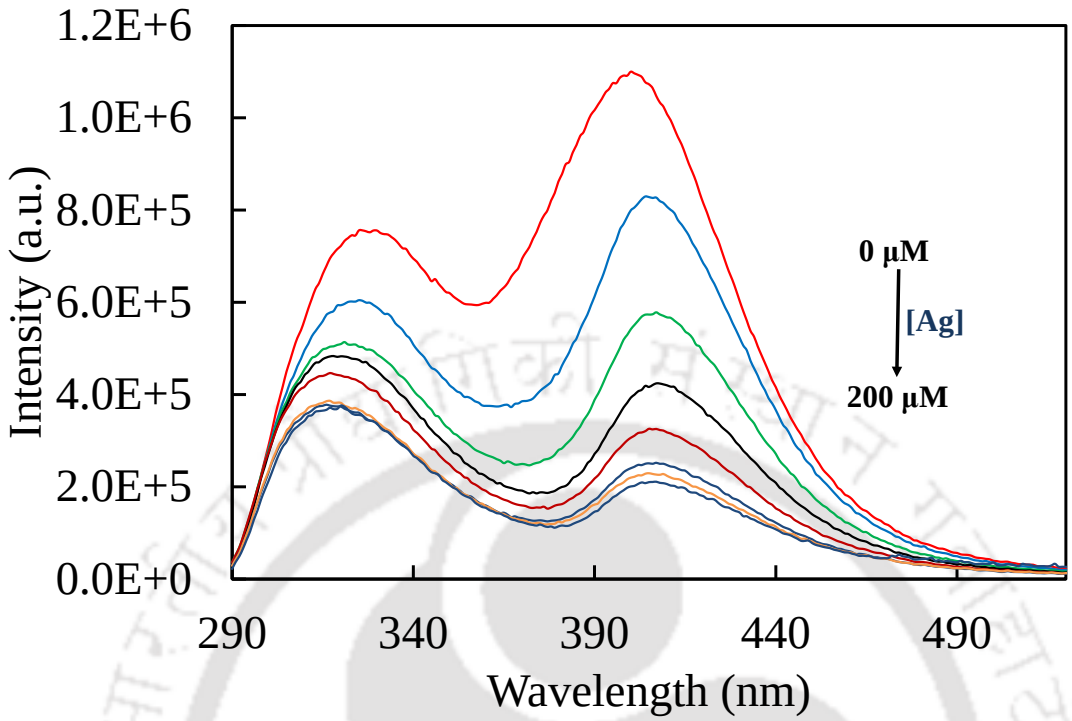

Figure 5.4: Emission spectra of DMAPBI-BSA (λ_{ex} = 280 nm) at different concentrations of silver nanoparticles.

In the earlier chapter **[Section 4.1]**, it was clearly observed that the emission intensity of DMAPBI in water diminished with addition of silver nanoparticles without any shift in the spectrum. But the effect of silver nanoparticles on fluorophore-BSA complex is different compared to free fluorophore in water. In the case of complex, the decrease in emission intensity of DMAPBI is less compared to that of free fluorophore. The emission maxima also bathochromically shifted by 10 nm in BSA complex. The bathochromically shifted emission of fluorophore suggests that unlike tryptophan of BSA, the fluorophore is more exposed to hydrophilic environment. These spectral changes suggest that though the fluorophore moved to more hydrophilic environment it did not detach from BSA, instead DMAPBI-BSA-nanoparticle composite is formed. The emission maximum of the BSA is blue shifted with decrease in intensity. The blue shift indicates that the tryptophan environment is hydrophobic than in the absence of silver nanoparticles. Dong et al. studied the effect of gold nanoparticle on BSA at different p^H **[280]**. They also observed a blue shift with quenching of fluorescence. It was attributed to the conformational change in BSA at tertiary structure levels and the quenching of the tryptophan fluorescence by gold

nanoparticle with a quenching constant of 5.4 X 10^{17}. Similar blue shift observed in the present work suggest that like gold nanoparticles, silver nanoparticles also induced the conformational change. The quenching of tryptophan fluorescence in the presence of silver nanoparticles are analyzed using the Stern Volmer equation **[281]**

$$\frac{I_0}{I} = 1 + k_q \tau_0 [Q] = 1 + K_{SV}[Q]$$

where I_0 and I are the maximum fluorescence intensities in the absence and presence of silver nanoparticles, respectively, k_q is the bimolecular quenching constant, τ_0 is the lifetime of the fluorophore in the absence of quencher and K_{SV} is the Stern Volmer fluorescence quenching constant, which is a measure of the efficiency of quenching, and [Q] is the quencher concentration. **Figure 5.5** shows the Stern Volmer plots. K_{SV} obtained by from this plot is 6.6 X 10^9 M^{-1}, which indicated a strong quenching ability of silver nanoparticles. For BSA, τ_0 is known to be approximately 5 X 10^{-9} s [13] thus, k_q 13.2 X 10^{17} M^{-1} s^{-1} is obtained. Therefore, the quenching constant for tryptophan in presence of silver nanoparticles is 2.44 times more compared to that gold nanoparticles. This implies the better efficiency of silver nanoparticles to quench the tryptophan emission compared to gold nanoparticles.

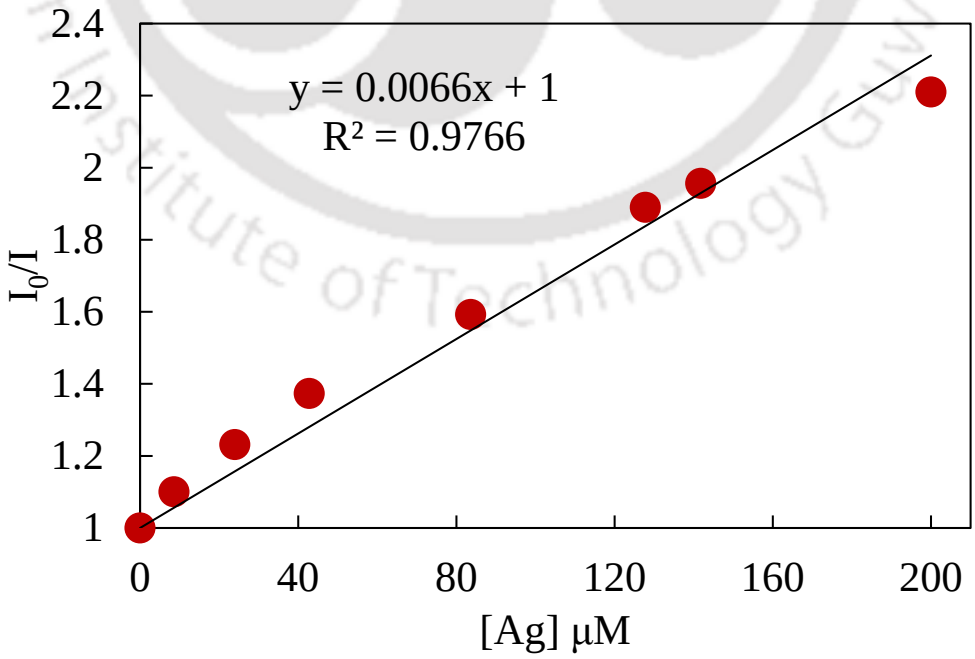

Figure 5.5: Stern Volmer plot of BSA at different concentration of silver nanoparticles.

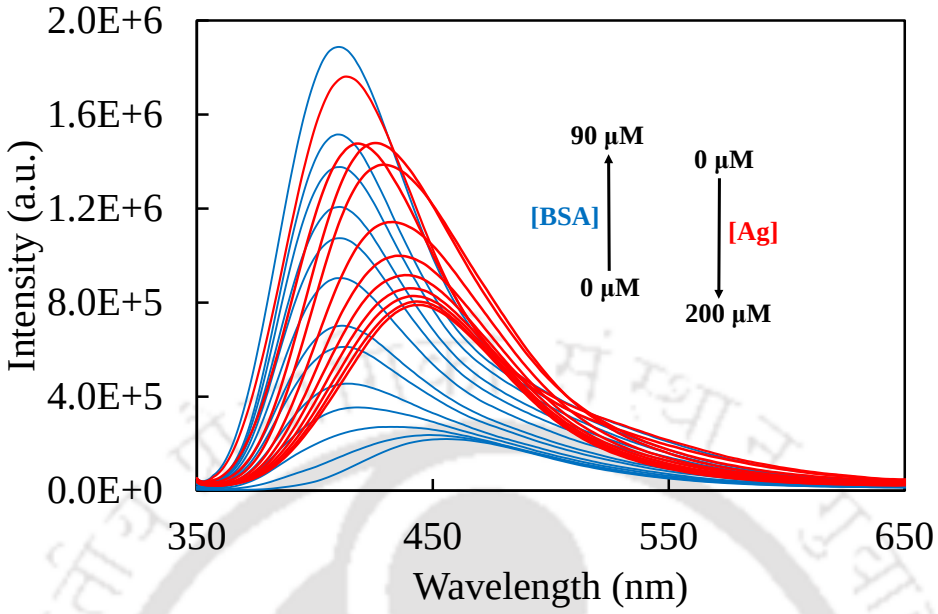

Figure 5.6: Emission spectra of DMAPIP-b with varying concentration of BSA (blue lines) and the red lines are the emission spectra of DMAPIP-b in 90 µM of BSA at different concentration of nanoparticles.

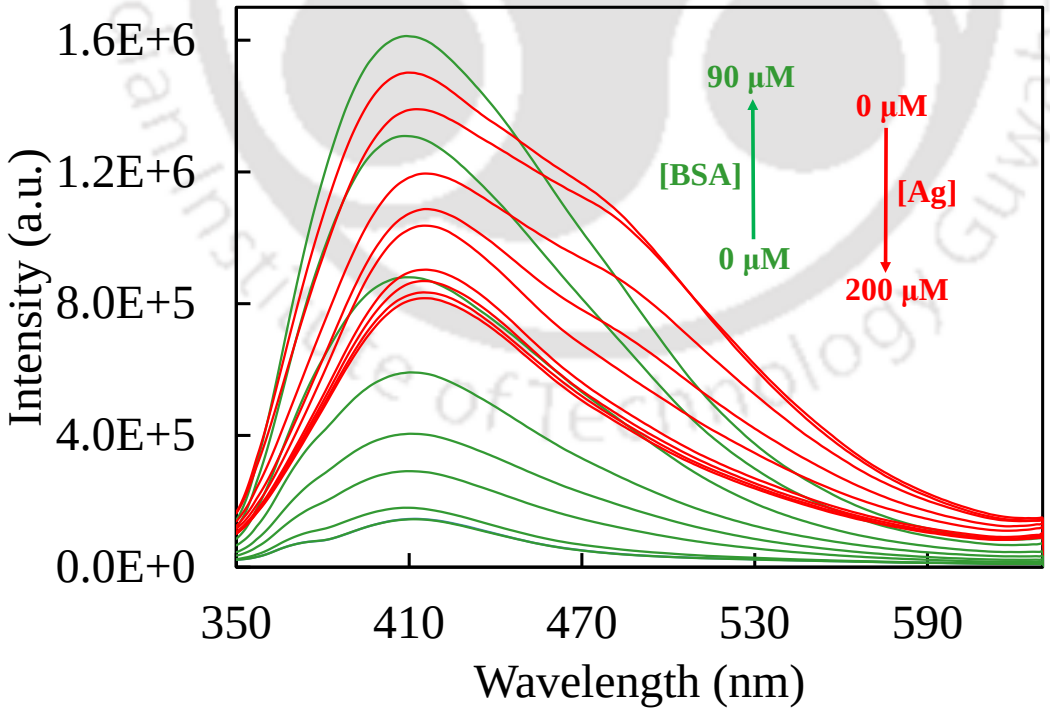

Figure 5.7: Emission spectra of DMAPIP-c at different concentrations of BSA followed by different concentrations of silver nanoparticles.

As discussed earlier, unlike the fluorescence of DMAPBI, the fluorescence of both pyridoimidazoles are enhanced upon encapsulation by BSA. But, same as that of DMAPBI, the fluorescence intensities of both BSA composites of DMAPIP-b and DMAPIP-c decreases with addition of silver nanoparticles **[Figure 5.6 and 5.7]**. However, even at saturation limit the fluorescence intensities of the fluorophores are much higher than that in water in the absence of nanoparticle. But the fluorescence emission intensities of these fluorophores were almost completely diminished by these nanoparticles in water **[section 4.1.]**. This clearly indicates like DMAPBI, the pyridoimidazole analogues are also not detached from the BSA during the interaction of nanoparticle with BSA. But the spectra of these fluorophores are red shifted. Therefore, it may be concluded that the conformational change induced by nanoparticle exposed the host more to hydrophilic environment though it moves the tryptophan to hydrophobic environment. In DMAPIP-b, the emission intensity decreases with a bathochromic shift of 30 nm whereas DMAPIP-c experienced a very little shift. This indicate that DMAPIP-c is less exposed than DMAPIP-b. The decrease in the fluorescence of DMAPIP-b is also more than that of DMAPIP-c.

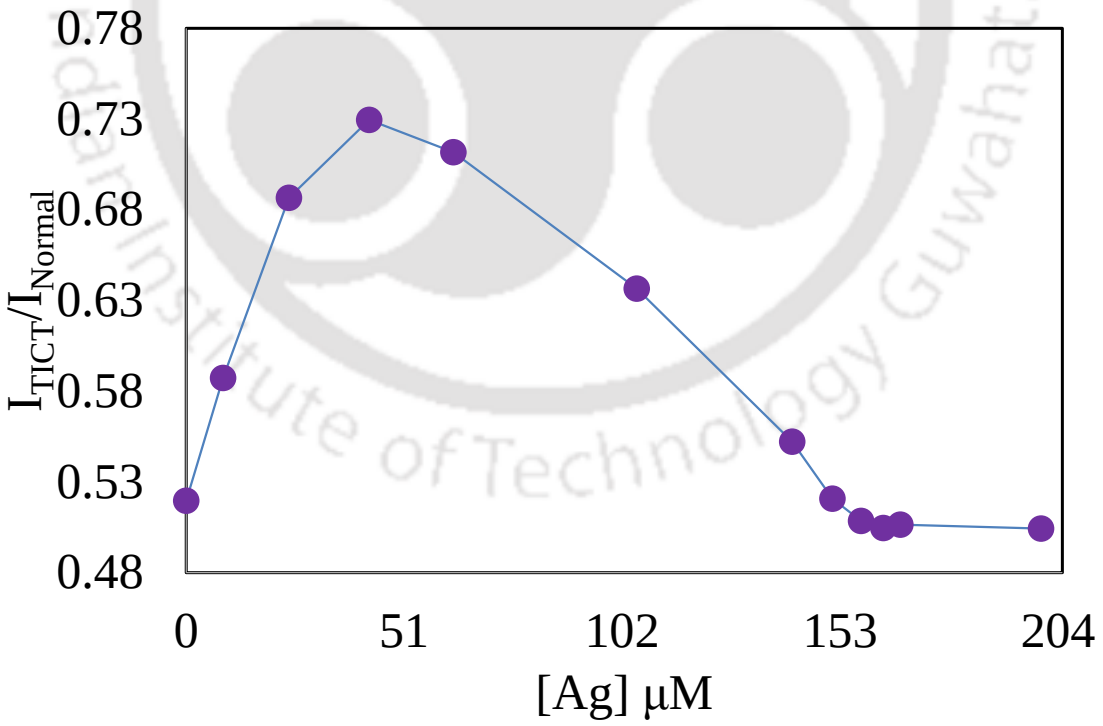

Figure 5.8: Plot of intensity ratio of TICT vs normal band of DMAPIP-c at different concentrations of silver nanoparticles.

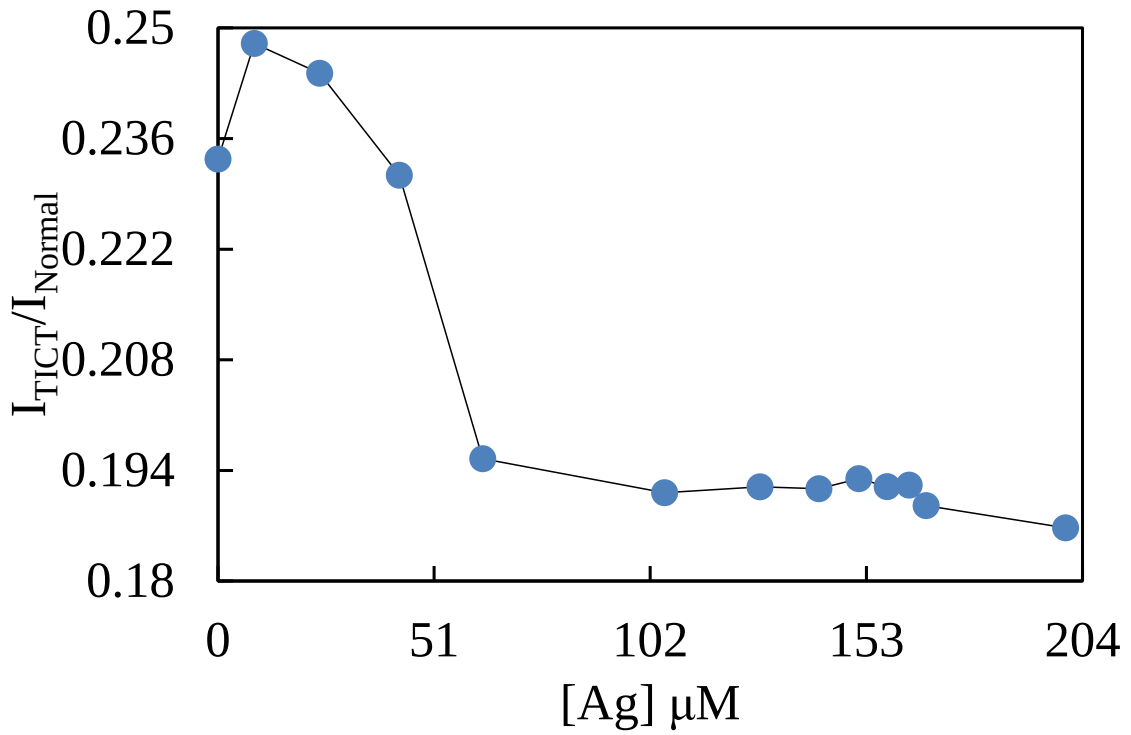

Figure 5.9: Plot of intensity ratio of TICT vs normal band of DMAPIP-b at different concentrations of silver nanoparticles.

The effect of nanoparticles on the TICT emissions of DMAPIP-b and DMAPIP-c is interesting. For the initial addition of nanoparticles to the inclusion complexes the TICT emissions increases. After reaching a maximum, the TICT emissions decreases with further addition of nanoparticles. The intensity ratio plot of TICT emission to normal emission clearly depicts that DMAPIP-c **[Figure 5.8]** suffers more change in TICT emission compared to that of DMAPIP-b **[Figure 5.9]**.

With enhancement in polarity the TICT is stabilized and it increase the rate of formation of TICT state. This led to enhancement in the TICT emission. However, greater stabilization decreases the energy gap between the TICT state and the low lying ground state. This increases the nonradiative decay. Therefore, the TICT emission after reaching a maximum decreases with increase in polarity.

5.3. Lifetime analysis:

The lifetime values of all the fluorophores in presence of BSA and silver nanoparticles are summarized in the table 5.1.

Table 5.1 Fluorescence lifetime values of DMAPBI, DMAPIP-b and DMAPIP-c in presence of BSA and silver nanoparticles.

Sample	τ_1 (ns)	τ_2 (ns)	χ^2
DMAPBI	1.09		1.08
DMAPBI + BSA	0.88		1.01
DMAPBI + BSA+ NPs	0.64		0.99
DMAPIP-b	0.26		1
DMAPIP-b + BSA	0.87 (33.0%)	2.0 (67.0%)	1
DMAPIP-b + BSA+ NPs	0.62 (48.0%)	2.2 (52.0%)	1
DMAPIP-c	0.91 (39.2%)	4.9 (60.7%)	1.06
DMAPIP-c + BSA	1.24 (33.0%)	5.3 (67.0%)	1.06
DMAPIP-c + BSA+ NPs	1.15 (33.5%)	5.4 (66.4%)	1.03

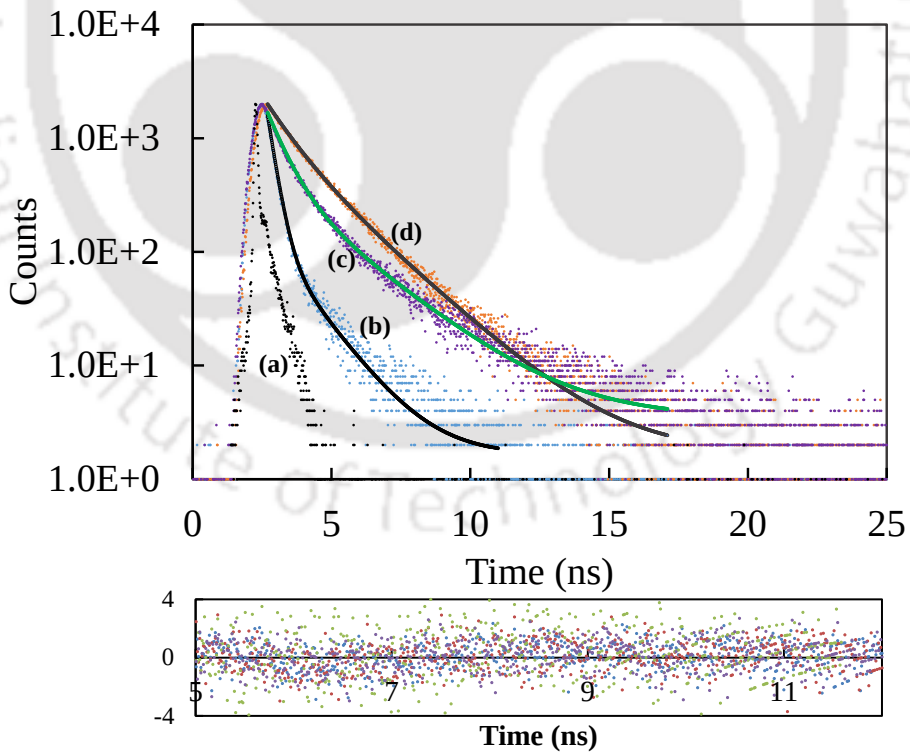

Figure 5.10. Fluorescence decay of DMAPIP-b in the (b) absence of BSA and nanoparticles (c) presence of BSA and nanoparticles (d) presence of BSA along with (a) instrument response function and residue.

As reported earlier [1-2], the lifetime of DMAPIP-b increases in presence of BSA and that of DMAPBI reduced inside the protein hydrophobic cavity. This is in accordance with the spectroscopic outcomes. In presence of nanoparticles, it was observed that the lifetime of the fluorophore-BSA composite decreases for the normal emission. This is due to the energy transfer from the fluorophores to the nanoparticles surface. Unlike the normal emission, the lifetime of the TICT emission increases in the presence of nanoparticles. As discussed earlier, the confinement of the $-N(CH_3)_2$ moiety by hydrophobic media enhanced the TICT emission which is reflected in the lifetime also. This also strengthened the conclusion that the BSA is not completely unfolded by the nanoparticles and the fluorophores were still in BSA and not in water. The florescence decay of DMAPIP-b in presence and absence of BSA nanoparticles is given as representative plot **[Figure 5.10.]**.

5.4. Conclusion:

Within BSA, the fluorescence emission of the fluorophores undergoes hypsochromic shift due to hydrophobic nature of the environment. Addition of nanoparticles to fluorophore-BSA complex resulted in the formation of a ternary complex. The nanoparticles induce conformational changes in the tertiary structure of the protein leading to exposure of the fluorophore towards more hydrophilic environment. Thus, the fluorescence emission of the fluorophores decreases with bathochromic shift. The emission of tryptophan also decreases in the presence of nanoparticles. But its emission is blue shifted this indicate that the conformational change moved the tryptophan more towards the hydrophobic environment rather than the hydrophilic environment. The reduction in the fluorescence of DMAPIP-b is more compared to that of DMAPIP-c. The TICT emission of both the fluorophore increases for initial addition of nanoparticle to fluorophore-BSA inclusion complex. After reaching a maximum it decreases due to increase in non-radiative decay.

Chapter 6

Suppression of Proton transfer of 2-(2'-hydroxyphenyl) benzimidazole (HPBI) and its nitrogenous analogues on the surface of nanoparticles

6.0. Introduction:

In the last few chapters, the interactions of silver nanoparticles with ICT fluorophores were described. The proton transfer is another important phenomenon which received huge attention in photochemistry and photobiology. Though the studies of nanoparticle-fluorophore interaction are quite common, studies of ESIPT exhibiting on the surface of nanoparticles are scarcely reported. Doroshenko et al. had studied the ESIPT of a 3-hydroxychromone in the vicinity of dodecanethiol-protected gold nanoparticles **[282]**. They found that the relative intensities of the normal band was increased compared to tautomer band. In addition, the unchanged lifetime nullified the fluorescence quenching of the both bands intensities. The ratiometric fluorescence changes was interpreted as a consequence of intermolecular hydrogen bonding between the probe and residual ethanol molecules, trapped into the dodecanethiol shell of gold nanoparticle during the synthesis.

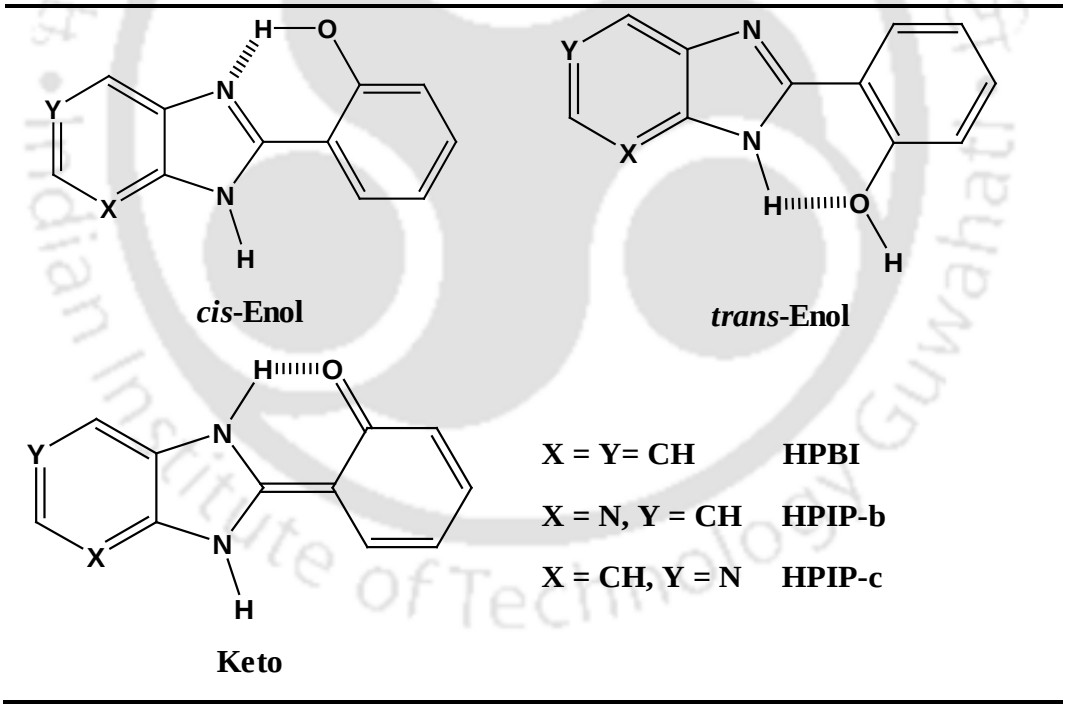

Chart 6.1. Structure of 2-(2′-hydroxyphenyl) benzimdazole (HPBI), 2-(2′-hydroxyphenyl)-3*H*-imidazo-[4, 5-*b*] pyridine (HPIP-b) and 2-(2'-hydroxyphenyl)-3*H*-imidazo-[4,5-*c*] pyridine (HPIP-c).

HPBI and its nitrogenous analogous belong to important class of ESIPT molecules. Depending on the polarity and hydrogen bonding capacity of the solvents, it exists as different conformers. The cis-enol **[Chart 6.1]** which is predominant in the nonpolar environment is responsible for the tautomer emission. The relatively more polar trans-enol **[Chart 6.1]** gives the normal emission. Studies on 2-(2'-hydroxyphenyl)benzimdazole **[Chart 6.1]** and its nitrogenous analogues made significant contribution to the understanding of ESIPT. Dual emission throws massive opportunity for these molecules in the age of sensing and imaging. Studies revealed that substitution of nitrogen on HPBI affects the photophysical characteristics **[283, 218, 284]**. Therefore, the ESIPT of HPBI and its analogues on the surface of silver nanoparticles is investigated. The stability of the silver nanoparticles in presence of the fluorophores is also emphasized in the context of synthesis of dye functionalized nanoparticles.

6.1. Synthesis and stabilization of the silver nanoparticles:

The silver nano particles were prepared by the reduction of silver ions by DMF as described **[materials and method]** in the absence of any common organic stabilizing agent. As mentioned earlier, the nanoparticles are unstable in the absence of fluorophores **[Figure 6.1]**. As ICT fluorophores, in presence of the ESIPT fluorophores also, the color of the solutions turn golden yellow with the increase in time signifying the formation of well separated nanoparticles in solutions. As earlier owing to the different extent of stabilization by different fluorophore, the small variation in color was observed in these solutions. HPBI supports the nanoparticles only up to 24 hours followed by little agglomeration. This was indicated by the broadening of the absorption spectrum **[Figure 6.1]**. Alike in ICT fluorophores, **[chapter 3]** in ESIPT molecules also the substitution of pyridyl nitrogen showed positive impact on the growth of the nanoparticles. However, the stabilization by ESIPT molecules are relatively lesser than that of ICT molecules. The growth process continued up to 14 days and 4 days in presence of HPIP-b and HPIP-c respectively **[Figure 6.1]**. For further study, the nanoparticles solutions were centrifuged at an rpm of 25000 at 5 °C for 10 minutes to remove the bigger particles. The bigger sized agglomerated particles were settled down during centrifugation and the remaining solutions of nanoparticles are collected for characterization.

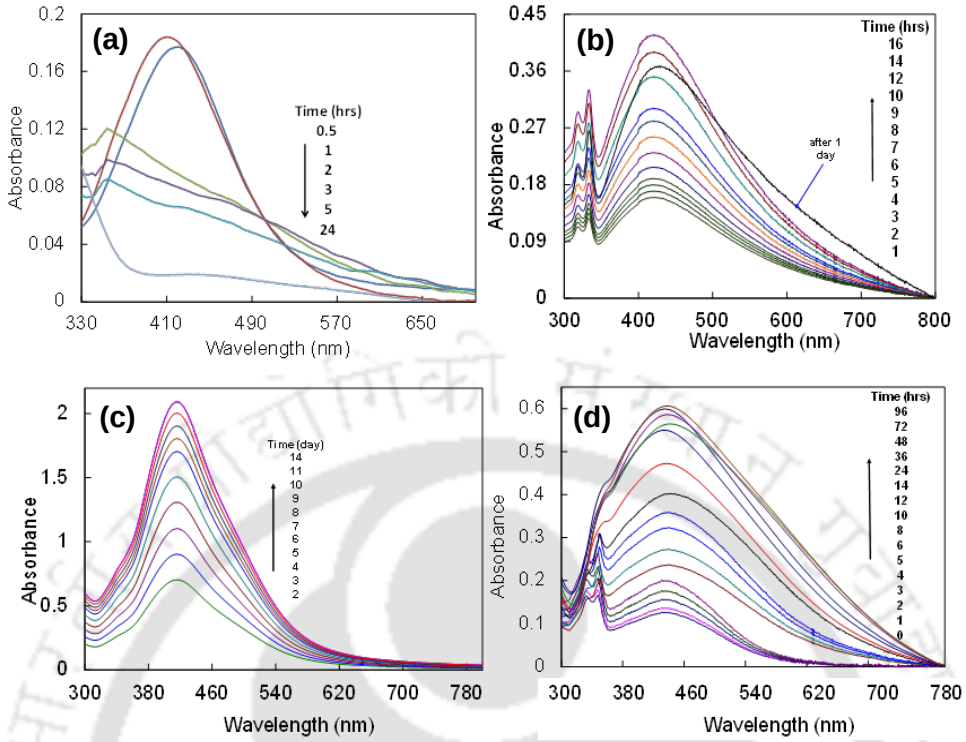

Figure 6.1: Growth of nanoparticles in (a) absence of fluorophores, and in presence of (b) HPBI, (c) HPIP-b, and (d) HPIP-c in DMF

6.2. Characterization from TEM, FESEM and DLS:

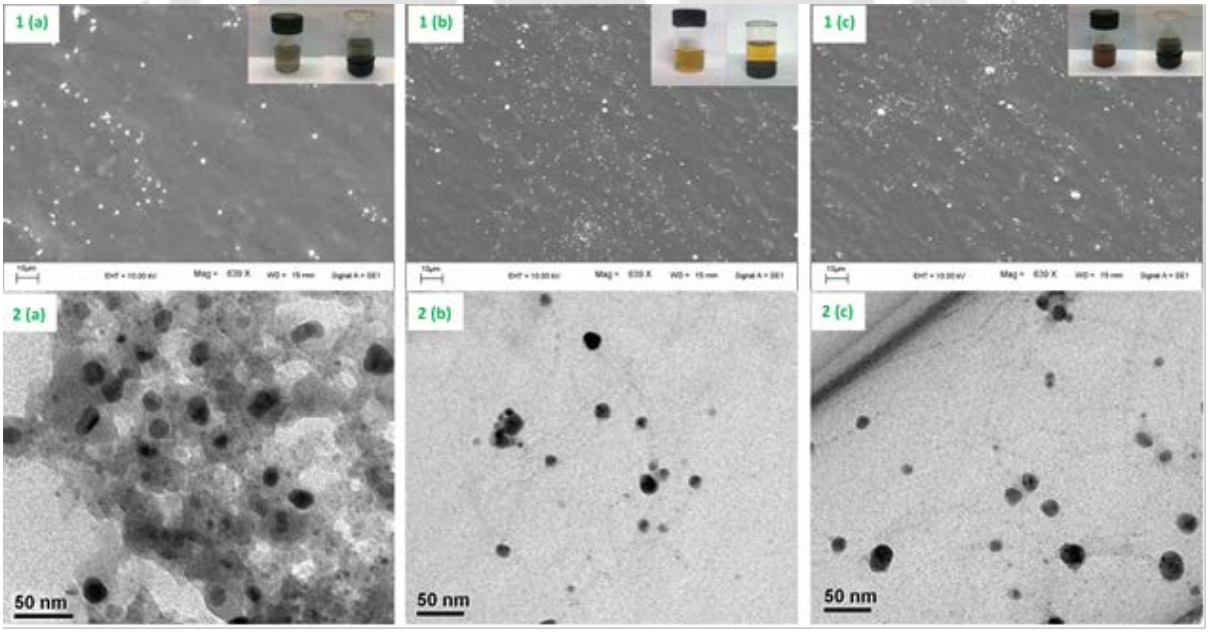

Figure 6.2: FESEM (upper panel) and TEM (lower panel) images of silver nanoparticles in presence of HPBI (a), HPIP-b (b) and HPIP-c (c) within an hour of preparation (inset: photograph of the vials containing nanoparticles)

The fluorophore assisted silver nanoparticles had different sizes depending on the stabilizing fluorophores. The mono-dispersity and homogeneity of the as synthesized nanoparticles were depicted by the FESEM images. The TEM image of the nanoparticles showed an average size around 30 nm diameters in presence of HPIP-b **[Figure 6.2 (b)]** and 70 nm with HPIP-c **[Figure 6.2 (c)]**. But in presence of HPBI, particles become aggregate to form higher diameter around 218 nm **[Figure 6.2 (a)].**

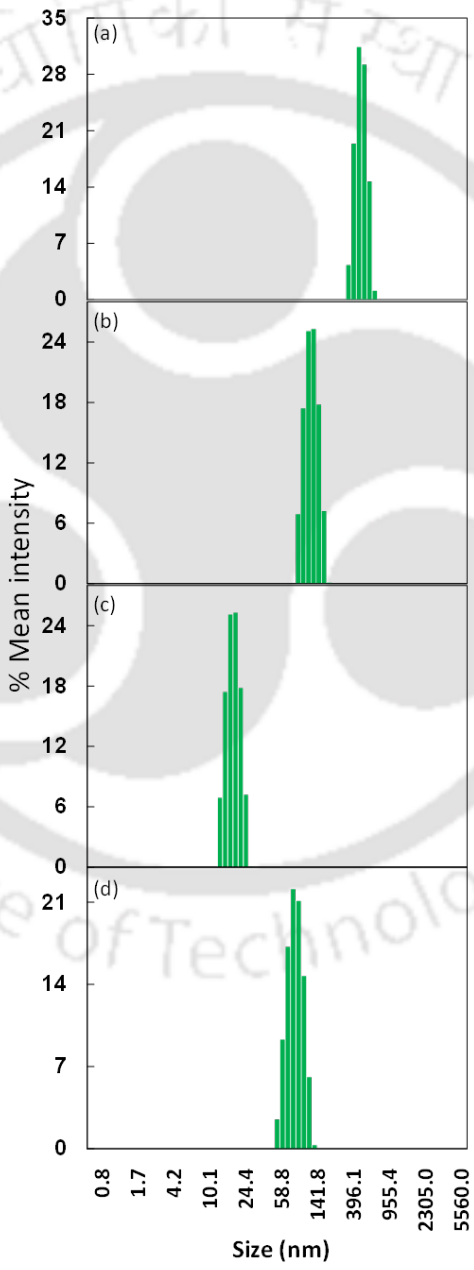

Figure 6.3: DLS study of silver nanoparticles in (a) absence of any fluorophore and in presence of (b) HPBI, (c) HPIP-b, and (d) HPIP-c.

Particle distribution was determined by using DLS method **[Figure 6.3]**. It was depicted that the distribution of nanoparticles in presence of all three fluorophores. The estimation of particle size was done by the instrument using a technique called Z-average particle size distribution. Larger particle size was found in case of HPBI which is also in accordance with the results of FESEM, TEM and absorption studies results. The nitrogenous analogues assisted the formation of mono-disperse and smaller particles compared to HPBI. The average size of HPBI, HPIP-b and HPIP-c assisted silver nanoparticles determined by DLS are 200 nm, 30 nm and 80 nm, respectively and are consistent with other studies.

The mean numbers of silver atoms per one particle can be calculated using the following equation (5.1) **[282]**

$$n = \frac{N_A \pi \rho D^3}{6M} \ldots\ldots\ldots\ldots\ldots\ldots\ldots\ldots\ldots\ldots\ldots\ldots\ldots\ldots\ldots\ldots\ldots\ldots\ldots\ldots\ldots\ldots 5.1$$

Where N_A is the Avogadro number (6.022×10^{23}), ρ is the density of silver (10.5 g/cm^3), D is the diameter of the silver nanoparticles in centimeters, and M stands for the atomic mass of silver (107.8682 g/mol). Silver nanoparticles formed with the support of HPIP-b and HPIP-c (with average diameter of 30 nm and 70 nm, respectively) were composed of ~ 8.2 x 10^4 and ~ 1.2 x 10^7 silver atoms respectively. But the estimated silver atoms in the clusters formed with the aid of HPBI were ~ 6.8 x 10^8. This huge difference obtained for HPBI clearly reveal less stabilization of silver nanoparticles in presence of HPBI than the nitrogen substituted analogues. This is consistent with the earlier observations.

6.3. Fluorescence characteristics:

HPBI and its nitrogen substituted analogues in DMF emit dual emissions **[Figures 6.4, 6.5 and 6.6]**. The shorter wavelength and longer wavelength emission bands are attributed to normal emission from excited *trans*-enol and tautomer emission from the phototautomer which is resulted by ESIPT from *cis*-enol **[Chart 6.1] [285-287]**. The effect of nanoparticles on the fluorescence characteristics of HPBI was depicted in Figure 6.4. Both normal and tautomer bands were quenched by nanoparticle without any notable shift in the spectra. But the fluorescence intensity of the normal band reduces little more compared to that of tautomer band for the initial addition of nanoparticles solution. This difference can be more clearly observed from the intensity ratio plot **[Figure 6.4 inset]**. However, for further addition of nanoparticles, the fluorescence intensity of both the bands

decreases almost in a similar fashion before getting saturated for addition of 32 µM concentrations of silver nanoparticles.

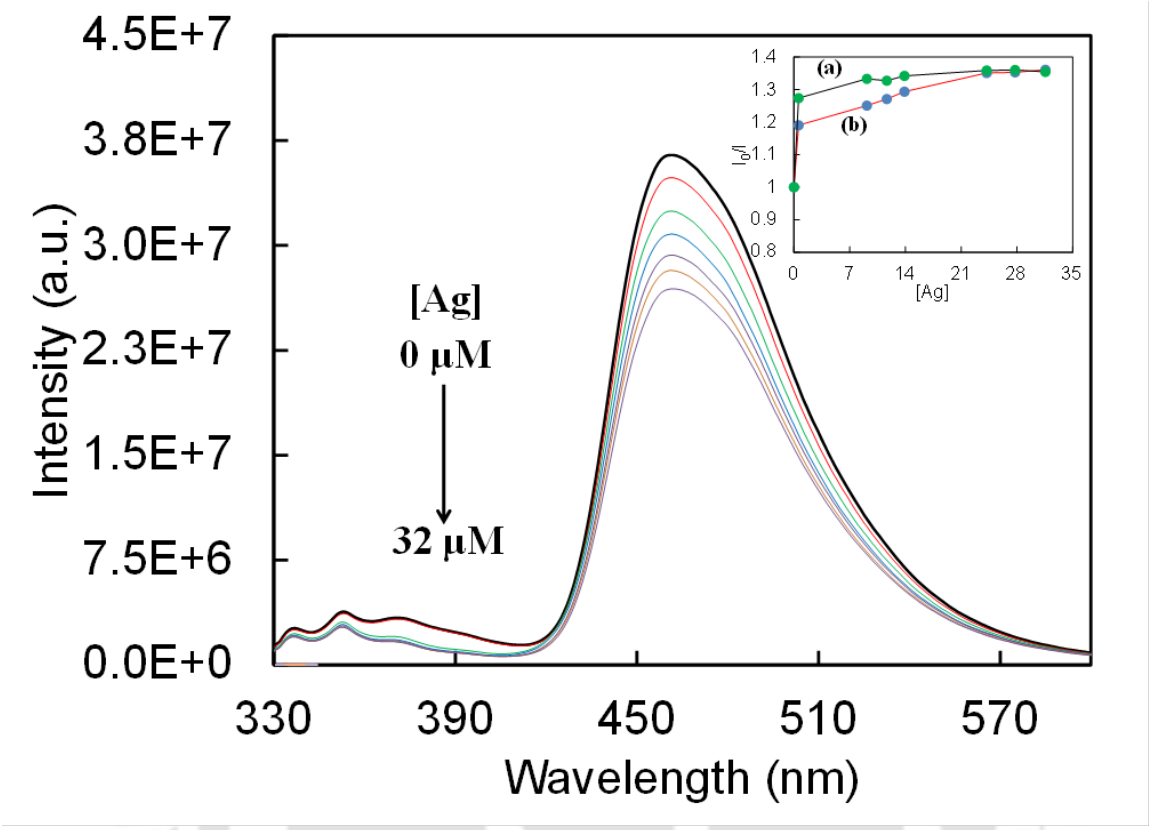

Figure 6.4: Fluorescence characteristics of HPBI with the increasing concentrations of silver nanoparticles [0-32 µM]. Inset shows the intensity ratio plot of (a) normal and (b) tautomer band at different concentrations of silver nanoparticles.

The substitution of HPBI with pyridyl ring made the derivatives more susceptible to the nanoparticles. Alike to HPBI, the fluorescence intensity of both normal and tautomer emissions were quenched by the nanoparticles **[Figures 6.5 and 6.6]**. But the quenching was found to be more in the pyridoimidazoles.

The quenching of both the emissions of HPIP-b by the nanoparticles was accompanied by bathochromic shift in the emission maxima **[Figure 6.5]**. The tautomer band endure a huge red shift of 60 nm compared to that of the normal band (5 nm). The quenching of fluorescence of both normal and tautomer emissions are different from each other. The intensity ratio plot **[Figure 6.5 inset]** cleared this fact. The normal emission suffered much more quenching compared to that of tautomer band for the initial addition of

silver nanoparticles which became constant for higher concentrations for both the emissions **[Figure 6.5 inset]**. The saturation point was found to be 2.5 µM of silver.

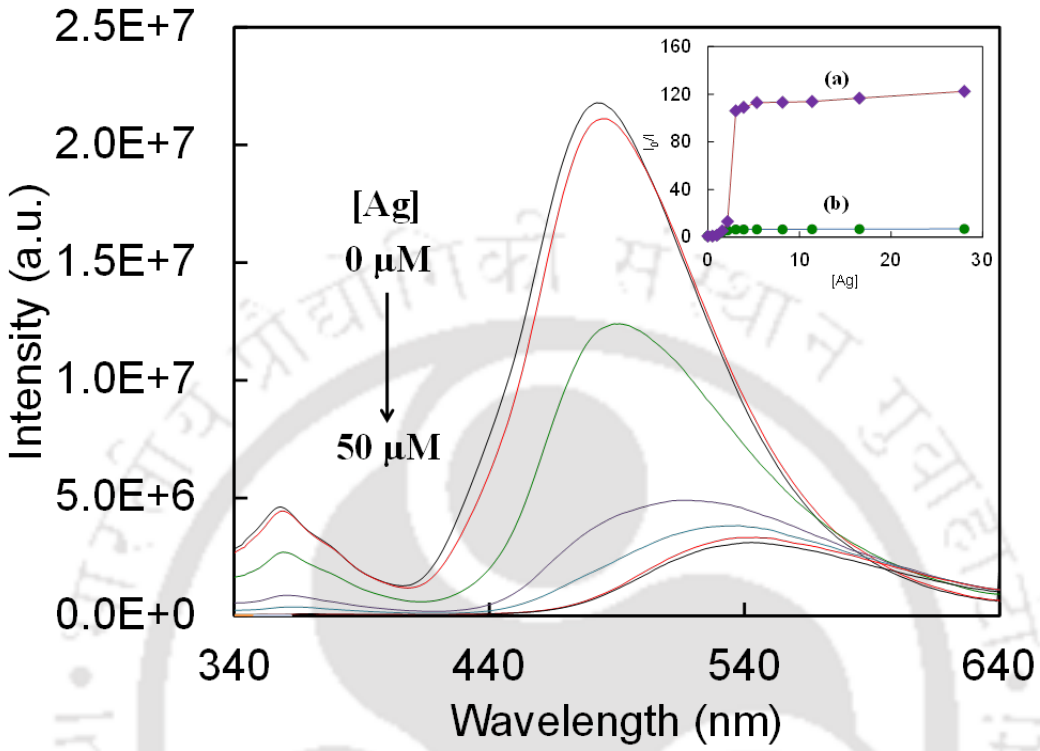

Figure 6.5: Fluorescence characteristics of HPIP-b with increasing concentrations of silver nanoparticles [0-50 µM]. Inset shows the intensity ratio plot of (a) normal and (b) tautomer band at different concentrations of silver nanoparticles [0-50 µM].

Unlike HPIP-b, only the tautomer emission of HPIP-c decreases with increase in concentration of nanoparticles. The fluorescence intensity of the normal band decreases up to 10 µM of silver **[Figure 6.6]**. Further addition of nanoparticles enhance the normal band intensity. Additionally the tautomer band underwent a bathochromic shift of around 14 nm while the shift in normal band is little.

In HPBI and its analogues the tautomer emission is more sensitive to environment than the normal emission **[218, 102, 288]**. Therefore, the spectral shift is expected to be more pronounced in tautomer emission than the normal emission in the nanoparticle-fluorophore composites. The shift observed in the tautomer emission of HPBI upon binding with nanoparticle is negligible, whereas the shifts in the tautomer emissions of HPIP-b and HPIP-c are 60 nm and 14 nm, respectively. This shows that HPIP-b has much stronger interaction with nanoparticles than HPIP-c whose interactions with nanoparticles are stronger than HPBI.

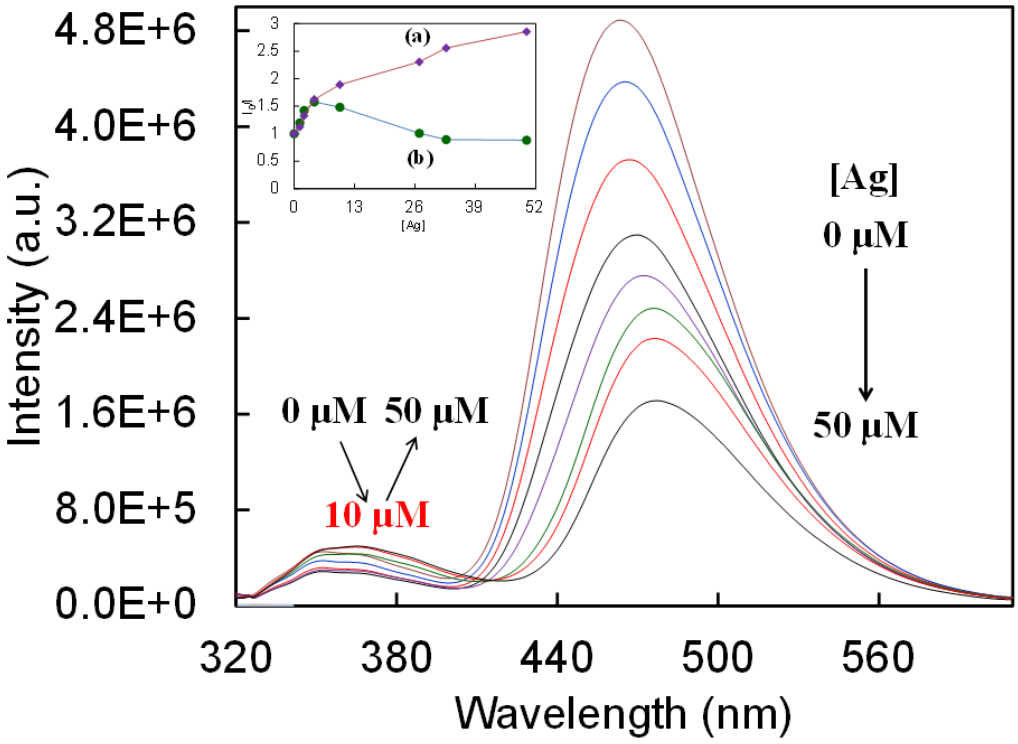

Figure 6.6: Fluorescence characteristics of HPIP-c with increasing concentrations of silver nanoparticles [0-50 µM]. Inset shows the intensity ratio plot of HPIP-b at various concentrations of silver nanoparticles.

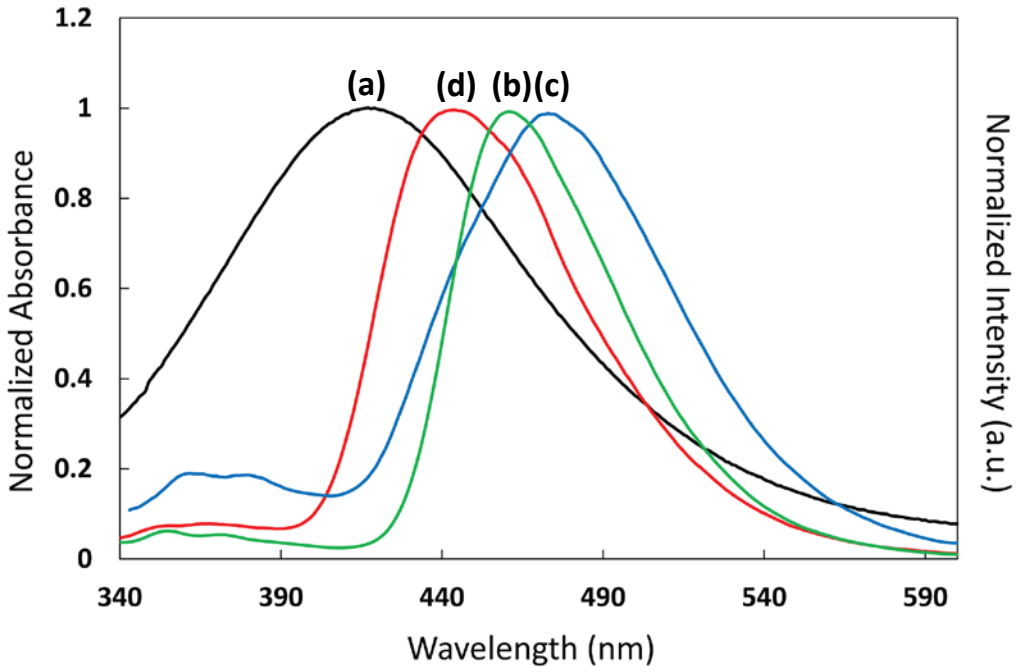

Figure 6.7. Normalized (a) absorption spectrum of silver nanoparticles, and fluorescence spectra of (b) HPBI, (c) HPIP-b and (d) HPIP-c with respect to tautomer emission.

This is consistent with the smaller sized particles formation in presence of HPIP-b and HPIP-c than HPBI, due to greater stabilization by pyido analogues. The smaller decrease in the emission intensity of HPBI than its analogues further support this. The I_0/I for the molecules follow the order HPIP-b > HPIP-c > HPBI. The extent of overlap between the absorption spectra of silver nanoparticles and emission spectra of all the fluorophores is depicted in **Figure 6.7.**

In HPBI and HPIP-b, the normal band is quenching more compared to the tautomer emission. It is well expected as the surface plasmon resonance band of silver nanoparticles completely overlapped the normal band whereas the tautomer band is only partially overlapped. This will lead to the more energy transfer from the trans-enol compared to that from the keto form. In HPBI, the normal band emission was quenched instantly in presence of nanoparticles due to the energy transfer to the nanoparticles surface. But surprisingly, with more addition of nanoparticles the emission intensity became steady. This is due to the formation of more trans enol during composite formation (see later). The lesser overlap in the tautomer emission produced less energy transfer which allowed smooth quenching of the emission. But this explanation seemed to be not satisfactory when the interactions with HPIP-c is considered. Here the increased normal band intensity with increasing nanoparticles concentration became a contradictory. **[Figure 6.6]**.

This fact is also well supported by the excitation spectra of the fluorophore monitored at both the bands in presence of nanoparticles **[Figure 6.8 and 6.9]**. The intensity of the excitation spectra monitored at normal band decreases with initial addition of nanoparticle, but increases after 10 µM, whereas the intensity of the spectra monitored at tautomer band decreases with concentration of nanoparticles. This gives a clear indication that in presence of nanoparticles, the normal band intensity increases after 10 µM at the cost of tautomer band intensity.

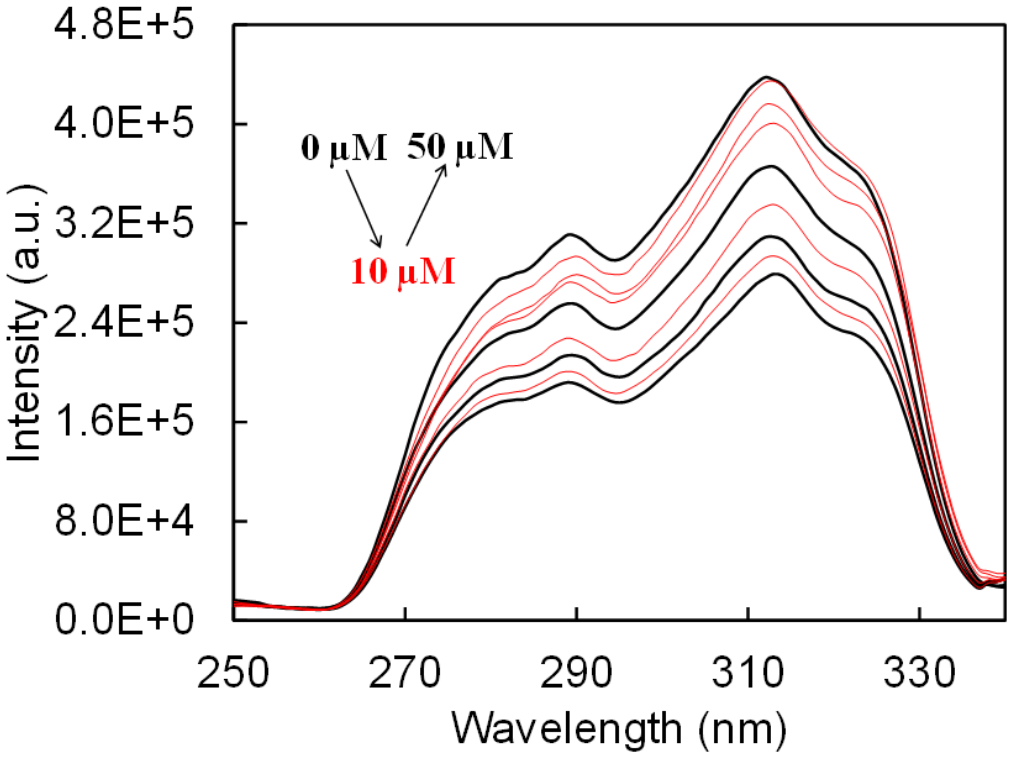

Figure 6.8: Excitation spectra of HPIP-c at various concentrations of silver nanoparticles [0-50 µM] monitored at λ_{em} = 346 nm.

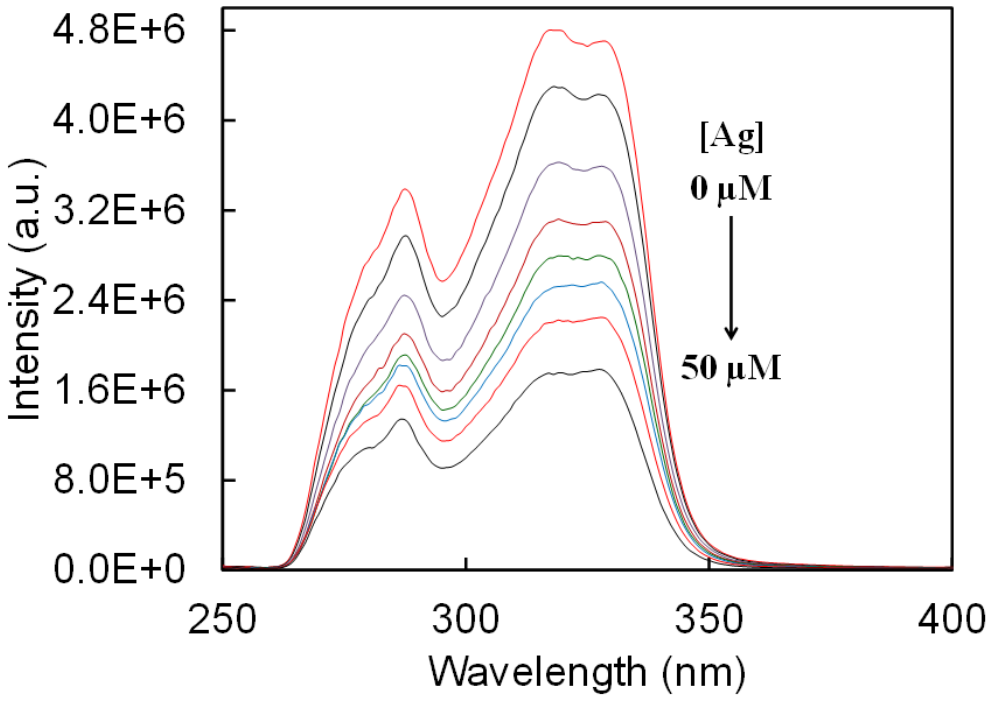

Figure 6.9: Excitation spectra of HPIP-c at various concentrations of silver nanoparticles [0-50 µM] monitored at λ_{em} = 457 nm.

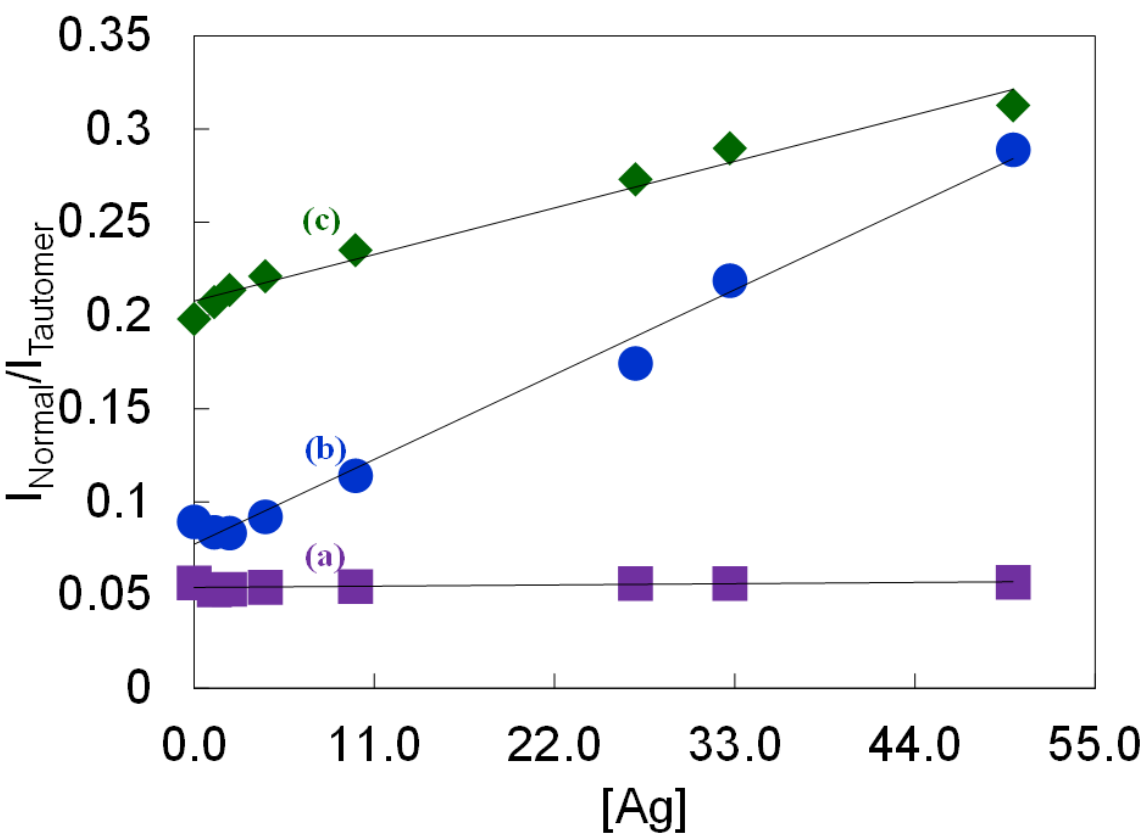

Figure 6.10: Intensity ratio plot of normal band to tautomer band of (a) HPBI, (b) HPIP-c and (c) HPIP-b at different concentrations of silver nanoparticles [0-50 μM]

To get more insight into this context, intensity ratio of the normal band to the tautomer band was plotted against concentration of silver nanoparticles **[Figure 6.10]**. The intensity ratio of HPBI underwent very negligible change. In both of the pyridyl nitrogen substituted analogous, the ratio increases with the increase in nanoparticles concentration. Despite the fact that the overlap between the absorption spectrum of nanoparticle with normal emission is more than the tautomer emission, the relative intensity of normal emission increases with amount of nanoparticles. This implies that the relative population of *tran*-enol increases upon addition of nanoparticles. In other words, the nanoparticles shift the *cis*-enol-*trans*-enol equilibrium towards *trans*-enol. The heteroatom present in the heterocyclic rings provided the site for the interaction between the fluorophores and the nanoparticles. The more stabilization of nanoparticle in presence pyridoimidazole analogues suggested that like in the ICT molecules, in these molecules also the pyridyl nitrogen ring is the primary site of interaction. This interaction involves the lone pair of nitrogen atom on the pyridyl nitrogen. The electron deficiency thus created in the pyridyl nitrogen induces

the charge transfer from the imidazole nitrogen. The decreases the electron density on imidazole nitrogen which weakens the intramolecular hydrogen bond and decrease in the proton transfer from –OH to the imidazole nitrogen.

But expect for HPIP-c, no increase in the normal band emission was found for other molecules. This may be due to the energy transfer from the Trans enol to the nanoparticles surface. However, the normal emission was quenched less compared to the tautomer emission. The relative intensities of normal to tautomer emissions are greatly affected by the hydrogen bonding capability of the solvent molecules **[285, 218, 102 and 289]**. In protic solvents, the relative population of *cis*-enol decreases thereby, it reduces the ESIPT process. During the interaction with silver nanoparticles, the role played by the protic solvent is served by the nanoparticles. However, the mechanism of weakening of intramolecular bond is different in both cases. In protic solvents, it is the competing intermolecular hydrogen bonding between the solvent molecules and the fluorophores breaks the intramolecular hydrogen bonded ring in *cis*-enol. But, nanoparticles-fluorophore composite, it is the reduction in charge on the azole nitrogen decreases the ESIPT process.

6.4. Fluorescence Lifetime:

Table 6.1. Lifetime values of the fluorophores and their composites with nanoparticles are summarized in the table.

	Monitored at λ_{em} = 363 nm	Monitored at λ_{em} = 461 nm
HPBI	1.49 ns	4.23 ns
HPBI-nanoparticle	1.55 ns	3.85 ns
	Monitored at λ_{em} = 362 nm	Monitored at λ_{em} = 480 nm
HPIP-b	1.26 ns	2.82 ns
HPIP-b- nanoparticle	1.19 ns	1.63 ns
	Monitored at λ_{em} = 346 nm	Monitored at λ_{em} = 457 nm
HPIP-c	1.26 ns	3.68 ns
HPIP-c- nanoparticle	1.22 ns	2.97 ns

The suppressed fluorescence intensity of the tautomer band compared to that of normal band is also rationalized by the lifetime data (Table 6.1). The τ_0 represents the lifetimes of the free fluorophores in DMF whereas τ gives the lifetimes of the fluorophores-

nanoparticles composites. The lifetime of the keto specie is considerably reduced in presence of nanoparticles compared to in absence of nanoparticles. However the enol specie did not show much change in lifetime in the presence and absence of nanoparticles. Hence only the ratio of the lifetime of keto species are plotted and presented **[Figure 6.11]**. The positive slopes of the plots for the pyridoimidazoles in presence of nanoparticles signifies the decrease in lifetime for the composites compared to the free fluorophores. The reason behind the much affected tautomer lifetime compared to that of Trans enol lies within the long lifetime of the keto species.

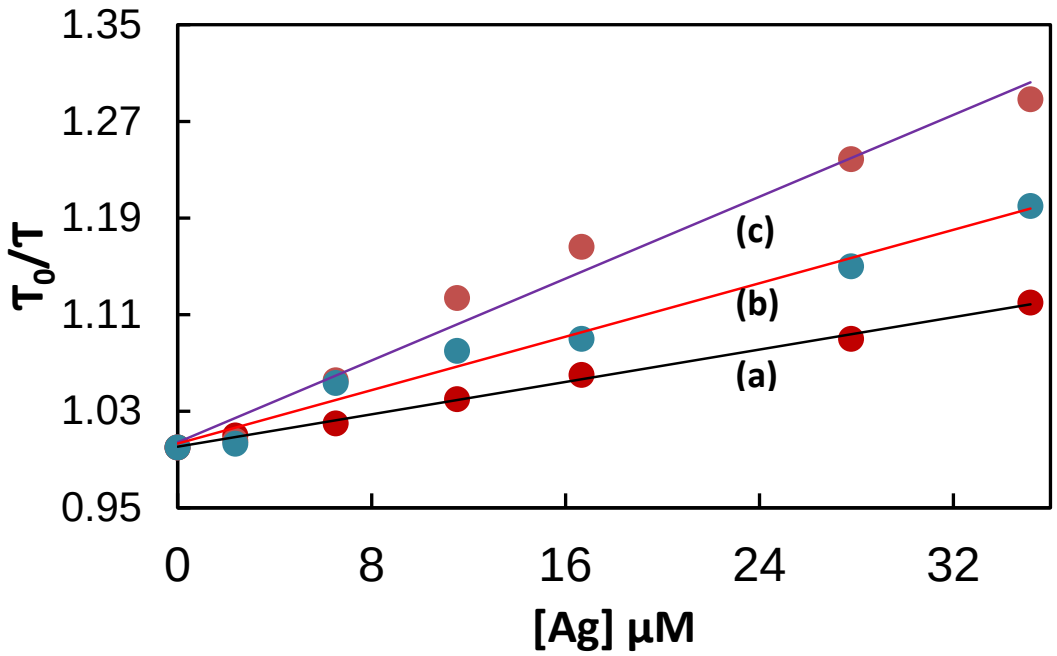

Figure 6.11: Plot of τ_0/τ of (a) HPBI, (b) HPIP-b and (c) HPIP-c at different concentrations of silver nanoparticles.

The lifetime observed for the tautomer was higher compared to that of enol conformer for free fluorophore. Hence in the excited state, the tautomer stayed more time compared to the Trans enol. This allowed nanoparticles to interact more with the keto form than the Trans enol. More the time of impact, more effect will be generated by the nanoparticles i.e. the energy transfer from the fluorophore to the nanoparticles. Hence the tautomer lifetime was found to be more affected compared to that of normal emission. Apart from this, HPBI showed increase in the normal band lifetime while the tautomer band shows the same trend as in the nitrogen analogues. In HPBI the interaction happened through the imidazole nitrogen which produced less energy transfer compared to those of

pyridoimidazoles. Hence the transforming of the cis enol to Trans enol during the interaction with nanoparticles overrides the effect of energy transfer and the result is an increase in normal band lifetime.

6.5. Conclusion:

Silver nanoparticles have the potential to interact with HPBI and its nitrogen substituted analogues. They subsequently affect the photophysical properties of the fluorophores. The interaction is more efficient with nitrogen substituted analogues HPIP-b and HPIP-c than HPBI. This efficiency primarily lies in the presence of pyridine nitrogen which proved to be the most preferable site of interaction for nanoparticles. Nanoparticles hampers the ESIPT process by withdrawing the electron density which affect the intensity ratio of normal to tautomer band. Unstable silver nanoparticles were found to be stable in solution in presence of these fluorophores. In this context, the nitrogen substituted analogues are one step ahead of HPBI in terms of stability of the silver nanoparticles owing to the presence of the pyridine nitrogen. This stability further furnishes evidence for the interaction through the pyridine nitrogen as nitrogen substituted analogues stabilize more than HPBI. The distinct red shifts in the spectra and decrease in the life time pointed towards the energy transfer from the surface bound fluorophore to nanoparticles. All these results revealed towards the importance of the pyridine nitrogen in stabilization of nanoparticles, energy transfer and interacting with the nanoparticles.

Chapter 7

Facile synthesis of spindles, rods and niddles from 2-(2′-hydroxyphenyl) benzimidazole analogues: Aggregation induced enhanced emission from excited state intramolecular proton transfer

7.0. Introduction:

The emission of light from fluorophores in concentrated solutions often differs from dilute solutions. The quenched fluorescence form the concentrated solutions created problems in real field applications such as biological sensing, OLEDs etc. **[290-294]**. Formation of aggregates at high concentration leads to the decrease in fluorescence intensity. This notorious effect of reduction in fluorescence pushed many researchers to work to overcome this phenomenon at any cost. After the pioneering work of Tang et al. **[295-302]**, a new picture has come to the field of aggregation termed as aggregation induced emission (AIE) or aggregation induced enhanced emission (AIEE). They developed a series of siloyl derivatives which are non-emissive at molecular level, but highly emissive in aggregates. Hence, constructive outcome of fluorescence enhancement was obtained from the aggregated solution. This phenomenon brought new perspective to the fluorescence field. The AIEE allows us to access a combo product which contains the effectiveness of both fluorophore and particles. This AIEE helps the researchers a lot to use this in different applications.

The mechanistic aspect of AIEE has also been explored **[299]**. A number of possible mechanistic pathways such as formation of J-aggregate, conformational planarization, restriction of TICT etc were suggested by various researchers **[303-311]**. De-excitation of the excited energy of any fluorophore by molecular motion is a common phenomenon. The highly active intramolecular rotation in solutions serves as a relaxation channel for the excited state to decay. This rotation is restricted in aggregates due to the physical constraint, which blocks the non-radiative path and activates the radiative decay. Hence, the restriction of the rotation (RIR) of the single bond connecting the donor and the acceptor of the fluorophores was hypothesized as the cause for the AIEE effect in number of systems **[300, 302, 312 and 313**]. Viscosity is a factor that retards the RIR process. It was already proved that in viscous medium the molecular rotations are restricted and radiative decay increases. Alike viscochromism, application of pressure also enhanced the RIR process. Despite the antagonistic effect of pressurization on light emission, it brings molecules closer hence decreasing the void volumes and densifies the molecular packing. The reduced distance decreases the freedom of their molecular motion compared to the loose packing and strengthens the RIR process. Similarly, lowering the temperature can also fortify RIR. The

enhanced emission form the AIEE molecules allowed us to use them as chemical and p^H sensors, biological probes, fabrication of efficient OLEDs etc.

In this chapter, the possible AIEE from HPBI and its nitrogen substituted analogous are explored. This chapter is divided into two sections. First section focuses the achievement of enhanced tautomer emission through aggregation of the fluorophores in proper solvent mixtures. In the second section, the effect of pyridyl substitution on AIEE was investigated.

7.1. Aggregation of HPBI:

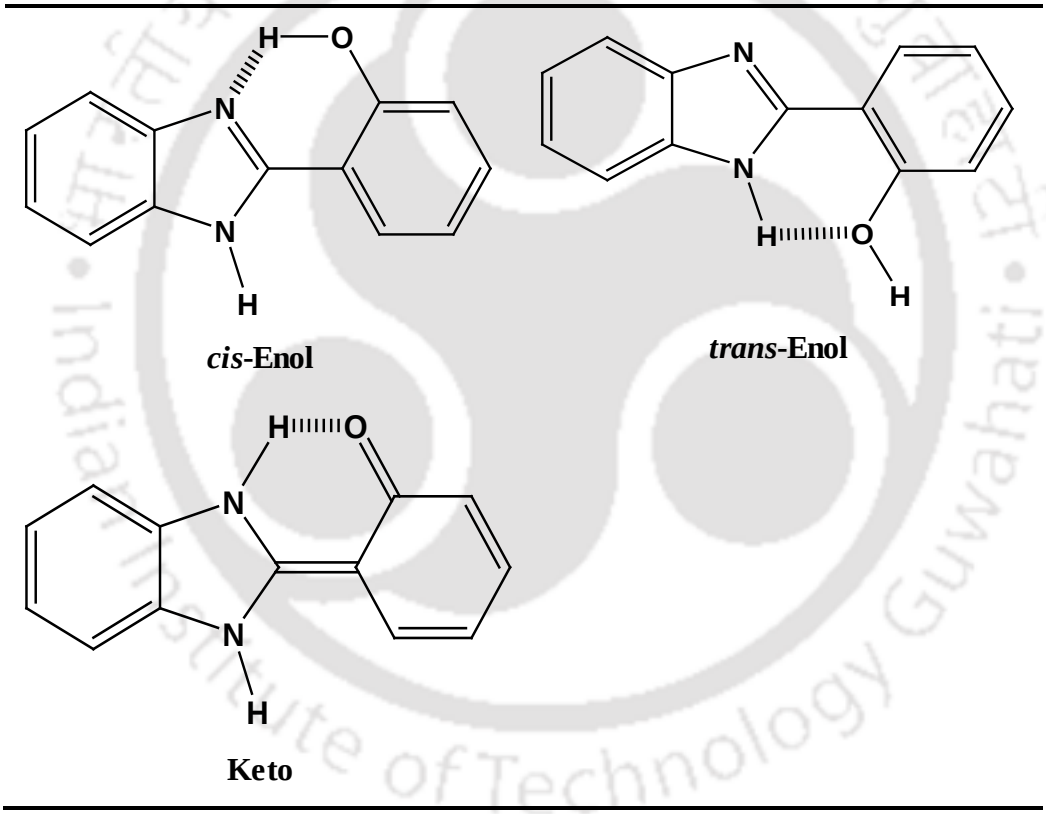

Chart 7.1.1. Different forms of HPBI

7.1.1. Absorption characteristics:

UV-visible spectra of HPBI in water and methanol were depicted along with the re-precipitation mixture at different time intervals **[Figure 7.1.1]**. Dramatic increase in the absorbance as compared to that in water was observed in the initial spectrum of the mixture.

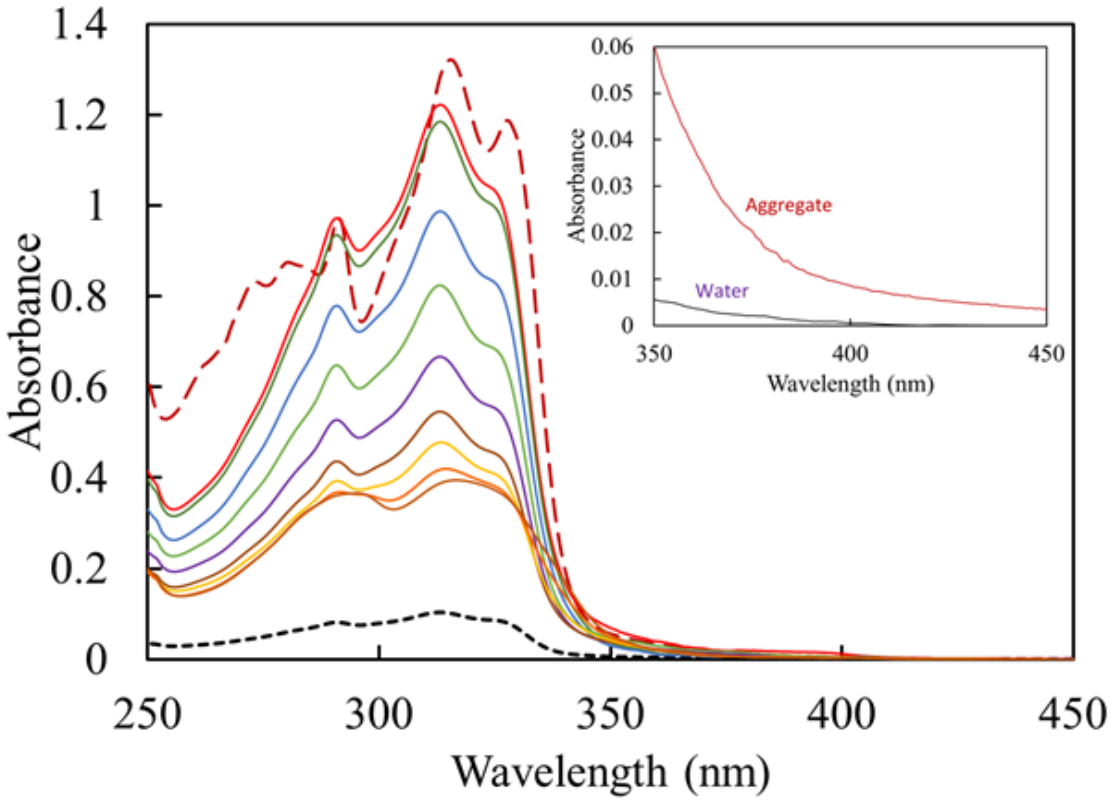

Figure 7.1.1: Absorption spectra of HPBI in water (▪▪▪▪▪), methanol (▬ ▪) and in re-precipitation mixture at ▬ 0 min, ▬ 10 min, ▬ 30 min, ▬ 60 min, ▬ 120 min, ▬ 180 min, ▬ 300 min, ▬ 360 min, ▬ 24 hrs. Inset shows the expanded spectra of HPBI in water and aggregated mixture in the 350 nm-450 nm region.

The absorption spectrum was well resolved with vibrational structures similar to that in methanol. But as the time progresses, the absorbance started to decrease with a bathochromic shift in the spectrum. The absorption spectra also gradually lost the vibrational structure. The reduction in absorbance of the initial band was accompanied by an increase in absorbance at the longer wavelength. This typical tail observed in the visible region was caused by Mie scattering **[314, 315]**. This can be attributed to the aggregation of the molecules to micro/nano particles. The absorption changes of HPBI were similar to those observed in other AIEE fluorophores **[314]**. In the re-precipitation process, it was described that upon addition into aqueous medium, organic solvents first form fine droplet and then diffuse in the bulk water **[314-323]**. Fery-Forgues et al. reported that after an ethanol solution of the dye was introduced into the water, the diffusion of ethanol molecules was not immediate and the first change in the surroundings of the dye continued for around 2 s

after mixing **[314]**. Hence at the beginning of the process, just after addition of the methanol solution of HPBI to water, the immediate environment of the HPBI molecules was richer in methanol than the bulk water.

This methanol rich environment may be responsible for the immediate increase in absorbance. The resemblance of initial spectrum of the mixture with that in methanol **[Figure 7.1.1]** strengthened this fact. Following this, methanol diffuses slowly into the bulk water resulting in the replacement of the alcohol rich environment by a water shell. This solvation may be a key factor for the formation of aggregates. When the fluorophores were exposed to the water, they started to aggregate.

7.1.2. Fluorescence characteristics:

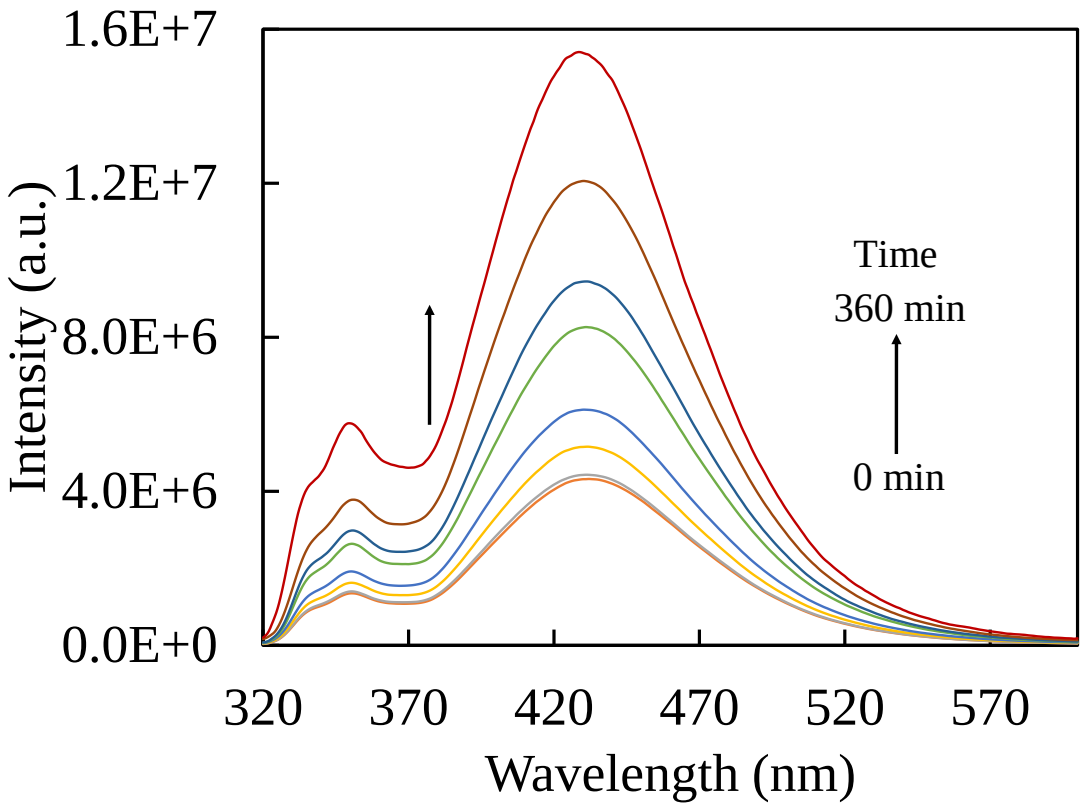

Figure 7.1.2: Fluorescence spectra of the re-precipitated mixture of HPBI with increasing time (λ_{exc} = 310 nm).

Fluorescence spectra of HPBI in water are characterized by dual emission. The normal and tautomer emissions were attributed to the emission from the excited trans-enol

and the phototautomer which is formed from cis-enol by ESIPT, respectively **[Chart 7.1.1]**. The relative intensities of normal to tautomer emissions are greatly affected by the hydrogen bonding capability of the solvent molecules.

In protic solvents, the intramolecular hydrogen bonded ring in cis-enol which is a prerequisite for the ESIPT process breaks due to intermolecular hydrogen bonding between the protic solvent molecules and the fluorophore through the imidazole nitrogen and phenolic proton of the fluorophore. This leads to shifting of equilibrium from cis-enol to trans-enol/solvated enol, thereby, increasing the relative intensity of the normal emission. HPBI shows weak emission in aqueous medium. The time dependent evaluation of fluorescence characteristics was used to observe the process of aggregation **[Figure 7.1.2]**.

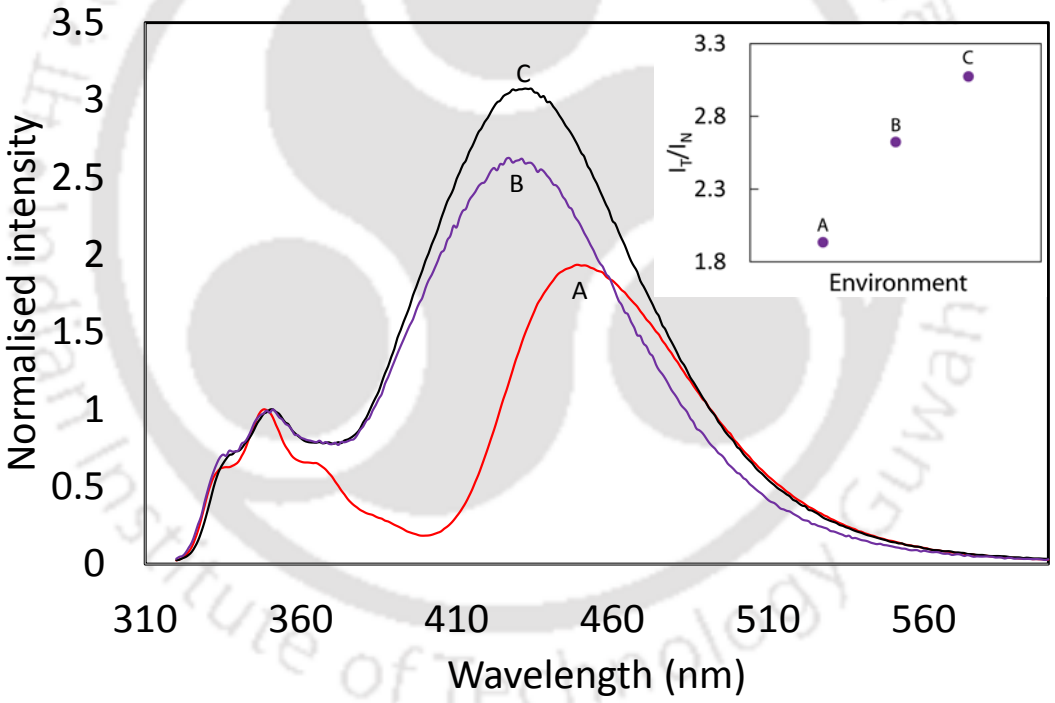

Figure 7.1.3: Fluorescence spectra of HPBI in (A) methanol, (B) water and (C) aggregate solution. Inset shows the intensity ratio of tautomer emission to normal emission (I_T/I_N).

The fluorescence emission intensity increases gradually with time. The enhancement in the fluorescence of the solution clearly suggests that the aggregates are not coagulating and precipitating. Instead they are well dispersed aggregates in solution. The intensity ratio of the tautomer to normal emission in methanol is 1.9 and in water it is 2.6 **[Figure 7.1.3]**.

If the changes are due to solvent interaction one could expect the ratio to be between 1.9 and 2.6. In contrast, the intensity ratio of the tautomer to normal emission in aggregate solution is 3.1 **[Figure 7.1.3]**. Thus, the solvent effect without aggregation being responsible for the change is ruled out. The enhancement in the relative intensity of tautomer emission advocates the cis enol population, is caused by the fact that aggregation provided a more hydrophobic environment, thus favoring cis-enol. After 24 hours the fluorescence enhanced more than 4 times. The little blue shift could be a result of increased rigidity in the system.

7.1.3. Time resolved fluorescence:

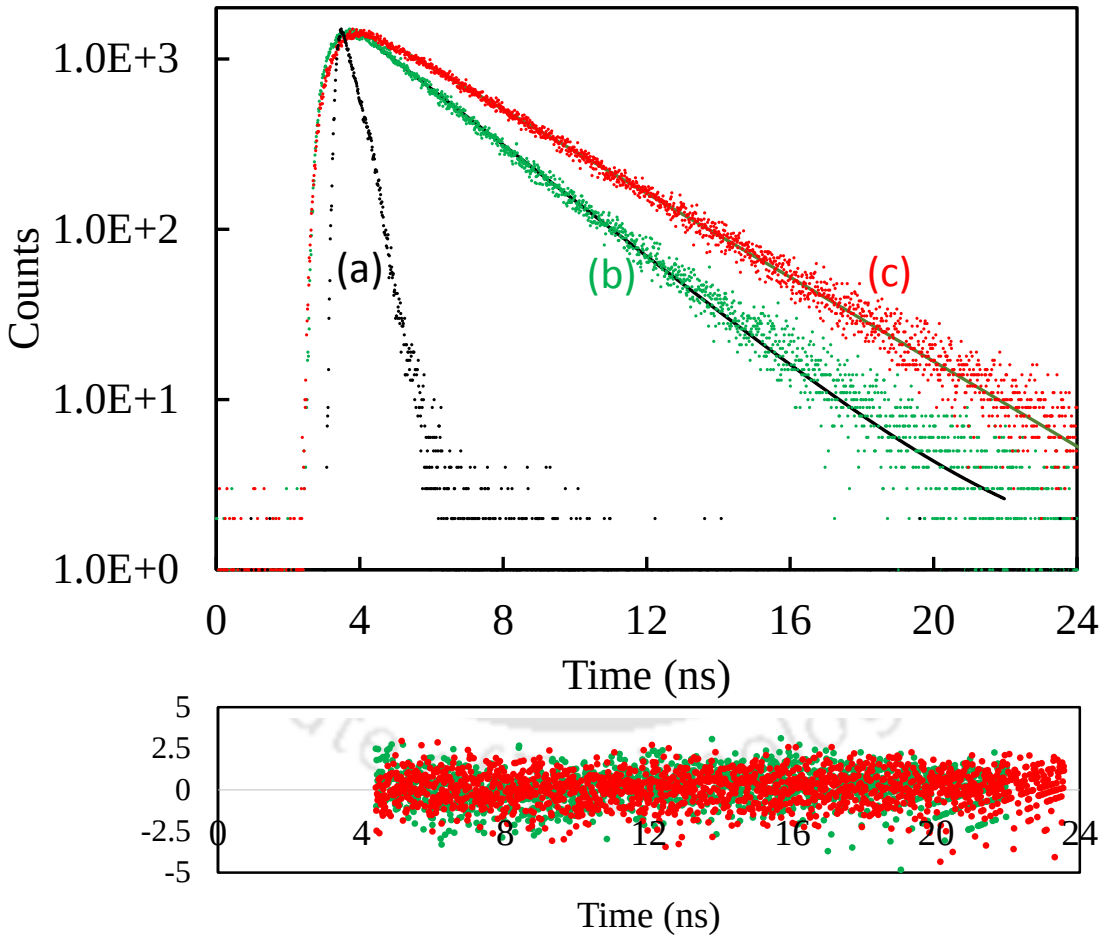

Figure 7.1.4: Fluorescence decay of (b) HPBI in water and the (c) re-precipitate solution along with (a) instrument response function and the residue.

The fluorescence decay of the monomer and the aggregate of HPBI were measured at two different wavelengths **[Figure 7.1.4]** and summarized in **Table 7.1.1**. When monitored at 360 nm (normal band maximum), clear dual lifetimes were observed for the monomer. The bi-exponential decay was due to mixing of strong tautomer emission with normal emission. The species with 0.56 ns lifetime corresponds to the excited trans-enol form of HPBI and the keto tautomer has longer excited state lifetime (1.69 ns). This conclusion was further supported by the lifetime obtained by monitoring at 480 nm, which yielded a single lifetime of 1.69 ns. In other solvents also it was reported that the excited state lifetime of trans-enol form is shorter than that of its tautomer **[316, 284]**. In the re-precipitated solution when monitored at the 360 nm (normal band emission maxima) same as in monomer solution bi-exponential decay was observed. While the lifetime of the excited trans-enol was unaffected (0.56 ns), the excited state lifetime of the tautomer increased from 1.69 ns to 2.59 ± 0.01 ns. This suggest that the excited trans-enol/solvated enol is present in the bulk solution as monomer and the cis-enol molecules which are the ground state precursor for the keto tautomer aggregates to form particles.

Table 7.1.1: Lifetime values of the monomer and the aggregates monitored at normal and tautomer band.

Fluorophore		Monitored at λ_{em}=360 nm			Monitored at λ_{em}=480 nm	
		τ_1	τ_2	χ^2	τ	χ^2
HPBI	Monomer	0.56 (88.24)	1.69 (11.76)	0.98	1.69	1.02
	Aggregate	0.56 (96.92)	2.59 (3.08)	0.98	2.60	1.04

Longer lifetime of tautomer is quite consistent in line with the other spectroscopic results. The tautomer emission enhanced upon aggregation due to reduction in the non-radiative process. Consequently, the lifetime for the keto tautomer increases. Such an enhancement in fluorescence lifetime upon aggregation was reported in other ESIPT exhibiting molecules also **[312, 324, 325]**.

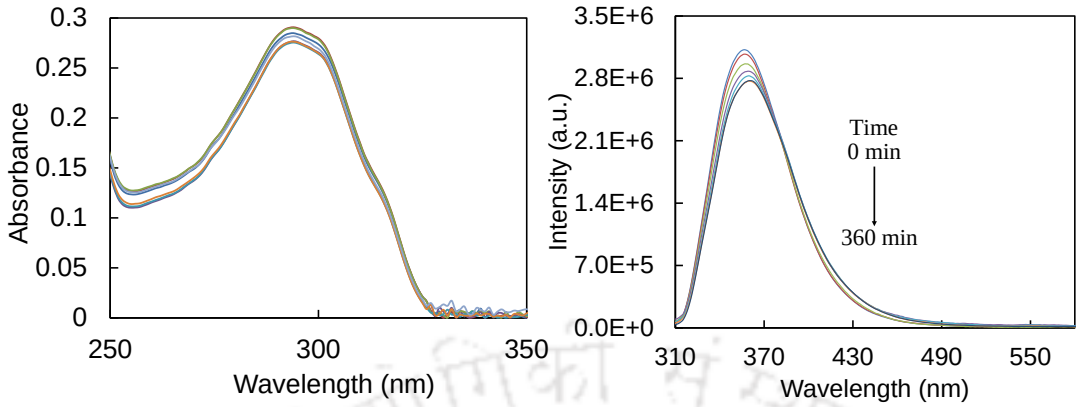

Figure 7.1.5: Absorption and fluorescence spectra of the re-precipitated mixture of PBI with increasing time.

To further understand the role of hydroxyl group in the aggregation process, 2-phenyl benzimidazole (PBI) was synthesized where the hydroxyl ion was absent. Re-precipitation of this compound in same solvent mixture did not result in AIEE. Unlike in HPBI, no substantial changes were found in the spectroscopic results. The absorption as well as fluorescence spectra of the solution at different time intervals yielded no apparent change with time **[Figure 7.1.5]**. It appears that the presence of hydroxyl group is critical for the AIEE of this molecule.

7.1.4. Morphology and Imaging:

The aggregates were investigated under FESEM to understand their morphology [**Figure 7.1.6]**. In addition to well dispersed aggregates, a few clusters of aggregates having common centers were observed. One such cluster was shown in expanded scale in **Figure 7.1.6**. Structures of aggregates were broad in the center and narrow at the end whose diameters were in the order of few hundred nanometers with length up to few micrometers.

Fluorescence microscopic images showed that the aggregates emit strong fluorescence upon excitation with 350 nm light **[Figure 7.1.7]**. The time dependent study of fluorescence images were well acquainted with the spectroscopic studies.

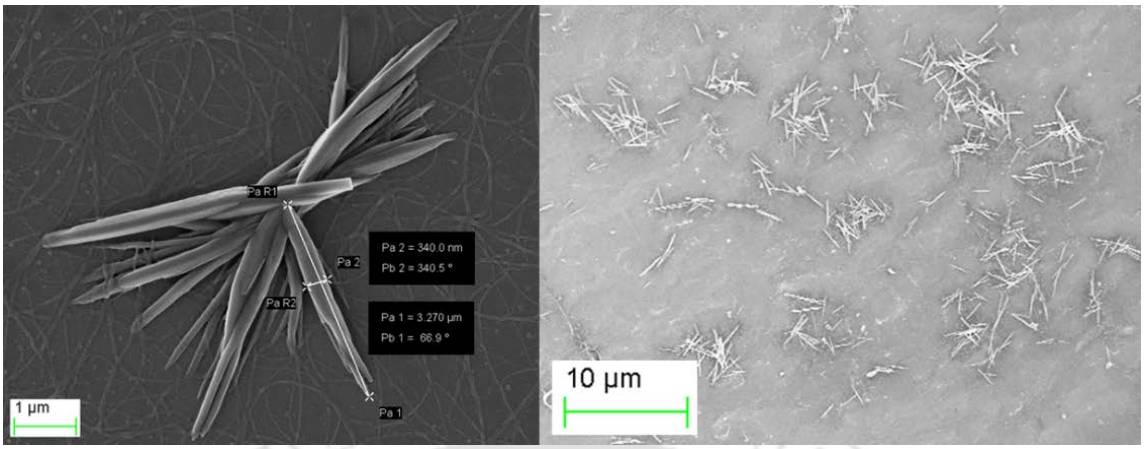

Figure 7.1.6: FESEM images of the samples made from aqueous suspensions of HPBI after re-precipitation after 10 minutes at different magnifications.

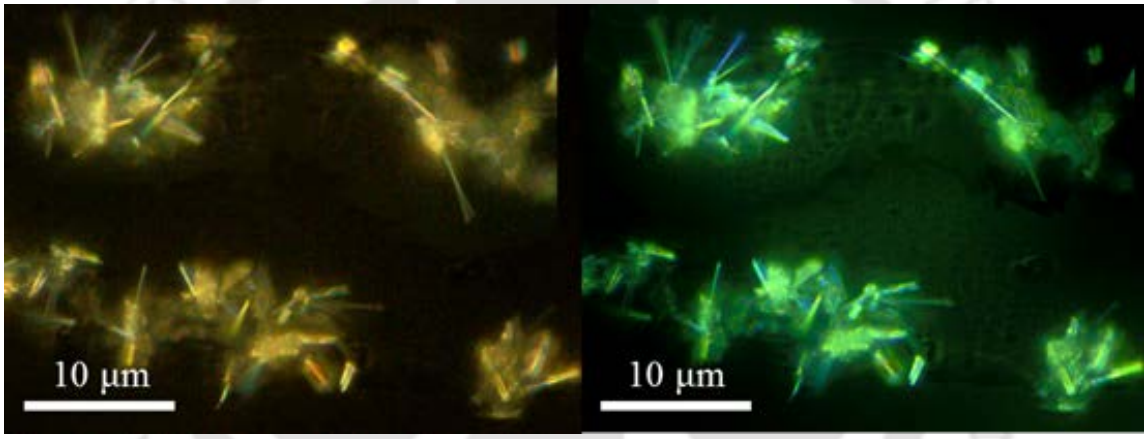

Figure 7.1.7: Fluorescence microscopy images of HPBI after 10 min of re-precipitation observed under white light [left] and excited with UV light (λ_{ex}=350 nm) [right].

After 30 minutes of continuation of the process small structures were formed. But as the time progresses, these structures became more branched and elongated. Along with this more aggregates were formed with aging **[Figure 7.1.8]**. The results were consistent with the spectral changes whose fluorescence intensity was enhanced. Hence these aggregates were responsible for the improved fluorescence and the imaging results also strengthened the spectroscopic analysis.

It is reported that the AIEE process can be used for cell imaging. To evaluate cellular compatibility, in vitro cytotoxicity test of HPBI on HeLa cells was performed using MTT assay. On assessing the mitochondrial activity using MTT assay, treated cells exhibited cell viability percentage similar to untreated group (control) $p < 0.01$. The cell viability test for any material/compound as a function of time is indicative of the cellular compatibility and

appropriateness for in vitro and in vivo applications. The graph shows percent cell viability varying with concentration **[Figure 7.1.9]**. There was a dose-dependent cell growth inhibition effect of the compounds on HeLa cells. However, even at 20 µM of HPBI near 90% cell viability was obtained. An added advantage of using HPBI over other available compounds is its aqueous-based origin unlike to other organic dyes which are present in non-aqueous medium.

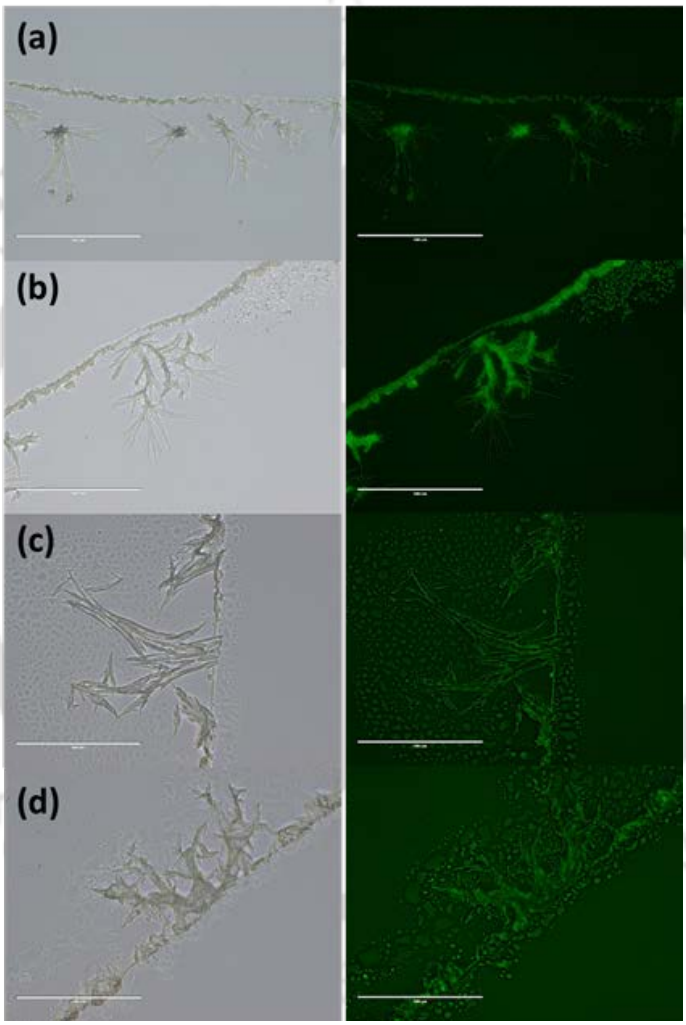

Figure 7.1.8: Time dependent evaluation of aggregate formation of HPBI. Left panel bright field and right panel fluorescence image of aggregates after (a) 30 min (b) 100 min (c) 300 min and (d) 24 hours. Scale bar represent 100 microns.

Bright field images for treated cells showed good cell viability and spindle morphology, suggesting biocompatibility of HPBI. The results suggest that the compound may be utilized as biomedical sensor in future for in vivo applications. Further, the application of these compound for imaging living cells was explored using HeLa cells.

There was no emission from HeLa cells treated with monomers [**Figure 7.1.10]**. On the other hand, the cells glow green when stained with aggregates due to the strong emission from the aggregates of HPBI [**Figure 7.1.10]**.

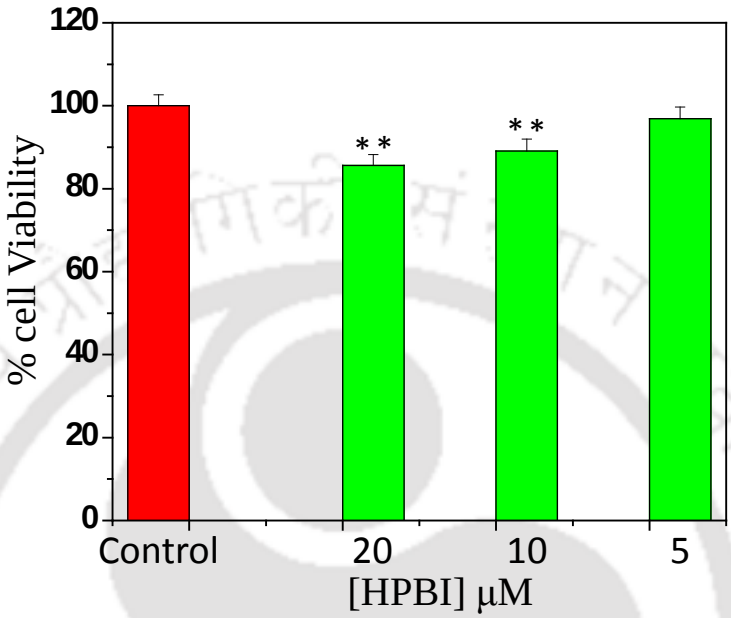

Figure 7.1.9: In vitro cytotoxicity test of HPBI on HeLa cells using MTT assay. Each point represents the mean SD (n = 3). ** show significant differences between control and respective group at $p < 0.01$.

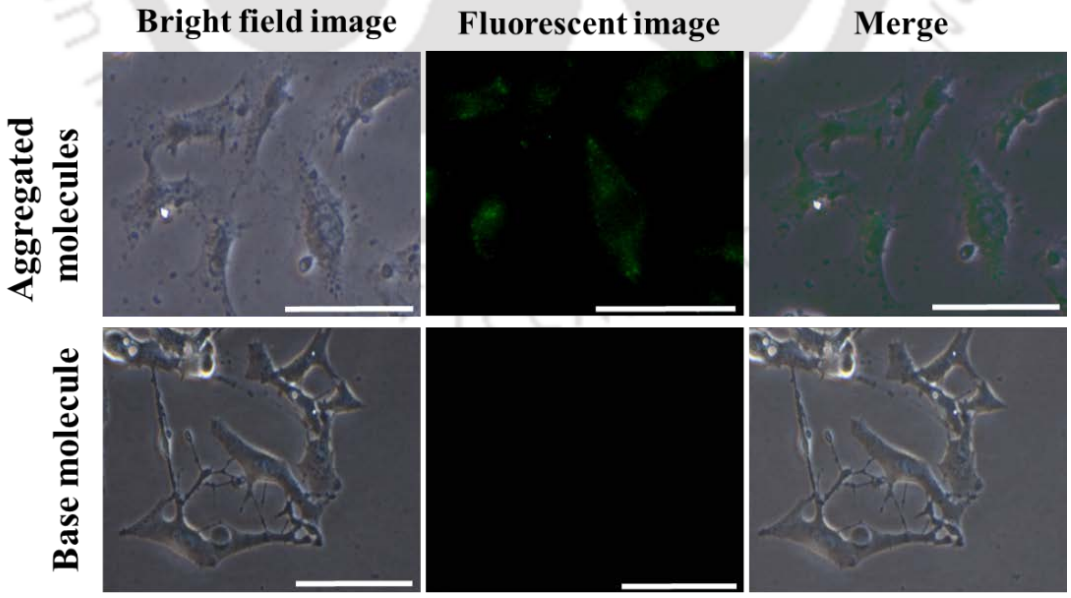

Figure 7.1.10: Representative phase and fluorescent images showing HeLa cells treated with 5 µM aggregates of the HPBI [1st row] and with base molecule [2nd row] (4 hrs.). Scale bar represents 50 microns.

7.1.5. Mechanism of AIEE:

The molecular fluorescence of HPBI rises upon aggregation **[Figure 7.1.2]**. Restricted intramolecular rotation (RIR) process was reported to be responsible for the AIEE process in numerous systems **[312, 313 and 302]**. As the viscosity and temperature strongly perturb the RIR process, the temperature dependent or viscosity dependent studies will substantiate the RIR hypothesis. Temperature effect on the fluorescence characteristics of HPBI was already reported **[316]**. While the fluorescence intensity of the tautomer decrease with increases in temperature in all solvents, the effect of temperature on the fluorescence intensity of the normal emission is solvent dependent. In HPBI and its analogues, it was reported that the torsional rotation of hydroxyphenyl ring and the benzimidazole ring lead to non-radiative relaxation of the excited tautomer via the intramolecular charge transfer state **[283, 284, 326-329]**.

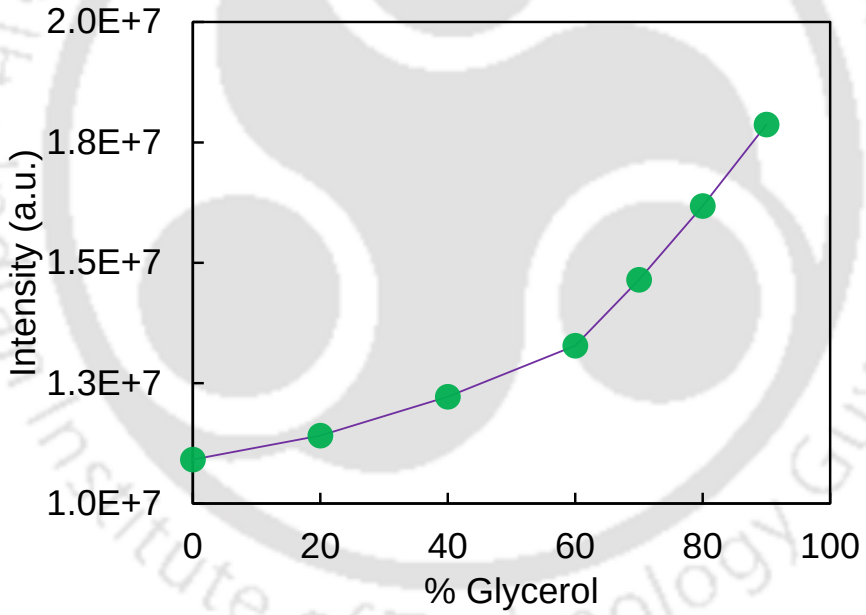

Figure 7.1.11: Plot of emission intensity of HPBI at 465 nm in methanol with the increasing concentration of glycerol (λ_{ex} = 310 nm).

Viscosity of the medium will affect the torsional rotation. Therefore, the fluorescence intensity of HPBI is measured in glycerol-methanol mixture **[Figure 7.1.11]**. The fluorescence intensity of HPBI increases as the viscosity of the medium increases. The fluorescence decay measurements suggested that it is the cis-enols those associated to form molecular aggregates. Upon excitation the cis-enol undergoes ESIPT to form the keto tautomer. The molecule is expected to experience more restriction of the torsional rotation

in the aggregated form than as free monomer. This restriction in rotation will reduce the non-radiative relaxation via ICT state which in turn enhances the radiative emission.

7.1.6. Molecular dynamics simulation:

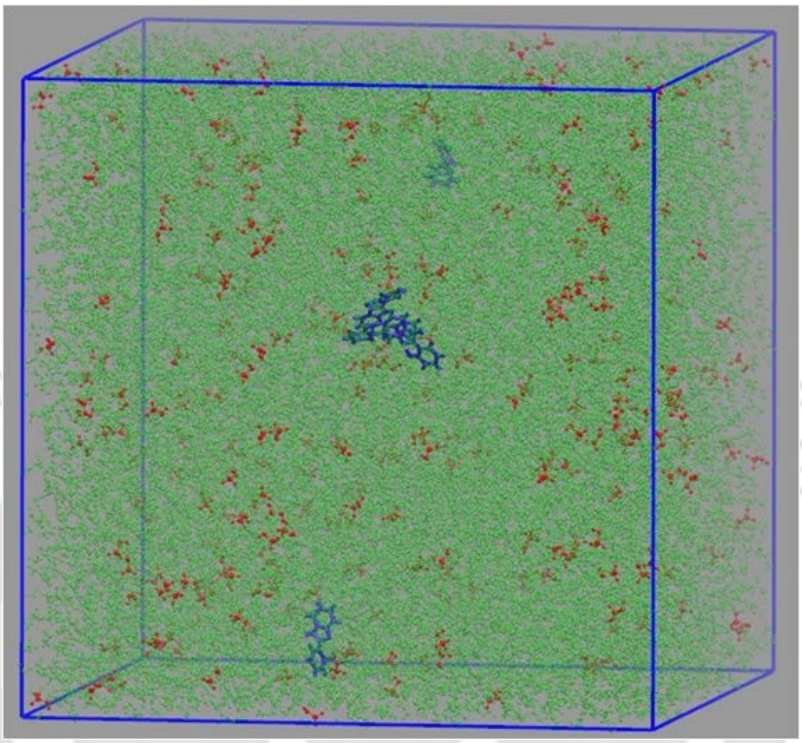

Figure 7.1.12: Snapshot of the simulation box at the end of 4 ns NVT run. Water molecules (green color), methanol molecules (red color), and HPBI molecules (blue).

Molecular simulation technique is a powerful tool to follow the aggregation process. However, such studies were limited **[330]**. Tang et al. preformed simulation of polyacetylenes without solvent molecules and they predicted the formation of aggregates by simulation **[330]**. Here, to comprehend the molecular aggregation of HPBI, simulation was performed with 5 HPBI molecules in methanol-water system and observed that 3 HPBI molecules aggregate to form a cluster **[Figure 7.1.12]**.

Classical molecular dynamics using NAMD **[331]** simulation engine was performed to simulate the aggregation process of HPBI molecules in water-methanol mixture at atomistic level. Initially 5 HPBI molecules were placed randomly in methanol solvent and performed short equilibration run. This system was merged with pre-equilibrated water box and then the overlapping water molecules were removed. The ratio of methanol and water

molecules was maintained carefully as that of experimental condition. Total system (5 HPBI, 267 methanol and 20000 water molecules) consisting of 61750 atoms, was equilibrated in isothermal-isobaric (NPT) ensemble for 2 ns and production run was performed for 5 ns in canonical (NVT) ensemble. All the bonded and non-bonded interactions between the atoms of the present simulation system were described by OPLS (Optimized Potentials for Liquid Simulations) force field [**332]** which is of the form given below

$$E_{total} = \sum_{bonds} K_r \left(r - r_0\right)^2 + \sum_{angles} K_\theta \left(\theta - \theta_0\right)^2 + \sum_{torsoins} \frac{V_n}{2}\left[1 \pm \cos\left(n\phi - \gamma\right)\right] + \sum_{non-bonded}\left[\frac{A_{ij}}{r_{ij}^{12}} - \frac{C_{ij}}{r_{ij}^{6}} + \frac{q_i q_j}{r_{ij}}\right] \quad \text{.....7.1.1}$$

where E_{total} is the total energy of the system. Simple harmonic functions were used to represent bond stretching and angle bending with force constants (K_r, K_θ) and equilibrium bond lengths (r_0) and angles (θ_0). Van der Waals (Vdw) interactions were computed with Lennard-Jones potential with A_{ij} and C_{ij} as the parameters. These parameters between the atoms of different types were obtained as A_{ij} = sqrt($A_{ii}A_{jj}$) and C_{ij}= sqrt($C_{ii}C_{jj}$). Coulomb's law was used for electrostatic interactions as shown above, where q_i and q_j are the partial charges present on the atoms. The simulation box after aggregate formation is shown in **Figure 7.1.12.** Temperature and pressure was maintained at 300 K and 1 atm respectively by Langevin piston Nose-Hoover method **[333, 334].** Particle Mesh Ewald method [**335, 336]** was used for the computation of electrostatic interactions with grid spacing of 1 Å with periodic boundary conditions in all the dimensions. TIP3P model **[337]** was used for water molecule and the bonds involving hydrogen were constrained by settle algorithm. Time step was 1 fs in all the simulations performed. The final equilibrated box length was found to be 85.66 Å. All the visualizations were done using Visual Molecular Dynamics (VMD) [**338].**

To obtain further insight into the aggregation phenomena, one of the HPBI molecule is followed. Here onwards referred as HPBI8, where "8" is its residue number which was far in the beginning from the aggregate of two HPBI molecules [HPBI1, HPBI6], but

reached them in less than 1 ns of simulation time to be in the aggregate and lasts till the end of the simulation run. For analyzing the hydrogen bond formation, the criterion that the distance between the donor and acceptor should be less than 3.0 Å and the donor-hydrogen-acceptor (D-H-A) angle should be less than 20° as mentioned in the hydrogen bond analysis plugin of VMD is used **[338, 328]**. In all the HPBI molecules, the intramolecular hydrogen bond was present between O1 (OH) and N1. Donor-Acceptor pairs between HPBI8 and the rest of the system, from this analysis are summarized in **Table 7.1.2**.

Table 7.1.2: List of possible intermolecular hydrogen bond Donor-Acceptor pairs from VMD analysis. For atoms refer Figure 10 (f).

Donor	**Acceptor**
N2 of HPBI8	O of water
O of water	O1 of HPBI8
O of water	N1 of HPBI8
O1 of HPBI8	O of water
O of water	C1 of HBPI8
O of Methanol	N1 of HPBI8
N2 of HPBI8	**N1 of HPBI6**
N2 of HPBI1	**N1 of HPBI8**
O of Methanol	O1 of HPBI8
O of Water	C2 of HPBI8
O of water	C10 of HPBI8
N2 of HPBI8	**O1 of HPBI6**
O of Water	C3 of HPBI8

In addition to solvent molecules, HPBI form hydrogen bond with other HPBI molecules. These intermolecular hydrogen bonds are through N2 (NH) with N1 and N2 (NH) with O1. Sekiya et al. investigated the crystals of HPBI and reported HPBI in two polymorphs **[326]**. They also showed the N2 (NH) with O1 intermolecular hydrogen bond between HPBI molecules interconnect the HPBI molecules in both the polymorphs. Interestingly neither their crystal structure nor the present simulation of aggregates predict

any intermolecular O1 (OH) and N1 hydrogen bond between HPBI molecules. This advocates that excited state proton transfer of HPBI is an intramolecular process in aggregates/crystals also. The water molecules around HPBI8 were tracked throughout the simulation run and it was observed that there was no water molecules between HPBI8 and other HPBI molecules in the aggregate as shown in **Figure 7.1.13 (e).** This suggest some hydrophobic interactions between the HPBI molecules. The representative orientations of the HPBI molecules in the aggregate are as shown in **Figure 7.1.13 (a), (b), (c), (d).** It is clear from the molecular orientation that the molecules are not in the planar conformation and the individual HPBI molecules embrace twisted conformations. To summarize, molecular dynamics simulation study provides an explanation for aggregation of HPBI molecules in the presence of water-methanol mixture. The hydrophobic induced attraction, in addition to the existence of hydrogen bonds between the atoms of HPBI molecules could be playing an important role in the aggregation process. The twisted conformations of the molecules present in the aggregates precludes the π-π stacking which lead to fluorescence quenching.

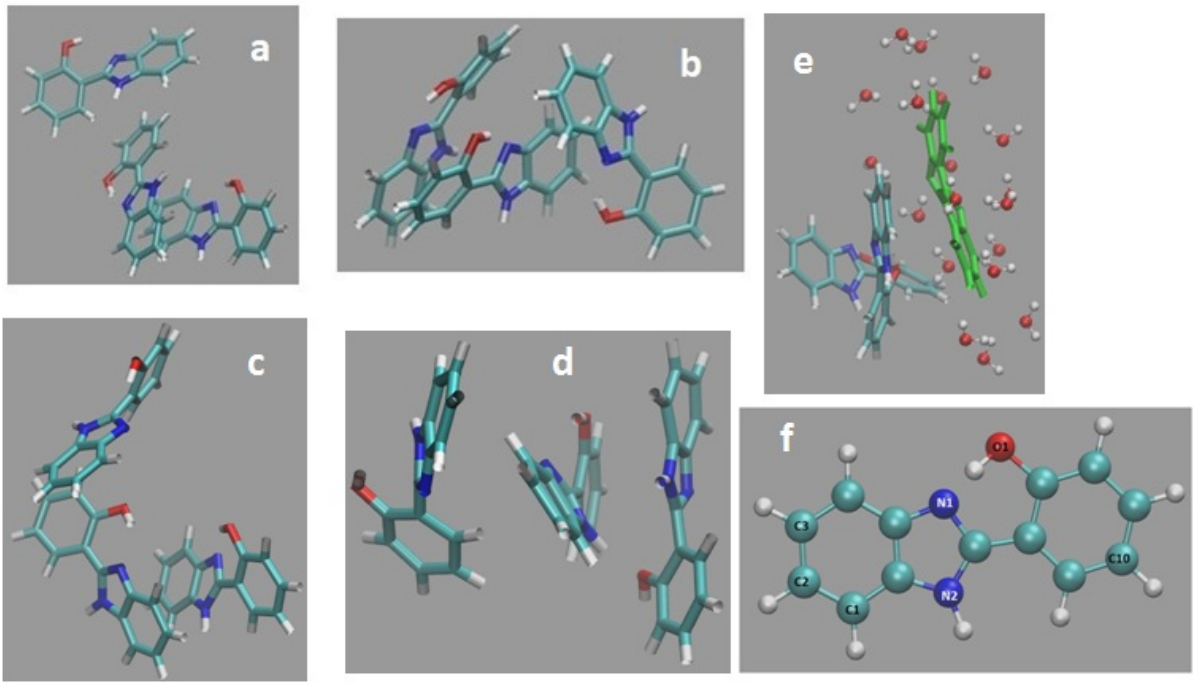

Figure 7.1.13: Orientation of HPBI molecules in aggregates from molecular dynamics simulation at various time steps in the "BONDS" representation of VMD.

7.1.7. Conclusion:

HPBI is an AIEE active fluorophore and shows enhanced emission upon aggregation. The enhancement was found to be 4 times compared to that in water. The fluorescence lifetime of the HPBI also increases upon aggregation. The restricted intramolecular rotation of the single bond resulted in highly intensified emission from aggregates. Comparative study with PBI suggests that the hydroxyl group is crucial for AIEE from HPBI. The aggregated structures were measured to be few hundred nm diameter and few μM long. The permeability of the aggregated structures inside the HeLa cells was also studied. These aggregations make HPBI as effective system for cell straining as the monomeric compounds were failed to give any visible fluorescence inside the cells. The whole system is in water which is another positive and bio-friendly aspect of this study. Simulation studies indicate the formation of aggregates. It suggests that both hydrophobic interaction and hydrogen bonding play the roles in the aggregation. It also reveals that HPBIs exhibit twisted conformation in the aggregated structure thereby they avert the π-π stacking.

7.2. Effect of nitrogen substitution of aggregation:

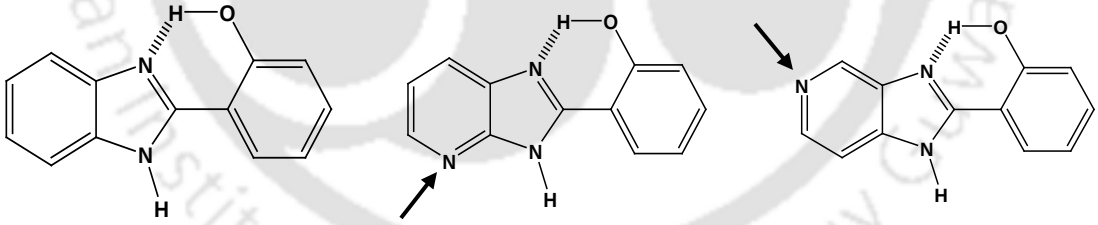

Chart 7.2.1. Structure of HPBI, HPIP-b and HPIP-c.

Previous section described how intermolecular hydrogen bonding and hydrophobic interactions between the molecules lead to the formation of highly emissive aggregates of HPBI. Nitrogen substitution in the benzene ring significantly affects the characteristics of HPIP-b and HPIP-c **[Chart 7.2.1] [339, 286, 287]**. A comparative theoretical study of nitrogen substitution in the benzene ring of HPBI revealed that the quantum yield of tautomer emission decreases with nitrogen substitution. The excited state lifetimes also strongly depend on the presence of nitrogen. The substitution of N-heteroatom in the

benzene ring also brought changes in the responses of dye towards environmental factors like temperature **[284]**, ions **[288]**, micro-heterogeneous medium like β-CD **[218]**, micelle, BSA **[102]** etc. With rise in temperature, the population of cis-enol of HPBI decreases and the nonradiative decay of tautomer increases **[284]**. Nitrogen substitution in the benzene ring increases the nonradiative deactivation to the ground state. Nitrogen substitution changes the response of the fluorophores towards Cu^{2+} ion. The 140 folds increase in intensity ratio of HPBI decreased to 2-3 folds upon pyridyl nitrogen substitution **[288]**. The pyridyl nitrogen substituted molecules showed more affinity towards β-CD compared to HPBI **[218]**. All the three molecules donate the proton to DMSO to form monoanion. The presence of extra nitrogen stabilizes the monoanion of HPIP-b and HPIP-c and makes them more sensitive to environment than HPBI. HPBI and HPIP-c bind in the hydrophobic site of BSA **[102]**. On the other hand, HPIP-b binds at the hydrophilic site of BSA. Though both HPBI and HPIP-c bind at hydrophobic sites, their binding pockets and interaction with BSA are different. Therefore, the aggregation of HPIP-b and HPIP-c is investigated. The biocompatibility and utility of all the fluorophores as aggregates within cells are discussed in this chapter.

7.2.1. Absorption characteristics:

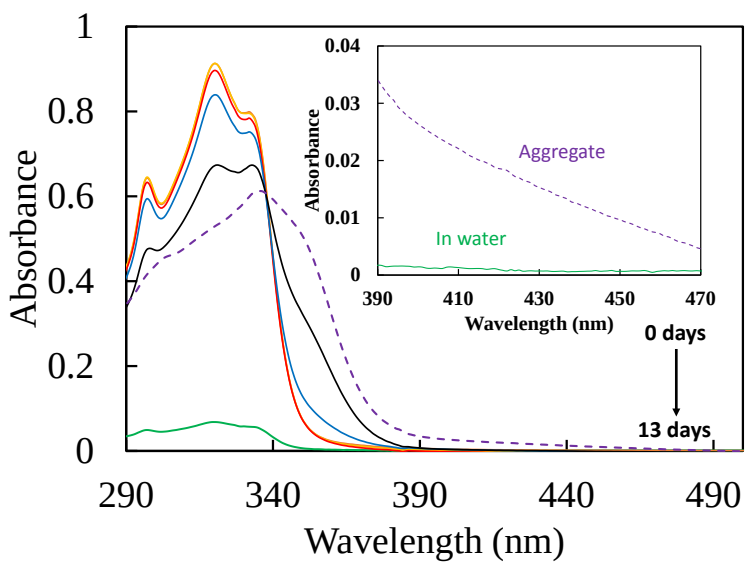

Figure 7.2.1: Absorption spectra of HPIP-b in water (green line) and of reprecipitate mixture (dotted line) after 13 days. Inset shows the expanded spectra of HPBI in water and aggregated mixture in the 350 nm-450 nm region.

Alike HPBI, the pyridoimidazoles also experienced increase in the absorbance for the re-precipitation mixture initially **[Figure 7.2.1 and 7.2.2].** The instant increase in absorbance was due to presence of methanol rich environment as explained in earlier section. With increase in time, it started decreasing with a bathochromic shift. The long tailing due to Mie scattering was also observed. The absorption spectra of HPIP-b and HPIP-c are red shifted by 16 nm and 2 nm, respectively. The absorption spectra of the aggregated structures became less structured. The decreased absorbance, less structured absorption band and scattering in the longer wavelength indicated the formation of particles through aggregation. But from the absorbance point of view, the decrease in absorbance for HPIP-c with time is 1.3 fold whereas for HPIP-b, the absorbance decreases by 2 fold. Compared to these nitrogen substituted analogous, HPBI undergoes more decrease (3 fold) in absorbance. This gives clear indication that N substitution of HPBI has effect on the aggregate formation.

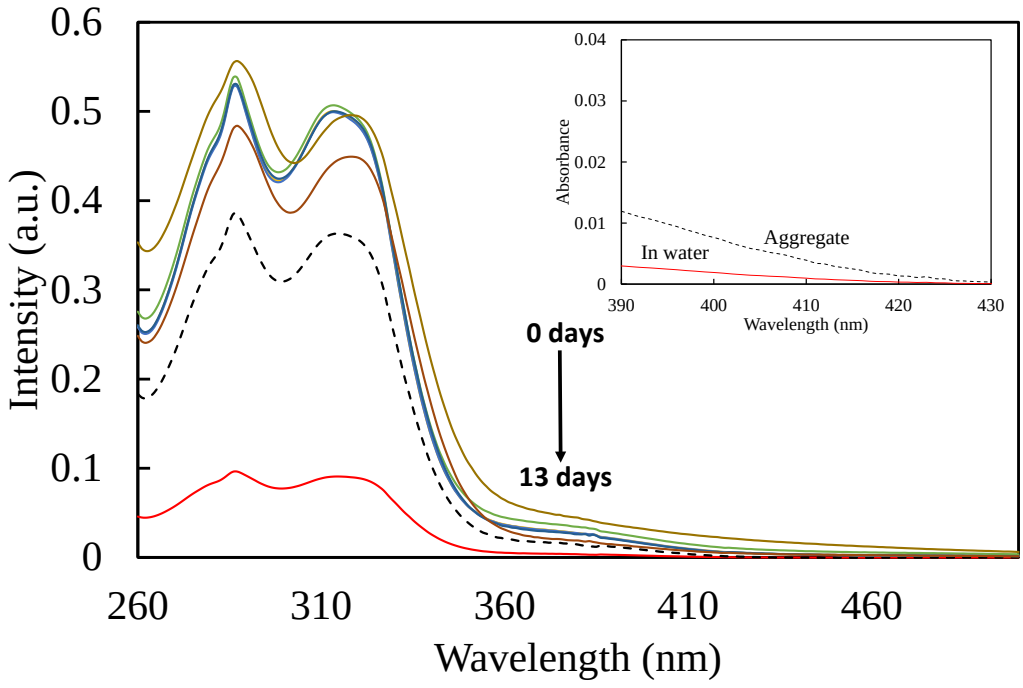

Figure 7.2.2: Absorption spectra of HPIP-c in water (Red line) and of reprecipitate mixture (dotted line) after 13 days. Inset shows the expanded spectra of HPBI in water and aggregated mixture in the 400 nm-450 nm region.

7.2.2. Fluorescence characteristics:

Both HPIP-b and HPIP-c have weak emission in aqueous medium. Upon aggregation, the fluorescence of both fluorophores have impressive enhancement. From the **Figures 7.2.3 and 7.2.4**, it is obvious that aggregation of the fluorophores led to the enhancement in the emission intensity. The enhancement varies depending on the position of the substitution. The ratio of the tautomer emission to normal emission of HPIP-b was 2.5 and 1.04 in the monomeric and aggregated states. The same of HPIP-c is 5.0 and 3.33 in the monomeric and aggregated states. In contrast, ratio of the tautomer emission to normal emission increases upon aggregation of HPBI (2.6 to 3.1). Alike to absorbance, this shows the effect of pyridyl nitrogen substitution.

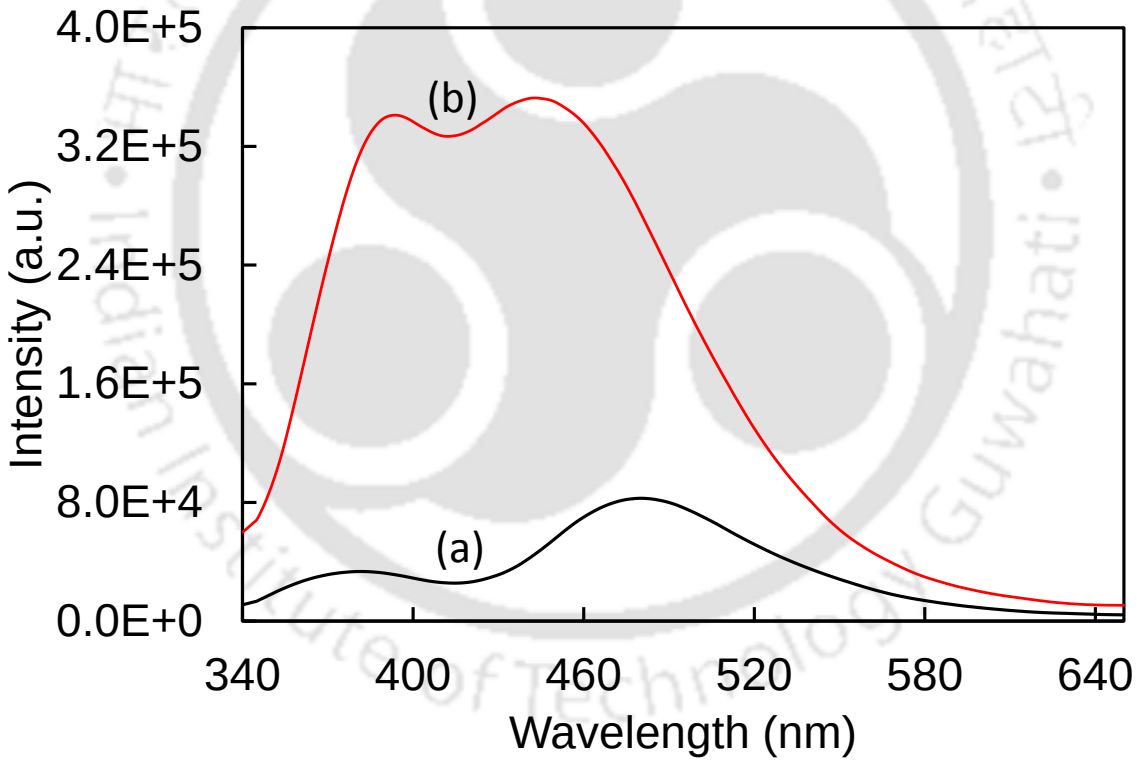

Figure 7.2.3: Fluorescence spectra of HPIP-b in (a) water and (b) 2% v/v water methanol re-precipitation mixture. (λ_{exc} = 320 nm)

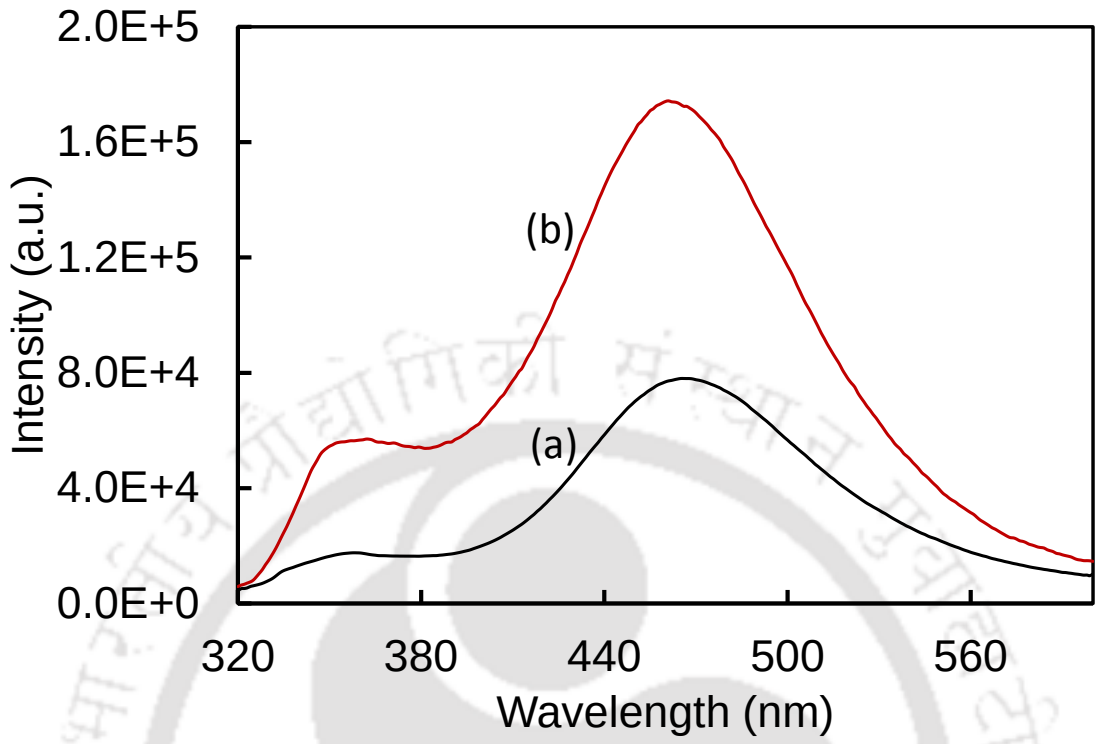

Figure 7.2.4: Fluorescence spectra of HPIP-c in (a) water and (b) 2% v/v water methanol re-precipitation mixture. (λ_{exc} = 310 nm)

7.2.3. Lifetime analysis:

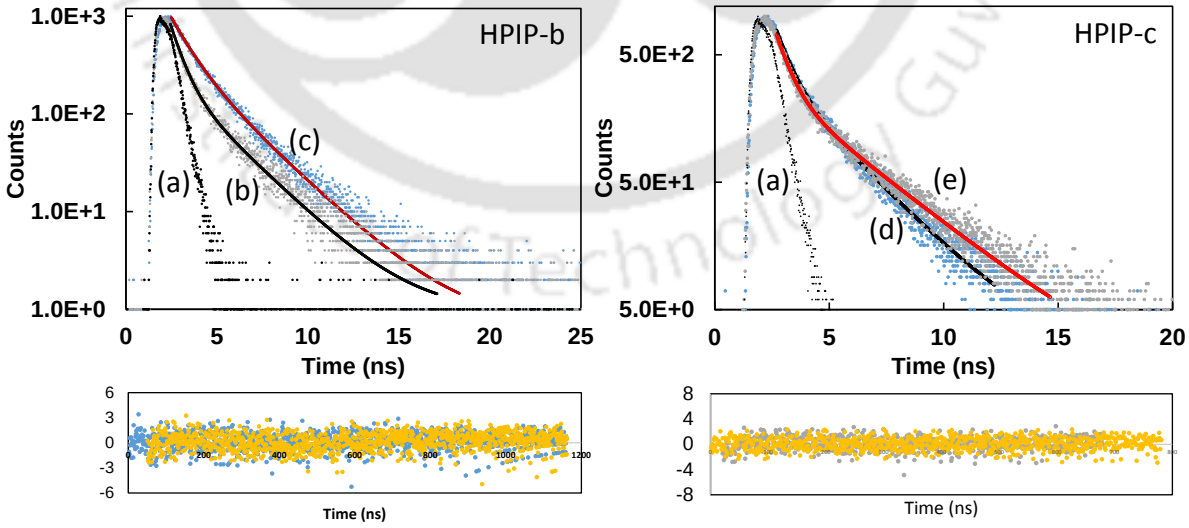

Figure 7.2.5: Fluorescence decay of normal emission of HPIP-b (b) in water, (c) in reprecipitate solution and HPIP-c (d) in water, (e) reprecipitate solution, (a) is the instruments response function with residuals.

Table 7.2.1. Fluorescence lifetime of the monomer and the aggregates of HPIP-b and HPIP-c.

Fluorophore		τ_N	τ_T	χ^2	Relative Enhancement in lifetime with respect to monomer	
					τ_N	τ_T
HPIP-b	Aggregate	0.92 (36.24)	2.51 (63.76)	1.0	51 %	4 %
	Monomer	0.61 (42.46)	2.41 (57.54)	1.0		
HPIP-c	Aggregate	0.62 (27.83)	3.06 (72.17)	1.1	5 %	23 %
	Monomer	0.59 (26.6)	2.48 (73.4)	1.0		

The lifetimes of monomer and the aggregates of HPIP-b and HPIP-c are summarized in the **Table 7.2.1**. Unlike that of HPBI, the fluorescence lifetime of both the emissions increases upon aggregation **[Figure 7.2.5]**. Hence, not only the cis enols but the Trans enols are also present in the aggregates. But the relative enhancement in lifetime is much higher in the normal emission of HPIP-b whereas that of tautomer is little. The reverse is true for HPIP-c. It is clear that like in TICT here too the presence and the position of the pyridyl nitrogen plays a significant role.

7.2.4. Morphology:

Fluorescence microscopic images showed that the aggregates emit strong fluorescence upon excitation with 350 nm light **[Figure 7.2.6]**. HPIP-b aggregated to form long needle type structures which showed green fluorescence. These needles are appeared to be originating from one center. Unlike to HPIP-b for another nitrogenous analogue HPIP-c, small rods were formed and emits green color.

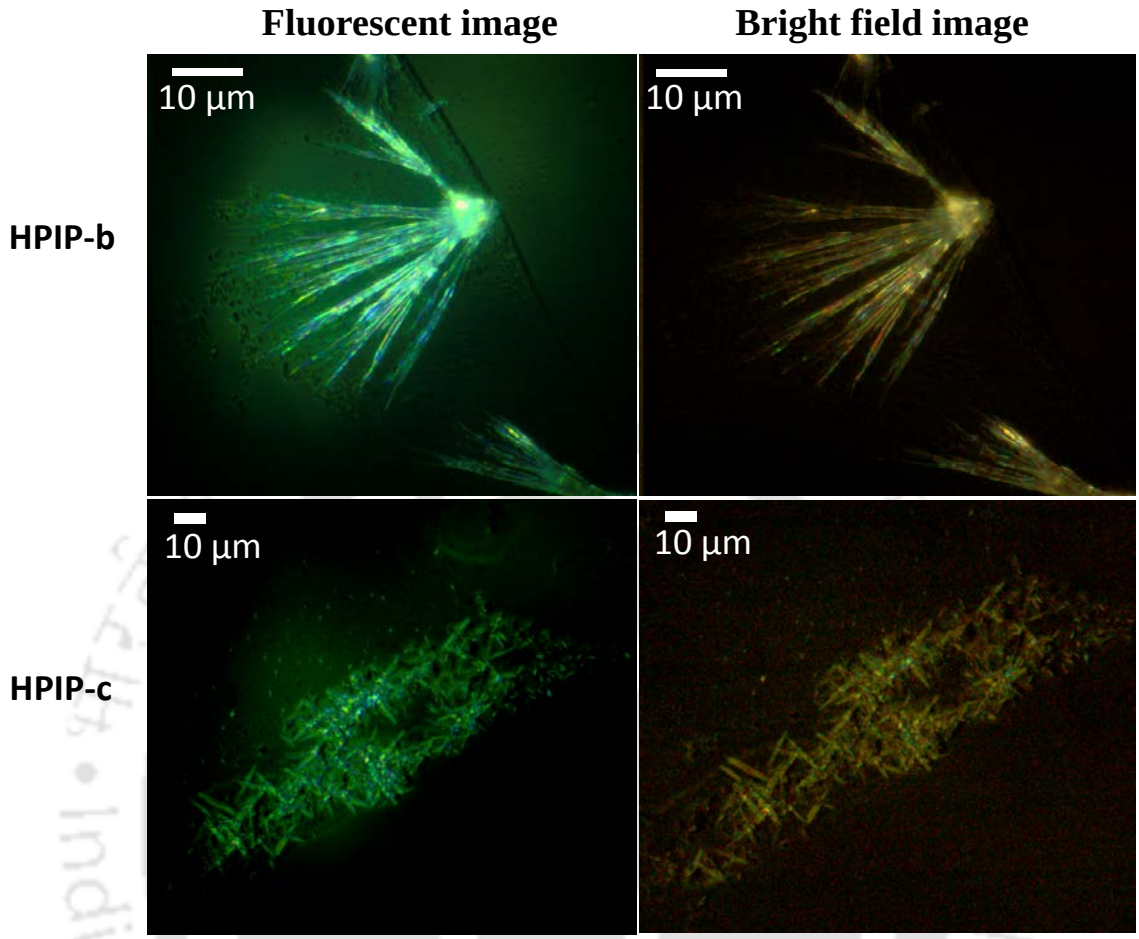

Figure 7.2.6: Fluorescence microscopy images of HPIP-b and HPIP-c after 10 min of re-precipitation observed under white light [right] and excited with UV light (λ_{ex}=350 nm) [left].

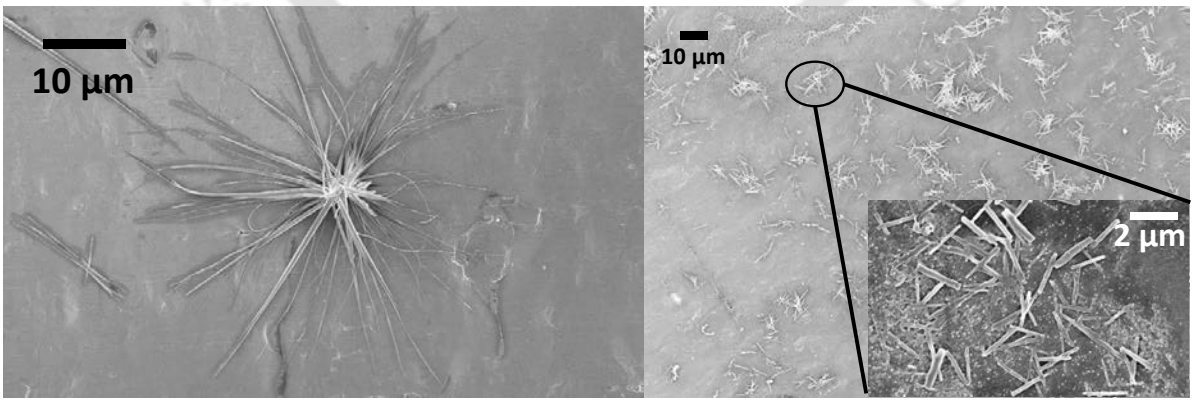

Figure 7.2.7: FESEM images of the samples made from aqueous suspensions of HPIP-b (left side) and HPIP-c (right side) after re-precipitation in water with 2% v/v methanol after 24 hours.

To understand the morphology of the aggregates, the re-precipitation mixtures are characterized by FESEM. **Figure 7.2.7** demonstrates the shape and size of the aggregates prepared from these two fluorophores. For HPIP-b, long niddle type structures were obtained which measures around 20 μM in length and 400 nm in diameter. These structures are seemed to be originating from the same center. But the other pyridine analogue, HPIP-c upon aggregation forms rod shaped structures. These rods were 4 μM in length and 300 nm in diameter. Unlike to HPIP-b, these nano rods did not originate from the same center and are scattered. On the other hand, HPBI forms small spindle shaped structures **[Figure 7.1.4]**. The nitrogen substitution changes the size and shape of the aggregated structures. The morphological difference between the aggregates of HPIP-b and HPIP-c empathized that the position of nitrogen can change the shape of the aggregation.

7.2.5. Cell Culture and Imaging:

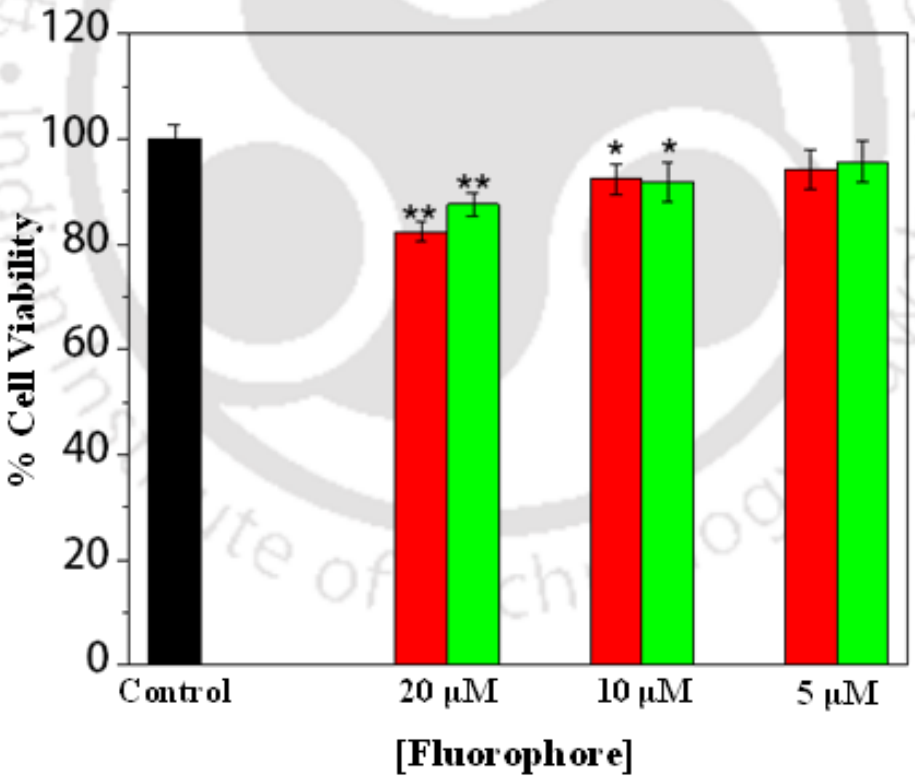

Figure 7.2.8: In vitro cytotoxicity test of compounds on HeLa cells using MTT assay. Each point represents the mean ± SD (n = 3). ** and * show significant differences between control and respective group at $p < 0.01$ and $p < 0.05$, respectively.

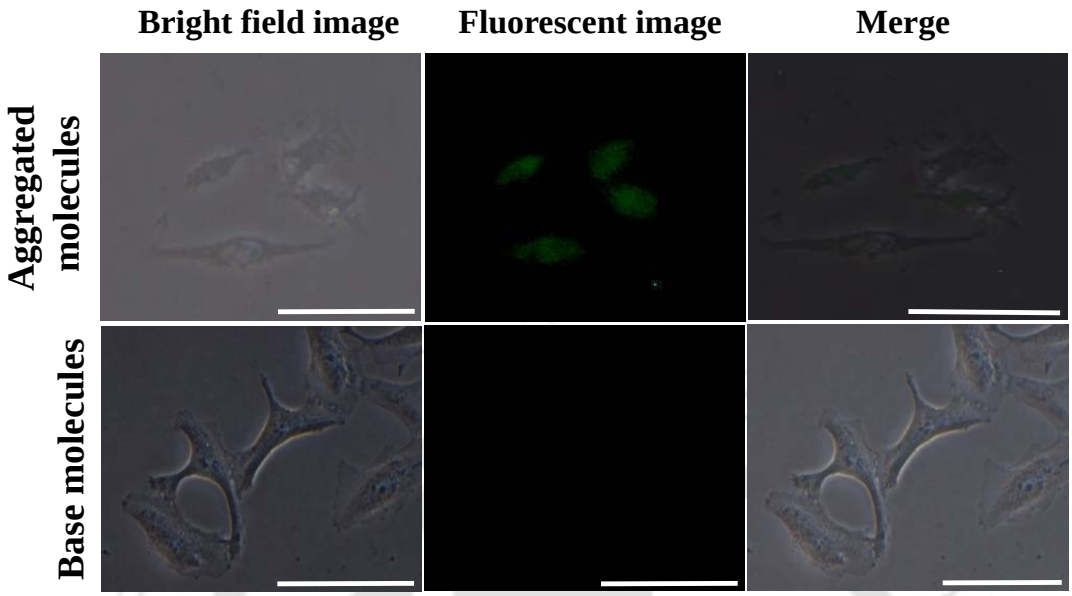

Figure 7.2.9: Representative phase and fluorescent images showing HeLa cells treated with 5 μM aggregates of the HPIP-b (4 hrs). Scale bar represents 50 microns.

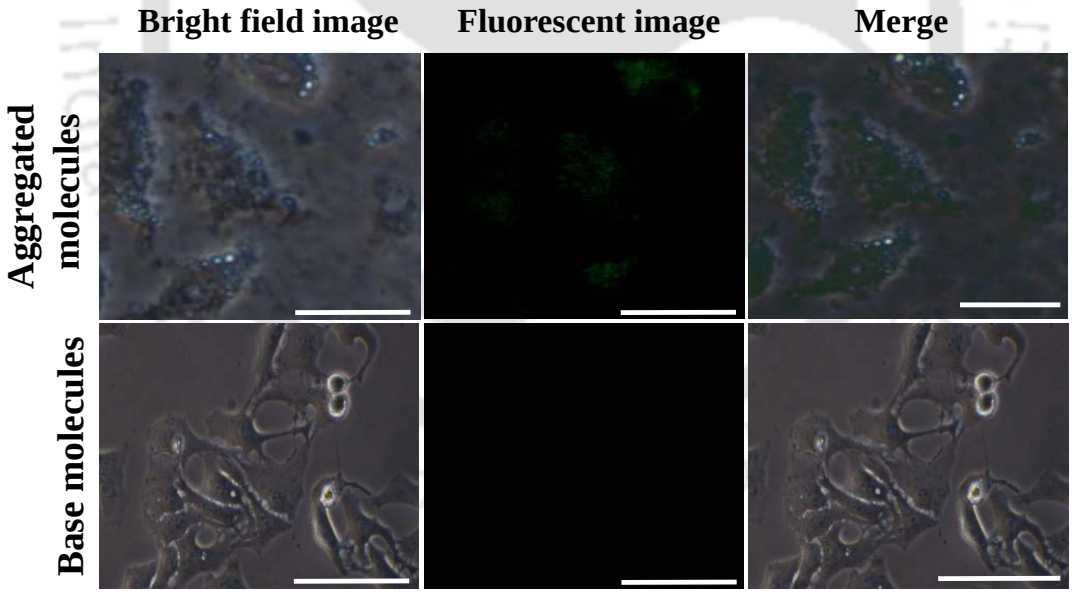

Figure 7.2.10: Representative phase and fluorescent images showing HeLa cells treated with 5 μM aggregates of the HPIP-c (4 hrs.). Scale bar represents 50 microns.

The application of the fluorophores for imaging living cells was explored using HeLa cells. Cytotoxicity study was done for the fluorophores at different concentrations. At 20 μM fluorophore concentration more than 80% cell viability was obtained **[Figure 7.2.8]**.

82 % and 87 % viability was observed with HPIP-b and HPIP-c, respectively. Bright field images for treated cells showed good cell viability and spindle morphology suggests biocompatibility of the compounds. The results suggest that like HPBI, these compounds may be utilized for biomedical sensors in future for in vivo applications. There was no emission from HeLa cells treated with base compounds and fluorescence was obtained from the aggregated molecules **[Figure 7.2.9 and Figure 7.2.10]**.

7.2.6 Molecular Dynamics Simulation study:

To understand the aggregation process of HPIP-b and HPIP-c molecules in water and methanol mixture, classical atomistic molecular dynamics simulations with all atom OPLS force-filed [**340**] was performed. All the simulations were performed with NAMD package [**331**]. Initial configurations were generated with the help of Packmol **[316, 341**] and Topo Tools plugin in VMD [**338**]. The orientations of the HPIP molecules were also random in the initial configuration. The SETTLE algorithm **[342**] was used to keep water molecules rigid. Electrostatic interactions were treated using particle-mesh Ewald (PME) summation method [**343, 344**], which is commonly used for computing long-range electrostatic interactions for periodic systems in the field of computational chemistry. In the present simulations, PME grid spacing of 1.0 Å and PME direct space tolerance of 1.0×10^{-6} w used. Lennard-Jones potential was used for van der Waals interactions, which are truncated smoothly at a cut-off distance of 12 Å using a switching function. The simulated system consisted of 5 HPIP, 30000 water and 267 methanol molecules, making a total of 91727 atoms as shown in **Figure 7.2.11c**. A periodic boundary condition was applied in all three directions. Temperature was maintained at 300 K by using Langevin dynamics with a damping coefficient of 5/ps. Pressure was maintained at 1.03125 bar using Langevin piston Nose-Hoover method [**332, 333**], where piston period was 200 fs and damping time scale was 100 fs. Equations of motion were integrated with the velocity-Verlet [**345**] algorithm with a time step of 1 fs. Simulation protocol involves a short equilibration run in NPT (1 atm, 300 K) ensemble, where the positions of HPIP molecules were constrained and 10 ns NVT run where HPIP molecules were free to move in the simulation box.

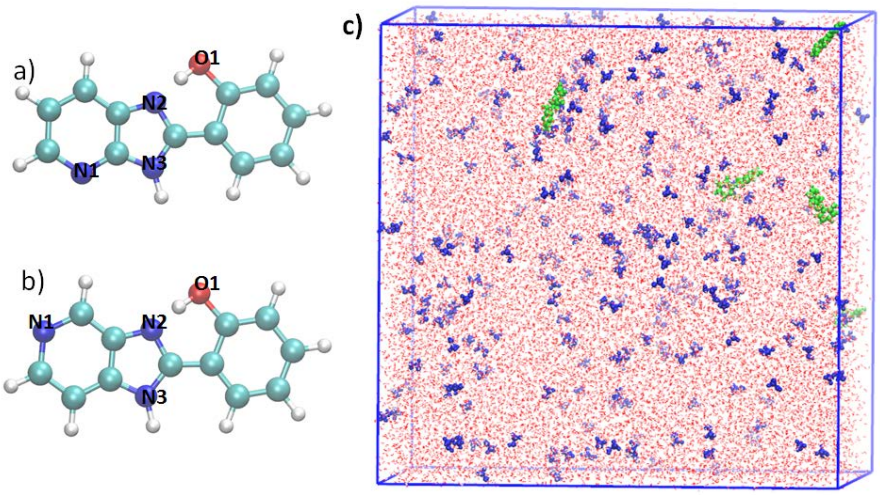

Figure 7.2.11: Chemical structures of HPIP-b (a) and HPIP-c (b) with atom labels. Simulation snapshot (c), Color code: Methanol (blue), HPIP-b (green) and water (red).

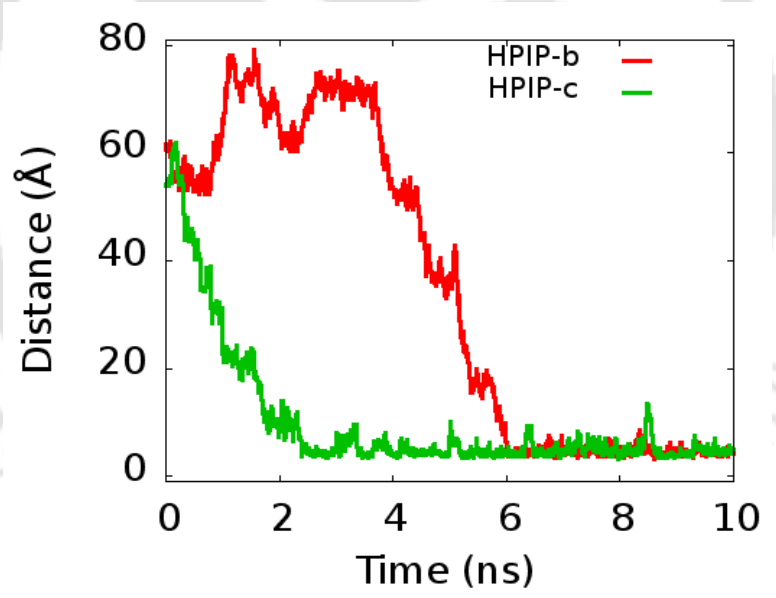

Figure 7.2.12: Distance between two HPIP molecules as a function of simulation time.

Initially two HPIP molecules which were at very large distance (close to 60 Å) and prior to set their direction of movement towards each other, the distance between them fluctuated randomly (roughly 4 ns for HPIP-b and 0.2 ns for HPIP-c). Since their distance was greater than 12 Å, which is cut-off for Van der Waals interactions, only collisions with water molecules might have played a role in setting the direction of movement of HPIP

molecules. The average center-center distance of two HPIP molecules was 4.65 Å (HPIP-b) and 4.82 Å (HPIP-c) in the aggregated state as shown in **Figure 7.2.12**.

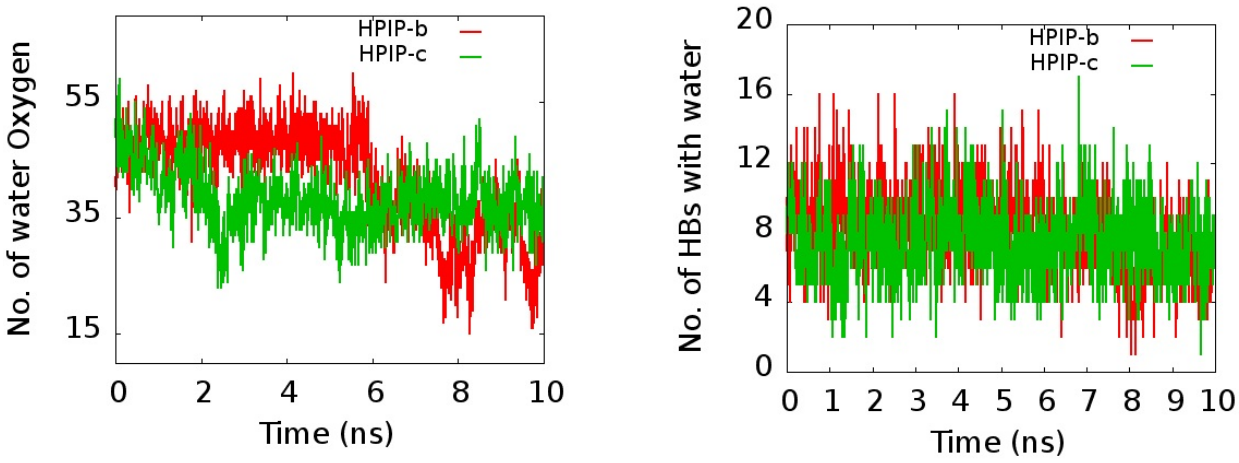

Figure 7.2.13: Number of water molecules around HPIP molecules and hydrogen bonds with water.

The number of water molecules within a distance of 3.5 Å from the two HPIP molecules which forms an aggregate as a function of simulation time was analyzed. The average number of water molecules is 48 (before aggregation) and 33 (after aggregation) for HPIP-b and it is 44 (before aggregation) and 37 (after aggregation) for HPIP-c **[Figure 7.2.13]**. In addition to number of water molecules, the number of hydrogen bonds between water and HPIP molecules was computed. Hydrogen bond is expected to be present between an atom with a basic lone pair of electrons and a hydrogen atom covalently bound to an electronegative atom. The main donor-acceptor pairs for possible hydrogen bond formation (between water and HPIP molecules) will be oxygen atom of water, nitrogen and oxygen atoms of HPIP molecules. H bonds plugin in VMD was used [**338**] to compute hydrogen bond statistics. The criterion we have chosen for hydrogen bond formation is that donor-acceptor distance should be less than 3.5 Å and D-H-A angle should be less than 30 degrees. The mean number of hydrogen bonds is 9 (before aggregation) and 7 (after aggregation) for HPIP-b, whereas this number was 7 for HPIP-c molecules prior to and after aggregate formation **[Figure 7.2.13]**. This suggests that water molecules were squeezed out between two molecules as they approach each other to form an aggregate.

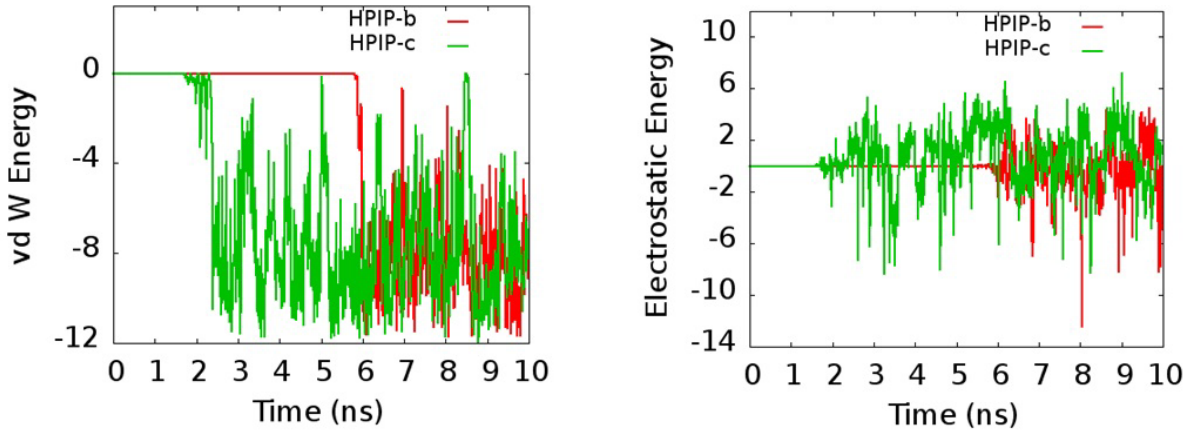

Figure 7.2.14: L-J potential energy and electrostatic potential energy between HPIP molecules.

Electrostatic potential energy was observed to be slightly lower than the L-J potential energy, Vdw attraction (since vdW potential is negative) could be more important than electrostatic interaction in the aggregation process. Moreover electrostatic potential energy is alternating between positive and negative values as shown in **Figure 7.2.14**. Though PME summation method was used to compute long-range electrostatic interactions, in the above plot **[Figure 7.2.14**], short-range Columbic interactions was plotted to make a comparison between vdW and electrostatic potentials.

Hydrogen bond is expected to be present between an atom with a basic lone pair of electrons and a hydrogen atom covalently bound to an electronegative atom. These electronegative atoms in HPIP molecules are Nitrogen and Oxygen. Hence the distances between possible donor-acceptor pairs as a function of simulation time was plotted [**Figure 7.2.15.]** If N1-O1 distance between two HPIP-b molecules was considered, it varies between 2.9 Å to 11.2 Å. Normally if the criterion stated above (D-A distance 3.5 Å and D-H-A angle less than 30 degrees) is satisfied, it is considered as a strong hydrogen bond formation. However in the present analysis of aggregation of HPIP molecules, based on N – O distances and D-H-A angle, we can infer that weak hydrogen bonded interactions exist between HPIP molecules. Moreover the N-O distance follows the same trend as center –center distance of HPIP molecules, hence we can understand that N and O atoms may not be the ones which contact first.

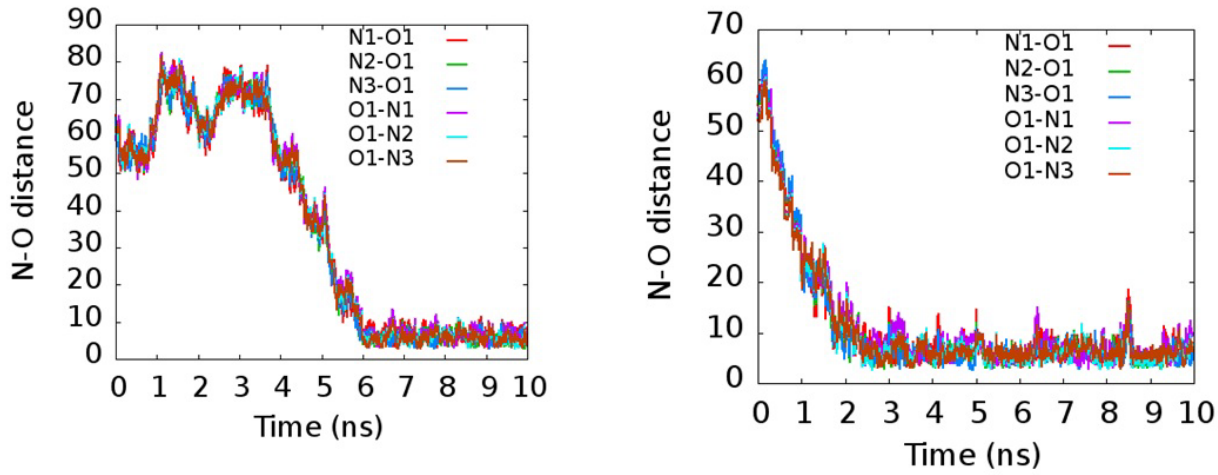

Figure 7.2.15**:** Distance between Nitrogen atoms of one HPIP and oxygen atom of other HPIP molecule, which formed an aggregate.

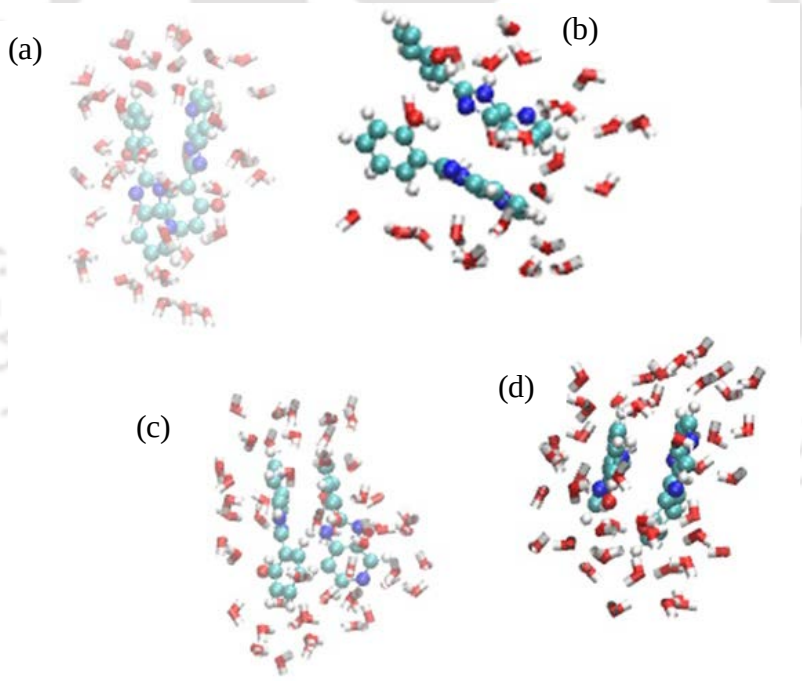

Figure 7.2.16: Representative orientations of two HPIP molecules in the state of aggregation. (a-b) for HPIP-b and (c-d) for HPIP-c.

Orientation of HPIP molecules in the aggregate is dynamic in nature, there is a twist of phenyl ring, but not 90 degree rotation about the imidazole ring, which is also needed AIEE **[66]**. From **Figure 7.2.16**, water molecules were not present between HPIP molecules in the aggregated state.

To summarize, molecular dynamics study explains that vdW attraction, weak hydrogen bond between HPIP molecules could be the reason for aggregate formation. Rate of aggregation is faster in HPIP-c compared to HPIP-b, which could be attributed to hydrophobic nature of HPIP-c compared to HPIP-b. This also can be verified by dipole moment calculations [**283**].

7.2.7. Conclusion:

Alike to HPBI, the pyridoimidazoles molecules are also AIEE active. The nitrogen substitution of HPBI changes the size and shape of the aggregated structures. The pyridoimidazoles demonstrated aggregated structures different from that of HPBI. HPIP-b showed long needles having a length of 20 μM whereas HPIP-c aggregated to form small rods of 4 μM long during re-precipitation process. The position of nitrogen atom also laid an impact as both the nitrogen substituted analogous aggregated in different sizes and shapes. Alike to HPBI, these pyridoimidazoles also succeeded in cytotoxicity test and showed good cell viability at 20 μM concentrations. HPIP-b and HPIP-c showed 82% and 87% cell viability respectively. The aggregated structures showed emission within cell whereas the monomers failed to show any fluorescence. Molecular dynamics simulation study demonstrated that aggregation is due to van der Waals and also weak hydrogen bonded interactions.

Chapter 8

Summery and Scope of the future work

8.1. Summary:

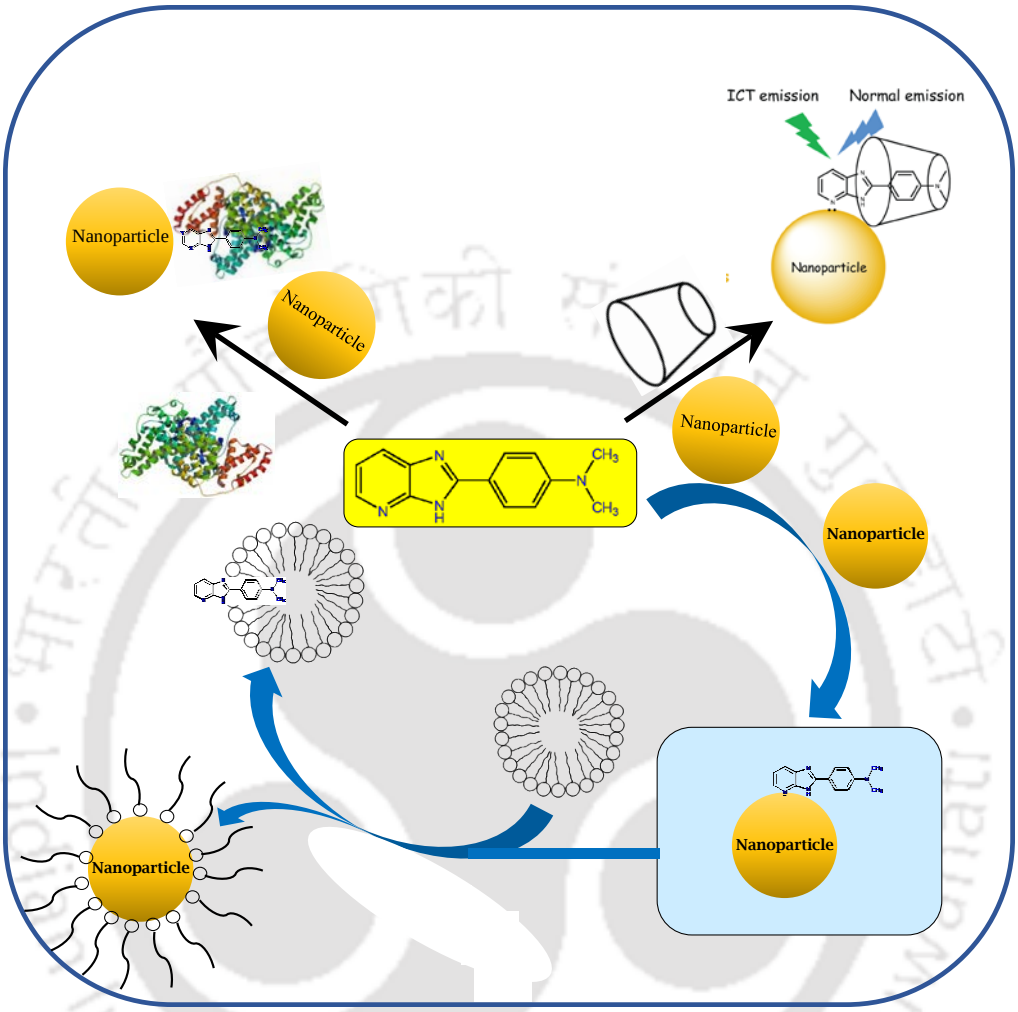

The photophysical behavior of ICT and ESIPT fluorophores were investigated in different heterogeneous environments. The ICT molecules, DMAPBI and its nitrogenous analogous showed strong affinity for the silver nanoparticles in non-aqueous solvent and also stabilized the nanoparticles. DMAPIP-b stabilizes the nanoparticles most followed by DMAPIP-c and DMAPBI. The nanoparticles quench the fluorescence of all the fluorophores. The charge transfer from DMAPIPs to the nanoparticles induce dual emission. The TICT emission was enhanced by confined environment. The complexation with β-CD decreases the nonradiative rate and enhances the fluorescence. The ternary composite was formed by the encapsulation of the dimethylaminophenyl group inside the β-CD nanocavity. The TICT emission was enhanced in the ternary composite. The observation of dual emission in DMAPIPs shows that they interact with the nanoparticles through pyridyl

nitrogen. In the absence of pyridyl nitrogen, DMAPBI interacts with the nanoparticle through the imidazole nitrogen.

Alike in DMF, all three fluorophores interact with silver nanoparticles prepared in water through the ring nitrogen. Static quenching was observed for all the fluorophores. The micelles were found to be well efficient to extract the fluorophores from the nanoparticle's surface into their hydrophobic cavities. CTAB is more efficient than TX-100 in the extraction process.

The effect of the nanoparticles on the fluorophores confined within hydrophobic cavity of BSA were also experimented. All three molecules interact with BSA and resides inside the hydrophobic cavity. The addition of silver nanoparticles to these systems induces some conformational changes in the tertiary structure of the protein. This led to exposure of the fluorophore to the nanoparticles surface. This fluorophore nanoparticle interaction led to the decrease in the emission intensity of all fluorophores.. Compared to DMAPIP-b, DMAPIP-c remained deeper inside BSA which allows less accessibility to the nanoparticles surface. Hence the quenching in DMAPIP-c is less compared to that in DMAPIP-b. However, the fluorescence quenching on the BSA bound fluorophore is less compared to free fluorophore in water. This may be due to the rigid environment of the fluorophore inside BSA compared to that in free water. After the conformational change the tryptophan residues moved to a hydrophobic environment in its native state

Following the ICT molecules, the interaction of ESIPT fluorophores, HPBI and its nitrogenous analogous with nanoparticles were investigated. As earlier, the interaction is more efficient in the pyridyl nitrogen substituted analogues HPIP-b and HPIP-c than HPBI. This efficiency primarily lies in the presence of pyridine nitrogen which proved to be the most preferable site of interaction for nanoparticles. Nanoparticles hampers the ESIPT process by withdrawing the electron density which affect the intensity ratio of normal to tautomer band. Unstable silver nanoparticles were found to be stable in solution in presence of these fluorophores. In this context, the nitrogen substituted analogues are one step ahead of HPBI in terms of stability of the silver nanoparticles owing to the presence of the pyridine nitrogen.

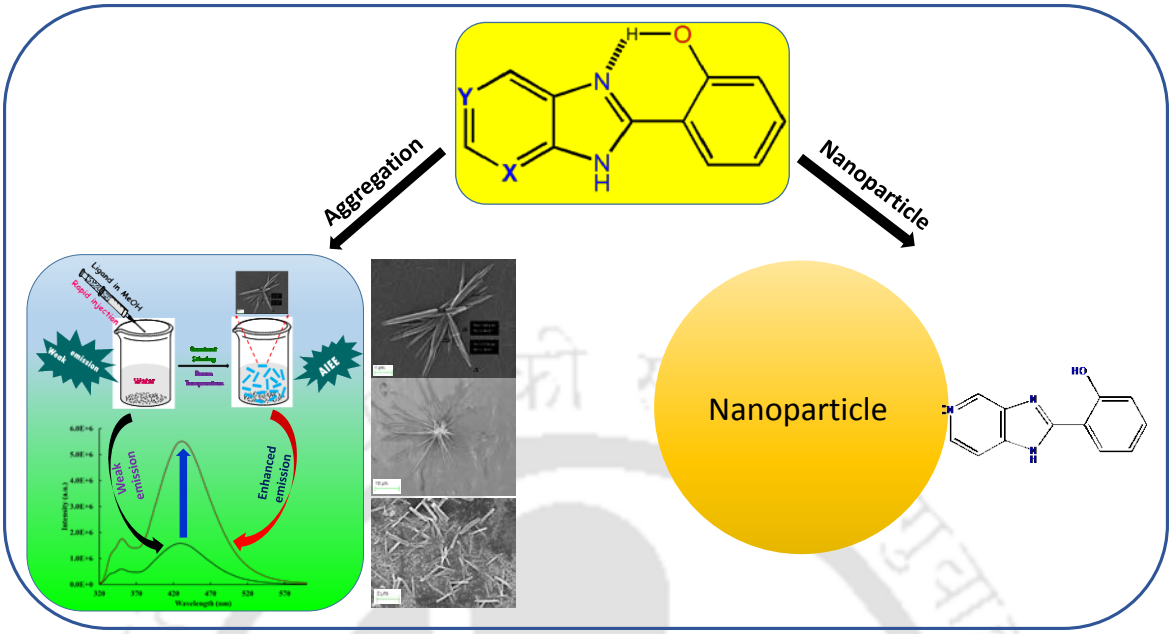

In the end the effect of aggregation of ESIPT molecules were studied. The studies reveal that AIEE is observed in all three molecules. HPBI aggregated to form spindle shaped structure. The nitrogen substitution in the benzene ring affected the size and shape of the aggregated structures. HPIP-b aggregated to form long needles, whereas HPIP-c aggregated to form small rods during re-precipitation process. The restriction in intramolecular rotations is responsible for the enhanced emission from aggregates. The permeability of the aggregated structures inside the HeLa cells was also studied. These highly emissive aggregates make these fluorophores as effective system for cell straining whereas the monomeric compounds failed to give any visible fluorescence inside the cells under identical condition. To obtain further insight, molecular simulation were carried out with explicit solvent system. Simulation study also indicates the formation of aggregates. It suggests that both hydrophobic interaction and hydrogen bonding play the roles in the aggregation process. It also reveals that the molecules exhibit some sort of twisted conformation in the aggregated structure thereby they avert the π-π stacking.

8.2. Scope for future Work:

The interaction of the nanoparticles with ICT fluorophores have been a useful research interest. The interaction of silver nanoparticles with DMAPIP-b and DMAPIP-c demonstrated for the first time that the environment sensitive TICT emission can also be

achieved through the interaction with nanoparticles. These composites of ICT fluorophore with nanoparticles can act as sensor system for different analytes.

The investigation on the extraction of fluorophore with micelle revealed that the micelles also affected by the presence of nanoparticles. Further studies on the effect of different nanoparticles with micelles may be useful to understand the interaction in detail.

The interaction of silver nanoparticles with these fluorophores inside BSA clearly showed that the fluorophores residing at the hydrophobic cavity of the protein are also accessible to the nanoparticles and energy transfer can be possible from fluorophore to the nanoparticles. This kind of study can be elaborated to other proteins also.

The ESIPT emissions of the fluorophores HPBI, HPIP-b and HPIP-c were altered by the silver nanoparticles. As these emissions are highly sensitive to environment, alternation of these emissions can be useful in different real field applications. Aggregation of these fluorophores enhances the emission intensity. The formation of the aggregates led to a platform with the availability of some nanostructures with very bright emission. These organic nanostructures can further be used for bright field imaging, biological sciences, chemical and biochemical sensing etc.

References:

1. H. Y. Xie, R. Zhen, B. Wang, Y. J. Feng, P. Chen and J. Hao. J. Phys. Chem. C., 2010, 114, 4825.
2. M. A. Smith, E. Prasad and K. R. Gopidas. J. Am. Chem. Soc., 2001, 123, 1159.
3. E. Prasad and K. R. Gopidas. J. Am. Chem. Soc., 2000, 122, 3191.
4. S. H. D. P. Lacerda, J. J. Park, C. Meuse, D. Pristinski, M. L. Becker, A. Karim and J. F. Douglas. ACS Nano, 2010, 4, 1, 365.
5. B. Valeur, Molecular fluorescence principles and applications. Wiley-VCH: Weinheim, 2002.
6. W. Rettig, Angew. Chem. Int. Ed. Engl., 1986, 25, 971-988.
7. W. Schuddeboom, S. A. Jonker, J. M. Warman, U. Leinhos, W. Kuhnle and K. A. Zachariasse. J. Phys. Chem., 1992, 96, 10809-10819.
8. A. L. Sobolewski and W. Domcke. Chem. Phys. Lett., 1996, 250, 428-436.
9. N. Chattopadhyay, C. Serpa, M. M. Pereira, J. S. de Melo, L. G. Arnaut and S. J. Formosinho. J. Phys. Chem. A, 2001, 105, 10025-10030.
10. C. Zhong. Phys. Chem. Chem. Phys., 2015, 17, 9248-
11. K. A. Zachariasse. Chem. Phys. Lett., 2000, 320, 8-13
12. M. Dekhtyar, W. Rettig and W. Weigel. Chem. Phys., 2008, 344, 237–250.
13. W. Weigel, W. Rettig, M. Dekhtyar, C. Modrakowski, M. Beinhoff and A. D. Schlu1ter. J. Phys. Chem. A, 2003, 107, 5941-5947.
14. W. Schuddeboom, S. A. Jonker, J. M. Warman, U. Leinhos, W. Kuhnle and K. A. Zachariasse. J. Phys. Chem. 1992, 96, 10809.
15. S. I. Druzhinin, S. A. Kovalenko, T. A. Senyushkina, A. Demeter and K. A. Zachariasse. J. Phys. Chem. A 2010, 114, 1621.
16. R. K. Everett, A. A. Nguyen and C. J. Abelt. J. Phys. Chem. A 2010, 114, 4946.
17. T. S. Singh, S. Mitra, A. K. Chandra, N. Tamai and S. Kar. J. Photochem. Photobiol. A 2008, 197, 295.
18. J. Dobkowski, W. Rettigb and J. Waluk. Phys. Chem. Chem. Phys. 2002, 4, 4334.
19. C. A. Guido, B. Mennucci, D. Jacquemin and C. Adamo. Phys. Chem. Chem. Phys. 2010, 12, 8016.
20. J. Dobkowski, J. Wójcik, W. Koski, R. Kołos, J. Waluk and J. Michl. J. Am. Chem. Soc. 2002, 124, 2406.
21. T. Yoshihara, S. I. Druzhinin and K. A. Zachariasse. J. Am. Chem. Soc. 2004, 126, 8535.
22. S. Cogan, S. Zilberg and Y. Haas. J. Am. Chem. Soc. 2006, 128, 3335.
23. A. L. Sobolewski and W. Domcke. Chem. Phys. Lett. 1996, 250, 428.
24. A. L. Sobolewski and W. Domcke. Chem. Phys. Lett. 1996, 259, 119.
25. K. A. Zachariasse, M. Grobys and E. Tauer. Chem. Phys. Lett. 1997, 274, 372.
26. K. A Zachariasse, T. Yoshihara and S. I. Druzhinin. J. Phys. Chem. A 2002, 106, 6325.
27. A. Ito, S. Ishizaka and N. Kitamura. Phys. Chem. Chem. Phys. 2010, 12, 6641.
28. X. Yang, R. Lu, H. Zhou, P. Xue, F. Wang, P. Chen and Y. Zhao. J. Colloid Interface Sci. 2009, 339, 527.
29. T. Fujiwara, J. -K. Lee, M. Z. Zgierski and C. L. Edward. Chem. Phys. Lett. 2009, 481, 78.

30. M. Shaikh, J. Mohanty, P. K. Singh, A. C. Bhasikuttan, R. N. Rajule, V. S. Satam, S. R. Bendre, V. R. Kanetkar and H. Pal. J. Phys. Chem. A 2010, 114, 4507.
31. F A. S. Chipem, S. Chatterjee and G. Krishnamoorthy. J. Photochem. Photobiol. A 2010, 214, 121.
32. Y. Park, D. C. Apodaca, J. Pullen and R. C. Advincula. J. Phys. Chem. A 2010, 114, 13084.
33. X. H. Qian, Y. Xiao, Y. F. Xu, X. F. Guo, J. H. Qian and W. P. Zhu. Chem. Comm. 2010, 46, 6418.
34. B. K. Paul, A. Samanta, S. Kar and N. Guchhait. J. Lumin. 2010, 130, 1258.
35. J. M. Hicks, M. Vandersall, E. V. Sitzmann and K. B. Eisenthal. Chem. Phys. Lett. 1987, 135, 413.
36. J. M. Hicks, M. Vandersall, Z. Babarogic and K. B. Eisenthal. Chem. Phys. Lett. 1985, 116, 18.
37. K. B. Eisenthal, in W. Kaiser (Ed.) Topics in Applied Physics, Springer-Vergang, New York 1988, 60, 319.
38. S. Tazuke, R. K Guo and T. Ikeda. J. Phys. Chem. 1990, 94, 1408.
39. K. A. Al-Hassan and T. Azumi. Chem. Phys. Lett. 1988, 121, 146.
40. K. A. Al-Hassan. Chem. Phys. Lett. 1991, 179, 195.
41. P. Changenet, P. Plaza, M. M. Martin and Y. H. Meyer. J. Phys. Chem. A 1997, 101, 8186.
42. K. A. Al-Hassan, M. A. Meetani, and Z. F. M. Said, J. Fluoresc. 1998, 8, 93.
43. W. Rettig, R. Fritz, J. Springer in K. Honda (Ed.) Photochemical Processes in Organized Molecular Systems, Elsevier Science, Amsterdam, North-Holland 1998, 61.
44. J. Paczkowski and D. C. Neckers. Macromolecules 1991, 24, 3013.
45. A. Haidekkar, D. Lichlyter, M. B. Johny and C. A. Grimes. Sens. Lett. 2006, 4, 257.
46. A. Mustafic, H. –M. Huang, E. A. Theodorakis and M. A. Haidekker. J. Fluores. 2010, 20, 1087.
47. A. Rei, G. Hungerford and M. I. C. Ferreira. J. Phys. Chem. B 2008, 112, 8832.
48. M. Li-Hua, C. Z-. Bin and J. Y-. Bao. Chem. Phys. Lett. 2003, 372, 104.
49. K. Dahl, R. Biswas, N. Ito and M. Maroncelli. J. Phys. Chem. B 2005, 109, 1563.
50. R. J. Visser, C. A. G. O. Varma, J. Konijenberg and P. C. M. Weisenborn. J. Mol. Struct. 1984, 114, 105.
51. A. Nag, T. Kundu and K. Bhattacharyya. Chem. Phys. Lett. 1989, 160, 257.
52. C. Cazeau-Dubroca, S. A. Lyazidi, P. Cambou, A. Peirigua, P. Cazeau and M. Pesquer. J. Phys. Chem. 1989, 93, 2347.
53. C. Cazeau-Dubroca, A. Peirigua, M. B. Brahim, G. Nouchi and Ph. Cazeau. Chem. Phys. Lett. 1989, 157, 393.
54. C. Cazeau-Dubroca, A. Peirigua, M. Ben Brahim, G. Nouchi and Ph. Cazeau. Proc. Indian Acad. Sci. (Chem. Sci.). 1989, 104, 209.
55. C. Cazeau-Dubroca, G. Nouchi, M. Ben Brahim, M. Pesquer, D. Gorse and Ph. Cazeau. J. Photochem. Photobiol. A 1994, 80, 125.
56. C. Cazeau-Dubroca, A. Peirigua, S. Ait-Lyazidi, G. Nouchi, P. Cazeau and R. Lapouyade. Chem. Phys. Lett. 1986, 124, 110.
57. R. B Singh, S. Mahanta, S. Kar and N. Guchhait. Chem. Phys. 2007, 324, 33.
58. M. Zakharov, O. Krauss, Y. Nosenko, B. B. Brutschy and A. Dreuw. J. Am. Chem. Soc., 2009, 131, 461-469.
59. J. Herbich, Z. R. Grabowski, H. Wojtowicz and K. Golankiewicz. J. Phys. Chem. 1989, 93, 3439.

60. J. Herbich, J. Karpiuk, Z. R. Grabowski, N. Tamai and K. Yoshihara. J. Lumin. 1992, 54, 165.
61. E. Fasani, A. Albini, P. Savarino, G. Viscardi and E. Barni. J. Heterocycl. Chem. 1993, 30, 1041.
62. Y. H. Kim, D. W. Cho, M. Yoon and D. Kim. J. Phys. Chem. 1996, 100, 15670.
63. Y. Kim, H. W. Cheon, M. Yoon, N. W. Song and D. Kim. Chem. Phys. Lett. 1997, 264, 673.
64. G. Krishnamoorthy and S. K. Dogra. Spectrochim. Acta. A 1999, 55, 2647.
65. G. Krishnamoorthy and S. K. Dogra. J. Phys. Chem. A 2000, 104, 2542-2551.
66. N. Dash, F.A.S. Chipem, R. Swaminathan and G. Krishnamoorthy. Chem. Phys. Lett., 2008, 460 119–124.
67. F. A. S. Chipem, A. Mishra and G. Krishnamoorthy. Phys. Chem. Chem. Phys., 2012, 14, 8775–8790.
68. J. Herbich, J. Karpiuk, Z. R. Grabowski, N. Tamai and K. Yoshihara. J. Lumin. 1992, 54, 165.
69. P. -T. Chou, M. L. Martinez and J. H. Clements. J. Phys. Chem. 1993, 97, 2618-2622.
70. D. D. Pant, H. C. Josh, P. B. Bisht and H. B. Tripathi. Chem. Phys. 1994, 185, 137-144.
71. P. B. Bisht, H. B. Tripathi and D. D. Pant. J. Photochem. Photobiol. A Chem. 1995, 90, 103-108.
72. G. Zhang, H. Wang, Y. Yu, F. Xiong, G. Tang and W. Chen. Applied Physics B - Lasers and optics 2003, 76, 677-681.
73. A. L. Sobolewski, W. Domcke and C. Hättig. J. Phys. Chem. A 2006, 110, 6301-6306.
74. A. Weller. Progr. React. Kinet. 1961, 1, 188.
75. A. U. Acuña, F. Toribio, F. Amat-Guerri and J. Catalan. J. Photochem. 1985, 30, 339-352.
76. F. Lahmani and A. Zehnacker-Rentien. J. Phys. Chem. A. 1997, 101, 6141-6147.
77. S. Nagaoka, A. Nakamura, and U. Nagashima. J. Photochem. Photobiol. A. 2002, 154, 23-32.
78. M. Fores, M. Duran, and M. Sola. Chem. Phys. 2000, 260, 53-64.
79. A. S. Klymchenko, V. G. Pivovarenko, T. Ozturk, and A. P. Demchenko. New J. Chem., 2003, 27, 1336-1343.
80. A. Ito, Y. Fujiwara, and M. Itoh. J. Chem. Phys. 1992, 96, 7474-7482.
81. D. A. Parthenopoulos, D. McMorrow, and M. Kasha. J. Phys. Chem. 1991, 95, 2668-2674.
82. E. Falkovskaia, P. K. Sengupta, and M. Kasha. Chem. Phys. Lett. 1998, 297, 109–114.
83. P. Chou, D. McMorrow, T. J. Aartsma, and M. Kasha. J. Phys. Chem. 1984, 88, 4596-4599.
84. S. Park, O. -H. Kwon, S. Kim, S. Park, M. -G. Choi, M. Cha, S. Y. Park, and D. -J. Chang. J. Am. Chem. Soc. 2005, 127, 10070-10074.
85. K. –Y. Chen, C. –C. Hsieh, Y. –M. Cheng, C. –H. Lai, and P. –T. Chou. Chem. Comm. 2006, 42, 4395-4397.
86. G. Zhang, H. Wang, Y. Yu, F. Xiong, G. Tang and W. Chen. Applied Physics B – Lasers and optics 2003, 76, 677-681.
87. M. Stein, J. Keck, F. Waiblinger, A. P. Fluegge, H. E. S. Kramer, A. Hartschuh, H. Port, D. Leppard, and G. Rytz. J. Phys. Chem. A 2002, 106, 2055-2066.
88. C. M. Estévez, R. D. Bach, K. C. Hass, and W. F. Schneider. J. Am. Chem. Soc. 1997, 119, 5445-5446.
89. S. S. Maity, S. Samanta, P. S. Sardar, A. Pal, S. Dasgupta, and S. Ghosh. Chem. Phys. 2008, 354, 162-173.

90. Y. Wu, X. Peng, J. Fan, S. Gao, M. Tian, J. Zhao, and S. Sun. J. Org. Chem. 2007, 72, 62-70.
91. J. E. Kwon, and S. Y. Park. Adv. Mater. 2011, 23, 3615–3642.
92. J. Zhao, S. Ji, Y. Chen, H. Guo, and P. Yang. Phys. Chem. Chem. Phys. 2012, 14, 8803–8817.
93. D. Beer and J. Weber. Opt. Commun. 1972, 5, 307-309.
94. X. Li, Y. Qian, S. Wang, S. Li and G. Yang. J. Phys. Chem. C 2009, 113, 3862-3868.
95. S. Kim, J. Seo, H. K. Jung, J. J. Kim, and S. Y. Park. Adv. Mater. 2005, 17, 2077-2082.
96. K. Szaciłowski. Chem. Rev. 2008, 108, 3481-354.
97. M. Irie. Chem. Rev. 2000, 100, 1685-1716.
98. N. Barooah, J. Mohanty, H. Pal and A. C. Bhasikuttan. Org. Biomol. Chem., 2012, 10, 5055 –5062.
99. H. N. Kim, W. X. Ren, J. S. Kim and J. Yoon. Chem. Soc. Rev., 2012, 41, 3210-3244.
100. R. I. Khan and K. Pitchumani. RSC Adv., 2016, 6, 20269-20275.
101. A. Chatterjee, B. Maity and D. Seth. RSC Adv., 2014, 4, 13989-14000.
102. F. A. S. Chipem, S. K. Behera and G. Krishnamoorthy. Photochem. Photobiol. Sci., 2014, 13, 1297-1304.
103. F. Chandra, S. Mallick and A. L. Koner. Phys. Chem. Chem. Phys., 2017, 19, 4337-4344.
104. N. Niamnont, A. Promchat, C. Siangma, C. Pramaulpornsatit and M. Sukwattanasinitt. RSC Adv., 2015, 5, 64763-64768.
105. F. Chandra, K. Pal, S. Lathwal and A. L. Koner. Mol. Bio Syst., 2016, 12, 2859-2866.
106. P. Alreja and N. Kaur. RSC Adv., 2016, 6, 23169-23217.
107. S. Inal, J. D. Kölsch, F. Sellrie, J. A. Schenk, E. Wischerhoff, A. Laschewsky and D. Neher. J. Mater. Chem. B, 2013, 1, 6373-6381.
108. Z. Sun, G. Cui, H. Li, Y. Liu, Y. Tian and S. Yan. J. Mater. Chem. B, 2016, 4, 5194-5216.
109. I. E. Serdiuk, M. Reszka, A. Synak, B. Liberek and P. Bojarski. Dyes and Pigments, 2018, 149, 224-228.
110. P. Shen, J. Hua, H. Jin, J. Du, C. Liu, W. Yang, Q. Gao, H. Luo, Y. Liu and C. Yang. Sensors and Actuators B: Chemical, 2017, 247, 587-594.
111. S. Singha, D. Kim, H. Seo, S. W. Cho and K. H. Ahn. Chem. Soc. Rev., 2015, 44, 4367-4399.
112. N. Barbero, M. Coletti, F. Catalano, S. Visentin. International Journal of Pharmaceutics, 2018, 535, 438-443.
113. A. Mansouri, M. Mousavi, F. Attar, A. A. Saboury and M. Falahati. International Journal of Biological Macromolecules, 2018, 106, 78-86.
114. G. Wang, H. Hou, S. Wang, C. Yan, Y. Liu. Colloids and Surfaces B: Biointerfaces, 2017, 157, 138-145.
115. S. Roy, S. K. Saxena, S. Mishra, P. Yogi and R. Kumar. Journal of Photochemistry and Photobiology B: Biology, 2017, 174, 284-290.
116. B. Maity, A. Chatterjee, S. Ashique Ahmed and D. Seth. Journal of Luminescence, 2017, 183, 238–250.
117. S. Ghosh, S. Jana and N. Guchhait. Spectrochimica Acta Part A, 2011, 84, 249– 255.
118. K. Pal, F. Chandra, S. Mallick and A. L. Koner. Journal of Photochemistry and Photobiology A: Chemistry, 2015, 306, 47–54.

119. M. Jozefowicz. Spectrochimica Acta Part A, 2012, 93, 169– 175.
120. B. Jana, S. Ghosh and N. Chattopadhyay. Journal of Photochemistry and Photobiology B: Biology, 2013, 126, 1–10.
121. A. K. Vasu and S. Kanvah. Dyes and Pigments, 2017, 142, 230-236.
122. C. Lu, J. Cao, Y. Cheng, Y. Jin, Y. Qu and J. Xu. Sensors and Actuators B, 2018, 255, 3102–3107.
123. J. Maiti, Y. Sarkar, P. P. Parui, S. Chakraborty, S. Biswas, R. Das. Journal of Luminescence, 2015, 163, 21–27.
124. R. Kumaran, M. Vanjinathan, P. Ramamurthy. Journal of Luminescence, 2015, 164, 146–153.
125. F.-Y. Wu, Z.-J. Ji, Y.-M. Wu, X.-F. Wan. Chem. Phys. Lett., 2006, 424, 387–393.
126. S. Naveenraj, R. V. Solomon, R. V. Mangalaraja, P. Venuvanalingam, A. M. Asiri, S. Anandan. Spectrochimica Acta Part A: Molecular and Biomolecular Spectroscopy, 2018, 192, 34–40.
127. Y. Hong, X. Zhang, B. Li, M. Li, Q. Shi, Y. Wang and L. Li. Journal of Rare Earths. 2013, 31, 1096-1101.
128. T. Woldu, B. Raneesh, P. Sreekanth, M. V. R. Reddy, R. Philip and N. Kalarikkal. Chemical Physics Letters. 2015, 625, 58-63.
129. J. Lian, Y. Liang, F.-l. Kwong, Z. Ding, D. H. L. Ng. Materials Letters. 2012, 66, 318-320.
130. M. Mashayekh and D. Dorranian. Optik - International Journal for Light and Electron Optics. 2014, 125, 5612-5617.
131. Y. S. Ma, M. Gu, S. Huang, X. Liu, B. Liu and C. Ni. Materials Letters. 2013, 100, 166-169.
132. I.A. Rahman, P. Vejayakumaran, C. S. Sipaut, J. Ismail and C. K. Chee. Materials Chemistry and Physics. 2009, 114, 328-332.
133. B. Ajitha, A. K. Reddy and S. Reddy. Journal of photochemistry and photobiology. 2015.
134. J. Gao, J. Xu, S. Wen, J. Hu and H. Liu. Microporous and Mesoporous Materials. 2015, 207, 149-155.
135. S. Joseph and B. Mathew. Journal of Molecular Liquids. 2015, 204, 184–191.
136. B.S. Srinath and V. R. Rai. Materials Letters. 2015, 146, 23–25.
137. S. Sareen, V. Mutreja, B. Pal and S. Singh. Microporous and Mesoporous Materials. 2015, 202, 219-225.
138. M. R. Bindhu and M. U. devi. Spectrochimica Acta Part A: Molecular and Biomolecular Spectroscopy. 2015, 135, 373–378.
139. R. Manikandan, B. Manikandan, T. Raman, K. Arunagirinathan, N. M. Prabhu, M. J. Basu, M. Perumal, S. Palanisamy and A. Munusamy. Spectrochimica Acta Part A: Molecular and Biomolecular Spectroscopy. 2015, 138, 120-129.
140. N. Jayaprakash, J. J. Vijaya, L. J. Kennedy, K. Priadharsini and P. Palani. Materials Science and Engineering: C. 2015, 49, 316-322.
141. S. A. kumar, S. Ravi, V. Kathiravan and S. Velmurugan. Spectrochimica Acta Part A: Molecular and Biomolecular Spectroscopy. 2015, 134, 34-39.
142. S.-Y. Heo, H.-J. Choi, B.-J. Park, J.-H. Um, H.-J. Jung, J.-R. Jeong and S.-G. Yoon. Sensors and Actuators A: Physical. 2015, 221, 131-138.

143. V. Kathiravan, S. Ravi, S. A. kumar, S. Velmurugan, K. Elumalai and C. P. Khatiwada. Spectrochimica Acta Part A: Molecular and Biomolecular Spectroscopy. 2015, 139, 200-205.
144. A. F. d. Faria, D. S. T. Martinez, S. M. M. Meira, A. C. M. d. Moraes, A. Brandelli, A. G. S. Filho and O. L. Alves. Colloids and Surfaces B: Biointerfaces. 2014 113, 115-124.
145. (a) T. A. Wertime. Science. 1973, 182, 875. (b) T. A. Wertime. Science. 1964, 146, 1257. (c) K. Branigan. Nature. 1982, 296, 701.
146. B. Wiley, Y. Sun and Y. Xia. Acc. Chem. Res. 2007, 40, 1067.
147. E. L. Ru and P. Etchegoin. Principles of Surface Enhanced Raman Spectroscopy; Elsevier: Oxford, U.K., 2009.
148. J. Belloni. Radiat. Phys. Chem. 2003, 67, 291.
149. L. Rivas, S. S.-Cortes, J. V. G.-Ramos and G. Morcillo. Langmuir. 2000, 16, 9722.
150. K.-S. Lee and M. A. E.-Sayed, J. Phys. Chem. B. 2006, 110, 19220.
151. I. Yoon, T. Kang, W. Choi, J. Kim, Y. Yoo, S.-W. Joo, Q.-H. Park, H. Ihee and B. Kim. J. Am. Chem. Soc.2009, 131, 758.
152. M. Rycenga, K. K. Hou, C. M. Cobley, A. Schwartz, P. H. C. Camargo and Y. Xia. Phys. Chem. Chem. Phys.2009, 11, 5903.
153. M. Rycenga, C. M. Cobley, J. Zeng, W. Li, C. H. Moran, Q. Zhang, D. Qin and Y. Xia. Chem. Rev. 2011, 111, 3669–3712.
154. Xia, Y.; Xiong, Y.; Lim, B.; Skrabalak and S. E.Angew. Chem., Int. Ed. 2009, 48, 60.
155. S. Halivni, A. Sitt, I. Hadar and U. Banin. ACS Nano. 2012, 6, 2758.
156. W. F. Falcoa, E. R. Botero, E. A. Falcão, E. F. Santiago, V. S. Bagnato and A. R. L. Caires. Journal of Photochemistry and Photobiology A: Chemistry. 2011, 225, 65–71.
157. L. Farzampour and M. Amjadi. Journal of Luminescence. 2014, 155, 226–230.
158. S. Freddi, L. D'Alfonso, M. Collini, M. Caccia, L. Sironi, G. Tallarida, S. Caprioli and G. Chirico. J. Phys. Chem. C.2009, 113, 2722–2730.
159. J.-Q. Gu, J. Shen, L.-D. Sun and C.-H. Yan. J. Phys. Chem. C letters.2008, 112, 6589-6593.
160. S.-C. Wei, P.-H. Hsu, Y.-F. Lee, Y.-W. Lin and C.-C. Huang. ACS Appl. Mater. Interfaces. 2012, 4, 2652−2658.
161. S. Chowdhury, Z. Wu, A. J.-Gerst, S. Liu, A. Dembska, B. A. Armitage, R. Jin and L. A. Peteanu. J. Phys. Chem. C 2011, 115, 20105–20112.
162. F. Tang, F. He, H. Cheng and L. Li. Langmuir. 2010, 26, 11774–11778.
163. R. I. Nooney, O. Stranik, C. McDonagh and B. D. MacCraith. Langmuir.2008, 24, 11261-11267.
164. A. J. Amali, N. H. Awwad, R. K. Rana and D. Patra. Analytica Chimica Acta. 708, 2011, 75–83.
165. J. S. Rania, V. Sasirekhab and V. Ramakrishnana. Journal of Luminescence. 144, 2013, 74–78.
166. J. Wang, S. Achilefu, M. Nantz and K. A. Kang. Analytica Chimica Acta. 2011, 695, 96–104.
167. T. Sen and A. Patra. J. Phys. Chem. C 2008, 112, 3216-3222.
168. C. Song, G.-Y. Wang and D.-M. Kong. Biosensors and Bioelectronics. 2015, 68, 239–244.
169. O.S. Adeyemi and C.G. Whiteley. Biochimica et Biophysica Acta - General Subjects. 2014, 1840, 701–706.

170. W. F. Falcoa, A. M. Queiroz, J. Fernandes, E. R. Botero, E. A. Falcão, F. E. G. Guimarães, J. -C. M'Peko, S. L. Oliveira, I. Colbeck and A. R. L. Caires. Journal of Photochemistry and Photobiology A: Chemistry. 2015, 299, 203–209.
171. M. R.-Vasic, L. D. Cola and H. Zuilhof. J. Phys. Chem. C. 2009, 113, 2235–2240.
172. M. Acar, E. Bozkurt, K. Meral, M. Arık and Y. Onganer. Journal of Luminescence. 2015, 157, 10–15.
173. G. R. Bardajee, Z. Hooshyar and M. Khanjari. Journal of Photochemistry and Photobiology A: Chemistry. 2014, 276, 113–121.
174. S. R. Kavithaa, M. Umadevia, S. R. Jananib, T. Balakrishnanc and R. Ramanibaic. Spectrochimica Acta Part A: Molecular and Biomolecular Spectroscopy. 2014, 127, 115–121.
175. P. Manikandana, S. Pushpama, V. Sasirekhab, J. S. Rania and V. Ramakrishnana. Spectrochimica Acta Part A: Molecular and Biomolecular Spectroscopy. 2014, 121, 276–281.
176. S. A. E.-Dalya, M. M. Rahmana, K. A. Alamrya and A. M. Asiri. Journal of Luminescence. 2014, 148, 303–306.
177. G. P. Acuna, M. Bucher, I. H. Stein, C. Steinhauer, A. Kuzyk, P. Holzmeister, R. Schreiber, A. Moroz, F. D. Stefani, T. Liedl, F. C. Simmel and P. Tinnefeld. ACS Nano. 2012, 6, 3189–3195.
178. M. P. Singh and G. F. Strouse. J. Am. Chem. Soc. 2010, 132, 9383–9391.
179. T. Sen, S. Jana, S. Koner and A. Patra. J. Phys. Chem. C. 2010, 114, 19667–19672.
180. S. Rouhani and S. Haghgoo. Sensors and Actuators B: Chemical. 2015, 209, 957–965.
181. A. Suslov, P. T. Lama and R. Dorsinville. Optics Communications. 2015, 345, 116–119.
182. P. Liu, L. Zhao, X. Wu, F. Huang, M. Wang and X. Liu. Spectrochimica Acta Part A: Molecular and Biomolecular Spectroscopy. 122, 2014, 238–245.
183. S. Thakur, P. Kumar, M. V. Reddy, D. Siddavattam and A. K. Paul. Sensors and Actuators B: Chemical. 178, 2013, 458–464.
184. Y. Jie, L. Yonghua, W. Pei and M. Hai. Optics Communications. 284, 2011, 494–497.
185. B. Xia, F. He and L. Li. Colloids and Surfaces A: Physicochemical and Engineering Aspects. 444, 2014, 9–14.
186. R. K. Verma, K. Kumar and S. B. Rai. Solid State Communications. 150, 2010, 1947–1950.
187. N. Yina, Y. Liua, L. Liu, J. Lei, T. Jiang, H. Wang, L. Zhu and X. Xu. Journal of Alloys and Compounds. 581, 2013, 6–10.
188. S. Bharill, C. Chen, B. Stevens, J. Kaur, W. Mandecki, I. Gryczynski, Z. Gryczynski, B. S. Cooperman and Y. E. Goldman. Biophysical Journal. 98, 2010, 262.
189. Y. Qi, Y. Zhou, L. Wu, F. Yang, S. Peng, S. Zheng, D. Yin and X. Wang. Materials Letters. 125, 2014, 56–58.
190. S. Bonacchi, E. Rampazzo, M. Montalti, L. Prodi, N. Zaccheroni, F. Mancin and P. Teolato. Langmuir. 2008, 24, 8387-8392.
191. M. L.-Viger, D. Brouard and D. Boudreau. J. Phys. Chem. C 2011, 115, 2974–2981.
192. F. Tang, F. He, H. Cheng and L. Li. Langmuir 2010, 26, 11774–11778.
193. J. Gersten and A. Nitzan. J. Chem. Phys. 1981, 75, 1139-1152.
194. R. R. Chance, A. Prock and R. Silbey. Adv. Chem. Phys. 1978, 37, 1-65.

195. J. R. Lakowicz. Anal. Biochem. 2005, 337, 171-194.
196. T. Jennings and G. Strouse. Adv. Exp. Med. Biol. 2007, 620, 34-47.
197. M. Kerker and C. G. Blatchford. Phys. Rev. B. 1982, 26, 4052-4082.
198. J. I. Gersten and A. Nitzan. Surf. Sci.1985, 158, 165-189.
199. J. R. Lakowicz. Anal. Biochem. 2001, 298, 1-24.
200. K. H. Drexhage. J. Lumin. 1970, 12, 693-701.
201. A. L. Simonian, T. A. Good, S.-S. Wang and J. R. Wild. Analytica Chimica Acta. 534, 2005, 69–77.
202. J. Zhao, Y. Yi, N. Mi, B. Yin, M. Wei, Q. Chen, H. Li, Y. Zhang and S. Yao. Talanta. 116, 2013, 951–957.
203. S. Shahabia, L. Treccani, R. Dringen and K. Rezwan. Acta Biomaterialia. 14, 2015, 208–216.
204. J. Xu, Y. Li, J. Guo, F. Shen, Y. Luo and C. Sun. Food Control. 46, 2014, 67–74.
205. Z. Wang, X. Zhang, P. Huang, W. Zhao, D. Liu, L. Nie, X. Yue, S. Wang, Y. Ma, D. Kiesewetter, G. Niu and X. Chen. Biomaterials. 34, 2013, 6194–6201.
206. N. Sui, L. Wang, T. Yan, F. Liu, J. Sui, Y. Jiang, J. Wan, M. Liu and W. W. Yu. Sensors and Actuators B: Chemical. 202, 2014, 1148–1153.
207. L. Shang and S. Dong. Anal. Chem. 2009, 81, 1465–1470.
208. Y. Leng, K. Xie, L. Ye, G. Li, Z. Lu and J. He. Talanta, 2015, 139, 89-95.
209. P. Botella, I. Abasolo, Y. Fernández, C. Muniesa, S. Miranda, M. Quesada, J. Ruiz, S. Schwartz and A. Corma. Journal of Controlled Release, 2011, 56, 246–257.
210. N. Vasimalai and S. A. John. Talanta. 2013, 115, 24–31.
211. P. Wang, T.-H. Wu and Y. Zhang. Talanta. 2016, 146, 175–180.
212. E. I. Altınoglu, T. J. Russin, J. M. Kaiser, B. M. Barth, P. C. Eklund, M. Kester and J. H. Adair. ACS Nano, 2008, 2, 2075–2084.
213. H. Zhou, H. Yue, Y. Zhou, L. Wang and Z. Fu. Sensors and Actuators B. 2015, 209, 744–750.
214. Z. Zhu, Y. Su, J. Li, D. Li, J. Zhang, S. Song, Y. Zhao, G. Li and C. Fan. Anal. Chem., 2009, 81, 7660-7666.
215. C. M. Orlando, J. G. Wirth and D. R. Heath. J Org. Chem. 1970, 35, 3147-3149.
216. R. W. Middleton and D. G. Wibberley. J Heterocyclic Chem. 1980, 17, 1757-1760.
217. D. W. Hein, R. J. Alheim and J. J. Leavitt, Journal of the American Chemical Society, 1957, 79, 427-429.
218. F. A. S. Chipem, S. K. Behera and G. Krishnamoorthy, J Phys. Chem. A, 2013, 117, 4084-4095.
219. A. Mishra, S. Sahu, N. Dash, S. K. Behera and G. Krishnamoorthy, J Phys. Chem. B, 2013, 117, 9469-9477.
220. I. Pastoriza-Santos and L.M. Liz-Marzán. Langmuir.1999, 15, 948–951.
221. H. Oikawa, H. Nakanishi, In Single Organic Nanoparticles; H. Masuhara, H. Nakanishi, K. Sasaki, Eds.; Springer-Verlag: Berlin, 2003.
222. H. Kasai, H. S. Nalwa, H.Oikawa, S. Okada, H. Matsuda, N. Minami, A. Kakuda, K. Ono, A. Mukoh and H. Nakanishi. Jpn. J. Appl. Phys. 1992, 31, 1132–1134.
223. M. Abyan, D. De Caro and S. Fery-Forgues. Langmuir 2009, 25, 1651–1658.

224. J. Chahine, N. Saffon, M. Cantuel and S. Fery-Forgues, Langmuir 2011, 27, 2844–2853.
225. J. R. Lakowicz. Principles of Fluorescence Spectroscopy, 3rd ed.; Springer: New York, 2006.
226. B. Valeur. Molecular Fluorescence: Principles and Applications; Wiley-VCH: Weinheim, Germany, 2002.
227. B. Valeur and J. -C. Brochon. New Trends in Fluorescence Spectroscopy: Applications to Chemical and Life Science; Springer: New York, 2001.
228. J. A. Ross and D. M. Jameson. Photochem. Photobiol. Sci. 2008, 7, 1301-1312.
229. M. Y. Berezin and S. Achilefu. Chem. Rev. 2010, 110, 2641-2684.
230. W. Becker. Advanced Time-Correlated Single Photon Counting Techniques; Springer: Berlin, 2005.
231. W. Becker. The bh TCSPC Handbook, 3rd Ed.; Becker & HicklGmbh: Berlin, Germany, 2008.
232. Fluorescence Analysis Software Technology (FAST), Edinburgh Intruments Ltd., 2 Bain Square, Kirkton Campus, Livingston EH54 7DQ, UK, 2007.
233. G. Krishnamoorthy, in: K.L. Han, G.-J. Zhao (Eds.), Hydrogen Bonding and Transfer in the Excited State, Wiley VCH, West Sussex, UK, 2011, pp. 313–329 (Chapter 14).
234. Aurora-A, Aurora-B and Aurora-C kinases play a key role in the regulation of mitosis, and are implicated in cancer initiation and progression.
235. V. Bavetsias, C. Sun, N. Bouloc, R. Jóhannes, W. Paul, L. Spiros Linardopoulos and M. Edward. Bioorg. Med. Chem. Lett. 2007, 17, 6567.
236. G. Krishnamoorthy and S.K. Dogra. J. Colloid Interface Sci. 2000, 228, 335–343.
237. N. Dash, F.A.S. Chipem and G. Krishnamoorthy. Photochem. Photobiol. Sci. 2009, 8, 1708–1715.
238. N. Dash, A. Mishra and G. Krishnamoorthy. J. Pharm. Biomed. Anal. 2013, 77, 55–62.
239. A. D. B.-Yaseen. Spectrochimica Acta Part A: Molecular and Biomolecular Spectroscopy, 2015, 148, 93-98.
240. Q. You, P. Zhang, S. Bai, W. Huang, Z. Jia, C. Zhou and D. Li. Colloids and Surfaces A: Physicochemical and Engineering Aspects 2015, 484, 130-135.
241. P. Tang, X. Ma, D. Wu, S. Li, K. Xu, B. Tang and H. Li. Carbohydrate Polymers 2016, 142, 16-23.
242. A. Stepniak, S. B.-Pacha, S. Rozalska, J. Dlugonski, P. Urbaniak and B. Palecz. Journal of Molecular Liquids 2015, 211, 288-293.
243. H. Huang, X. Yang, K. Wang, Q. Wang, Q. Guo, J. Huang, J. Liu, X. Guo, W. Li and L. He. Talanta 2015, 144, 529-534.
244. A. Nag, R. Dutta, N. Chattopadhyay and K. Bhattacharyay. Chem. Phys. Lett. 1989, 157, 83–86.
245. A. Mallick, P. Purkayastha and N. Chattopadhyay. J. Photochem. Photobiol. C. 2007, 8, 109–127.
246. N. Dash, A. Malakar, M. Kumar, B.B. Mandal and G. Krishnamoorthy. Sens. Actuator B Chem. 2014, 202, 1154–1163.
247. G. Krishnamoorthy and S.K. Dogra. J. Org. Chem. 1999, 64, 6566–6574.
248. G. Ramakrishna and H.N. Ghosh. J. Phys. Chem. A. 2002, 106, 2545–2553.
249. G. Ramakrishna and H.N. Ghosh. J. Phys. Chem. B. 2004, 108, 12489–12496.
250. A. Malakar and G. Krishnamoorthy. J Colloid Interf Sci 2015, 443, 23-29.

251. G. Raino, T. Stoferle, C. Park, H. Kim, T. Topuria, P. M. Rice, I. Chin, R. D. Miller and R. F. Mahrt. ACS Nano 2011, 5, 3536–3541.
252. S. Mandal, C. Ghatak, V. G. Rao, S. Ghosh and N. Sarkar. J. Phys. Chem. C 2012, 116, 5585−5597.
253. A. Maity, S. S. Jaffer, T. Das, P. Ghosh and P. Purkayastha. Langmuir 2011, 27, 4068–4075.
254. C. R. Martin. Science, 1994, 266, 1961.
255. A. Thomas, F. Goettmann and M. Antonietti. Chem. Mater. 2008, 20, 738.
256. B. L. Cushing, V. L. Kolesnichenko and C. J. O'Connor. Chem. Rev. 2004, 104, 3893.
257. C. Burda, X.Chen, R. Narayanan and M. A. El-Sayed. Chem. Rev. 2005, 105, 1025.
258. M. Maillard, S. Giorgio and M.-P. Pileni. J. Phys. Chem. B 2003,107, 2466.
259. W. Zhang, X. Q. Chen. J. Mater. Sci. Eng. B 2007, 142, 1.
260. S. H. Chen and D. L. Carroll. Nano Lett. 2002, 2, 1003.
261. D. O. Yener, J. Sindel, C. A. Randall and J. H. Adair. Langmuir 2002, 18, 8692.
262. D. B. Zang, C. X. Song, Z. S. Hu and X. D. Zhou. Mater. Lett. 2005, 59, 1760.
263. D. Zhang, L. Qi, J. Ma and H. Cheng. Chem. Mater. 2001, 13, 2753.
264. N. R. Jana, L. Gearheart and C. J. Murphy. Chem. Commun. 2001, 617.
265. Y. Liu, Y. Chu, L. K. Yang, D. X. Han, Z. X. Lu. Mater. Res. Bull. 2005, 40, 1796.
266. C. Y. Ni, P. A. Hassan and E.W. Kaler. Langmuir 2005, 21, 3334.
267. X. W. Zheng, L. Y. Zhu, A. H. Yan, X. J. Wang and Y J. Xie. Colloid Interface Sci. 2003, 268, 357.
268. J. L. Zhang, B. X. Han, M. H. Liu, D. X. Liu, Z. X. Dong, J. Liu, D. Li, J. Wang, B. Z. Dong, H. Zhao and L. X. Rong. J. Phys. Chem. B 2003, 107, 3679.
269. D. S. Bae, E. J. Kim, J. H. Bang, S. W. Kim, K. S. Han, J. K. Lee, B. I. Kim and J. H. Adair. Met. Mater. Int. 2005, 11, 291.
270. R. P. Bagwe and K. C. Khilar. Langmuir 2000, 16, 905.
271. A. Mishra, A. Malakar, H. T. Biswal, M. K. Barman and G. Krishnamoorthy. J. Mol. Recognit. 2015, 28, 299-305.
272. A. Granzhan, H. Ihmels and G. Viola. J. Am. Chem. Soc. 2007, 129, 1254–1267.
273. B. K. Paul, A. Samanta and N. Guchhait. J. Phys. Chem. B 2010, 114, 6183–6196.
274. X. Zeng, X. Zhang, B. Zhu, H. Ji, Y. Li and J. Xue. Analyst 2011, 136, 4008–4012.
275. A. Mallick, B. Haldar and N. Chattopadhyay. J. Phys. Chem. B 2005, 109, 14683–14690.
276. J. K. Dey and S. K. Dogra. J. Phys. Chem. 1994, 98, 3638–3644.
277. G. Krishnamoorthy and S. K. Dogra. J. Photochem. Photobiol. A: Chem. 1999a, 123, 109–119.
278. G. Krishnamoorthy and S. K. Dogra. Chem. Phys. 1999b, 243, 45–59.
279. A. Mishra and G. Krishnamoorthy. Photochem. Photobiol. Sci. 2012, 11, 1356–1367.
280. L. Shang, Y. Wang, J. Jiang and S. Dong, Langmuir 2007, 23, 2714 2721.
281. Lakowicz, J. R. Principles of Fluorescence Spectroscopy; Kluwer Academic/Plenum Publishers: Dordrecht, The Netherlands, 2004.
282. A. Kyrychenko, G. V. Karpushina, D. Svechkarev, D. Kolodezny, S. I. Bogatyrenko, A. P. Kryshtal and A. O. Doroshenko. J. Phys. Chem. C. 2012, 116, 21059−21068.
283. F. A. S. Chipem and G. Krishnamoorthy. J. Phys. Chem. A. 2009, 113, 12063–12070.
284. F. A. S. Chipem and G. Krishnamoorthy. J. Phys. Chem. B. 2013, 117, 14079−14088.

285. H. K. Sinha and S. K. Dogra. Chemical Physics 1986, 102, 337-347.

286. G. Krishnamoorthy and S. K. Dogra. J. Luminescence 2001, 92, 91-102.

287. M. M. Balamurali and S.K. Dogra. J Photoch Photobio A: Chemistry 2002, 154, 81–92.

288. F. A. S. Chipem, S. K. Behera and G. Krishnamoorthy. Sensors and Actuators B 2014, 191, 727 – 733.

289. E. L. Roberts, J. K. Dey and I. M. Warner. J. Phys. Chem. A, 1997, 101, 5296–5301.

290. Fluorescence Sensors and Biosensors, ed. R. B. Thompson, CRC, Boca Raton, 2006.

291. C. W. Tang and S. A. Vanslyke. Appl. Phys. Lett. 1987, 51, 913.

292. Advanced Concepts in Fluorescence Sensing, ed. C. D. Geddes and J. R. Lakowicz, Springer, Norwell, 2005.

293. E. A. Jares-Erijman and T. M. Jovin. Nat. Biotechnol. 2003, 21, 1387.

294. H. Saigusa and E. C. Lim. J. Phys. Chem. 1995, 99, 15738.

295. J. Luo, Z. Xie, J. W. Y. Lam, L. Cheng, H. Chen, C. Qiu, H. S. Kwok, X. Zhan, Y. Liu, D. Zhu and B. Z. Tang. Chem. Commun., 2001, 1740.

296. B. Z. Tang, X. Zhan, G. Yu, P. P. S. Lee, Y. Liu and D. Zhu. J. Mater. Chem. 2001, 11, 2974.

297. Q. Zeng, Z. Li, Y. Dong, C. Di, A. Qin, Y. Hong, L. Ji, Z. Zhu, C. K. W. Jim, G. Yu, Q. Li, Z. Li, Y. Liu, J. Qin and B. Z. Tang. Chem. Commun. 2007, 70–72.

298. J. Tong, Y. J. Wang, Z. Wang, J. Z. Sun, and B. Z. Tang. J. Phys. Chem. C 2015, 119, 21875−21881.

299. L. Tang, J. K. Jin, A. Qin, W. Z. Yuan, Y. Mao, J. Mei, J. Z. Sun and B. Z. Tang. Chem. Commun. 2009, 33, 4974–4976.

300. Y. Hong, J. W. Y. Lam and B. Z. Tang. Chem. Commun. 2009, 4332–4353.

301. B. Z. Tang, X. Zhan, G. Yu, P. P. S. Lee, Y. Liu and D. J. Zhu. Mater. Chem. 2001, 11, 2974–2978.

302. Y. Dong, J. W. Y. Lam, A. Qin, J. Liu, Z. Li, B. Z. Tang, J. Sun and H. S. Kwok. Appl. Phys. Lett., 2007, 91, 011111.

303. R. Wei, P. Song and A. Tong. J. Phys. Chem. C 2013, 117, 3467−3474.

304. D.-E. Wu, Q.-C. Yao and M. Xia. Phys. Chem. Chem. Phys. 2015, 17, 3287-3294.

305. V. S. Padalkar, D. Sakamaki, K. Kuwada, N. Tohnai, T. Akutagawa, K.-i. Sakai and S. Seki. RSC Adv. 2016, 6, 26941-26949.

306. Q.-C. Yao, X.-L. Lu and M. Xia. New J. Chem. 2014, 38, 2693-2700.

307. G. Yang, S. Li, S. Wang and Y. Li. C. R. Chimie 2011, 14, 789–798.

308. A. Maity, F. Ali, H. Agarwal, B. Anothumakkool and A. Das. Chem. Commun. 2015, 51, 2130-2133.

309. M. Cai, Z. Gao, X. Zhou, X. Wang, S. Chen, Y. Zhao, Y. Qian, N. Shi, B. Mi, L. Xie and W. Huang. Phys. Chem. Chem. Phys. 2012, 14, 5289–5296.

310. T. He, X. T. Tao, J. X. Yang, D. Guo, H. B. Xia, J. Jia and M. H. Jiang. Chem. Commun. 2011, 47, 2907–2909.

311. F. Wurthner, T. E. Kaiser and C. R. Saha-Moller. Angew. Chem. Int. Ed. 2011, 50, 3376 – 3410.

312. Y. H. Kim, S. G. Roh, S. D. Jung, M. A. Chung, H. K. Kimc and D. W. Cho. Photochem. Photobiol. Sci. 2010, 9, 722–729.

313. Y. Qian, S. Li, G. Zhang, Q. Wang, S. H. X. Wang, C. Li, Y. Li and G. Yang. J. Phys. Chem. B 2007, 111, 5861-5868.

314. J. Mei, Y. Hong, J. W. Y. Lam, A. Qin, Y. Tang and B. Z. Tang. Adv. Mater. 2014, 26, 5429–5479.
315. F. Bertorelle, D. Lavabre and S. Fery-Forgues. J. Am. Chem. Soc. 2003, 125, 6244–6253.
316. M. Abyan, F. Bertorelle and S. Fery-Forgues. Langmuir 2005, 21, 6030–6037.
317. H. Oikawa, H. Kasai and H. Nakanishi, in Anisotropic Organic Materials, ACS Symposium Ser. 798, ed. R. Glaser and P. Kasizynski. American Chemical Society, Washington, DC, 2002, ch. 11, pp. 158–168, and references therein.
318. H. S. Nalwa, H. Kasai, S. Okada, H. Oikawa, H. Matsuda, A. Kakuta, A. Mukoh and H. Nakanishi. Adv. Mater. 1993, 5, 758–760.
319. H. Kasai, H. Oikawa, S. Okada and H. Nakanishi. Bull. Chem. Soc. Jpn. 1998, 71, 2597–2601.
320. H. Kasai, H. Kamatani, Y. Yoshikawa, S. Okada, H. Oikawa, A. Watanabe, O. Itoh and H. Nakanishi. Chem. Lett. 1997, 1181–1182.
321. H. Kasai, H. Kamatani, S. Okada, H. Oikawa, H. Matsuda and H. Nakanishi. Jpn. J. Appl. Phys. 1996, 35, L221–L222.
322. H. Kasai, H. S. Nalwa, H. Oikawa, S. Okada, H. Matsuda, N. Minami, A. Kakuta, K. Ono, A. Mukoh and H. Nakanishi. Jpn. J. Appl. Phys. 1992, 31, L1132–L1134.
323. T. Onodera, T. Oshikiri, H. Katagi, H. Kasai, S. Okada, H. Oikawa, M. Terauchi, M. Tanaka and H. Nakanishi. J. Cryst. Growth. 2001, 229, 586–590.
324. N. Sarkar, K. Das, S. Das, A. Dutta, D. Nath and K. Bhattacharyya. J. Phys. Chem. 1995, 99, 17711-17714.
325. R. Hu, S. Li, Y. Zeng, J. Chen, S. Wang, Y. Li and G. Yang. Phys. Chem. Chem. Phys. 2011, 13, 2044-2051.
326. H. Konoshima, S. Nagao, I. Kiyota, K. Amimoto, N. Yamamoto, M. Sekine, M. Nakata, K. Furukawa and H. Sekiya. Phys. Chem. Chem. Phys. 2012, 14, 16448-16457.
327. F. A. S. Chipem, N. Dash and G. Krishnamoorthy. J. Chem. Phys 2011, 134, 104308-104316.
328. M. Mosquera, M. C. R. Rodríguez and F. Rodríguez-Prieto. J. Phys. Chem. A 1997, 101, 2766-2772.
329. M. C. R. Rodríguez, M. Mosquera and F. Rodríguez-Prieto. J. Phys. Chem. A 2001, 105, 10249-10260.
330. A. Qin, C. K. W. Jim, Y. Tang, J. W. Y. Lam, J. Liu, F. Mahta, P. Gao and B. Z. Tang. J. Phys. Chem. B 2008, 112, 9281-9288.
331. J. C. Phillips, R. Braun, W. Wang, J. Gumbart, E. Tajkhorshid, E. Villa, C. Chipot, R. D. Skeel, L. Kale and K. J. Schulten. Comput. Chem. 2005, *26*, 1781-1802.
332. W. L. Jorgensen, D. S. Maxwell and J. T. Rives. J. Am. Chem. Soc. 1996, 118, 11225—11236.
333. S. E. Feller, Y. Zhang, R. W. Pastor and B. R. Brooks. J. Chem. Phys. 1995, 103, 4613—4621.
334. G. J. Martyna, D. J. Tobias and M. L. Klein. J. Chem. Phys. 1994, 101, 4177-4189.
335. T. Darden, D. York and L. Pedersen. J. Chem. Phys. 1993, 98, 10089—10092.
336. U. Essmann, L. Perera, M. L. Berkowitz, T. Darden, H. Lee and L. G. A. Pedersen. J. Chem. Phys. 1995, 103, 8577—8593.
337. W. L. Jorgensen, J. Chandrasekhar, J. D. Madura, R. W. Impey and M. L. Klein. J. Chem. Phys. 1883, 79, 926—935.
338. W. Humphrey, A. Dalke and K. Schulten. J. Mol. Graph. 1996, 14, 33-38.

339. G. Krishnamoorthy and S. K. Dogra. J. Lumin. 2001, 92, 103-114.

340. W. L. Jorgensen, D. S. Maxwell and J. T. Rives. J. Am. Chem. Soc. 1996, 118, 11225–11236.

341. L. Martínez, R. Andrade, E. G. Birgin and J. M. Martínez. Journal of Computational Chemistry 2009, 30, 2157-2164.

342. S. Miyamoto and PA Kollman. Journal of Computational Chemistry 1992, 13, 952–962

343. T. Darden, D. York and L. Pedersen. J. Chem. Phys. 1993, 98, 10089–10092.

344. U. Essmann, L. Perera, M. L. Berkowitz, T. Darden, H. Lee and L. G. Pedersen. J. Chem. Phys. 1995, 103, 8577–8593.

345. M. P. Allen and D. J. Tildesley. Computer Simulation of Liquids. Oxford University Press, New York, 1987.

List of conference proceedings

1. **A. Malakar**, N. Dash, G Krishnamoorthy, Dual emission from 2-(4′-N, N-dimethylaminophenyl) pyridoimidazole–nanoparticle composite: Effect of β-cyclodextrin. Conference on photochemistry and Luminescence (CPL)-2012.

2. **A. Malakar**, F. A. S. Chipem, G Krishnamoorthy, Silver nanoparticles suppressed ESIPT of 2-(2'-hydroxyphenyl)benzimidazole derivatives. International Symposium on Advances in Chemical Sciences–2012.

3. **A. Malakar**, G Krishnamoorthy, Effect of silver nanoparticles on a few azole derivatives. International Conference on structural Chemistry of Molecules and Materials, (SCOMM)-2014.

4. **A. Malakar**, G Krishnamoorthy, Effect of silver nanoparticles on a set of ICT fluorophore inside BSA. Frontiers in Chemical Sciences, (FICS)-2014.

5. **A. Malakar**, G Krishnamoorthy, Aggregation Induced Enhanced Emission of 2-(2′-Hydroxyphenyl) benzimidazole. ChemConvene-2015.

6. H. T. Biswal, **A. Malakar**, G. Krishnamoorthy, Reversible association of a few ICT fluorophores with silver nanoparticles In micellar medium. 5th National Synposium On Functional Applications of colorants, (NSFAC)-2015

List of publications

1. Dual emission from 2-(4′-N, N-dimethylaminophenyl)pyridoimidazole – nanoparticle composite: Effect of β-cyclodextrin. **A. Malakar**, G. Krishnamoorthy. Journal of Colloid and Interface Science, 443, 2015, 23–29.
2. Aggregation induced enhanced emission of 2-(2'-hydroxyphenyl)benzimidazole. **A. Malakar**, M. Kumar, A. Reddy, H. T. Biswal, B. B. Mandal and G. Krishnamoorthy. Photochem. Photobiol. Sci.,
3. Interactions of a few azole derivatives with a transport protein: role of heteroatoms. A. Mishra, **A. Malakar**, H. T. Biswal, M. K. Barman and G. Krishnamoorthy, J. Mol. Recognit. 2015#
4. Intramolecular Proton Transfer in 2-(2-hydroxyphenyl)oxazolo[4,5-b]pyridine: Evidence for Tautomer in the Ground State. F. A. S. Chipem, **A. Malakar** and G. Krishnamoorthy, Photochemistry and Photobiology, 2014#
5. Metal ion dependent "ON" intramolecular charge transfer (ICT) and "OFF" normal switching of the fluorescence: Sensing of Zn^{2+} by ICT emission in living cells. N. Dash, **A. Malakar**, M. Kumar, B. B. Mandal and G. Krishnamoorthy, Sensors and Actuators B, 2014, 202, 1154–1163.#
6. N-substitution control dynamics and shape dependence in fluorescent nano aggregates: cell imaging. (Manuscript under preparation)
7. Extraction of fluorophores from nanoparticles composite by micelles. (Manuscript under preparation)
8. Effect of silver nanoparticles on a set of ICT fluorophore inside BSA. (Manuscript under preparation)
9. Silver nanoparticles suppressed ESIPT of 2-(2'-hydroxyphenyl) benzimidazole derivatives. (Manuscript under preparation)
10. Investigation of 2-(2'-hydroxyphenyl)-3H oxazo[4,5-b]pyridine in different heterogeneous environments. (Manuscript under preparation)

 # = not part of thesis